

Important Notice

This copy may be used only for the purposes of research and private study, and any use of the copy for a purpose other than research or private study may require the authorization of the copyright owner of the work in question. Responsibility regarding questions of copyright that may arise in the use of this copy is assumed by the recipient.

THE UNIVERSITY OF CALGARY

Seismic methods for heavy oil reservoir monitoring

by

Janet Helen Isaac

A DISSERTATION

SUBMITTED TO THE FACULTY OF GRADUATE STUDIES
IN PARTIAL FULFILMENT OF THE REQUIREMENTS FOR THE
DEGREE OF DOCTOR OF PHILOSOPHY

DEPARTMENT OF GEOLOGY AND GEOPHYSICS

CALGARY, ALBERTA

JULY, 1996

© Janet Helen Isaac 1996

THE UNIVERSITY OF CALGARY
FACULTY OF GRADUATE STUDIES

The undersigned certify that they have read, and recommend to the Faculty of Graduate Studies for acceptance, a dissertation entitled “Seismic methods for heavy oil reservoir monitoring” submitted by Janet Helen Isaac in partial fulfilment of the requirements for the degree of Doctor of Philosophy.

Supervisor, Dr. D. C. Lawton,
Department of Geology and Geophysics.

Dr. R. R. Stewart, Department of Geology and Geophysics.

Dr. J. C. Hopkins, Department of Geology and Geophysics.

Dr. D. G. Smith, Department of Geography.

External Examiner, Dr. G. D. Spence,
University of Victoria, B.C.

ABSTRACT

Two time-lapse three-dimensional (3-D) seismic surveys, provided by Imperial Oil from a heavy oil production area at Cold Lake, Alberta, were processed concurrently and a procedure was developed to minimise differences between them above the reservoir. Interpretation of the processed data reveals variations in interval traveltimes and reflectivity. These responses are mapped to present a spatial distribution of the interpreted steamed reservoir. Inversion of the data confirms that amplitude anomalies observed on the stacked data are caused by zones of low velocity.

Two experimental time-lapse multicomponent (3-C) surveys were also acquired. Modifications to the converted-wave processing routine included a revised method of determining the large shear-wave static corrections, iterative velocity analysis and deconvolution after normal moveout corrections. Analysis of V_p/V_s showed that this ratio is lower during steaming than during production and that, in general, lowest values are seen at the injection well locations. The average measured V_p/V_s in the cold reservoir and the lowest measured value in the heated reservoir are in excellent agreement with the theoretically calculated values. Areas of heated and cold reservoir mapped from the V_p/V_s analysis agree well with those determined from Imperial Oil's analysis of 3-D seismic data.

Selected amplitude anomalies from the two stacked 3-D seismic data sets were analysed by investigating amplitude variations with offset. In general, the AVO results confirm the interpretation of amplitude anomalies as due to low velocity zones. Analysis of data along a 3-C P - P line indicates a good correlation between positive AVO response and injection well locations.

The techniques of time-lapse 3-D, converted-wave and AVO analysis provide information complementary to that obtained through standard seismic imaging, and result in enhanced interpretations and greater confidence in the mapping of reservoir conditions.

ACKNOWLEDGEMENTS

I would like to thank my supervisor, Don Lawton, for his guidance and counsel during the course of my work. I appreciated his pragmatic approach to this project, especially during the times when progress was slow.

Imperial Oil Resources Ltd. very generously provided the seismic data used in this dissertation. In particular, Dr. John Eastwood is thanked for his support, assistance and useful suggestions.

I thank the members of the CREWES Project, especially Henry, Darren and Sue, for all their help, and the CREWES sponsors for their positive feedback on this work.

Finally, the patience of my husband, Alasdair Fergusson, should not be understated. He plied me with sherry when I was tired and crabby and acted as my taxi driver when the weather was cold or wet.

TABLE OF CONTENTS

Approval page	ii
Abstract	iii
Acknowledgements	v
Table of Contents	vi
List of Tables	ix
List of Figures	x
List of Abbreviations	xvii
Chapter 1 Introduction	1
1.1 Motivation.....	1
1.2 Dissertation objectives	2
1.3 The study area.....	3
1.3.1 Geology.....	3
1.3.2 Reservoir development at the D3 and AABBW pads.....	6
1.4 Reservoir monitoring	8
1.4.1 Theoretical and experimental studies of seismic wave velocities	8
1.4.2 Seismic reflection data experiments	10
1.4.3 Cold Lake data	12
1.5 Discussion.....	15
1.6 Data and software summary	15
1.7 Dissertation outline	16
Chapter 2 3-D seismic data acquisition and processing	18
2.1 Introduction.....	18
2.2 Concurrent 3-D seismic data processing	20
2.3 Processing flow.....	22
2.4 Discussion.....	44
Chapter 3 3-D seismic data analysis	45
3.1 Seismic data - well-log correlation	45
3.2 Forward modelling.....	50
3.3 Analysis of the processed 3-D seismic data	55

3.3.1	Traveltime analysis	55
3.3.2	Amplitude analysis.....	65
3.4	Analysis of the "difference" data volume	67
3.5	Frequency analysis.....	80
3.6	3-D inversion	85
3.7	Discussion.....	87
Chapter 4	3-C seismic data acquisition and processing	91
4.1	Introduction.....	91
4.2	Field Acquisition	92
4.3	Vertical component data processing.....	94
4.4	Radial component ray-trace modelling.....	98
4.5	Radial component data processing	101
4.5.1	Rotation analysis	101
4.5.2	Near-surface statics determination.....	104
4.5.3	Stacking velocity analysis and final section generation.....	113
4.6	Discussion.....	118
Chapter 5	3-C seismic data analysis	121
5.1	Data interpretation	121
5.1.1	Well log data	121
5.1.2	<i>P-P</i> data interpretation	123
5.1.3	<i>P-S</i> data interpretation.....	125
5.1.4	<i>P-P</i> and <i>P-S</i> line pairs	135
5.2	<i>V_p/V_s</i> analysis.....	144
5.2.1	Measured <i>V_p/V_s</i>	144
5.2.2	<i>V_p/V_s</i> prediction.....	156
5.3	<i>V_p/V_s</i> and 3-D seismic data interpretation.....	160
5.3.1	470-93 (3-C) and 126-93 (3-D).....	160
5.3.2	<i>V_p/V_s</i> and 3-D seismic data discriminant analysis.....	163
5.4	Discussion.....	167
Chapter 6	Amplitude variation with offset.....	170
6.1	Introduction.....	170
6.1.1	Data analysed	170
6.1.2	Theoretical background.....	171

6.1.3 The Chiburis method of AVO analysis.....	175
6.2 AVO modelling of Cold Lake data.....	176
6.2.1 Model and synthetic seismic gathers	176
6.2.2 Amplitude extraction.....	187
6.3 AVO analysis of Cold Lake data	195
6.3.1 3-D data selection.....	195
6.3.2 AVO analysis of 3-D data.....	203
6.3.3 AVO Analysis of <i>P-P</i> 3-C data.....	215
6.4 Discussion.....	218
Chapter 7 Conclusions	219
7.1 3-D seismic data	219
7.2 3-C seismic data.....	220
7.3 AVO analysis.....	222
7.4 Summary.....	223
References	225

LIST OF TABLES

2.1	Representative stacking velocities for the 3-D data.....	40
3.1	Statistical analysis of the amplitudes.	79
4.1	Parameters used in the ray trace modelling.	100
4.2	Predicted <i>P-S</i> stacking velocities based on V_p/V_s of 2.4 and the <i>P-P</i> stacking velocities.	104
4.3	Representative <i>P-S</i> stacking velocities for line 470-93.	113
5.1	V_p/V_s , as determined from the two alternative correlations.	130
5.2	Mean and standard deviations of data points plotted in Figures 5.23 and 5.24.....	155
5.3	Parameters used to calculate V_p/V_s over the analysed interval.	157
5.4	Reservoir condition correlation between V_p/V_s and discriminant analysis	164
6.1	Analysed amplitude anomalies from the 1990 stacked data and shallow difference data maps in Figure 6.16.....	200
6.2	Analysed amplitude anomalies from the 1992 stacked data and deep difference data maps in Figure 6.17.....	200
6.3	AVO difference values calculated for supergathers 1-6, chosen to analyse anomalies observed on the 1990 data at about 0.42 s.	211
6.4	AVO difference values calculated for supergathers 7-12, chosen to analyse anomalies observed on the 1992 data at about 0.437 s.	211
6.5	Summary of AVO results for the 3-D data.	214

LIST OF FIGURES

1.1	Cold Lake oil sands study area (after Harrison et al., 1979).....	4
1.2	Generalised stratigraphic chart for the Cold Lake area.....	5
1.3	Some results of theoretical modelling and experiments on core from the D3 pad.	13
2.1	Layout of the 3-D seismic surveys at the D3 pad.	21
2.2	Processing flow for the 3-D seismic data processing.	23
2.3	A field shot record from the 1990 survey (with 1.0 s AGC and pre-first break mutes applied).	24
2.4	Portion of the field shot record from the 1990 survey.	25
2.5	Portion of the corresponding field shot record from the 1992 survey.	26
2.6	Amplitude spectra for the (a) 1990 and (b) 1992 field shot gathers.	27
2.7	The difference between the 1990 and 1992 field shot gathers displayed in Figures 2.4 and 2.5.....	29
2.8	Plot of first break time against source-receiver offset for some of the CDPs in the centre of the survey.....	30
2.9	The same 1990 shot gather as in Figure 2.4, after deconvolution.	31
2.10	The same 1992 shot gather as in Figure 2.5, after deconvolution.	32
2.11	Amplitude spectra for the (a) 1990 and (b) 1992 deconvolved records.....	33
2.12	The difference between the 1990 and 1992 deconvolved gathers displayed in Figures 2.9 and 2.10.	34
2.13	Offset ranges for CDPs in the centre of the survey.....	36
2.14	The range of azimuths stacked at 234 CDP locations in the centre of the survey.	37
2.15	Four windowed semblance plots used in velocity analysis.....	38
2.16	Some results of the difference analysis used during data processing.	42
2.17	Normalised rms amplitudes of residual data sets after application of varying bulk shifts to the 1992 data.	43
3.1	Initial identification of seismic reflectors from the OB5 well log correlation.	46
3.2	Correlation of seismic data with sonic logs using the extracted wavelet, which is displayed at the upper left.....	49

3.3	The initial sonic log from OB5 with three modifications used for the forward modelling.	52
3.4	Synthetic seismic sections generated by forward modelling.	54
3.5	Reprocessed, migrated crossline 50 from the centre of the (a) 1990 and (b) 1992 data volumes.	56
3.6	Reprocessed, migrated inline 34 from the centre of the (a) 1990 and (b) 1992 data volumes.	57
3.7	The Clearwater to Devonian isochron traveltimes from the (a) 1990 and (b) 1992 data sets.	62
3.8	Traveltime differences for the Devonian event.	63
3.9	The time structure differences between the 1992 and 1990 data sets for the top Clearwater event.	64
3.10	Plot of traveltime delay versus thickness of steamed zone for three values of steamed zone interval velocity.	65
3.11	Scaled rms amplitudes of the seismic data calculated over a 10 ms window.	66
3.12	The differences between the 1992 and 1990 data along crossline 50, displayed in Figure 3.5.	68
3.13	The differences between the 1992 and 1990 data along inline 34, displayed in Figure 3.6.	69
3.14	Amplitudes of the Devonian event for the (a) 1990 and (b) 1992 data.	72
3.15	Residual amplitudes between the 1990 and 1992 surveys of the (a) Devonian event and (b) Clearwater event.	73
3.16	Rms amplitudes extracted from the "difference" data volume over a 10 ms window centred on (a) 0.420 s and (b) 0.437 s, within the reservoir zone.	74
3.17	Map view of the rms amplitudes calculated over a 50 ms window extracted from the "difference" data volume (a) above and (b) within the reservoir.	77
3.18	Map showing the combination of Clearwater-Devonian interval traveltime anomalies and rms amplitudes from the "difference" data set.	78
3.19	Average instantaneous frequency measured in a zone above the reservoir from the (a) 1990 and (b) 1992 data.	83

3.20	Average instantaneous frequency measured over the Clearwater to Devonian interval from the (a) 1990 and (b) 1992 data.....	84
3.21	Inversion at the location of the OB5 well on inline 38.	89
3.22	Seismic data and inversion for part of inline 35.	90
4.1	Layout of the 3-C seismic survey over the AABBW pads with the locations of two wells for which sonic log data were available initially.	92
4.2	Sketch of <i>P-P</i> raypaths, from a shot S1 on line 469, and <i>P-S</i> raypaths, from a shot S2 on line 468.	93
4.3	(a) A raw shot gather (with an AGC of window length 0.05 s) and (b) the same gather after application of statics and <i>f-k</i> filtering.	96
4.4	Final migrated <i>P-P</i> section for line 470 from the 1993 survey.	97
4.5	<i>P</i> - and <i>S</i> -wave sonic velocities, obtained from dipole logs in well BB13a, and the corresponding V_p/V_s	99
4.6	Synthetic shot gather of <i>P-S</i> energy, modelled by ray-tracing.	100
4.7	Processing flow for <i>P-S</i> data.	102
4.8	A shot gather of the radial component from line 469-93.	105
4.9	Receiver gather of the radial component from line 470-93.	107
4.10	Two receiver gathers from the 1994 survey showing (a) low frequency coherent noise and (b) incoherent noise and <i>P</i> -wave energy overwhelming the <i>P-S</i> data.	110
4.11	The stacked 1993 receiver gathers, (a) before and (b) after alignment of the high amplitude event at 1.2 s and (c) the 1994 aligned receiver gather.	111
4.12	Comparison of values of <i>P</i> -wave and <i>S</i> -wave receiver statics for the vertical and radial components, respectively, of line 470-93.	112
4.13	The same shot gather as in Figure 4.8 but with receiver statics applied.	112
4.14	Frequency spectra of raw records from the (a) vertical and (b) radial components and the spectra of the final migrated sections from the (c) vertical and (d) radial components of line 470-93.	115
4.15	Plot of offsets as a function of depth for the <i>P-S</i> data.	116
4.16	Final fold of data at (a) each CDP along the vertical component section and at (b) each CCP along the radial component section of line 470-94.	117
4.17	Final migrated <i>P-S</i> section for line 470-93.	120

5.1	Tie between synthetic <i>P-P</i> seismogram and line 470-94- <i>P-P</i> .	123
5.2	Interpreted line 470-93- <i>P-P</i>	126
5.3	Interpreted line 470-94- <i>P-P</i> .	127
5.4	Line 126-93 extracted from the 1993 3-D survey.	128
5.5	Tie between <i>P-S</i> synthetic seismogram and part of line 470-93- <i>P-S</i> .	129
5.6	Two alternative correlations between the <i>P-P</i> and <i>P-S</i> components of line 470-93.	131
5.7	Interpreted line 470-93- <i>P-S</i> .	133
5.8	Interpreted line 470-94- <i>P-S</i> .	134
5.9	Locations of the injection and production wells and the three pairs of lines analysed: 469 and 468, 470, 471 and 472.	135
5.10	Example of the ties between the <i>P-P</i> data and <i>P-S</i> data for line 470 from the (a) 1993 and (b) 1994 surveys.	137
5.11	Lines 469- <i>P-P</i> and 468- <i>P-S</i> from the 1993 survey.	138
5.12	Lines 469- <i>P-P</i> and 468- <i>P-S</i> from the 1994 survey.	139
5.13	Lines 470- <i>P-P</i> and 470- <i>P-S</i> from the 1993 survey.	140
5.14	Lines 470- <i>P-P</i> and 470- <i>P-S</i> from the 1994 survey.	141
5.15	Lines 471- <i>P-P</i> and 472- <i>P-S</i> from the 1993 survey.	142
5.16	Lines 471- <i>P-P</i> and 472- <i>P-S</i> from the 1994 survey.	143
5.17	Measured values of V_p/V_s from line 470- <i>P-P</i> and 470- <i>P-S</i> for the 1993 data.	147
5.18	Measured values of V_p/V_s from line 470- <i>P-P</i> and 470- <i>P-S</i> for the 1994 data.	148
5.19	Measured values of V_p/V_s from line 469- <i>P-P</i> and 468- <i>P-S</i> for the (a) 1993 and (b) 1994 data.	149
5.20	Measured values of V_p/V_s from line 471- <i>P-P</i> and 472- <i>P-S</i> for the (a) 1993 and (b) 1994 data.	150
5.21	Ratio of V_p/V_s from the 1993 survey to V_p/V_s from the 1994 survey along line 470.	151
5.22	Contoured V_p/V_s from the three pairs of seismic lines analysed for (a) the 1993 data and (b) the 1994 data.	152
5.23	V_p/V_s plotted against <i>P-P</i> one-way interval traveltimes along line 470 in (a) 1993 and (b) 1994.	153
5.24	V_p/V_s plotted against <i>P-S</i> upcoming interval traveltimes along line 470 in (a) 1993 and (b) 1994.	155

5.25	Plot of thickness of steamed zone versus theoretical V_p/V_s for steamed zone P -wave interval velocities of 1650, 1800 and 2000 m/s.	158
5.26	Model for steamed reservoir interval of thickness d m.	159
5.27	Minimum thickness of steamed zone, calculated from V_p/V_s along line 470-93 and using an interval velocity of 1650 m/s for the steamed zone.	160
5.28	Plots of V_p/V_s along line 470-93 from the 3-C survey and average absolute amplitudes extracted from line 126-93 from the 3-D survey.	161
5.29	Plot of V_p/V_s measured along line 470-93 from the 3-C survey against average absolute amplitudes extracted from line 126-93 from the 3-D survey.	162
5.30	Plot showing the agreement between heated and cold zones as interpreted from V_p/V_s analysis and those zones as determined from the discriminant analysis of seismic attributes done by Imperial Oil for the 1993 data.	165
5.31	Plot showing the agreement between heated and cold zones as interpreted from V_p/V_s analysis and those zones as determined from the discriminant analysis of seismic attributes done by Imperial Oil for the 1994 data.	166
6.1	Plot of Poisson's ratio versus V_p/V_s	173
6.2	Plot of V_p/V_s against gas saturation (after Ostrander, 1984).	173
6.3	Plot of P -wave reflection coefficient versus angle of incidence.	174
6.4	Plots of the P -wave and S -wave sonic logs and calculated Poisson's ratios used to generate the synthetic seismic offset gather displayed.	180
6.5	Plots of the P -wave and S -wave sonic logs and calculated Poisson's ratios used to generate the synthetic seismic offset gather displayed.	181
6.6	Synthetic offset gathers generated from gas models.	183
6.7	Synthetic offset gathers generated from steam models.	184
6.8	An interpreted gas anomaly in the 1990 stacked data and the synthetic stacked section created from the model with gas below a tight streak (case b).	186
6.9	An interpreted steam anomaly in the 1992 data and the synthetic stacked section created from a model with a 6 m steamed zone at the perforation depth (case d).	186
6.10	Model for the McMurray/Devonian interface, which occurs at 530 m.	187

6.11	Modelled amplitudes extracted from the synthetic seismic gathers over 10 ms windows.....	190
6.12	Modelled rms amplitudes for the Devonian (reference) event.	191
6.13	Modelled conditioned amplitude ratios for the gas cases.	192
6.14	Modelled conditioned amplitude ratios for the steam cases.	193
6.15	Modelled conditioned amplitude ratios from synthetic seismic data created with extracted wavelet (2), from the 3-C data.	194
6.16	Analysed anomalies from the (a) 1990 time amplitude map and (b) shallow difference amplitude map, over a 10 ms window centred on a time of 0.42 s.....	198
6.17	Analysed anomalies from the (a) 1992 time amplitude map and (b) deep difference amplitude map, over a 10 ms window centred on a time of 0.437 s.	199
6.18	Examples (numbered) of amplitude anomalies selected from the 1990 amplitude and shallow difference amplitude maps.....	201
6.19	Examples (numbered) of amplitude anomalies selected from the 1992 amplitude and deep difference amplitude maps.....	202
6.20	Supergather 6, created to analyse an amplitude anomaly observed on the 1990 stacked data but not on the 1992 data.	204
6.21	Supergather 11, created to analyse an amplitude anomaly observed on the 1992 stacked data but not on the 1990 data.	205
6.22	Plot of the (a) raw amplitudes of the target and reference events and the (b) conditioned amplitude ratio.....	206
6.23	Plots of conditioned amplitude ratio against offset squared (after Chiburis, 1984 and 1993) for supergathers 1 to 6, extracted from the 1990 data.	207
6.24	Plots of conditioned amplitude ratio against offset squared for supergathers 1 to 6, extracted from the 1990 data.	207
6.25	Plots of conditioned amplitude ratio against offset squared for supergathers 1 to 6, extracted from the 1992 data.	208
6.26	Plots of conditioned amplitude ratio against offset squared for supergathers 7 to 12, extracted from the 1992 data.	210
6.27	Plots of conditioned amplitude ratio against offset squared for supergathers 7 to 12, extracted from the 1990 data.	210
6.28	Chiburis AVO values for line 470-93.	216

6.29	Plot of AVO value against V_p/V_s for line 470-93.....	217
6.30	Plot of AVO value for line 470-93 against scaled average amplitude for line 126-93 extracted from the 3-D survey.	217

LIST OF ABBREVIATIONS

3-C	Three-component
3-D	Three-dimensional
AGC	Automatic gain control
AVO	Amplitude variation with offset
bopd	Barrels of oil per day
CCP	Common conversion point
CDP	Common depth point
CSS	Cyclical steam stimulation
$f-k$	Frequency-wavenumber
$f-x$	Frequency-distance
Hz	Hertz
MPa	MegaPascal
NMO	Normal moveout
Pa.s	Pascal.second
P -wave	Compressional-wave
S -wave	Shear-wave
rms	Root mean square
V_p	Compressional-wave velocity
V_s	Shear-wave velocity

Chapter 1

INTRODUCTION

1.1 Motivation

The Western Canadian Sedimentary Basin holds major reserves of hydrocarbons, including large deposits of heavy oil. Maximum recovery of the established resources entails knowledge of many factors, including geological parameters such as reservoir geometry and continuity, lithology and pore fluid distribution. Seismic techniques are used extensively in hydrocarbon exploration to predict gross reservoir features but to a lesser extent in exploitation, where detailed knowledge of reservoirs is necessary for optimum development. A challenge to geophysicists, therefore, is to utilise all available techniques to extract as much detailed information as possible from seismic data. The benefit of this will be more realistic reservoir models and, consequently, better reservoir management. New techniques, such as multicomponent seismic methods, which have the potential to be beneficial, need to be proved effective before they will be widely accepted.

Conventional geological and engineering data are acquired at individual control points (wells) whereas for accurate reservoir modelling, estimates must be made of the lateral and vertical distribution of the important parameters throughout the reservoir. During enhanced oil recovery (EOR) operations, which involve injection of fluids into the reservoir, it is important to understand the volumetric distribution of the target hydrocarbons which have been contacted by the injected fluids. Seismic reflection data, three-dimensional (3-D) in particular, provide a way of estimating reservoir parameters away from the wells. The benefits of using 3-D seismic data in reservoir surveillance are being acknowledged and it is expected that seismic techniques will play an increasingly greater role in reservoir development (White and Sengbush, 1987; Nur, 1989; Nolen-Hoeksema, 1990). Seismic data resolution is lower than that achieved from core data or

well logs, and interpretations are sometimes ambiguous. However, the volumetric information obtained from seismic data can be invaluable for estimating reservoir properties away from well locations.

At Cold Lake, Alberta, Imperial Oil Resources Limited has put in place a major programme to develop the bitumen contained in oil sands. The EOR technique used here is that of cyclical steam stimulation of the reservoir. It has been demonstrated theoretically (e.g., Wang and Nur, 1990) and in practice (den Boer and Matthews, 1988; de Buyl, 1989) that 3-D seismic data can be a useful tool in monitoring steam-injection EOR processes. Integration of information obtained from seismic data into reservoir models at Cold Lake should enable these models to predict more accurately the lateral continuity of reservoir parameters.

1.2 Dissertation objectives

The main objective of this dissertation is to investigate the applicability of different seismic methods to reservoir monitoring at Cold Lake. Two time-lapse three-dimensional seismic surveys and two experimental time-lapse converted-wave (3-C) seismic surveys were acquired by Imperial Oil Resources Ltd. over neighbouring production pads at Cold Lake. The first goal is to develop a 3-D data processing scheme that results in the two 3-D data volumes having similar seismic character above the reservoir zone. By demonstrating repeatability above the reservoir, any variances between the two data sets within or below the reservoir itself are attributed to changes in reservoir conditions between the times of acquisition of the surveys. Assessment of these variances is undertaken, with the objective of mapping spatially those areas of the reservoir most likely to have been steamed.

The purpose of the study of converted-wave seismic data at Cold Lake is to determine whether the analysis of such data enhances the interpretation of conventional

compressional-wave seismic data. The approach involves processing the data to obtain interpretable stacked *P-P* (incident compressional-wave; reflected compressional-wave) and *P-S* (incident compressional-wave; reflected shear-wave) sections. The objective of deriving compressional-wave to shear-wave velocity ratios from these data is to show their significance in the prediction of the lateral extent of heated reservoir.

The final purpose of this dissertation is to evaluate the method of amplitude variation with offset (AVO) analysis for the identification of low velocity intervals in the reservoir. The ultimate objective is to demonstrate that use of these specialised seismic techniques (time-lapse 3-D, converted-wave data and AVO analysis) enhances the interpretation of the conventional compressional-wave seismic data, thus providing refined input into the reservoir models.

1.3 The study area

1.3.1 Geology

The Cold Lake oil sands occur in East Central Alberta and are part of the trend of Lower Cretaceous heavy oil deposits that are found in the eastern part of the Western Canadian Sedimentary Basin (WCSB). They cover an area of about 6,500 km², from Twp. 52, Rge. 4, W4M to Twp. 67, Rge. 10, W4M (Figure 1.1) and are second only to the Athabasca heavy oil deposits in size. In this study, the specific areas of interest are the D3 production pad in Range 4 and the AA, BB and W (henceforth referred to as AABBW) production pads in Range 3, both in Township 65, W4M. The locations of these pads are shown in Figure 1.1.

The hydrocarbons at Cold Lake are classified as bitumen rather than heavy oil because the viscosity (100 Pa.s at 30°C) is too high for primary production. The bitumen contained in the oil sands deposits in Alberta decreases in gravity northwards to the shallower parts of the WCSB (to as low as 6 °API at Athabasca), in conjunction with a

decrease in water salinity and an increase in sulphur content. The decrease in gravity, loss of paraffins and increase in sulphur content are interpreted to indicate progressive biodegradation of the oils by bacteria. Reserves are estimated by the Energy Resources Conservation Board to be $34 \times 10^9 \text{ m}^3$ of bitumen in place. The oil sands accumulations at Cold Lake are structurally controlled; sands to the east and west of the main deposit are wet because they are structurally low. Oil saturation is controlled by the amount of clay present, the presence of shale interbeds and the structural elevation of the reservoir.

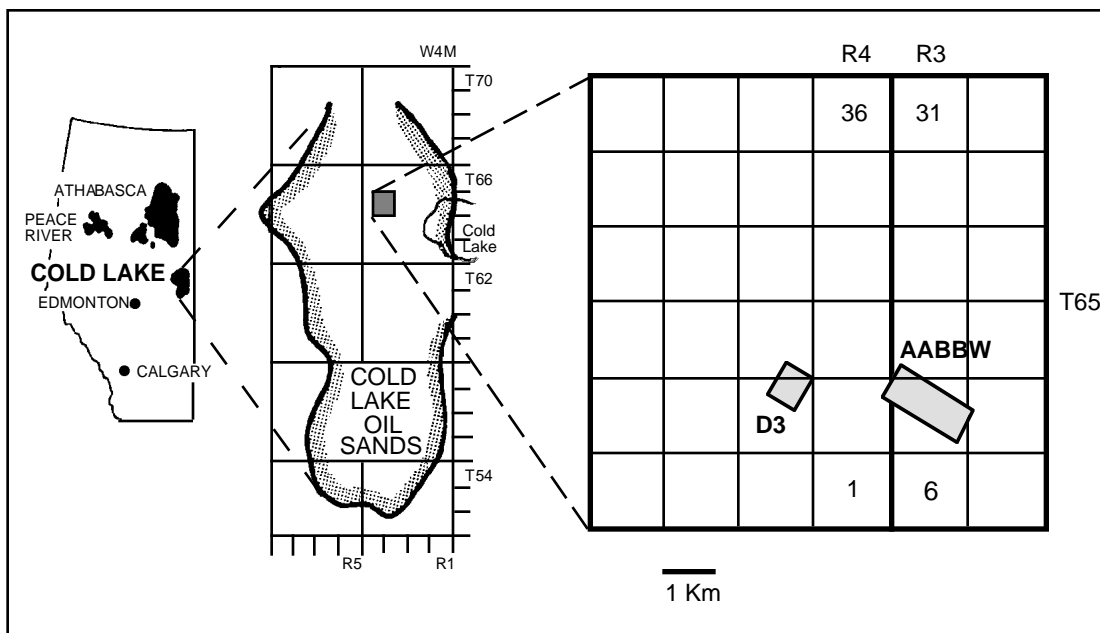


Fig. 1.1 Cold Lake oil sands study area (after Harrison et al., 1979).

A generalised stratigraphic column for the Cold Lake area is shown in Figure 1.2. The oil sands are contained within the Lower Cretaceous Mannville Group. Mannville Group sediments were deposited near the eastern edge of the WCSB on the Palaeozoic erosional surface. The Lower Mannville (McMurray Formation) is dominated by sediments, derived from the Precambrian shield to the east, which infilled the Palaeozoic

topography. They were mainly fluvial deposits but became marine as the Cretaceous Boreal sea transgressed southwards. Sediments derived from the Cordilleran region to the west dominate the Upper Mannville (Clearwater and Grand Rapids formations) and are generally nearshore or deltaic. Transgressing seas subsequently engulfed the area and shales of the Colorado Group were deposited over the Mannville sands, creating a reservoir seal (Harrison et al., 1979; Rühl, 1982; Putnam and Pedskalny, 1983).

Depth (m GL)			Lithology	
100	Quaternary		glacial till	
200	Cretaceous	Colorado Group	La Biche	
			Viking	sandstone
			Joli Fou	shale
400		Mannville Group	Grand Rapids	sandstone and shale
			Clearwater	sandstone
	McMurray		sandstone and shale	
600	Devonian		carbonates	

Fig. 1.2 Generalised stratigraphic chart for the Cold Lake area.

The primary reservoir in the Upper Mannville is the Clearwater Formation, which contains about 33% of the reserves at Cold Lake (Gallant and Dawson, 1988). The Clearwater Formation is a transgressive wedge, ranging in thickness at Cold Lake from 61 m in the north to 6 m in the south. Most of this formation at Cold Lake was deposited in a lowstand systems tract having two depositional settings: deltaic and foreshore/shoreface. The deltaic deposits are predominantly sandstones deposited in distributary channel, interdistributary mouth bar and delta front environments. The

deltaic system is river dominated and the best reservoir occurs where outer distributary mouth bar sequences are stacked vertically within parasequence sets (Taylor, 1990). Both the resource distribution and reservoir performance are affected by the quality of the sand. At the D3 pad, where the time-lapse 3-D seismic data were acquired, the environment of deposition is interpreted, on the basis of core analyses and log correlations by Imperial Oil geologists, to be tidal/estuarine.

Esso Resources Canada Ltd. (now Imperial Oil Resources Ltd.) acquired permits at Cold Lake in 1959 and began a research, exploration and development programme in 1963 to develop the Clearwater sands. In 1975 the Leming pilot plant was opened, commercial production began in 1985, and by 1989 production had reached 14,300 m³/d of oil or 90,000 bopd (Robinson and Jessop, 1990). Imperial Oil currently produces 15,900 m³/d of oil (100,000 bopd) at Cold Lake.

The Clearwater sands at the Cold Lake D3 pad have an average porosity of 32% and permeability of about 1 Darcy (Eastwood et al., 1994). The sands have a gross thickness of 55 m and are at depths of 420-475 m. They are highly saturated with bitumen, which is of low specific gravity (1000 kg/m³ or 10° API) and high viscosity (100 Pa.s at 30°C). Surface mining methods are impossible because of the depth of the reservoir and the viscosity is too high for primary production. In order to produce the bitumen, therefore, the reservoir must be stimulated by an in-situ thermal recovery process.

1.3.2 Reservoir development at the D3 and AABBW pads

At the D3 and AABBW pads the reservoir is heated by steam injection in order to reduce the viscosity of the bitumen (to .006 Pa.s at 200°C) and allow it to be lifted to the surface using an artificial lift system. The process, known as cyclical steam stimulation (CSS), initially involved a 30-50 day injection period followed by a production period of

about a year, the same wells being used for both injection and production. As CSS progresses, the length of each cycle increases as the heated bitumen becomes harder to extract. At the beginning of the D3 pad development in 1985, it was expected that ten CSS cycles would be needed to recover 20% of the bitumen in place. Steam is injected into the reservoir at a fluid pressures up to 8-10 MPa and at temperatures as high as 315°C. The cold reservoir temperature is 15°C, whereas reservoir temperatures measured at injection/production wells during a production phase varied from 120°C to 200°C. At Cold Lake the bitumen has to be heated to at least 75°C before it will flow.

The recovery level of bitumen from the Clearwater sands is a function of areal and vertical conformance and the displacement efficiency. Displacement efficiency is mainly dependent on the recovery process and for CSS is impaired because of the resaturation during production of zones swept of bitumen during the injection cycle (Boone et al., 1993). When injection takes place at rates below the fracture pressure, the formation's effective permeability to steam and water is the primary control over the distribution of heat in the reservoir. Injection of steam into the bitumen-saturated formation takes place by parting or fracturing of the tar sand (Tortike and Farouq Ali, 1990). Ideally the parting would occur in the relatively cool, unswept bitumen zones. However, the steam flows preferentially through the relatively hot and bitumen-depleted high-permeability channels which have developed in the reservoir during CSS (Boone et al., 1993). As a result, the reservoir is not swept efficiently and some bitumen remains unrecovered. The inhomogeneity of the steam penetration at the D3 pad is confirmed by monitoring at observation wells, in which low temperatures have been recorded during steam injection cycles. The parting orientation and consequent channel development are functions of local parameters such as lithology, pore pressure, material properties and stress fields. The presence of diagenetic calcite cemented tight streaks in the reservoir plays a significant role in inhibiting the vertical and lateral movement of the steam.

At the D3 pad Imperial Oil has experimented with high pressure injection to induce horizontal fracturing. It is hoped to divert the heat from the channels and into the cooler parts of the reservoir. During injection cycle seven, the volume of injected steam at D3-8 was increased to 19,000 m³, from 8,000 m³ during each of the first six cycles. The high rate of steam injection appears to have induced fracturing and increased rapidly the areal thermal conformance. The fractures are expected to remain horizontal over a radial distance of at least 80 m from the injector wells (Boone et al., 1993).

Following several cycles of CSS at the AABBW pads, further development was undertaken to increase recovery. Horizontal injection wells were drilled at the AA pad in 1990 and steaming initiated in 1991. At the BB and W pads, infill wells were drilled in 1988 to halve the original well spacing.

1.4 Reservoir monitoring

1.4.1 Theoretical and experimental studies of seismic wave velocities

Physical properties affecting seismic wave velocities in a rock include the elastic constants of the rock, porosity, pore fluid characteristics, pore geometry, consolidation, hydrocarbon saturation and effective pressure. During thermal EOR processes some of these parameters are changed, resulting in changes in seismic velocity and acoustic impedance. Some of the most relevant changes are those of pressure and compressibility of the pore fluid.

It has been shown, experimentally and theoretically (Hicks and Berry, 1956), that a decrease in the difference between overburden pressure and pore fluid pressure (known as effective or differential pressure) results in a decrease in compressional-wave (*P*-wave) velocity. The high pore fluid pressures generated by thermal volume expansion of heavy oils were found experimentally to affect *P*-wave velocity (Wang and Nur, 1988a). Abnormally high pore pressure in unconsolidated rocks containing wax caused the

compressional-wave velocities to decrease rapidly; this effect was smaller in consolidated rocks. Thus, an increase in pore fluid pressure, which occurs during steam injection, will cause a decrease in effective pressure and a corresponding decrease in *P*-wave velocity.

Laboratory measurements of seismic velocities in heavy oil-saturated rock samples have been carried out (e.g., Nur et al., 1984; Nur, 1987); some specifically in relation to thermal EOR projects (Tosaya et al., 1987; Wang and Nur, 1988a and b). The results of these experiments show that, in general, compressional-wave velocities in heavy hydrocarbon-saturated rocks decrease with increasing temperature. However, the amount of velocity decrease depends on the composition and viscosity of the hydrocarbons in the sample and on the nature of the host rock, and so is unique for each sample.

Over a temperature range of 20°C to 130°C, Wang and Nur (1988b) observed velocity decreases in heavy hydrocarbon-saturated sands of 15% to 30%, and in heavy hydrocarbon-saturated sandstones of 9% to 22%. They suggested that the observed temperature dependency of velocity in hydrocarbon-saturated rocks is not sensitive to frequency, therefore similar effects to those obtained at ultrasonic frequencies in the laboratory should be expected at seismic frequencies. Measured velocity decreases in heavy oils were determined to be caused chiefly by the increasing compressibility of the fluid with increasing temperature (Wang and Nur, 1992). These authors also concluded that velocity changes in reservoirs associated with EOR processes may be caused by changes in temperature and the resulting changes in the compressibility of the pore fluids. Other factors that could also affect velocity are pore fluid pressure changes and certain production processes, such as those causing the formation of gas and causing pressure depletion. Most of the laboratory experiments indicated a decrease in shear-wave velocity with increasing temperature although the effect was not as substantial as for compressional-waves. However, none of the published data referred to above includes

experimental results for shear-wave (*S*-wave) velocities in bitumen-saturated unconsolidated sands such as those found at Cold Lake.

Ito et al. (1979) measured compressional- and shear-wave velocities (V_p and V_s , respectively) in water-filled Berea sandstone samples as the water converted to steam with a decrease in pore pressure. Temperature and confining pressure were kept constant, at values simulating those of reservoir conditions. Their results showed that V_p changed abruptly to a lower value at the water/steam transition while V_s changed smoothly to a higher value. They also found that V_p/V_s was lower during the steam phase, dropping from the values measured during the water phase by about 13% at 198°C and 16% at 145°C. The bulk modulus of the medium was higher during the water phase, because of the higher bulk modulus of water compared to steam, while the shear modulus was unchanged.

Paulsson et al. (1994) cautioned that actual reservoir temperatures cannot be determined from seismically-derived velocities but that knowledge of heat movement can be obtained. The velocity response to temperature changes is a function of several factors, including the bitumen saturation, and will vary throughout a reservoir.

1.4.2 Seismic reflection data experiments

The application of seismic reflection data to steam-based EOR projects began in the 1980s. Britton et al. (1983) found that velocity anomalies at steam injection wells in a steam-flooded zone at the Street Ranch steam flooding pilot in Texas were clearly visible on seismic data.

Time-lapse (repeated) seismic surveys were used to monitor heat movement at the Gregoire Lake in-situ steam pilot (GLISP) in Athabasca, Alberta, where the McMurray reservoir sands are subject to a steam stimulation process. A base survey was acquired prior to injection (Pullin et al., 1987) and monitoring surveys were acquired after

injection. Den Boer and Matthews (1988) interpreted interval transit time anomalies measured from the seismic reflection data and found excellent correlations between the locations of steam injection wells and the position of interval transit time anomalies. They stated that the shape of these anomalies could be used to infer the direction of steam movement and the extent of penetration of steam into the reservoir, but that the vertical location of heated zones could not be determined from the travelttime analysis. Reflection amplitude changes were also observed and were attributed to lowered acoustic impedances in the heated zones. Travelttime inversion of these data (Lines et al., 1989) validated the existence of the interpreted low velocity zones obtained from the interval transit time analysis.

Greaves and Fulp (1987) utilised time-lapse 3-D seismic data to monitor the propagation of a fire-flood process in Texas. Anomalous reflection amplitudes at the top of the reservoir were interpreted to represent the extent of the combustion; an interpretation confirmed by post-burn well data and cores. Difference data sets were created by subtracting time-lapse data volumes to monitor the propagation of the heat through time.

Laine (1987) showed that seismic tomography methods can be used to observe changes at a heavy oil steam-flood. Significant reductions in *P*-wave velocity were demonstrated by seismic tomography studies in heavy oil reservoirs undergoing steam injection (Paulsson et al., 1992; Paulsson et al., 1994) and at a fire-flood site (Bregman et al., 1989). Tomography studies of the Clearwater sands at Cold Lake (Macrides et al., 1988) indicated that measurable decreases in *P*-wave velocity should occur with steam injection. They also proposed that the spatial occurrence of velocity anomalies and frequency attenuation could be used to infer the distribution of the steam phase.

1.4.3 Cold Lake data

At Cold Lake the original reservoir temperature before CSS was 15°C and the original in-situ vertical stress at the perforation depth of well D3-8 has been estimated to be 9.7 MPa (Boone et al., 1993). Steam was injected into the reservoir at a temperature of 315°C and fluid pressure of 10 MPa at the D3 pad in 1990 and at a temperature of about 280°C and fluid pressure of 4-6.5 MPa at the AABBW pads in 1993. Temperatures are higher and fluid pressures lower during production but these values at the well locations do not return to those of the original cold reservoir. During one production survey at the AABBW pads, fluid pressures of 2-3 MPa and temperatures around 120°C were recorded in the wells at the perforation depth. Other parts of the reservoir away from the wells, however, may still be cold. Thus, two important factors that can contribute significantly to lower compressional-wave velocities, increased temperature and decreased effective stress, are present during steam injection cycles.

To investigate the magnitude of changes in velocity that might be expected at the D3 pad, Eastwood (1993) compared theoretical model predictions of seismic wave propagation with results obtained from experiments on ultrasonic velocities in core samples from the pad. His theoretical seismic wave propagation models predict a significant decrease in the *P*-wave velocity and a very small increase in the *S*-wave velocity of the sands for a temperature rise from 22°C to 125°C at a constant effective pressure. The theoretical and experimental results for *P*-wave velocities agree to within 5% for this temperature range; experimental results for *S*-wave velocities were not obtained.

For a temperature increase from 22°C to 200°C at a constant effective pressure of 1 MPa, the theory predicts a major fall in *P*-wave velocity from 2130 m/s to 1660 m/s. At a constant effective pressure of 8 MPa, the *P*-wave velocity falls from 2330 m/s to 1960 m/s. Figure 1.3 shows a graph compiled from Eastwood's work.

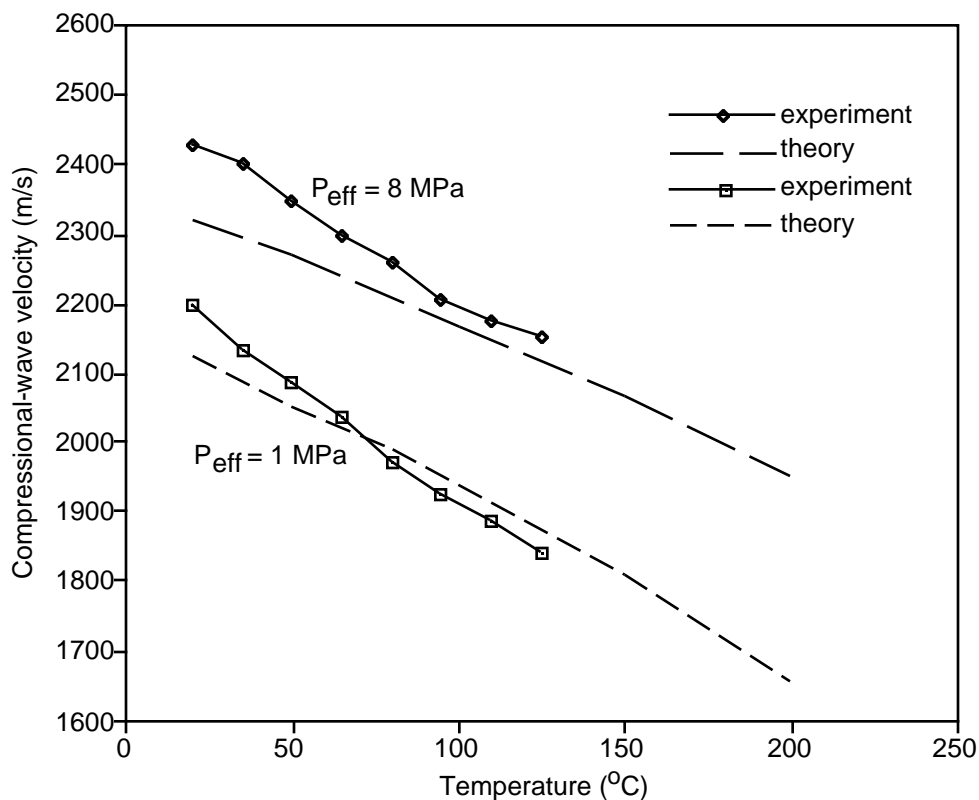


Fig. 1.3 Some results of theoretical modelling and experiments on core from the D3 pad. The results show significant decreases in P -wave velocity with increasing temperature at effective pressures of 1 MPa and 8 MPa (after Eastwood, 1993).

Plotted are his experimental and theoretical results, for effective pressures of 8 MPa and 1 MPa. For both theoretical and experimental results the P -wave velocity decreases substantially, although the values are not the same. Assuming cold reservoir conditions to be a temperature of 15°C and effective pressure of 8 MPa, this previous work implies a cold reservoir velocity of 2300 m/s - 2400 m/s. During and after steam injection, reservoir temperatures are in excess of 200°C and effective stress is reduced to near 1 MPa. Temperatures in the heated reservoir may, therefore, be as low as 1650 m/s - 1700 m/s.

Gas comes out of solution during the production phase. A series of laboratory experiments was performed for Imperial Oil Resources Ltd. to investigate the effect on

seismic velocities of different amounts of gas saturation in the Cold Lake oil sands. As could be predicted by Biot-Gassmann theory, a small percentage (less than 5% of the pore space) of gas causes a significant reduction in the effective bulk modulus of the pore fluid and hence a decrease in compressional-wave velocity. The experiments showed a decrease in *P*-wave velocity from 2400 m/s at zero gas saturation to 2175 m/s at 5% gas saturation and to 2100 m/s at 10% gas saturation in these bitumen sands. An appreciable decrease in *P*-wave velocity was measured for as little as 2% gas saturation. Eastwood (*pers. comm.*) reports a theoretical decrease in *P*-wave velocity for the Cold Lake oil sands from 2350 m/s to 1850 m/s when gas saturation is greater than 2-5% and suggests that a velocity anomaly should be apparent on the seismic data for a gas saturation of over 2%.

The behaviour of shear-wave velocities under steaming conditions is less well understood than that of compressional-wave velocities. Theoretical modelling by Eastwood (1993) predicts a small rise in *S*-wave velocity from 1180 m/s to 1190 m/s over a temperature range of 22°C to 200 °C at a constant effective pressure of 1 MPa. Wang and Nur (1990), however, observed an *S*-wave velocity decrease with increasing temperature in tar sands and attributed this to the decrease in shear modulus. They also observed decreases in *V_s* with decreasing effective pressure. Overall, the combined effect of temperature and stress on the bitumen-saturated unconsolidated Clearwater sands is not well understood. Physical experiments on samples from Cold Lake may help in the prediction of *S*-wave velocity behaviour during and after steam injection.

It has already been shown that 3-D seismic methods are appropriate for use in reservoir monitoring at Cold Lake. The original processed 3-D seismic data at the D3 pad were analysed for interval transit time delays, amplitude variations and frequency attenuation (Eastwood et al., 1994). Attributes such as these were combined to produce an areal conformance map for the 1990 data set. The distribution of heated reservoir as

predicted from the seismic data was found to correlate well with that of the reservoir simulation model. Spectral analysis of the two data sets (Dilay and Eastwood, 1995) revealed attenuated zones, particularly beneath reservoir intervals that were gas-saturated during the production phase.

1.5 Discussion

Theoretical and experimental studies on heavy oil-saturated sandstones predict that a measurable decrease in compressional-wave velocity will occur after the introduction of steam into a reservoir, due to the conditions of increased temperature and increased pore fluid pressure. Some pilot studies using 3-D seismic data to monitor EOR projects in Alberta have produced encouraging results.

Results of theoretical and modelling studies on the Cold Lake bitumen sands by Eastwood (1993) indicated that a significant, measurable response to steam injection should be observed on conventional reflection seismic data because of the lowered compressional-wave velocity. Both interval transit time delays and seismic reflectivity changes associated with steamed zones may be expected. Although the response to steam of the *S*-wave velocities is not well known, theoretically predicted shear-wave velocity changes are very small. Values of V_p/V_s or Poisson's ratio, determined from seismic data at Cold Lake, may therefore be useful for investigating *P*-wave velocity variations in the reservoir. Geological data show that other factors affecting V_p/V_s , such as changes in porosity and lithology, vary much less significantly than does the temperature across the area covered by the seismic surveys in this study area.

1.6 Data and software summary

The seismic data used in this dissertation are courtesy of Imperial Oil Resources Ltd. Two time-lapse 3-D and two experimental time-lapse 3-C seismic surveys were

donated to the CREWES Project in the form of raw field data, with survey information and observer's notes. Processed versions of the 3-D data, processed by an outside contractor, were also supplied. Migrated data and extracted attributes for one seismic line from a 3-D survey, corresponding to a line of 3-C data, were made available. Well data (sonic and density logs) and well logs correlations from Imperial Oil were also used.

All the seismic data were processed using Landmark/IT&A software. The seismic data were interpreted and analysed using Landmark Seisworks3D and Photon SeisX interpretation software. 3-D fold, offset and azimuth plots were generated by FDTools (Seismic Images Software). Three Hampson-Russell software packages were utilised: GLI3D (refraction statics), Strata3D (3-D travelttime inversion) and AVO (AVO modelling). GMA's WAVX and LOGM were used for wavelet extraction, generation of synthetic *P-P* seismograms and log modelling. Converted-wave ray tracing was achieved with Sierra software and converted-wave synthetic seismograms created using SYNTH. (Lawton and Howell, 1992) Matlab was invoked to create crossplots and calculate polynomial curve fits.

Word processing was carried out using Microsoft Word and Expressionist on an Apple Macintosh. Figures were made with Adobe Photoshop, Deneba Canvas and Cricketgraph.

1.7 Dissertation outline

This dissertation has several components, dealing with the application of different seismic methods to reservoir monitoring at Cold Lake. Chapters 2 and 3 cover the processing and analysis of two 3-D time-lapse seismic data sets, which were acquired over the same producing pad in 1990 and 1992. In Chapter 2 a processing procedure is developed that results in repeatability of data in the two seismic data volumes above the reservoir. Such repeatability is very important if differences in seismic character between

the two time-lapse data sets within the reservoir zone are to be attributed to temporal changes in reservoir conditions alone.

In Chapter 3 I demonstrate that the differences between the two reprocessed data volumes above the reservoir zone have been minimised successfully and an analysis of the data is presented. Differences in seismic reflectivity and interval transit times between the two surveys are assessed in terms of changes in reservoir conditions.

The technique of three-component (3-C) reflection seismic data has not yet been established as a common tool in reservoir monitoring, although the benefits to petroleum explorationists of the additional geological information afforded by 3-C data have been described (Tatham and McCormack, 1991). Experimental converted-wave seismic data were acquired at Cold Lake in 1993 and 1994 to investigate whether 3-C data would be useful in reservoir monitoring. In Chapter 4 a processing procedure is developed which results in interpretable converted-wave seismic sections. In particular, I present a revised method of determining receiver statics and modifications to the established processing flow.

Analysis of the converted-wave data is discussed in Chapter 5. V_p/V_s values calculated from the converted-wave sections correlate well with theoretical predictions of maximum and minimum V_p/V_s over the analysed interval. These values are shown to provide complementary information to that obtained from compressional-wave data.

The final objective of this dissertation is to investigate the applicability of amplitude variation with offset (AVO) analysis as a tool for monitoring pore fluid changes within the reservoir at Cold Lake. Chapter 6 documents the AVO analysis performed on selected amplitude anomalies from the two 3-D data sets and along a line of compressional-wave data from the multicomponent survey. In Chapter 7 the dissertation is summarised and the relevance of the results discussed.

Chapter 2

3-D SEISMIC DATA ACQUISITION AND PROCESSING

2.1 Introduction

Two high-resolution time-lapse 3-D seismic reflection surveys were acquired by Esso Resources Canada Ltd. (E.R.C.L.; now Imperial Oil Resources Ltd.) over the D3 pad at Cold Lake. The two surveys were acquired for the purpose of reservoir monitoring. The first survey was acquired in 1990, during the sixth production cycle of CSS, and the second in 1992, during the eighth steam injection cycle. A base survey prior to the commencement of CSS had not been acquired.

It was anticipated that temporal changes in reservoir conditions, caused by the injection of steam, could be detected by analysis of seismic character and attribute changes between the two surveys. Theoretical and experimental studies on bitumen sands, including these sands at the D3 pad, suggest that a measurable drop in the compressional-wave velocity of the reservoir would occur as a result of steam injection.

In the original processed data there are seismic character differences between the two data sets well above the reservoir, in a zone where the geological conditions can be expected to have remained constant. Temporal variances in time-lapse seismic images of a reservoir are meaningful only if the seismic data volumes above the reservoir are consistently similar between the two surveys. To ensure repeatability in the seismic section above the reservoir, the two seismic surveys were reprocessed concurrently for this study, using identical processing parameters. It is acknowledged that obtaining a perfect match is not likely because of differences in acquisition conditions. However, the parameters used during the processing stream were chosen to match the two data sets as closely as possible above the reservoir zone.

Subtraction of one processed, stacked 3-D seismic data volume from another, used for monitoring of EOR processes, has been done previously. Greaves and Fulp (1987) monitored the progression of an in-situ combustion process using pre-burn, mid-burn and post-burn seismic data. They created difference volumes by subtracting the pre-burn horizon envelope amplitude at each level of interest from corresponding values in the mid-burn and post-burn data volumes. They determined that there were no continuous, coherent anomalies substantially above or below the reservoir reflection in the difference volumes and that the background noise level was lower than the observed anomalies. This implied that the differences substantially above and below the reservoir zone were small enough, so that variances within the reservoir zone were meaningful. However, no examples of pre-stack subtractions, performed as a means of quality control during processing, have yet been published.

It was found in the original processed data supplied that there is a bulk shift of 2-4 ms between the two data sets. This delay varies across the survey and is thought to be the result of different near-surface conditions at the times of acquisition. Although this variable delay might not be important if isochrons are mapped rather than single events, examination of the isochron values between two seismic reflections above the reservoir showed differences in these values at corresponding locations on the two surveys. Hence, both data volumes were reprocessed to eliminate this delay as well as to minimise the residual seismic character differences between the two processed data volumes above the reservoir zone.

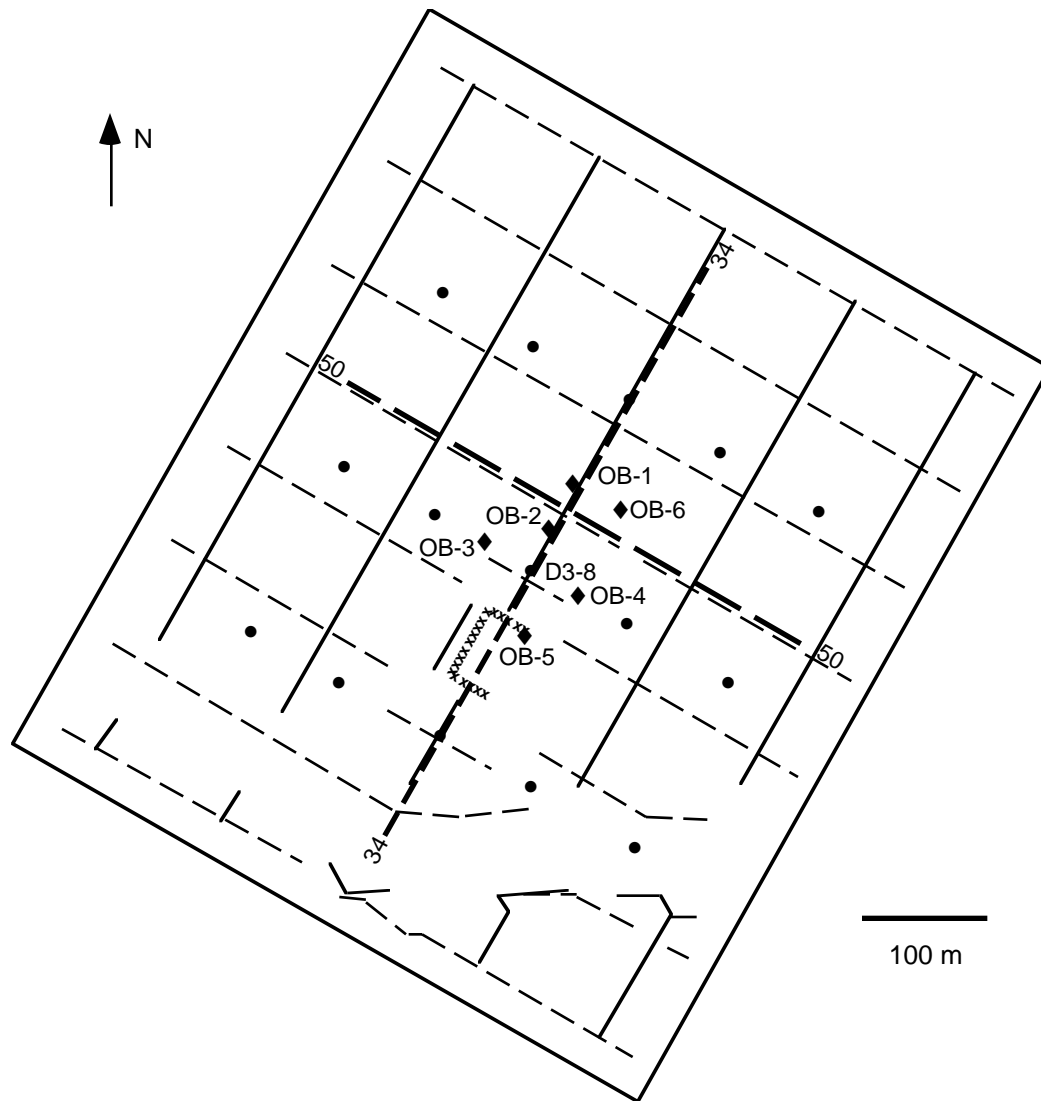
To observe the differences, a computer program was developed which allows the user to select any corresponding parts of two data sets and subtract these parts for the purposes of comparison. Use of this program allows selection of processing parameters on the basis of those which minimise the differences between the two 3-D data sets above the reservoir. Any residual static shift between the two data sets may be calculated

automatically by crosscorrelation of the two extracted data volumes on a trace to trace basis, or a value may be selected. Differences in absolute trace amplitude between the two data sets, which would cause erroneous results, are compensated for prior to subtraction by using a normalisation factor calculated from the data within a selected time window.

2.2 Concurrent 3-D seismic data processing

The survey layout is shown in Figure 2.1. Although the field layout was identical for each survey, the 1990 data were acquired in April whereas the 1992 data were acquired in January, resulting in different near-surface conditions for the two surveys. Recording systems were Sercel 386 in 1990 and I/O System One in 1992. The two seismic surveys each cover the same area of the D3 pad. This area (576 m x 672 m) encompasses fifteen directional production/injection wells and six vertical observation wells. In Figure 2.1 the locations of the six vertical observation wells are represented by diamonds and the bottom hole locations of the fifteen directional injection/production wells by dots. The survey layout was designed to give a full-fold image (20-fold) over an area of 200 m x 300 m, centred on the bottom hole location of production well D3-8.

For the surveys, five northeast-southwest source lines were laid out 128 m apart and eight northwest-southeast receiver lines 96 m apart. Surface elevations within the area of the survey varied by only 6 m. Along each source line (represented by solid lines in Figure 2.1) shots were fired at 43 stations, 16 m apart, for a total of 215 shots. The source for both surveys was 0.125 kg of dynamite buried at a depth of 16 m. Each shot was recorded by eight lines each of 37 individual buried geophones stationed 16 m apart (a total of 296 receivers, represented by dashed lines), which were common for both surveys. Some of the shot and receiver stations had to be skidded because of surface and buried facilities at the D3 pad.



Legend			
Source line	————	Vertical observation well	◆
Receiver line	- - - -	Directional injector/producer well (BHL)	●
Inline 34	- - - -	Production facilities	xxxxxx
Crossline 50	————		

Fig. 2.1 Layout of the 3-D seismic surveys at the D3 pad. Crossline 50 and inline 34 will be referred to later in the dissertation.

Four test holes drilled by E.R.C.L. to examine the surface geology had encountered a surface layer of ablative till, which is about 6 m thick. Below this layer is basal till, which is quite well consolidated as it was at the base of the ice sheet during the last period of glaciation. The test holes encountered a significant increase in consolidation at depths between 9 m and 10 m below the surface. Further tests were done by E.R.C.L. to examine seismic signals received by geophones buried at 2 m depth intervals. It was found that there was a significant limit to the frequency content of the data recorded by geophones buried at depths of less than 6 m. Only at 8 m was an increase in frequency content observed. As a consequence of these tests, the geophones were buried at a depth of 10 m. It was anticipated that the burial of the geophones (Sensor SM-7, 14 Hz) in fairly well-consolidated till would limit the effects of surface noise and enable reflections with high frequency content to be recorded.

2.3 Processing flow

The two data sets were reprocessed concurrently at The University of Calgary through a standard 3-D processing stream using Landmark/IT&A processing software. The data were recorded to 3 s at a sample rate of 1 ms but only the first 1 s of data were processed because the zone of interest is above 0.6 s. The basic processing flow is shown in Figure 2.2.

A field shot record from the 1990 survey is displayed in Figure 2.3. A 1.0 s AGC and pre-first break mutes were applied. The discontinuous pattern of first breaks on receiver lines two and three are caused by receivers being located off the line due to surface hazards. Windowed portions of this field record and the corresponding field record from the 1992 survey are shown in Figures 2.4 and 2.5, respectively. Displayed in these figures are data covering the zone of interest, from 0.3 s to 0.6 s.

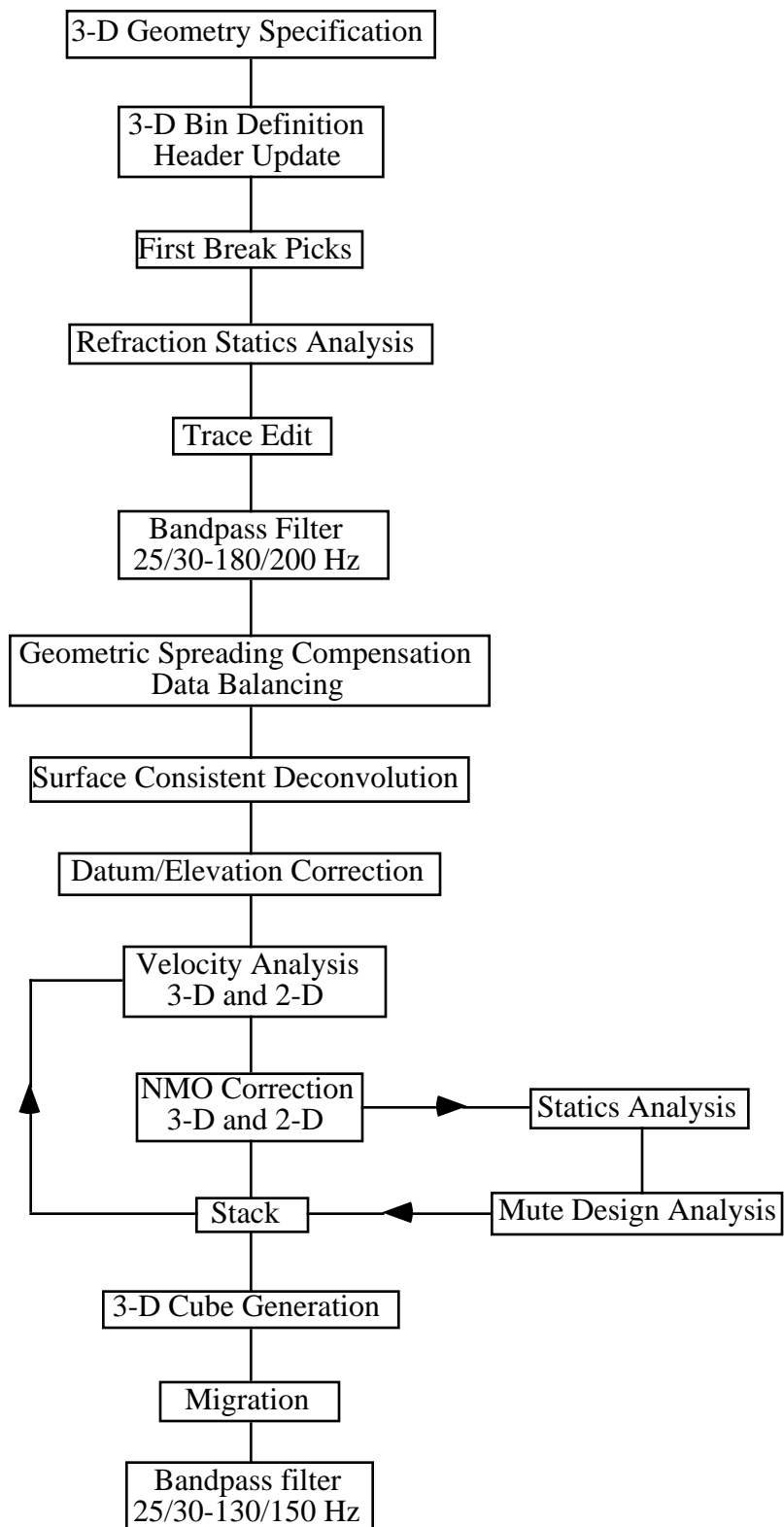


Fig. 2.2 Processing flow for the 3-D seismic data processing.



Fig. 2.3 A field shot record from the 1990 survey (with 1.0 s AGC and pre-first break mutes applied).

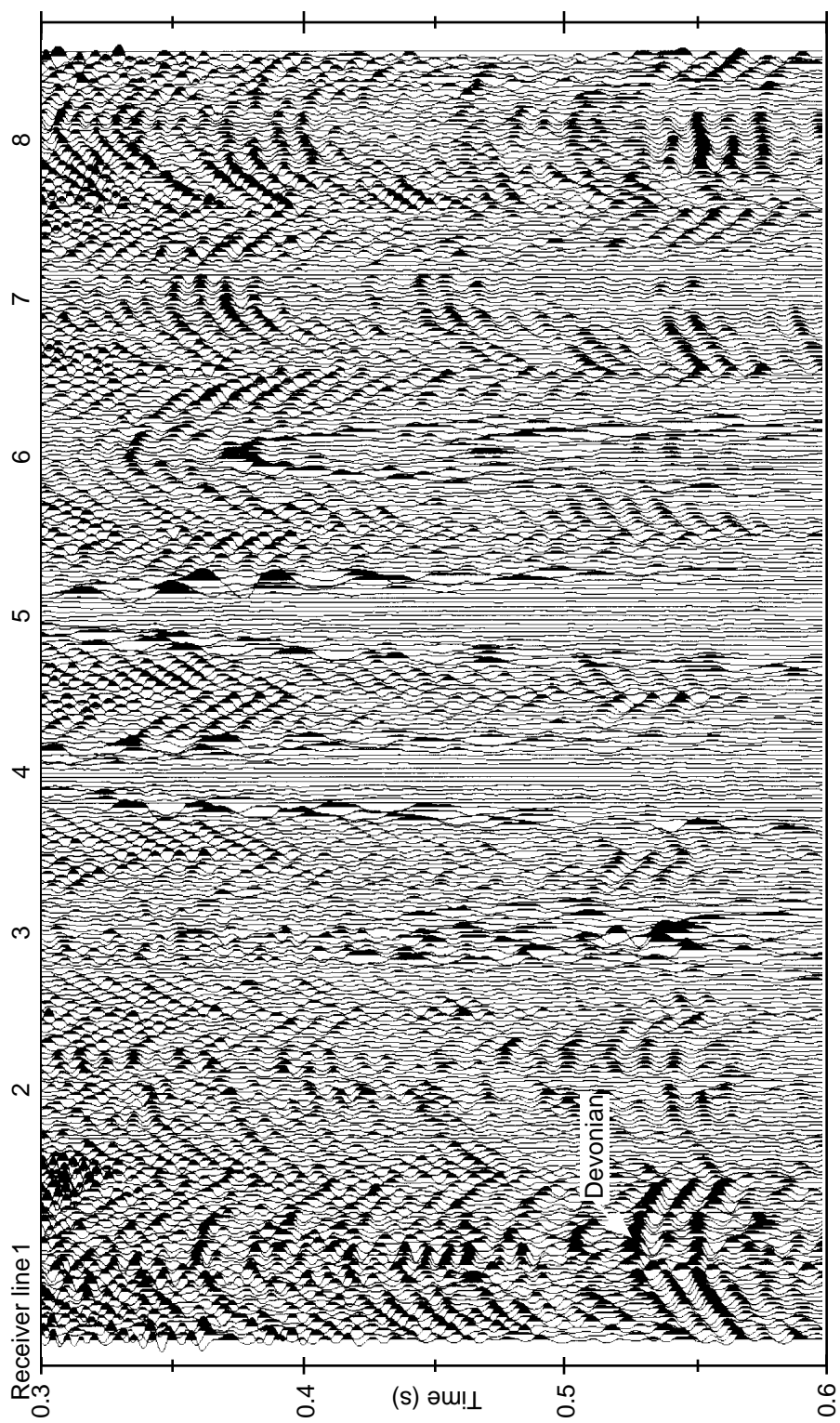


Fig. 2.4 Portion of the field shot record from the 1990 survey. The zone of interest, from 0.3 s to 0.6 s, is displayed and the Devonian reflection is indicated.

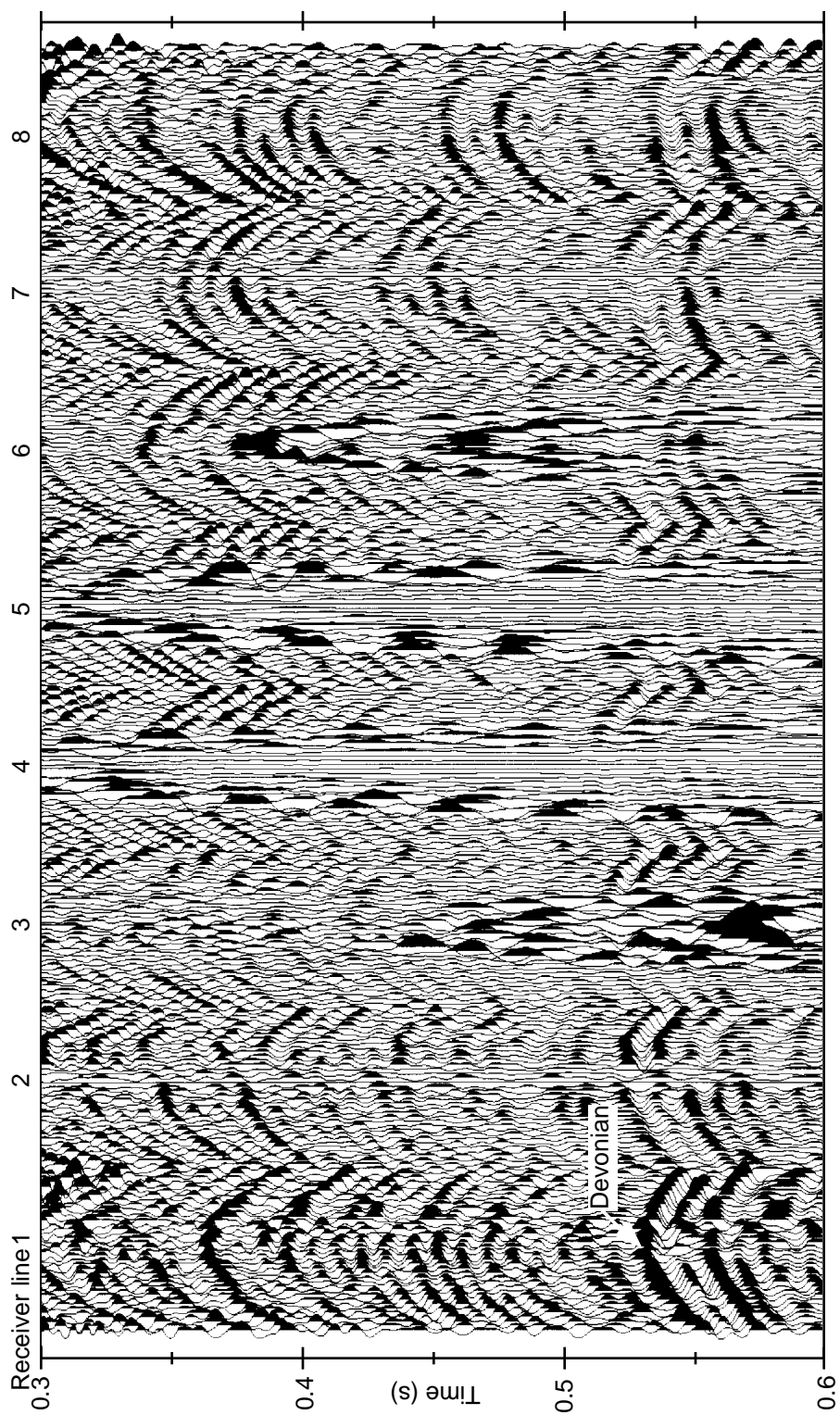


Fig. 2.5 Portion of the corresponding field shot record from the 1992 survey. The zone of interest, from 0.3 s to 0.6 s, is displayed and the Devonian reflection is indicated.

These are typical common-shot gathers from the middle of each survey, each having eight receiver lines of data. The source-receiver offsets in the displayed gathers range from 14 m to 469 m. The peak indicated on receiver line one (at approximately 0.53 s) is the top Devonian reflection and the zone of interest, the Clearwater Formation, extends 50-100 ms earlier than this event. Both gathers show high amplitude, low frequency surface-wave energy which overwhelms reflections within the zone of interest on several of the receiver lines.

Figures 2.6a and 2.6b display the average amplitude spectra for these 1990 and 1992 field records, respectively. The spectra were averaged over a time window of 0.3 s to 1.0 s for all the traces in the record. A starting time of 0.3 s was chosen to avoid the high frequency chatter associated with the first breaks. Frequencies above 150 Hz are not displayed as they were not included in the processing. Low frequencies are seen to dominate these spectra and higher frequencies are attenuated. The dominant frequency of reflections is slightly higher in the 1990 data than in the 1992 data.

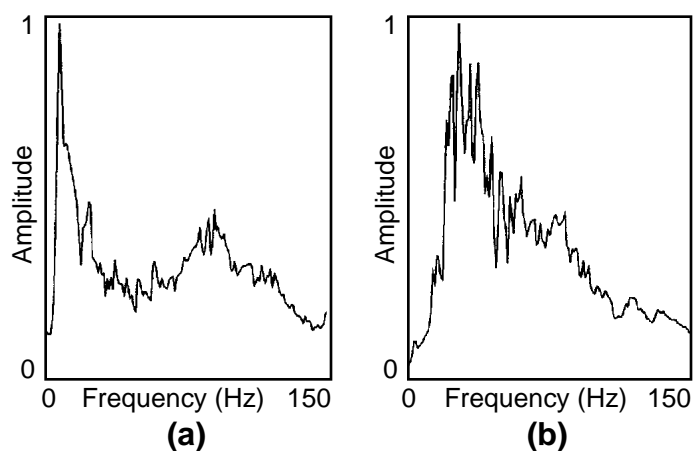


Fig. 2.6 Amplitude spectra for the (a) 1990 and (b) 1992 field shot gathers.

Subtraction of the 1992 field shot gather from the 1990 field shot gather results in a residual record, an enlarged portion of which is shown in Figure 2.7. High amplitude, low frequency energy is seen and there are some amplitude differences above the reservoir zone which are probably due to different bandwidths of reflection data (Figure 2.6). It is desired to minimise these amplitude differences during processing. A bulk shift of -4 ms was applied to the 1992 data before subtraction. The large amplitude variances observed below the reservoir zone at around 0.53 s are due to the delayed arrival times of these events in the 1992 survey.

First breaks were picked on the 1990 data and copied to the 1992 data. It was seen that the first break picks from the 1990 survey fitted very well the 1992 data and little editing was needed, apart from a small time shift of about 3 ms. Bad and reverse traces were edited and out of order shots corrected. Refraction statics analysis was undertaken using Hampson-Russell “GLI3D” software. The first breaks lie on a straight line with no break in slope and a sub-weathering velocity of 1750-1800 m/s is indicated (Figure 2.8). It is surmised that the burial of the geophones at a depth of 10 m has put them below the weathering layer everywhere throughout the survey and thus refraction statics were not applied.

Geometric spreading compensation was applied using a velocity function derived from sonic log velocities. The data were also balanced on a record basis by scaling to a defined energy level, while keeping relative amplitudes through the trace. A bandpass filter with a low-cut of 25 Hz was applied to remove low frequency components from the data. On some of the records this low frequency noise is dominant and it was found that this relatively high low-cut filter was effective at eliminating this noise without damaging reflections. A high-cut filter of 200 Hz was applied initially to maintain high bandwidth in the data but reduced to 150 Hz in the deconvolution process in order to eliminate the high frequency spikes observed on the records.

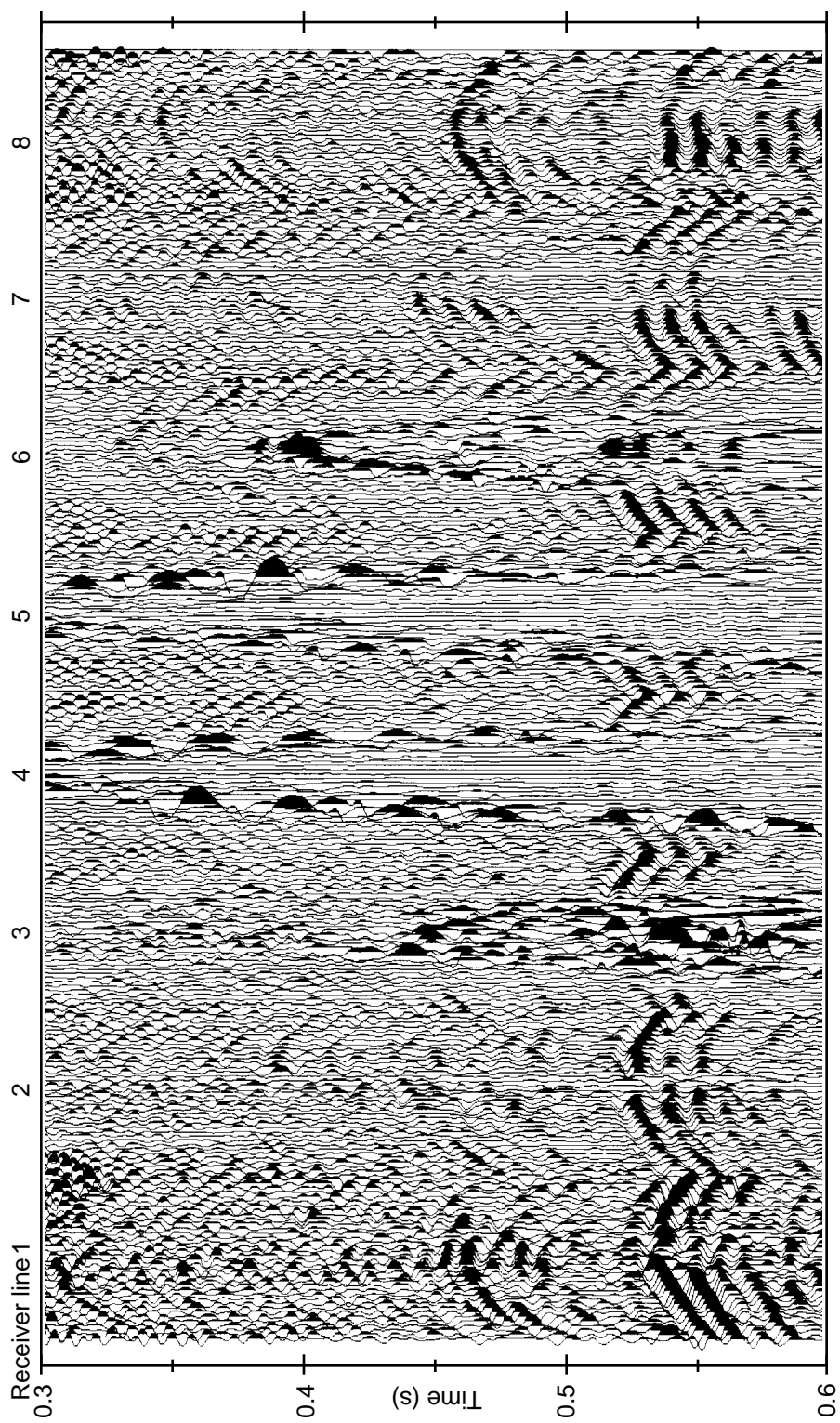


Fig. 2.7 The difference between the 1990 and 1992 field shot gathers displayed in Figures 2.4 and 2.5. The zone of interest, from 0.3 s to 0.6 s, is displayed.

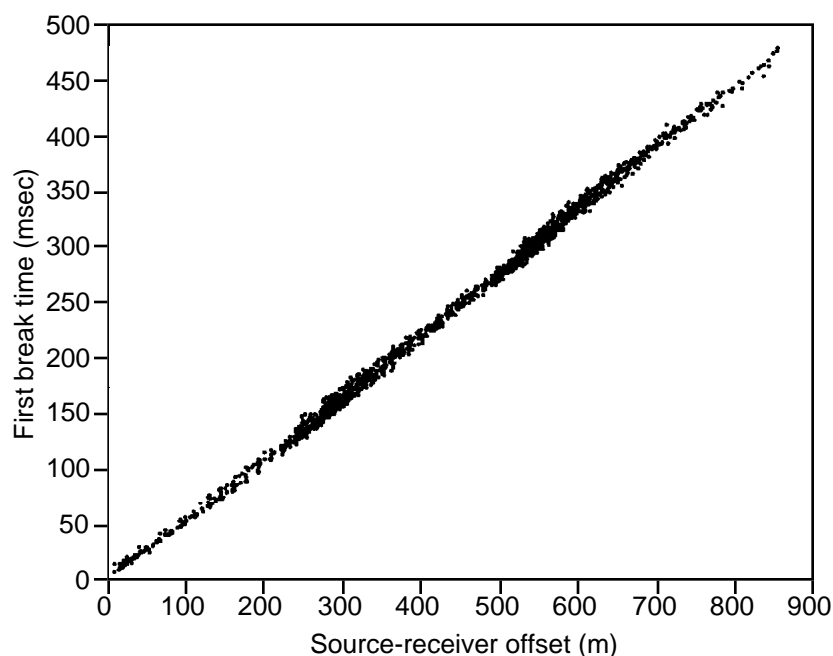


Fig. 2.8 Plot of first break time against source-receiver offset for some of the CDPs in the centre of the survey. The first breaks lie on a straight line, indicating a sub-weathering velocity of 1750-1800 m/s.

Surface consistent spiking deconvolution was performed by deconvolution on common-source gathers followed by deconvolution on common-receiver gathers using the same parameters. These parameters were chosen on the resulting character of the deconvolved data and to minimise the differences between two test records. After a few tests with different lengths of operator, the operator length was chosen to be 150 ms. The frequency limits used in the deconvolution were 25/30-130/150 Hz. An offset-dependent front-end mute, designed to eliminate noise prior to the first arrivals, was applied before and after deconvolution.

Figures 2.9 and 2.10 show the same shot gathers as in Figures 2.4 and 2.5 after surface consistent deconvolution using these parameters. These data have also had geometric spreading compensation and pre-first break mutes applied. A 0.5 s AGC was applied for display purposes.

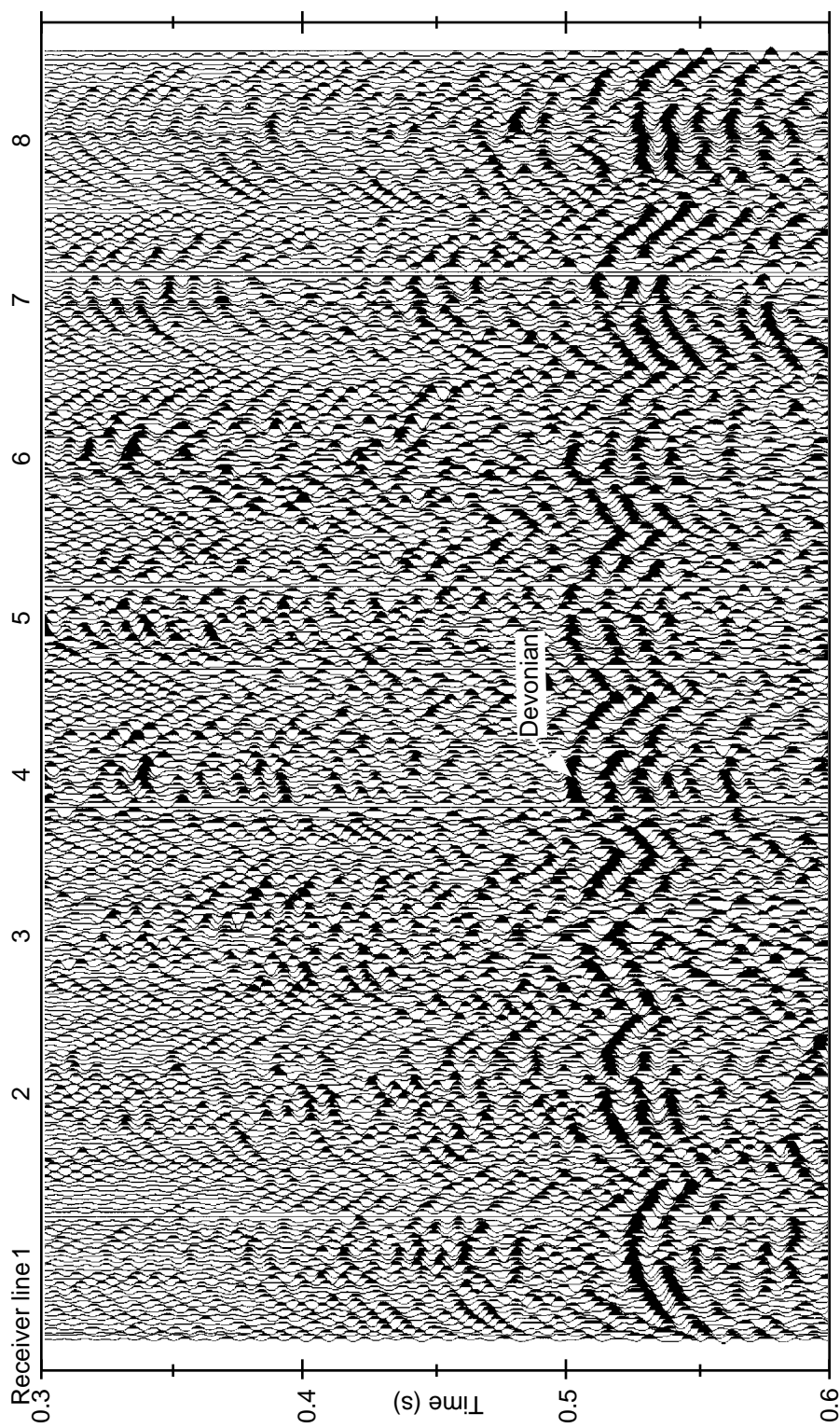


Fig. 2.9 The same 1990 shot gather as in Figure 2.4, after deconvolution. The zone of interest, from 0.3 s to 0.6 s, is displayed and the Devonian reflection is indicated.

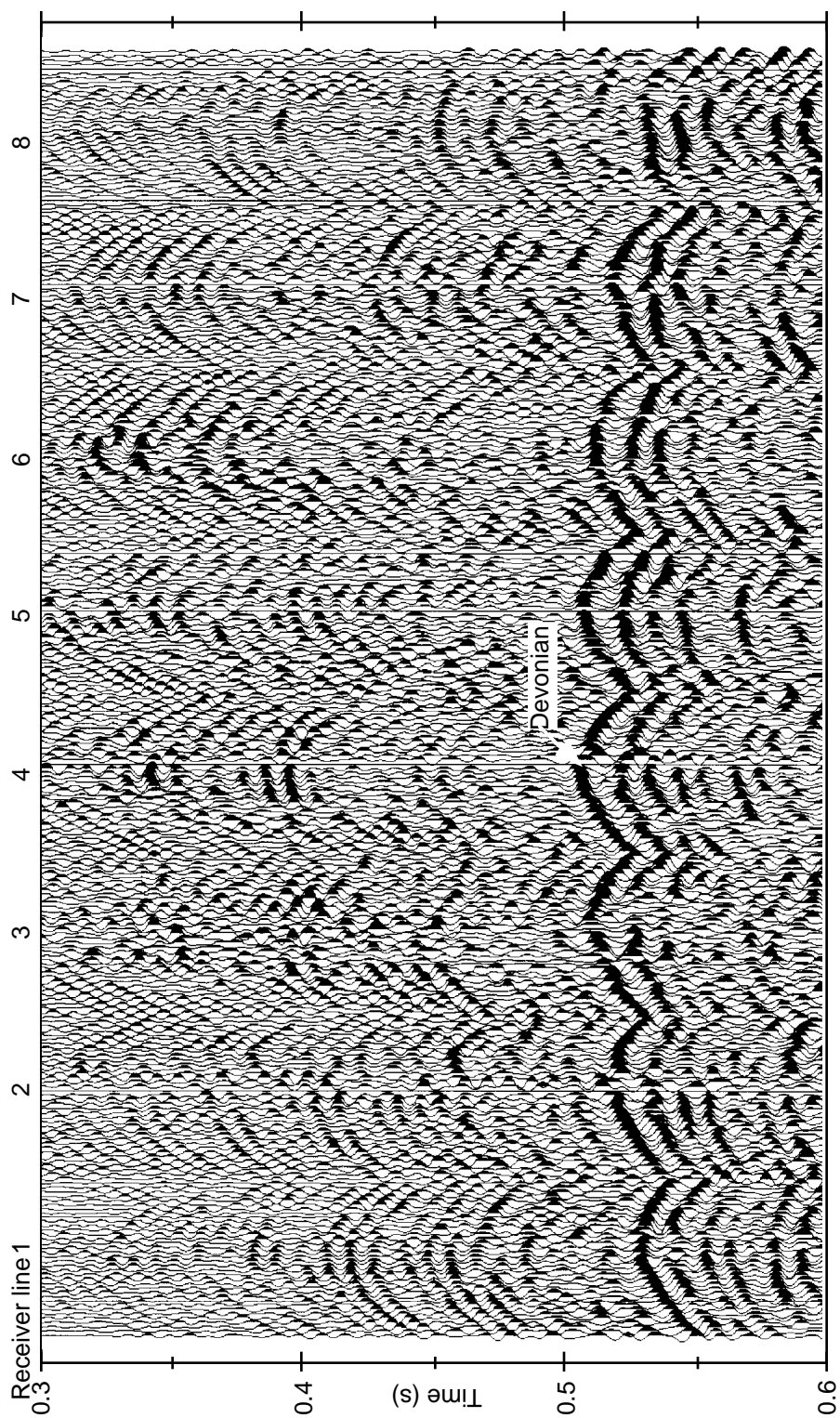


Fig. 2.10 The same 1992 shot gather as in Figure 2.5, after deconvolution. The zone of interest, from 0.3 s to 0.6 s, is displayed and the Devonian reflection is indicated.

Events in the zone of interest have been enhanced and the two records are much more similar in terms of character and frequency content than are those in Figures 2.4 and 2.5. The Devonian reflection (indicated) has been improved considerably and is now seen clearly on all the receiver lines. The spectra for these deconvolved data are shown in Figure 2.11. Low frequencies have been removed and the higher frequencies have been boosted so that the spectra are much better balanced than those for the field shot records (Figure 2.6).

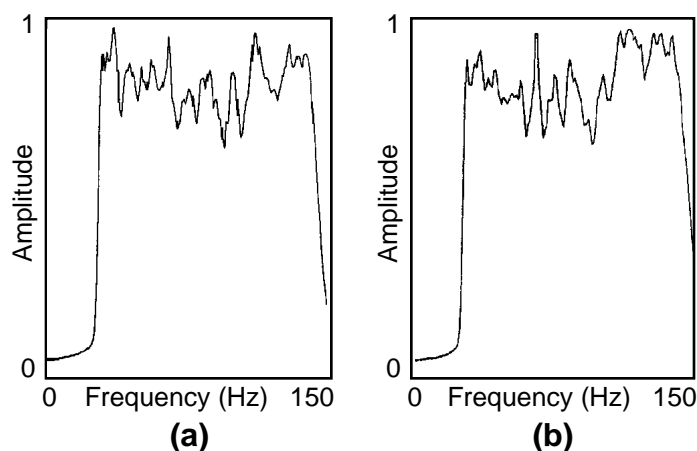


Fig. 2.11 Amplitude spectra for the (a) 1990 and (b) 1992 deconvolved records.

The difference between these deconvolved records is shown in Figure 2.12. A bulk shift of -3 ms was applied to the 1992 data before subtraction. No scaling was applied to the data after subtraction and the difference record is displayed with the same gain scalar as the deconvolved records in Figures 2.9 and 2.10. The residuals observed here are much lower in amplitude than those seen on the raw residual (Figure 2.7) and are quite low in the zone above the reservoir (0.3 s to 0.4 s). The higher amplitude residuals noted at the Devonian event below 0.5 s are due to the delayed arrival time of this event in the 1992 survey.

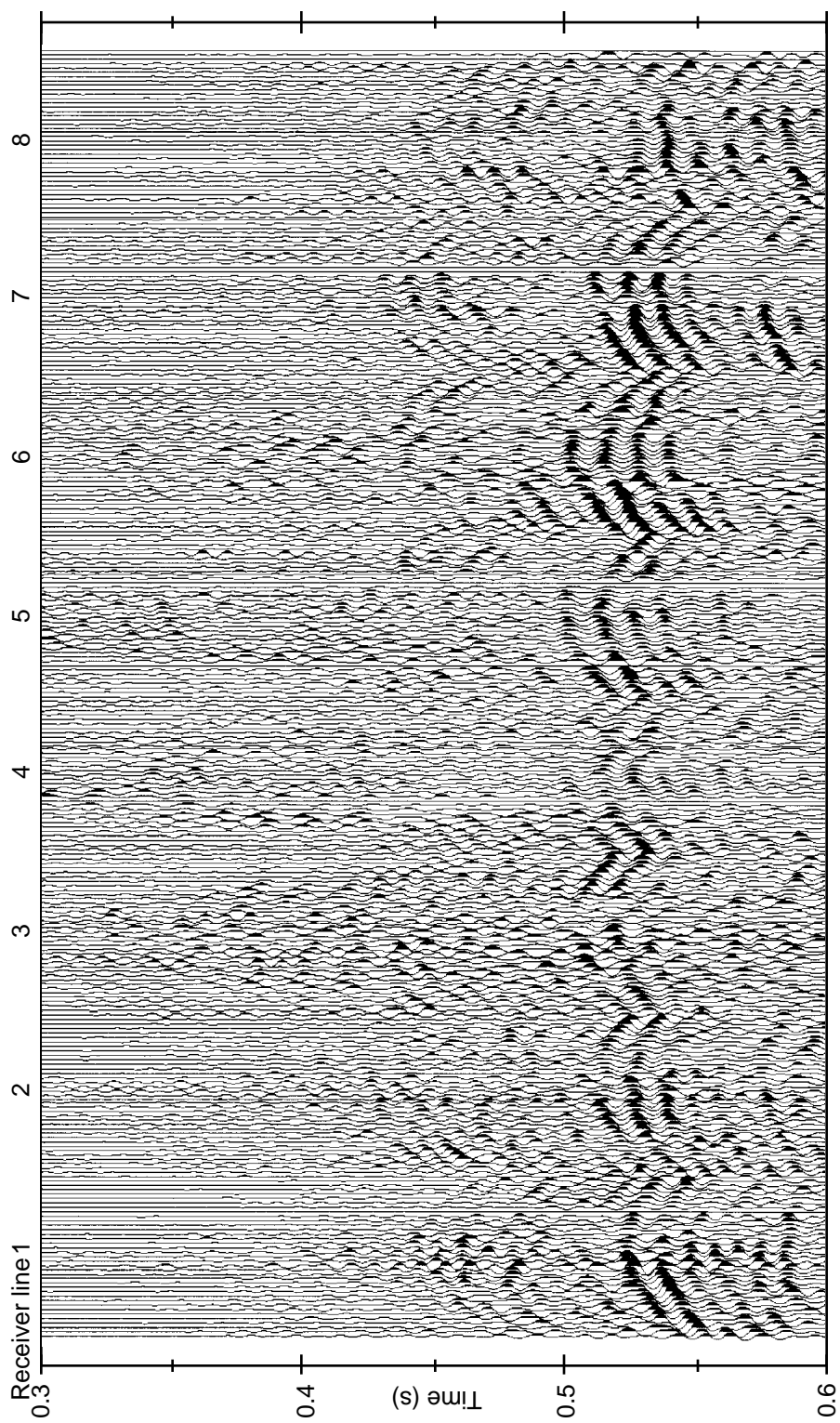


Fig. 2.12 The difference between the 1990 and 1992 deconvolved gathers displayed in Figures 2.9 and 2.10. The zone of interest, from 0.3 s to 0.6 s, is displayed.

The common depth point (CDP) binning grid coordinates were based on those used by Western Geophysical in the original processing of the 1990 data. The CDP bin spacing was 8 m x 8 m, which is half of the shot and receiver spacing; the highest fold achieved in the centre of the survey was 45. The source-receiver offset and azimuth ranges of the traces at each CDP location were generated using FDtools software (Figures 2.13, 2.14). The area shown is in the centre of the survey and it is seen that there is a good range of offsets and azimuths for the traces to be stacked at these CDPs. Such a range is desirable for good velocity analysis. While the longest offsets here are about 1000 m, normal moveout (NMO) stretch mutes later limit the offsets in the zone of interest to less than 500 m.

The data were corrected to a floating datum for each CDP gather with a replacement velocity of 1800 m/s. After the CDP gathers had been stacked, a datum of 600 m was applied, using the same replacement velocity.

Stacking velocities were analysed using both 3-D and 2-D velocity semblance plots generated at 35 locations spaced at 80 m intervals across the 1992 survey. The 3-D semblance analysis algorithm created supergathers and sorted the data into four sectors by the azimuth of the shot-receiver direction, so that velocities could be selected according to azimuth. Five semblance plots were created for each supergather: one using all offsets and four using data sorted into azimuth sector. In Figure 2.15 are displayed four windowed semblance plots representing the four azimuth sectors for one supergather (three adjacent CDPs from each of three consecutive lines) selected from the centre of the survey. The sectors are as follows: (a) north (-22.5° to 22.5°), (b) northeast (22.5° to 67.5°), (c) east (67.5° to 112.5°) and (d) southeast (112.5° to 157.5°), with the complementary angles (angle + 180°) included in the appropriate sector. Annotated by a black disk is the pick for the Devonian event and is seen to be the same value of stacking velocity on each semblance.

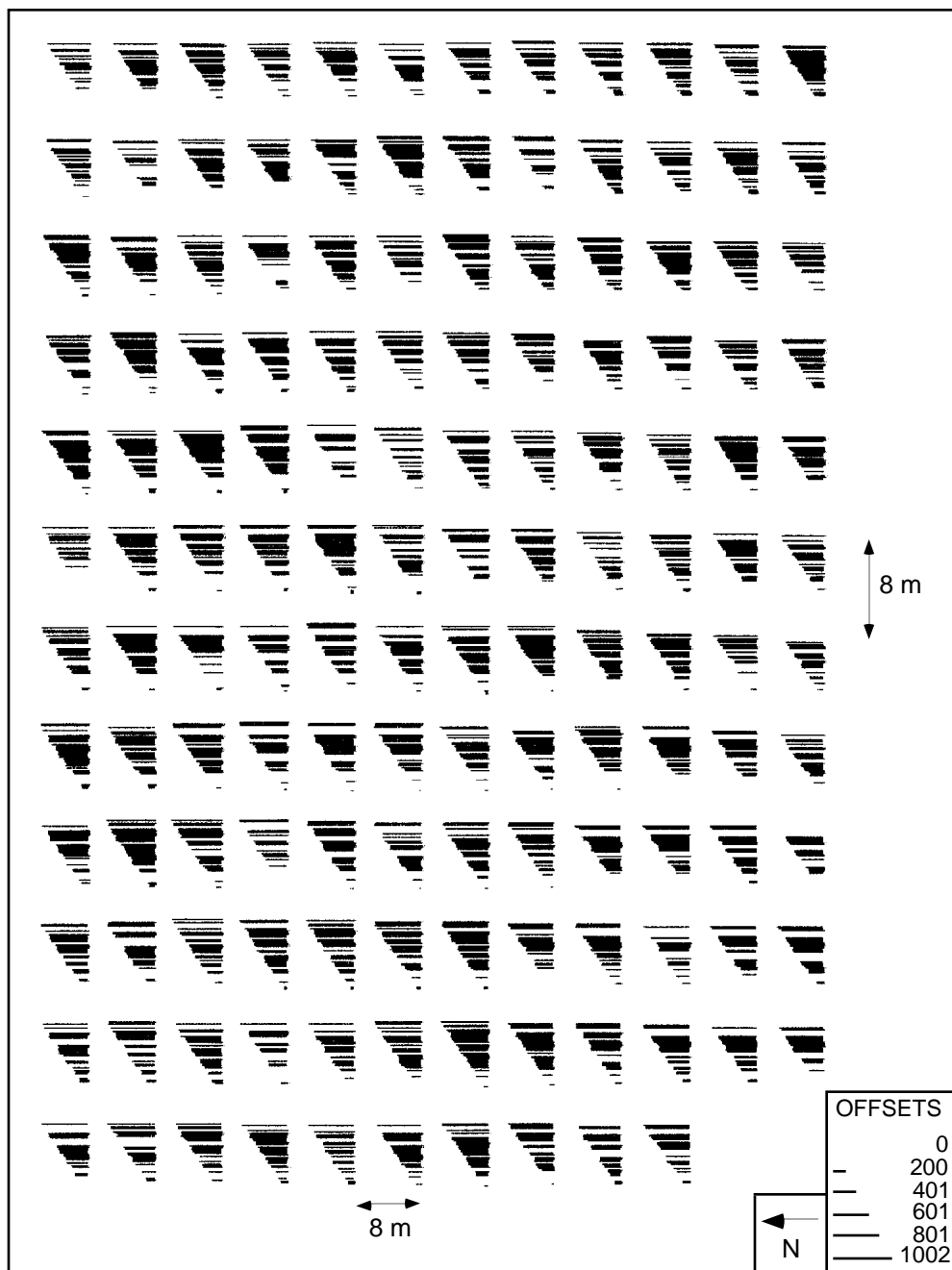


Fig. 2.13 Offset ranges for CDPs in the centre of the survey. 142 CDP bins (8 m x 8 m) are displayed.

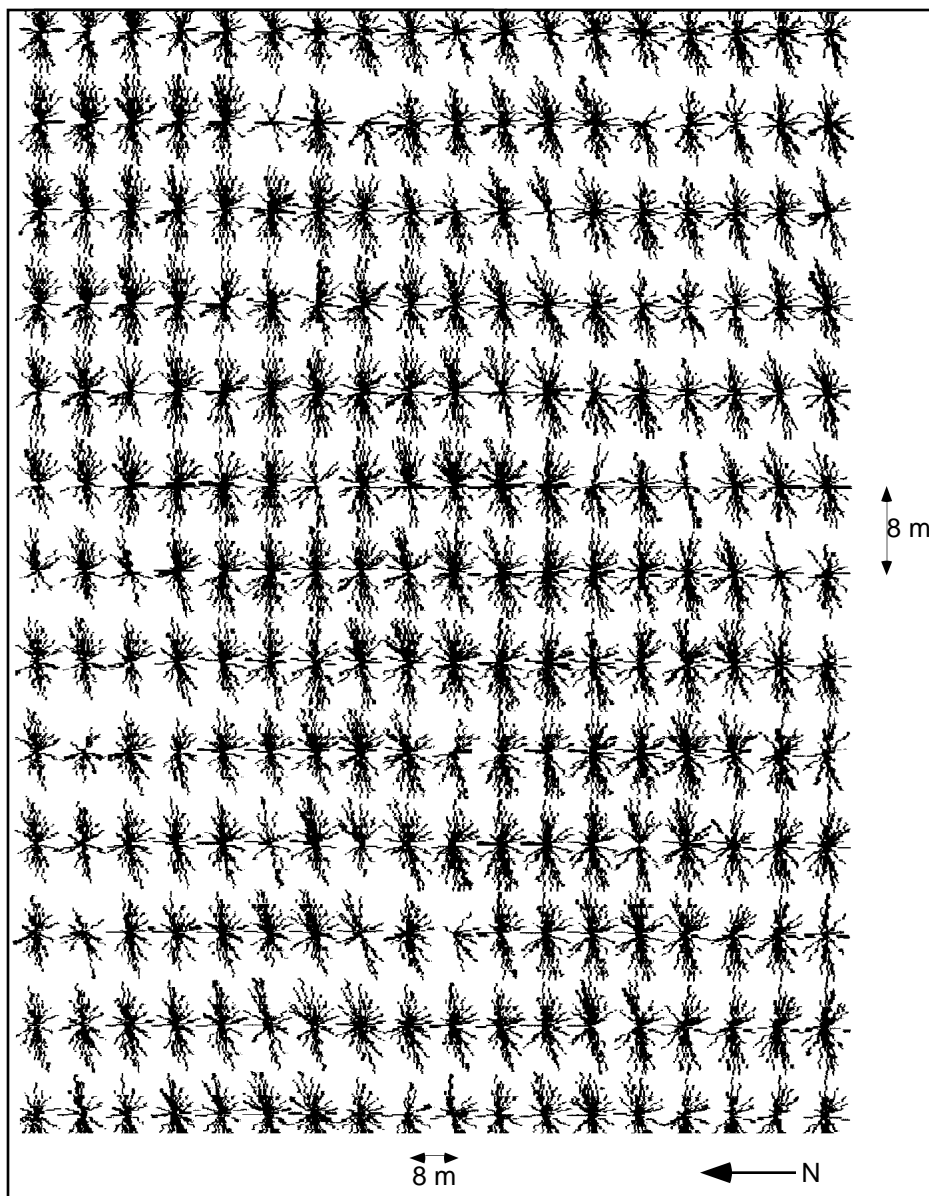


Fig. 2.14 The range of azimuths stacked at 234 CDP locations in the centre of the survey. The direction of each line represents the azimuth of that source-receiver pair and its length represents the source-receiver offset.

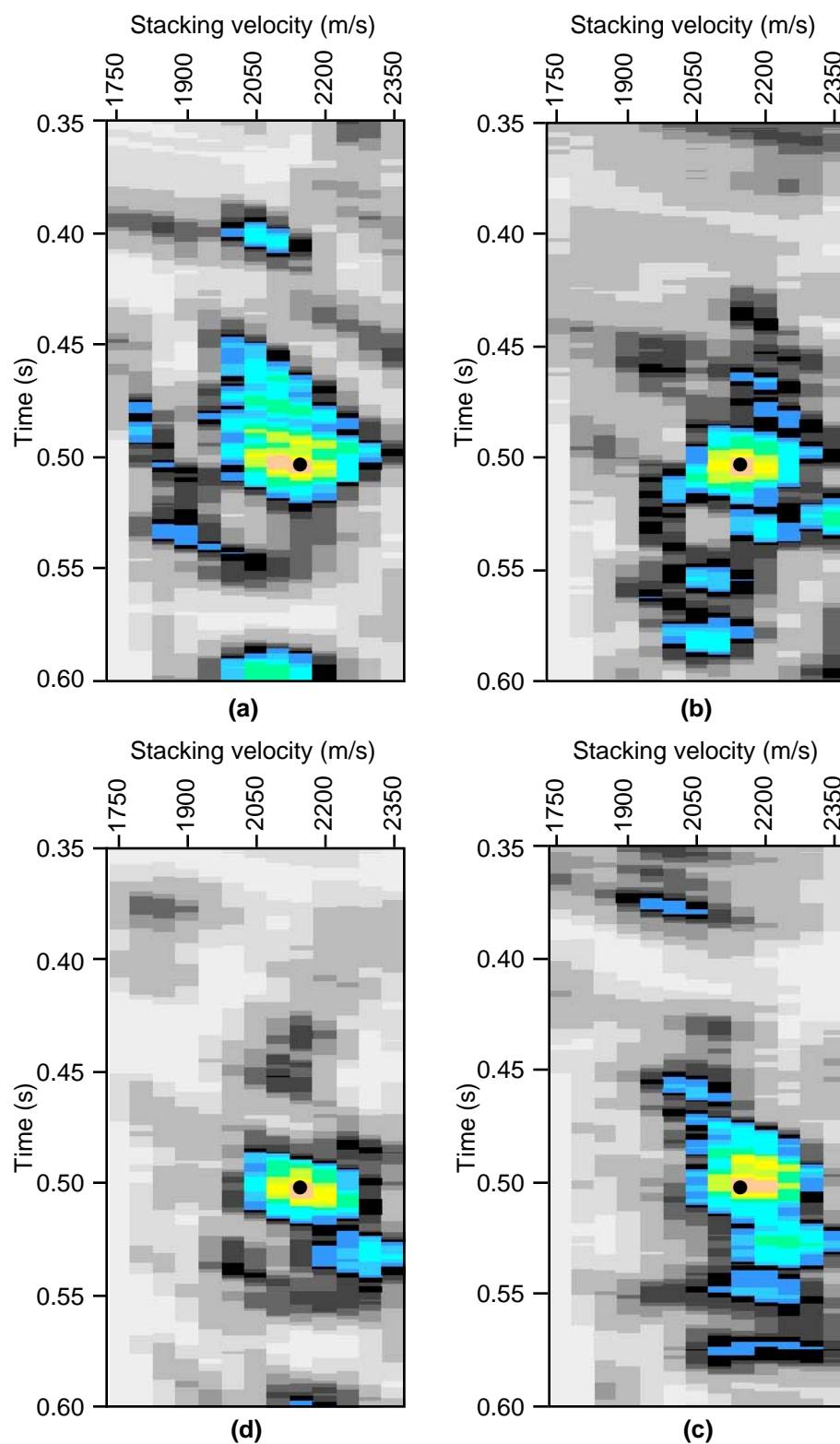


Fig 2.15 Four windowed semblance plots used in velocity analysis. The data were sorted by azimuth into four sectors: (a) north, (b) northeast, (c) east and (d) southeast.

Not all of the azimuthally sorted semblance plots had a good range of offsets or an adequate number of traces to determine the stacking velocities. However, it was observed on the good semblance plots in the centre of the survey that the velocities are not azimuthally dependent.

In areas of dip the apparent NMO velocity will differ from the true velocity according to the angle between the true dip direction and the source/receiver azimuth. Levin (1974) showed that the ratio of apparent NMO velocity to true velocity is related by

$$V_{app}/V = (1 - \sin^2\phi \cdot \cos^2\theta)^{-1/2}$$

where V_{app} = apparent NMO velocity, V = true velocity, ϕ = dip angle and θ = angle between profile line and dip line.

It is seen that for small dip angles the apparent velocity will be very close to the true velocity, so azimuthal effects will be negligible. From wireline logs run in the observation and production wells at the D3 pad, geological dip across the pad appears to be very small ($< 2.5^\circ$). For a dip angle of 2.5° the difference between the true velocity and the apparent velocity is less than 0.1%, so the observed independence here of velocity and azimuth is reasonable.

Stacking velocities were subsequently selected on the basis of the 3-D semblance plots and 2-D constant velocity stacks and were seen to be consistent throughout the survey. The velocities picked on the 1992 data were seen to apply equally well to the 1990 data for all times. It had been anticipated that the stacking velocities through the reservoir zone would be lower for the 1992 data than for the 1990 data because of the presence of steam, which lowers the compressional-wave velocity. This effect was not seen at the velocity analysis locations, possibly because the change in stacking velocity due to a change in interval velocity was too small to be detected. For the Clearwater

Formation, the picked stacking velocities were only about 50 m/s higher than the rms velocities calculated from the sonic logs. Although 35 spatially varying stacking velocities at a spacing of 80 m were used, the values did not vary greatly across the survey area. Representative stacking velocities and the corresponding average and interval velocities (calculated using the Dix equation) are listed in Table 2.1. Also listed are the standard deviations from these values of the spatially-variant velocities.

Table 2.1 Representative stacking velocities for the 3-D data. The standard deviation away from these values of the spatially variant velocities is listed, as are the average and interval velocities (calculated from the Dix equation).

Time (s)	Stacking Velocity (m/s)	Standard Deviation (m/s)	Average Velocity (m/s)	Interval Velocity (m/s)
0.051	1757	9	1757	1757
0.108	1803	9	1802	1843
0.200	1872	20	1870	1950
0.310	2012	9.5	2003	2244
0.350	2077	8	2062	2525
0.430	2142	11	2126	2406
0.496	2165	8.5	2150	2309
0.525	2187	11.9	2171	2534
0.568	2375	10.4	2310	4014
0.627	2895	15.6	2648	5896
0.702	3070	16.6	2820	4260
0.829	3372	17.3	3110	4704

Residual statics could not be applied because the processing subroutine was not properly set up for 3-D data. Tests were undertaken using data correlation routines for each data set independently and trim statics selected on the basis that the differences

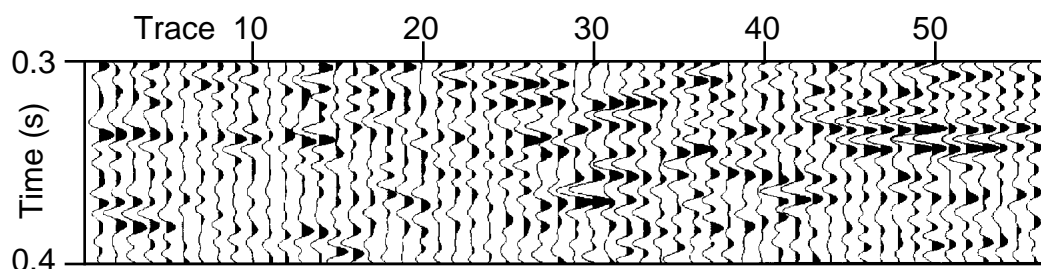
between the data sets on a selected test line were the least. Trim statics were applied to NMO-corrected, muted CDP gathers.

The data were migrated by two orthogonal passes of 2-D f - k migration using a constant velocity of 1670 m/s, this being 95% of the initial stacking velocity. F - k migration was selected because it retained the seismic character observed on the stacked sections and kept the measured differences between the two data sets above the reservoir to a minimum. The only one-pass 3-D migration algorithm available at the time produced a less satisfactory result in terms of seismic character and measured differences. A single time-varying velocity function was used to apply the Stolt stretch to the t - x data prior to constant velocity migration and was approximately 95% of the representative stacking velocity function listed in Table 2.1. Tests were done to determine the best velocities to use, concentrating on the zone of interest between 0.3 s and 0.6 s.

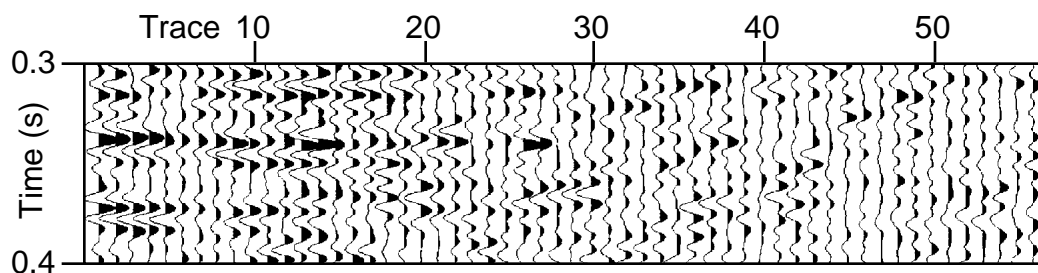
An example of the difference analysis is given in Figure 2.16. Each panel shows the difference between the 1990 and 1992 data sets for the same crossline selected from the original and reprocessed data. Static shifts and compensations for amplitude differences between corresponding traces and were applied prior to subtraction. The data panels were selected from an interval of good data above the reservoir in order to observe the differences there, which should be minimal.

The data used to produce the differences seen in Figure 2.16 were bandpass filtered between frequencies of 25/30-130/150 Hz and plotted with the same gain scalar. Figures 2.16a and 2.16b show the effect of the varying static shift observed between the original 1990 and 1992 data sets. They show that a static shift of 2 ms is best for traces 1 to 22 and a shift of 3 ms best for traces 23 to 56. Figure 2.16c is the difference obtained from the reprocessed data sets with a static shift of 3 ms applied. The static shift between the 1990 and 1992 surveys is thought to be the result of different near-surface conditions at the times of acquisition; either the depth of the water table or of the frozen layer.

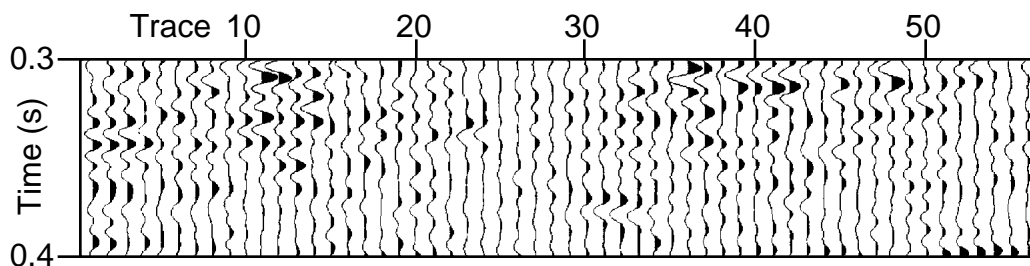
Panels such as those in Figure 2.16c were generated during the reprocessing to observe the effects of changing the processing parameters. Parameters were subsequently chosen on the basis of the panel which showed the lowest amplitudes (or the fewest differences) in the zone above the reservoir.



(a) Original processing with 2 ms shift



(b) Original processing with 3 ms shift



(c) Reprocessed data with 3 ms shift

Fig. 2.16 Some results of the difference analysis used during data processing. Each panel shows the residual from the subtraction of the 1992 data from the 1990 data. The data are selected from a zone above the reservoir which is unaffected by the steam.

In order to establish the optimum value of the time delay, several residual data sets were created with different time shifts applied prior to subtraction. Data tested were the field and deconvolved shot records, displayed in Figures 2.4, 2.5, 2.9 and 2.10, as well as a line from the final migrated data. Rms amplitudes were calculated for each trace, then the average for each record was normalised. In Figure 2.17 are shown the rms amplitudes of the residual data, with bulk time shifts ranging from -8 ms to +2 ms applied to the 1992 data. For the raw data, a shift of -4 ms minimises the rms amplitudes of the residual data record. After deconvolution it appears that a -3 ms shift is optimum. Tests of phase rotation of the 1992 record instead of a time shift produced worse results in terms of minimised differences as well as altering the character of the data.

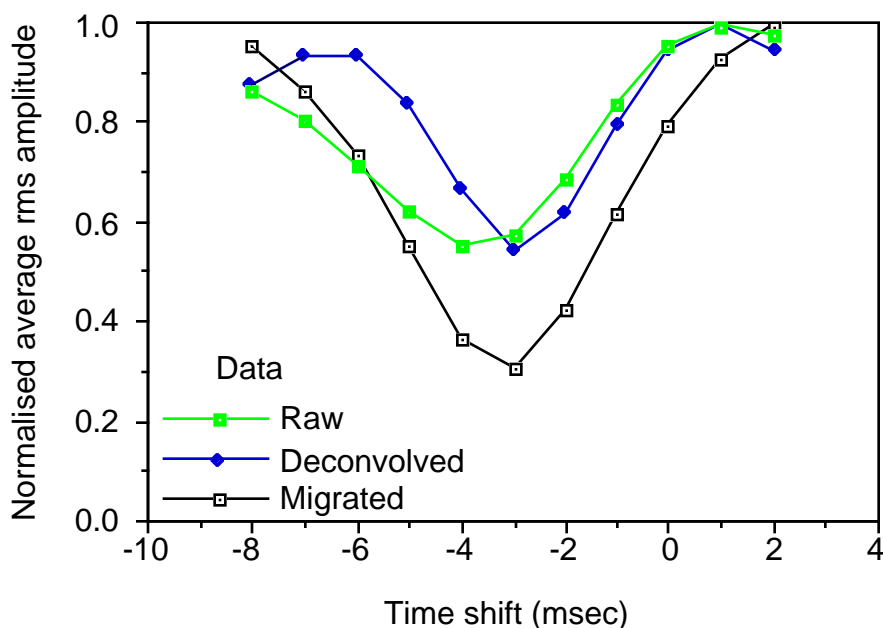


Fig. 2.17 Normalised rms amplitudes of residual data sets after application of varying bulk shifts to the 1992 data. Plots are shown for the raw and deconvolved gathers shown in Figures 2.4, 2.5, 2.9 and 2.10 and for a migrated line from the centre of the survey.

The residual rms amplitudes calculated from two corresponding lines from the migrated data volumes are also shown. The minimum rms value is lower for the differenced migrated data and occurs at -3 ms. Since I could not be sure before stack that a -3 ms shift was appropriate for all 60,000 traces, the shift was applied post-stack. Also, it was not desired to apply an artificial datum to a data set by bulk shifting it before velocity analysis. Application of the subtraction program to the entire migrated data volumes showed a shift of -3 ms to be consistent across all of the survey.

2.4 Discussion

Two time-lapse 3-D seismic surveys had been acquired as part of a reservoir monitoring program at the Cold Lake D3 pad. It was anticipated that temporal changes in reservoir conditions, caused by steam injection, would result in observable variances between the two processed seismic data sets. The two surveys were processed concurrently specifically to ensure that the character and amplitude differences between the two processed data volumes were minimised above the reservoir. To facilitate this, a computer program was written which allowed the differences between selected test records or lines of data to be measured throughout the reprocessing. Processing parameters were then chosen to minimise these differences.

Application of this new method of quality control resulted in high repeatability of the two surveys above the reservoir zone and ensured that the differences there were minimised. Now the variances observed between the seismic data volumes within the reservoir zone itself may be attributed to temporal changes in the reservoir caused by the introduction of steam and by changes in reservoir pressure.

Chapter 3

3-D SEISMIC DATA ANALYSIS

3.1 Seismic data - well-log correlation

Before interpretation of seismic character and attribute changes within the reservoir zone can be initiated, the position of this zone and of the major reflectors on the seismic data must be determined precisely. The major reflectors to be identified are the tops of the Grand Rapids, Clearwater and McMurray formations and the top of the Devonian section.

Figure 3.1 shows the initial identification of seismic reflectors based on the correlation at the location of OB5 between the sonic log, synthetic seismogram and a few traces of seismic data from the 1990 data. The synthetic seismogram was generated by convolution of the reflectivity series with a standard Ormsby wavelet with frequency limits matching those of the seismic data. The correlation is based on the character match between the synthetic seismogram and the seismic data of an event from a tight streak in the Grand Rapids Formation, at a log depth of 400 m. This event is seen clearly on the sonic log, synthetic seismogram and seismic data as a strong peak, representing a positive reflection coefficient.

After correlation of this event, the Grand Rapids and Clearwater formations were identified on the seismic data. The character tie between the synthetic seismogram and the seismic data is not particularly good, especially below the top of the Grand Rapids tight streak. It is seen that significant stretch is necessary to tie the Clearwater seismic event to the sonic logs. Tests were undertaken to tie the log data to a series of phase-rotated panels of seismic data but there was no improvement in the quality of the character match.

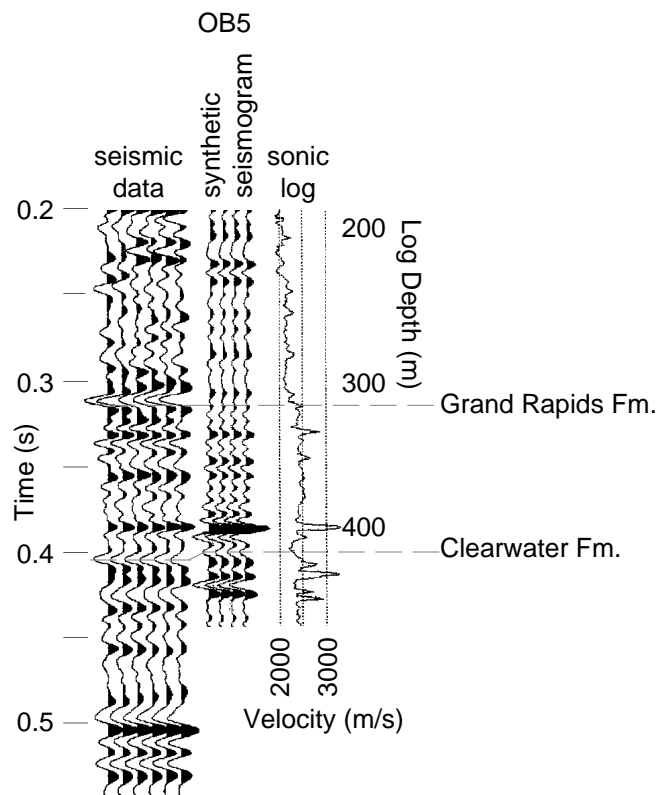


Fig. 3.1 Initial identification of seismic reflectors from the OB5 well log correlation.

Out of the well logs available, the logs from OB5 gave the best tie to the seismic data. Unfortunately, no sonic digits were available below the top of the McMurray Formation in any of the wells, except for a few metres in D3-8. The sonic log at OB5 was acquired in 1985, prior to the commencement of CSS, so it may not provide an accurate measure of the rock velocities at the time of acquisition of the seismic data, which was in 1990. Although the response to tight streaks would not have been altered, the presence of any gas brought out of solution in 1990 by the CSS process would undoubtedly affect the composite seismic response.

To better identify the reflections within the reservoir zone, a wavelet was extracted from the processed seismic data. Tests were done to determine if synthetic seismograms created using a wavelet extracted from the data would correlate better with

the data than those created using a standard Ormsby wavelet. Several extractions were done using the sonic and density digits from well OB5 and nine traces of 1990 seismic data from near that well's location.

The wavelet extraction program used was GMA WAVX, which utilises the Wiener-Levinson method of wavelet estimation. A wavelet is extracted for each of the nine traces and the wavelets summed after tapering to shorten and smooth them. The ideal window to use for the sonic log-seismic data correlation should be one in which the reflectivity series is generally of low amplitude but with sparse, high amplitude events (Brown et al., 1988) at a spacing comparable to the length of the wavelet (Lazear, 1984). The window should also cover data with high signal-to-noise ratio. In the study area the portion of log available is limited because of the shallow depth of the reservoir (420-475 m). The window was selected to exclude the high amplitude events above the Colorado Formation and to avoid the noisy, shallower seismic events. The final window used was one from about 130 m to 475 m on the OB5 sonic log. Too short a window gave poor results, probably because the wavelet and window were then of comparable length.

Parameters such as wavelet length and window length were varied, as was the amount of editing done to the wavelet, to create several different extracted wavelets. Synthetic seismograms for the wells OB1, OB2, OB5 and D3-8 were generated using these wavelets and the final wavelet selected was that which gave the best overall synthetic seismogram/seismic data tie for all these wells (Figure 3.2). The sonic logs used were acquired in 1985 at OB1 and OB5 and in 1991 at OB2 and D3-8. None of the logs was, therefore, acquired at the same time as the 1990 seismic data.

Wells OB5, OB2 and OB1 are vertical observation wells and D3-8 is a deviated well. However, the log shown in Figure 3.2 for D3-8 is a true vertical depth log. The location on the seismic data of the projection of the deviated D3-8 wellbore was calculated using the known bottom hole location (BHL), the angle of deviation and the

depths of the BHL and Grand Rapids tight streak. The extracted wavelet, displayed in Figure 3.2, is 100 ms long and is composed of a primary event followed by a secondary one 25 ms later. This second event could be the result of a shot ghost reflection from the ground surface, since the geophones were at a depth of 10 m.

The well-seismic data correlation is based on an isolated tight streak in the Grand Rapids Formation at about 400 m depth. This tight streak is observed to be present on the logs from OB5 and D3-8 but not from OB2 or OB1. It correlates well to a peak observed on the seismic data at about 0.38 s, which is present at the location of OB5 and D3-8 but not at OB2 or OB1. The well log/seismic data correlation shows that it is not easy to relate seismic peaks directly to thin, closely spaced tight streaks in the reservoir because of the composite wavelet response. The synthetic seismogram/seismic data tie for the Clearwater Formation is better at well OB5 in Figure 3.2 than in Figure 3.1 but the character match at later times is still not very good. However, these correlations are considered to be adequate for the identification of the tops of the Grand Rapids and Clearwater formations at all four well locations.

In both wells D3-8 and OB2, the sonic logs were terminated when the McMurray Formation was penetrated, at 479 m and 476 m, respectively. These depths correspond to the events at the locations of D3-8 and OB2 at about 0.450 s and 0.445 s, respectively. To estimate the arrival time of the top of the Devonian section, use was made of a paper plot of a density log from OB2, which showed the top of the Devonian section to be at 537 m log depth. An interval velocity of 2700 m/s for the McMurray Formation was estimated from the bottom of the D3-8 sonic log. This interval velocity, applied to a thickness of 61 m, results in an estimated interval traveltime of 45 ms for the McMurray Formation. Such a time places the top of the Devonian section at 0.5 s, where a strong peak is observed on the seismic data. This peak is consistently strong and continuous

across the data sets. After having identified the major reflectors and, consequently, the reservoir zone, interpretation and analysis of the seismic data was undertaken.

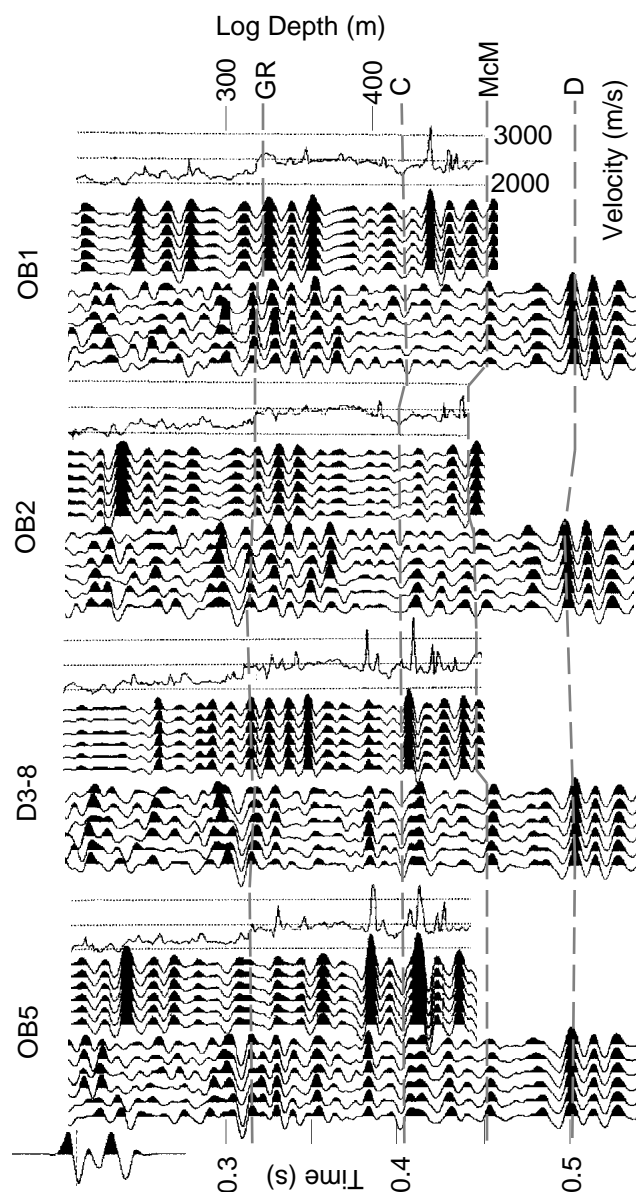


Fig. 3.2 Correlation of seismic data with sonic logs using the extracted wavelet, which is displayed at the upper left. "GR" denotes the top of the Grand Rapids Fm., "C" the top of the Clearwater Fm., "McM" the top of the McMurray Fm. and "D" the top of the Devonian section.

3.2 Forward modelling

To assist in the interpretation of the seismic data within and below the reservoir zone, a simple depth model was created. The model was designed to predict the synthetic response of introducing a low velocity zone, to simulate a steamed interval, into the reservoir. The sonic and density logs from well OB5 were used to create the model but densities were not altered in any of the model perturbations. A zone with velocities representative of the basal Clearwater and topmost McMurray formations was appended to the base of the sonic log so that the seismic response to the top of the McMurray Formation could also be modelled.

Three modifications were made to the original sonic log and are displayed, along with the original log from OB5, in Figure 3.3. In each case, a layer with an interval transit time of 600 $\mu\text{sec/m}$ replaced a layer in the original log. This sonic log interval transit time of 600 $\mu\text{sec/m}$ corresponds to a velocity of 1666 m/s, which, as discussed in Chapter One (section 1.4.3), is a realistic estimate of the lowest interval velocity in a steamed zone close to an injection well under the conditions of high temperature and low effective pressure. Velocities of this order were predicted by forward modelling of these Cold Lake oil sands by Eastwood et al. (1994; their Figure 12). A low interval transit time of 600 $\mu\text{sec/m}$ was recorded over a 24 m zone in a sonic log acquired in an observation well situated less than 12 m from an injection well at Cold Lake (Kry, 1989). For the first two modifications, the thickness of the low velocity zone was 6 m, which is the thickness of the perforated zones in the injection wells. The third modification was to increase the thickness of the steamed zone, in this case to 21 m, which is the total thickness of the interval between the lowermost tight streak and the top of the McMurray Formation at this well.

Each log model consisted initially of three pairs of sonic and density logs. Interpolated logs were then calculated at four regular intervals between both the first and

second logs and the second and third logs. Each pair of sonic and density logs was then converted to a reflectivity series and convolved with the extracted wavelet. The extracted wavelet was used so that the resulting synthetic seismic sections would have a propagating wavelet close to that of the 3-D seismic data. For the model perturbations, only the central sonic log of the initial three was modified. The synthetic zero-offset seismic sections resulting from the initial model and the three modifications, created using GMA LOGM software, are shown in Figure 3.4. The initial synthetic seismic section is shown in Figure 3.4a. On this section, the top of the Clearwater Formation is represented by the trough just below 0.40 s and the top of the McMurray Formation by the trough just below 0.44 s. Although the OB5 sonic log shows a slight increase in velocity at the top of the Clearwater Formation, the OB5 density log (not displayed) shows a clear decrease (from 2170 kg/m³ to 2080 kg/m³) so the reflection coefficient is negative. The top of the McMurray Formation event was expected to be a peak because of the velocity increase there but on this model was observed to be a trough. This is probably due to the long, complex extracted wavelet that was used and interference from earlier events. The thickness, in time, of the low velocity zone is indicated by a bar at the side of each section.

For the first modification of the sonic log (Figure 3.3b), the low velocity zone was placed between depths of 460 m and 466 m, coinciding with the perforated zone in these wells. Figure 3.4b shows the synthetic seismic response to this first modification. Compared to the initial section, a decrease in amplitude of the trough at 0.43 s and the peak at 0.44 s is observed, together with a corresponding increase in amplitude of the trough at 0.445 s (the McMurray event), the peak at 0.45 s and the underlying trough at 0.46 s. These amplitude increases are not seen at the level of the low velocity zone but slightly later. The McMurray event also exhibits a time delay after the low velocity zone. These effects are due mainly to the long extracted wavelet.

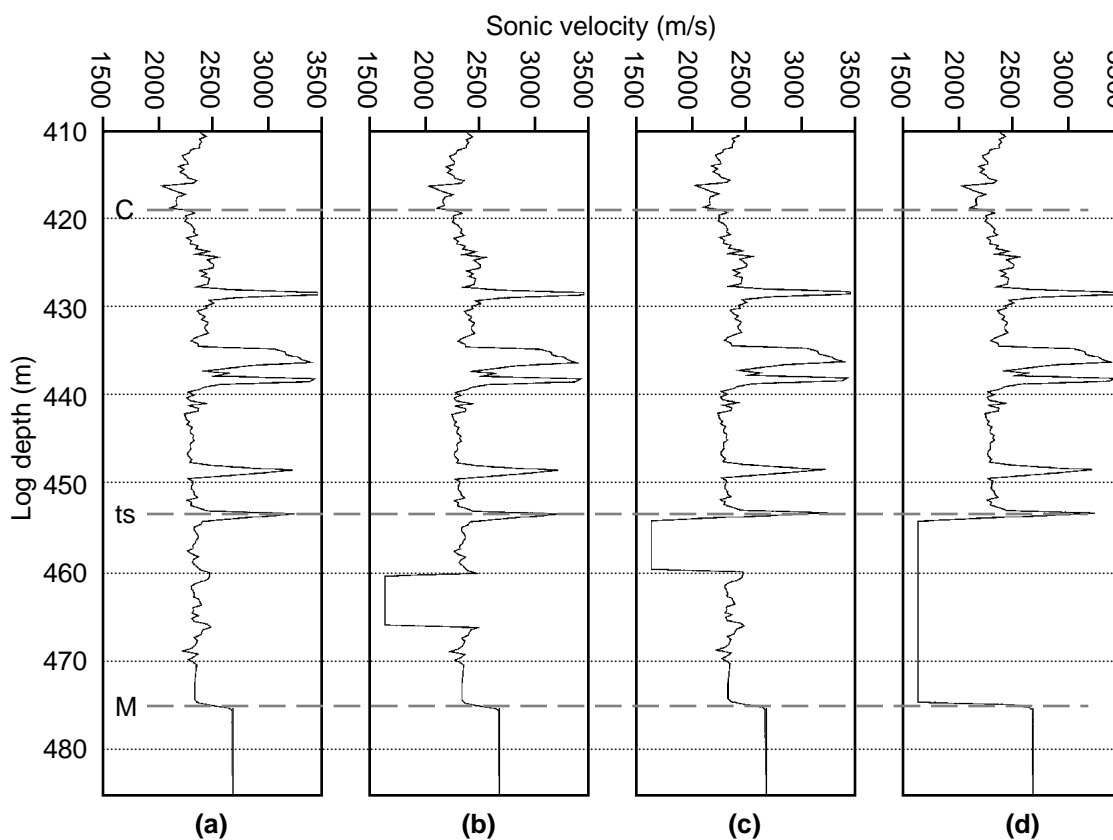


Fig. 3.3 The initial sonic log from OB5 with three modifications used for the forward modelling. A zone representing the basal Clearwater and topmost McMurray formations has been appended to the logs. The logs presented are: **(a)** initial log, **(b)** first modification, with a low velocity zone from 460 m to 466 m, **(c)** second modification, with a low velocity zone from 454 m to 460 m, **(d)** third modification, with a low velocity zone from 454 m to 475 m. "C" represents the top of the Clearwater Formation, "M" the top of the McMurray Formation and "ts" a tight streak.

For the second modification of the model, the low velocity zone was moved 5 m shallower, to depths between 454 m and 460 m, so that it was directly below a tight streak (Figure 3.3c). Such tight streaks are known to inhibit the vertical migration of steam. The results from this model (Figure 3.4c) show an increase in amplitude of the trough at 0.43 s, which is at the level of the low velocity zone. The McMurray event exhibits a time delay but its change in character, from a trough to a zero-crossing, is more pronounced. The peak and trough immediately following the McMurray event have increased amplitudes and a small time delay of 2 ms is also observed. Increasing the

thickness of the low velocity zone to 21 m results in the synthetic seismic section in Figure 3.4d. The underlying McMurray event changes character from a trough to a strong peak and has a large time delay of 7 ms. The amplitudes of events earlier than 0.45 s are similar in Figures 3.4c and 3.4d but in Figure 3.4d the amplitude of the event at 0.46 s is less than it is in Figure 3.4c. A more pronounced time delay in the McMurray event and the event after it is observed in Figure 3.4d. This is expected since a larger low velocity zone had been introduced into this model. However, because of the change in phase, the time delay is not obvious at the McMurray Formation level but can be seen later in the section, at 0.475 s. The positive impedance contrast observed for the McMurray event is that which was expected and is seen now that this reflection is at the base of a 21 m thick homogeneous section, thus reducing interference effects. In the rest of this dissertation the McMurray event is interpreted as a peak to avoid confusion over polarities.

In Figures 3.4b, 3.4c and 3.4d, lateral and vertical changes in seismic amplitudes result from the introduction of a low velocity interval, representing the steamed zone, into the well logs. In each case, a zone of increased amplitude is seen but its position in time does not necessarily correspond to the position in depth of the anomalous zone. In Figure 3.4b the increased amplitudes are later than the low velocity zone while in Figures 3.4c and 3.4d they both coincide and are later than the zone. In part this is due to the length and complexity of the extracted wavelet used.

These results indicate that the presence of an amplitude anomaly in the seismic data can be taken as an indication of a lateral change in interval velocity but that the depth of this change cannot necessarily be determined easily. The location of the anomaly in x-y space shows the spatial position of the velocity anomaly. A time delay in some of the reflectors underlying the low velocity zone is apparent in each case. The McMurray event displays a small time delay in Figure 3.4b while in Figures 3.4c and

3.4d the delay is not obvious because of the change in phase. This delay is noticeable, however, on later events. The magnitude of the time delay is directly proportional to the thickness of the low velocity zone in this model. In addition, temperatures vary considerably throughout the reservoir as the steam moves away from the injection wells so that velocities will also vary laterally more than those shown by the simple model in Figure 3.3. A travelttime delay observed on a seismic section is an indication of lower interval velocities but a distinction between a thin zone of very low velocity and a thicker zone with an intermediate velocity cannot be made.

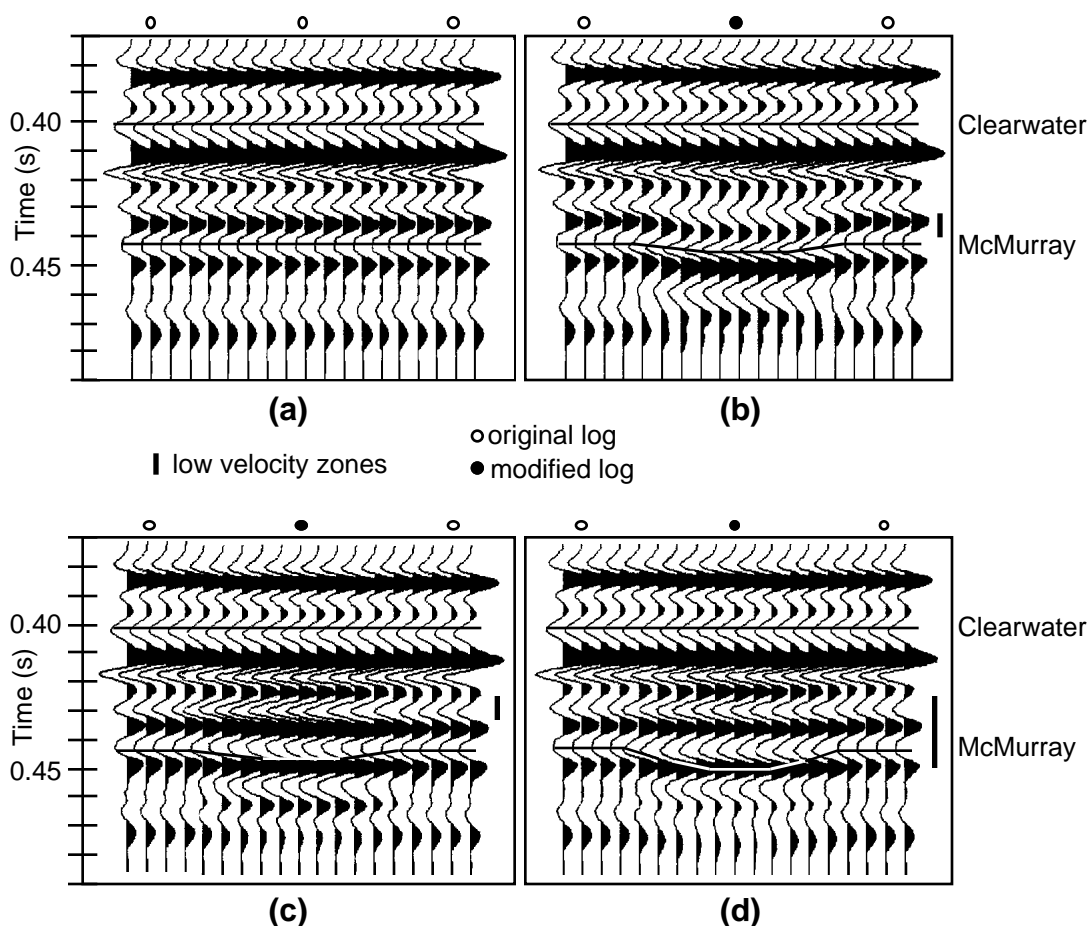


Fig. 3.4 Synthetic seismic sections generated by forward modelling. (a) is the initial unperturbed model while (b), (c) and (d) show the results of introducing low velocity zones into the well logs. The black bars at the sides of the models indicate the extent and location of the low velocity zone in each case.

3.3 Analysis of the processed 3-D seismic data

3.3.1 Traveltime analysis

Examples of lines from the migrated data sets are presented in Figures 3.5 and 3.6. Figures 3.5a and 3.5b show examples of crossline 50, selected from the central part of the 1990 and 1992 surveys, respectively, while in Figures 3.6a and 3.6b are displayed inline 34. The locations of these lines are shown in Figure 2.1. Crossline 50 was selected because it shows nicely an amplitude anomaly in the reservoir zone and inline 34 was selected because it goes through the locations of two observation wells. End portions of the lines, where data quality is poor because of low fold, are not displayed and the data have been bandpass filtered between frequencies of 25/30-130/150 Hz. The same gain scalar has been applied to each line for these plots. Asterisks along the tops of the lines indicate the projected locations of the nearest wells, which are offset 48 m from crossline 50 and 8 m from inline 34.

The top of the Clearwater Formation is identified in Figures 3.5 and 3.6 as the trough which occurs just after 0.4 s, and the top of the Devonian section as the peak at 0.5 s. A peak at 0.455 s was picked as the top of the McMurray Formation. These events are annotated on the sections. Above the reflection from the Clearwater Formation, the two sections appear very similar in terms of seismic character and frequency content. High amplitude events at 0.32 s and 0.36 s are present on both sections in Figure 3.5 and have similar character changes along each line. In Figure 3.6 the Grand Rapids tight streak is very clearly imaged, at about 0.385 s on the southwest part of the line. Note how this reflection terminates at crossline number 44 in Figure 3.6 and that this event is not seen on crossline 50 in Figure 3.5.

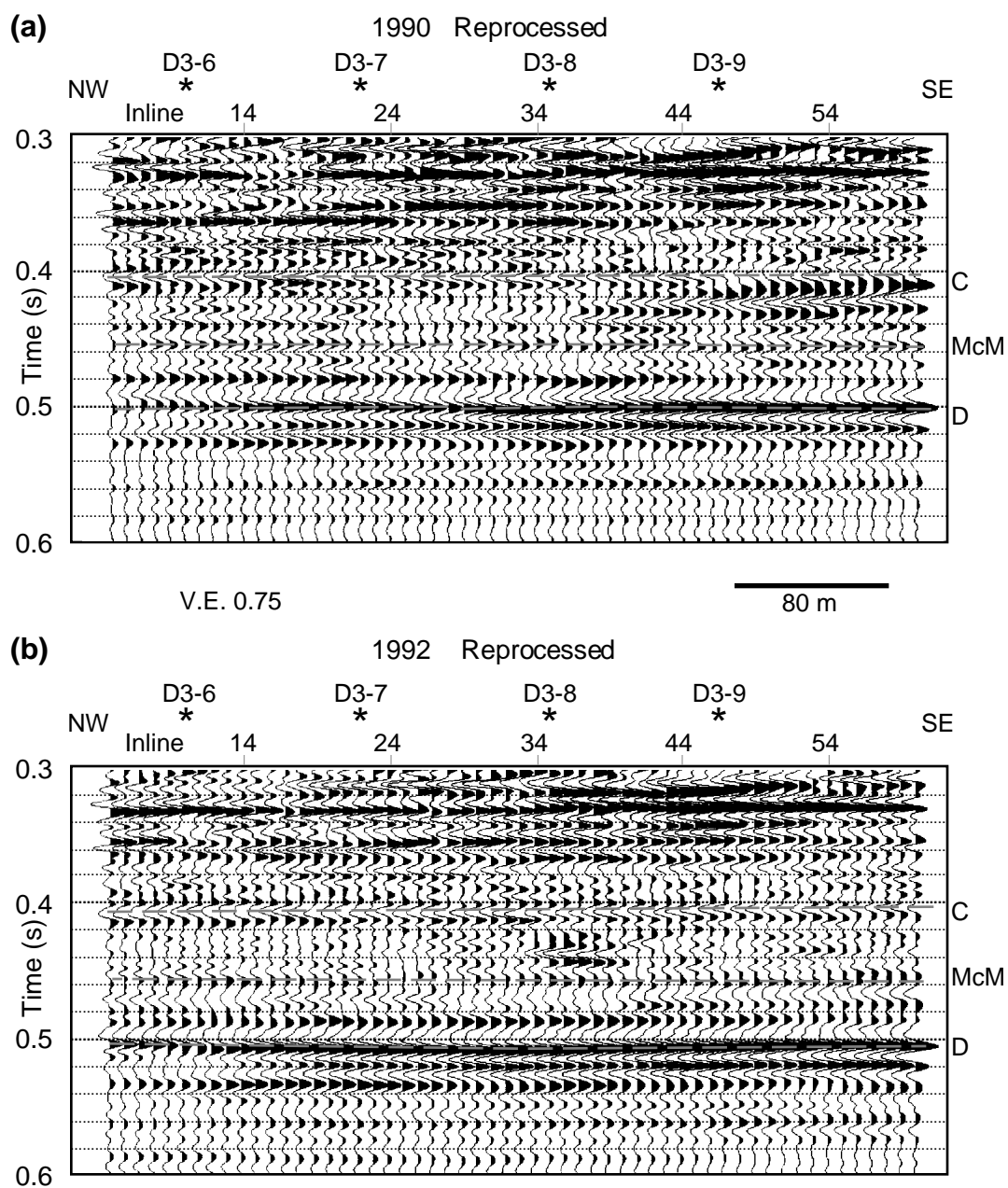


Fig. 3.5 Reprocessed, migrated crossline 50 from the centre of the (a) 1990 and (b) 1992 data volumes. The projected locations of steam injection wells are indicated by asterisks. "C" denotes the top of the Clearwater Fm., "McM" the top of the McMurray Fm. and "D" the top of the Devonian section.

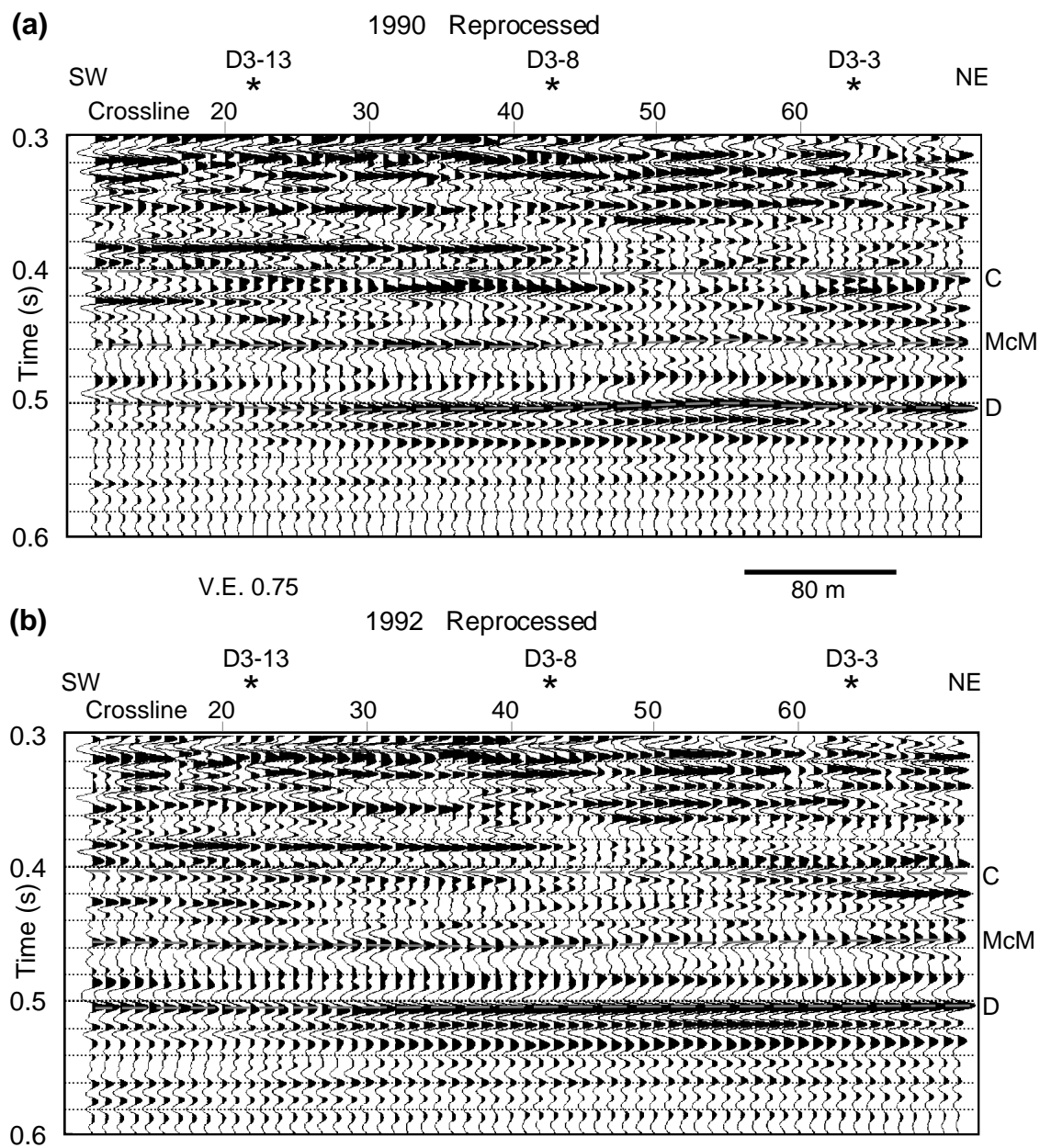


Fig. 3.6 Reprocessed, migrated inline 34 from the centre of the (a) 1990 and (b) 1992 data volumes. The projected locations of steam injection wells are indicated by asterisks. "C" denotes the top of the Clearwater Fm., "McM" the top of the McMurray Fm. and "D" the top of the Devonian section.

Few coherent high amplitude events are present within the reservoir zone, which extends from 0.405 s to 0.455 s. However, comparison of the 1990 and 1992 lines, in both Figures 3.5 and 3.6, reveals two major seismic character differences within the reservoir zone. In Figure 3.5b (the 1992 crossline) a high amplitude event can be seen on inline traces 34 to 40 at a time of 0.435 s. This event is not seen on the 1990 line (Figure 3.5a) and its arrival time corresponds to the depth of the perforations in the injection wells, although the results of the modelling, discussed in section 3.2, suggest that the position in time of an amplitude anomaly may not always reflect the position in depth of the velocity anomaly. This high amplitude anomaly is situated near the location of injection well D3-8 at inline 35. A corresponding decrease in frequency content of events deeper than this anomaly is also apparent, between 0.46 s and 0.48 s (Figure 3.5b). Such attenuation of the higher frequencies could be caused by a decrease in viscosity of the pore fluid. Hickey et al. (1991) state that the main cause of attenuation in high viscosity fluids is viscous dissipation. Velocity and viscosity are strongly dependent on temperature and decrease considerably during steam injection. Hence, this anomaly is interpreted to be due to the presence of steam in the reservoir during the acquisition of the 1992 survey.

The presence of a high amplitude trough on the 1990 line (Figure 3.5a) at about 0.425 s over traces 40 to 60, which is absent on the 1992 line, also indicates a temporal change in reservoir conditions. It is possible that it is due to the localised presence of a gas-saturated zone. These zones were present during the production cycle in 1990 but absent in 1992, when pore fluid pressures were too high for the existence of gas, except in very thin zones (Eastwood et al., 1994).

Detailed analysis of the Clearwater-Devonian interval in Figures 3.5 and 3.6 reveals an increased interval transit time for the 1992 line. This is particularly apparent in Figure 3.6. In Figure 3.6a (1990) the Devonian event exhibits a structural high over

crosslines 48 to 60. In Figure 3.6b (1992) this event appears to have been flattened because of a significant travelt ime delay at this location. Interestingly, the anomaly does not coincide with an injection well location but is between two wells, D3-8 and D3-3. This travelt ime increase is attributed to a reduction in interval velocities in the steamed zone in 1992 due to the conditions of higher temperature and lower effective pressure. A comprehensive analysis of the causes of the travelt ime anomalies observed on the original processed data is discussed by Eastwood et al. (1994).

A slightly different approach was taken in this study using the reprocessed data. Initially, the extents of the travelt ime anomalies were mapped. The Clearwater to Devonian time interval isochron maps (Figure 3.7) show the variation across the two surveys of the interval travelt imes. On all the following maps inlines and crosslines are both 8 m apart and the approximate map size is 380 x 560 m. The locations of the steam injection and observation wells are shown and the wells are numbered (the observation wells are prefixed by OB). The areas of the map where the fold is low and the seismic data unreliable are not displayed. Reds and yellows (light greys) indicate the lowest isochron values while dark blues and purples (dark greys) indicate the highest isochron values. In general, the isochron values are seen to be higher across the 1992 survey (Figure 3.7b). The greatest difference between the two surveys is in the area bounded by the two most northerly lines of wells.

Subtraction of the 1990 isochrons from the corresponding 1992 isochrons was done to create a map which shows the areal differences in the interval travelt imes (Figure 3.8a). Red and yellow (dark grey) coloured areas indicate those of high positive interval travelt ime differences and dark blue and purple (light grey) coloured areas those of negative differences. Values of the interval travelt ime differences vary from -3 ms to +7 ms. A positive difference denotes a larger interval travelt ime for the 1992 data while a negative isochron difference represents a larger interval travelt ime for the 1990 data. The

lowest negative values occur at the left edge of the survey near inline 30, where the Devonian event appears to be poorly imaged on the 3-D seismic data, so the values may not be reliable at this location. Negative and near-zero delay times occur in the northeastern part of the survey. Here the fluid pressure was lower than over the rest of the field during the acquisition of the 1992 data (J. Eastwood, *pers. comm.*). Thus the interval velocity in this area is not expected to be decreased by an effective stress component in 1992. The highest interval traveltimes differences occur in the centre of the survey, from around crosslines 45 to 58 and inlines 10 to 54. In this area the Devonian event is delayed by the greatest amount on the 1992 data; a phenomenon well illustrated in Figure 3.6b, where the Devonian event is clearly delayed. Observation wells OB1, OB2 and OB6 are seen to lie in the most anomalous area of Figure 3.8a. Measurements made at the six observation wells showed the most significant temperature increases between 1990 and 1992 to be at wells OB1 and OB6. On the traveltimes anomaly map (Figure 3.8a), anomalies are present at the locations of wells OB1 and OB6. As discussed in Chapter One, higher temperatures in the reservoir will result in lower interval velocities and, consequently, increased traveltimes for any interval straddling the low velocity zone. Since this map reflects correctly the increased traveltimes to be expected at the locations of wells OB1 and OB6, it can be used to view the spatial distribution of low velocity zones across the survey.

To test the repeatability of the arrival time of the top Clearwater event on the 1990 and 1992 surveys, difference maps were made of the 1992-1990 Devonian and Clearwater time structures. These maps are shown in Figures 3.8b and 3.9, respectively. The Clearwater arrival times should be very similar, so that the traveltimes anomalies on the Devonian time structure difference map (Figure 3.8b) should be the same as the interval traveltimes anomalies on the Clearwater-Devonian isochron difference map (Figure 3.8a) and the Clearwater time structure difference map (Figure 3.9) should display only small

differences. Very similar areas of traveltime anomalies are seen in Figures 3.8a and 3.8b. Approximately 80% of the survey shows an increased traveltime for the 1992 survey. Notable are the areas of relatively high traveltime delays around crosslines 45-58 and inlines 10-50. The distribution of traveltime anomalies observed in Figure 3.8 matches closely that of Eastwood et al. (1994) in their Figure 3. Similar values to theirs of 4 ms to 6 ms for the time delay over inlines 10-50 and crosslines 45-58 are obtained. Assuming a picking error of 0.5 ms for each horizon, the standard error in each isochron value is ± 0.7 ms. Figure 3.9 shows that the arrival time of the top of the Clearwater Formation varies by only 2 ms between the two surveys and that over the greater part of the map the difference is only 1 ms.

The theoretical traveltime delays expected from a low velocity steamed zone were calculated and are plotted in Figure 3.10. An original cold reservoir interval velocity of 2350 m/s was used and time delays calculated for steamed zone thicknesses up to 50 m. To observe the effect of different interval velocities, steamed zone velocities of 1700 m/s, 1900 m/s and 2100 m/s were used. The temperature of the reservoir varies considerably, both areally and vertically, and so the interval velocity of the steamed zones will do so likewise.

The minimum value used here is 1700 m/s, which occurs under conditions of high temperature and high pore fluid pressure. Some dilation of the reservoir, resulting in higher porosity, can also contribute towards lower interval velocities. Theoretical values of the time delay range up to 8 ms while the measured values range up to 7 ms. It is not possible to determine the thickness of a steamed zone without knowledge of the temperature and stress conditions. However, for each value of time delay, a minimum value of steamed zone thickness can be established.

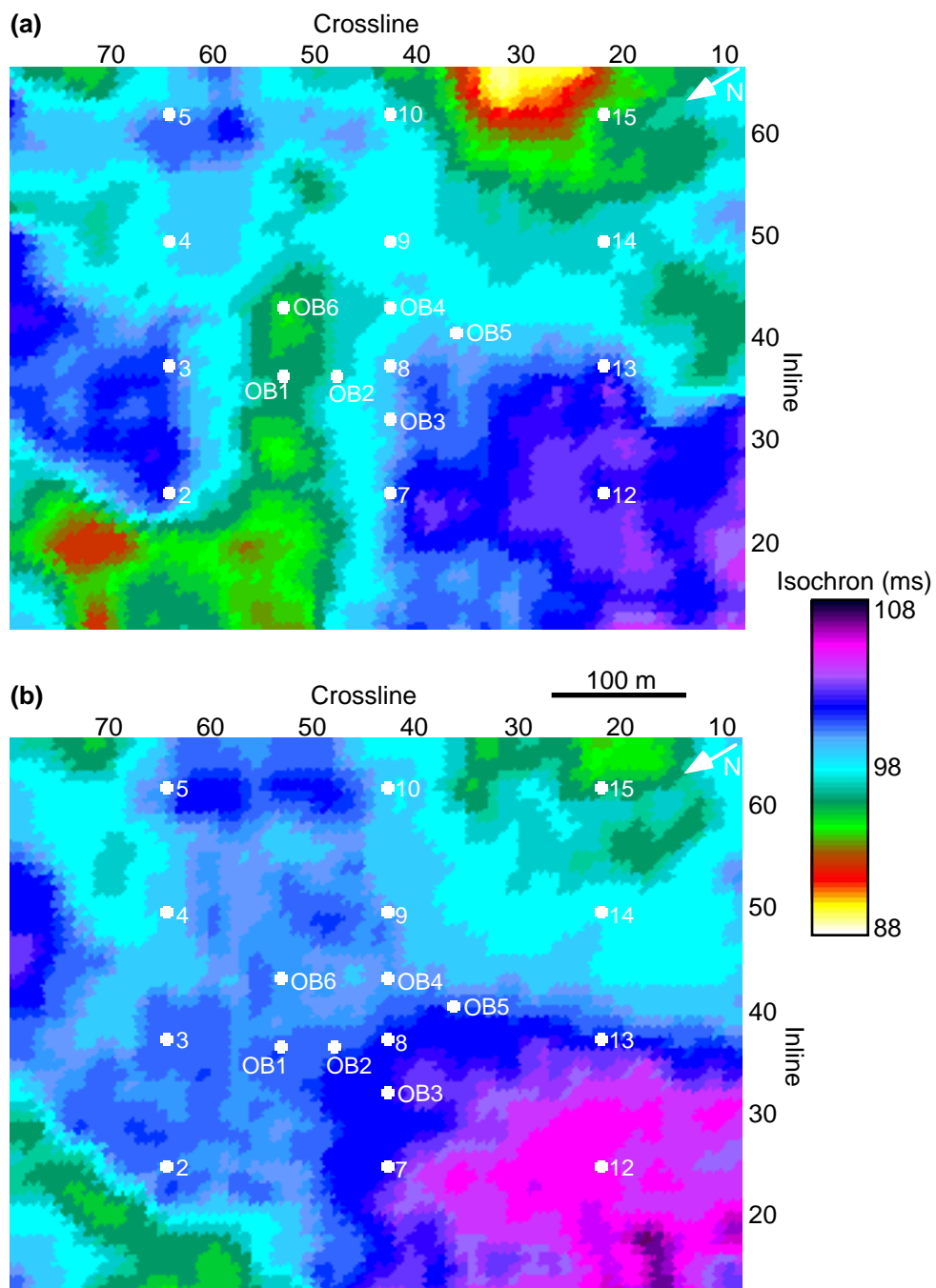


Fig. 3.7 The Clearwater to Devonian isochron traveltimes from the (a) 1990 and (b) 1992 data sets.

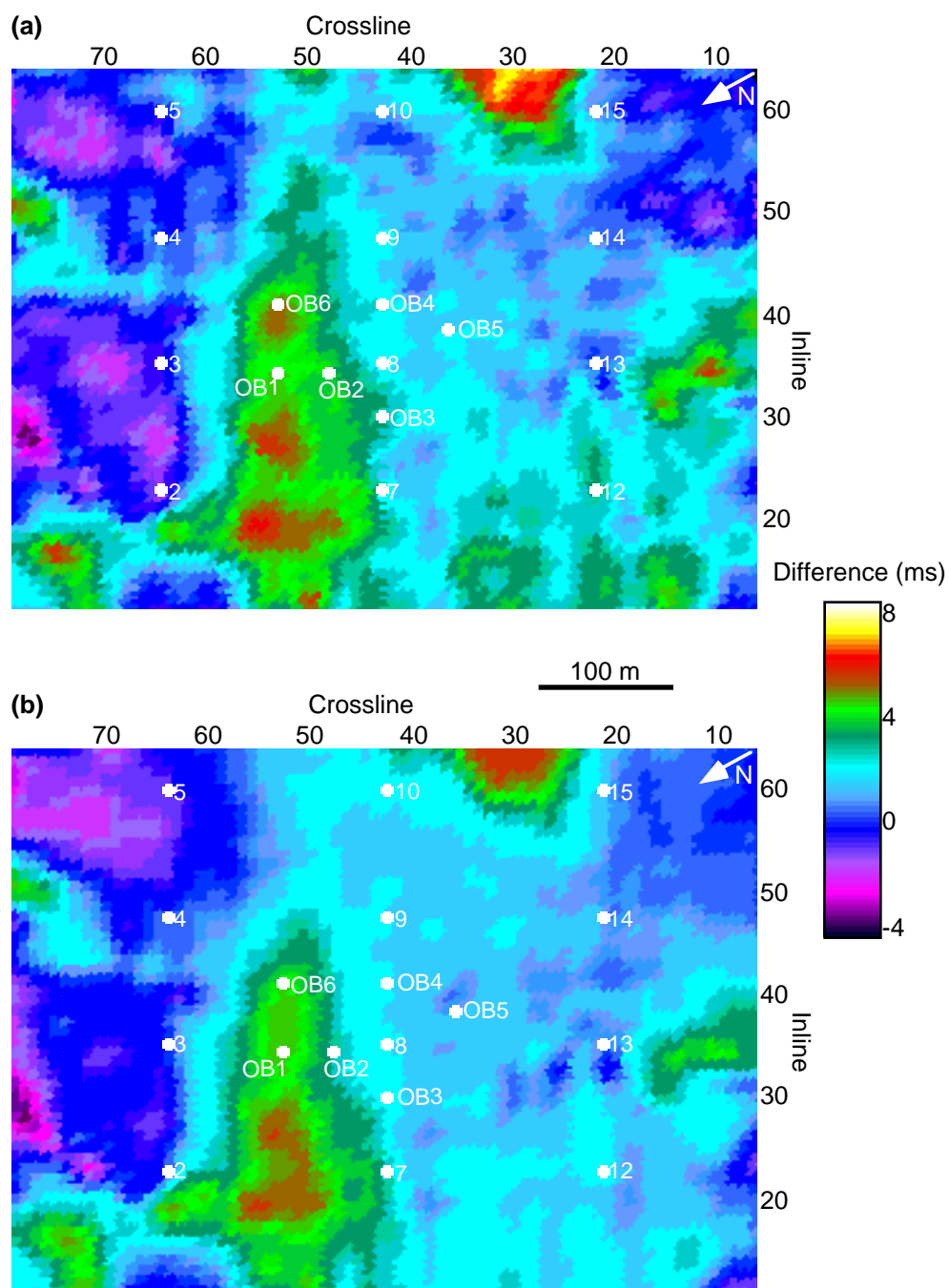


Fig. 3.8 Traveltime differences for the Devonian event. **(a)** The Clearwater to Devonian isochron traveltime differences calculated by subtracting the 1990 isochron values from the 1992 values. **(b)** The Devonian time structure differences calculated by subtracting the 1990 times from the 1992 times. Positive values indicate a later arrival time for events on the 1992 data than on the 1990 data.

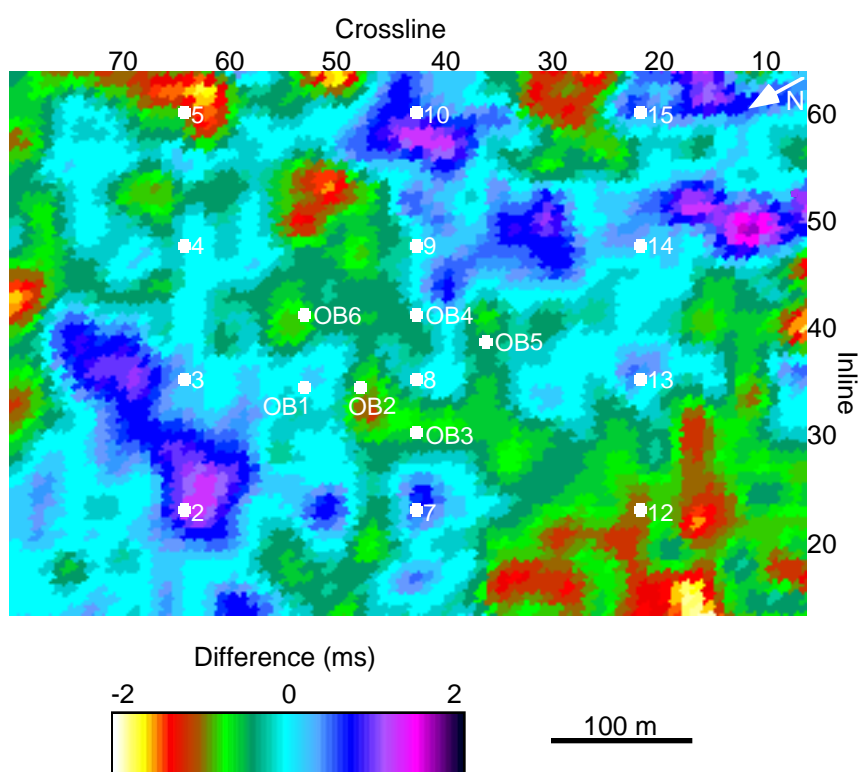


Fig. 3.9 The time structure differences between the 1992 and 1990 data sets for the top Clearwater event. The 1990 values were subtracted from the 1992 values. Positive values indicate a later arrival time for events on the 1992 data than on the 1990 data.

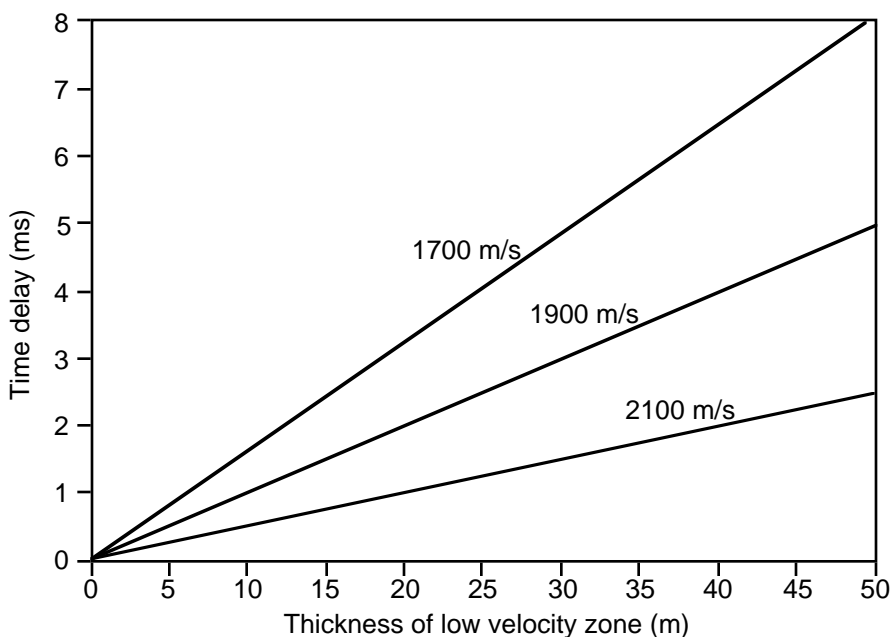


Fig. 3.10 Plot of travelt ime delay versus thickness of steamed zone for three values of steamed zone interval velocity.

3.3.2 Amplitude analysis

The areal extents of anomalous high amplitude zones, such as those seen in Figures 3.5a and 3.5b (discussed earlier), are shown in Figure 3.11. This figure shows the scaled rms amplitude of the seismic data calculated over a window of 10 ms. Figure 3.11a displays this amplitude for a window centred on a time of 0.420 s from the 1990 data while Figure 3.11b shows the amplitude for a window centred on 0.437 s from the 1992 data volume. Red and yellow (dark grey) areas are those of the highest amplitudes. The area of higher amplitudes at the eastern end of crossline 50, coloured green (grey) in Figure 3.11a, corresponds to the trough observed in Figure 3.5a at 0.425 s over inlines 49 to 60. An event of very high amplitude is seen on Figure 3.11b around the intersection of inline 37 and crossline 52. This event corresponds to the high amplitude trough seen on Figure 3.5b at 0.435 s over inlines 35 to 39.

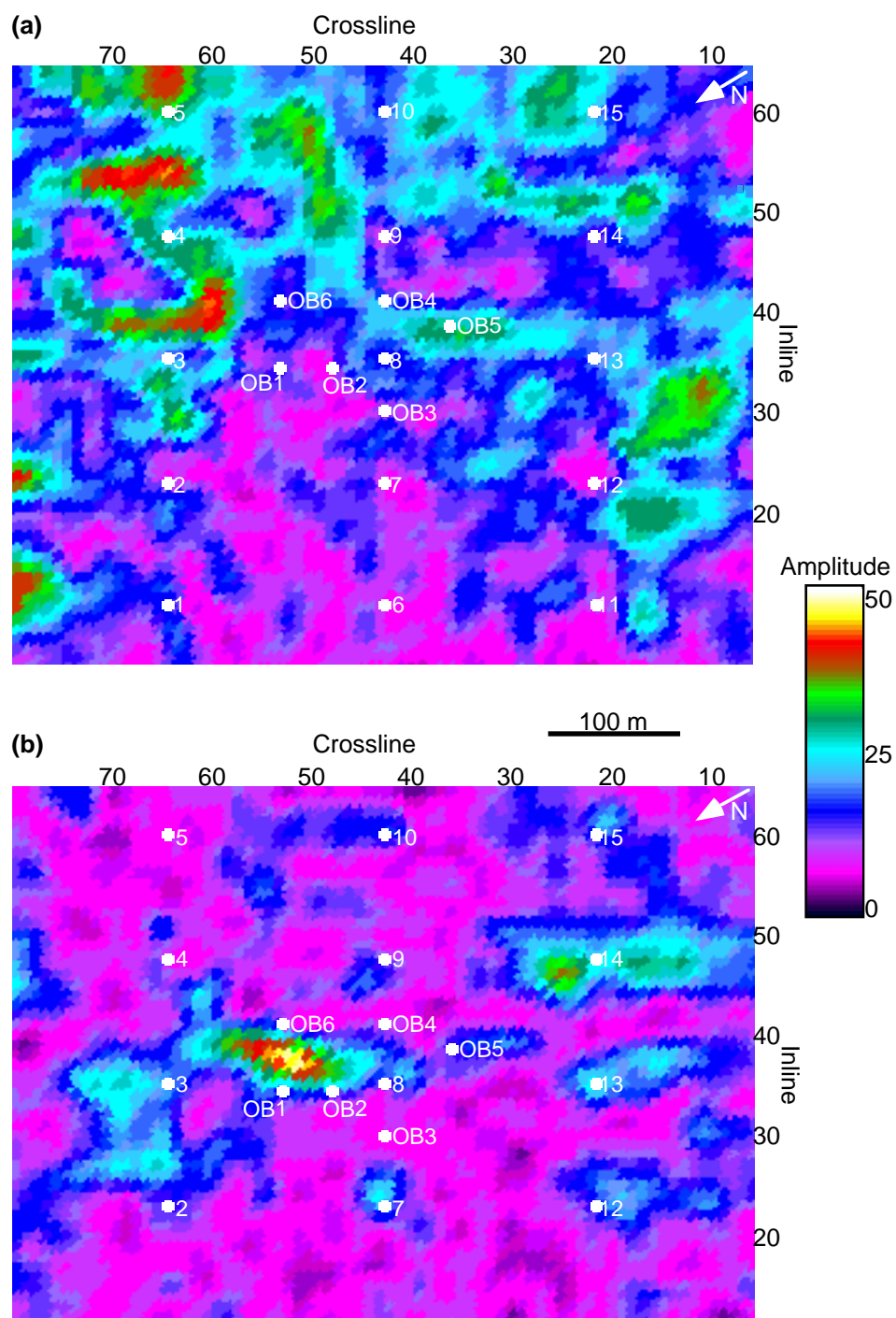


Fig. 3.11 Scaled rms amplitudes of the seismic data calculated over a 10 ms window. These amplitudes were calculated from (a) the 1990 data with the window centred on 0.420 s and (b) the 1992 data with the window centred on 0.437 s.

Higher amplitude zones are seen clearly around each of the injection wells on the most southerly row in Figure 3.11b (wells D3-12, D3-13, D3-14 and D3-15) and at wells D3-3 and D3-7. It is interpreted that the high amplitude areas observed in Figure 3.11b represent steamed zones in 1992. In some places the steamed zones are localised around the injection wells but between wells D3-3 and D3-8 appears a linear zone of communication. Boone et al. (1993) state that a channel of communication between OB6 and D3-8 appeared in early 1992, which is the time of this survey. This area of high amplitude is also close to the locations of OB1 and OB6; in agreement with the recorded temperature increases. Anomalous amplitudes are not seen at all the injection well locations, perhaps because the steam has diffused up through the reservoir and is no longer confined to the depth of injection. The historical direction of communication at the D3 pad, southwest to northeast, is reflected in the linear high amplitude zones seen in Figure 3.11b. On the travelttime difference maps (Figure 3.8), however, the orientation of the anomalies is northwest to southeast.

3.4 Analysis of the "difference" data volume

A “difference” data volume was created by subtracting the 1990 data from the 1992 data and it was interpreted using the same techniques as for the regular 3-D data. Amplitude normalisation above the reservoir zone and a constant time delay of 3 ms were applied prior to subtraction. A design window above the reservoir zone was used for the amplitude normalisation to exclude amplitude differences within and below the reservoir caused by different reservoir conditions. All the data volumes were loaded onto a workstation and analysis was undertaken using Landmark Seisworks3D software.

Examples from this data volume are shown in Figure 3.12 for the same crossline 50 as in Figure 3.5 and in Figure 3.13 for the same inline 34 as in Figure 3.6. The locations of these lines are shown in Figure 2.1. The data used to produce Figures 3.12

and 3.13 were bandpass filtered between frequencies of 25/30-130/150 Hz and trace amplitudes were plotted with the same gain scalar as used for the data in Figures 3.5 and 3.6. In these figures “C” denotes the top of the Clearwater Formation and “D” the top of the Devonian section. From a time of 0.300 s to the top of the reservoir zone at 0.405 s, the residual amplitudes are small but increase considerably once the reservoir is entered. A high amplitude residual event is present on the right end of both lines at a time around 0.420 ms. This event corresponds to the high amplitude event observed at the right end of the 1990 line in Figure 3.5a and which is absent from the 1992 line in Figure 3.5b.

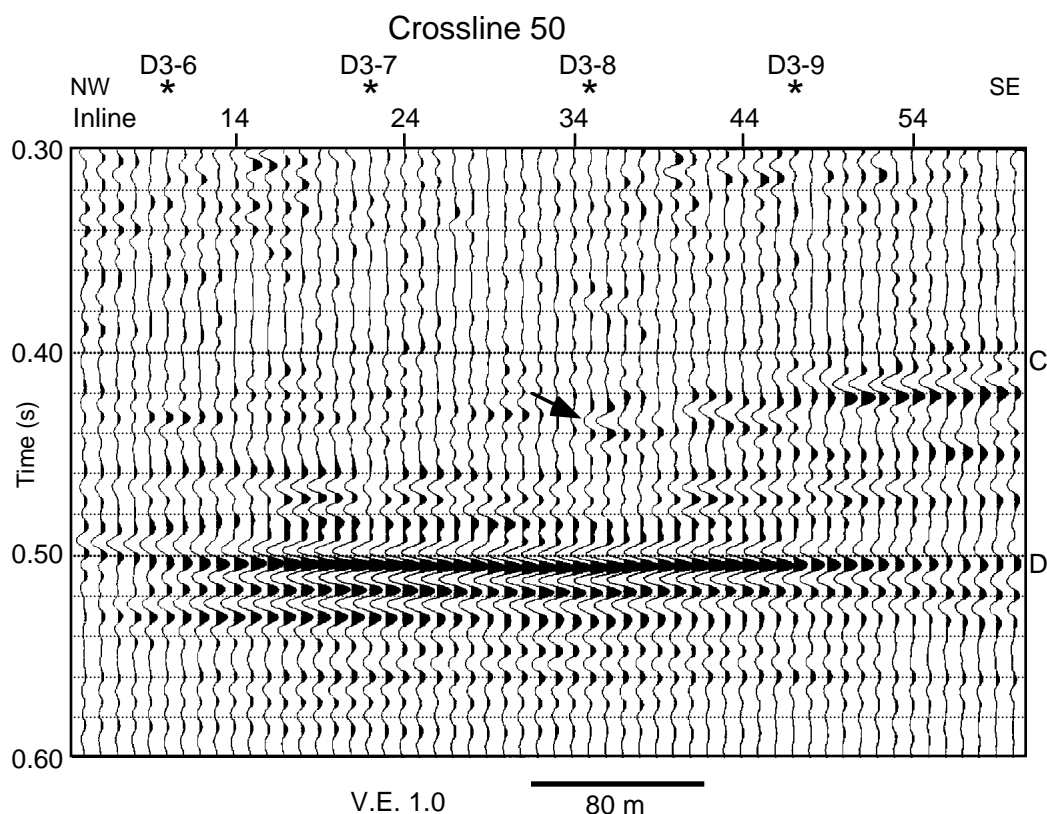


Fig. 3.12 The differences between the 1992 and 1990 data along crossline 50, displayed in Figure 3.5. Asterisks above the line denote the projected locations of the nearest steam injection wells. The top of the Clearwater Formation is identified by the letter “C” and the top of the Devonian section by “D”.

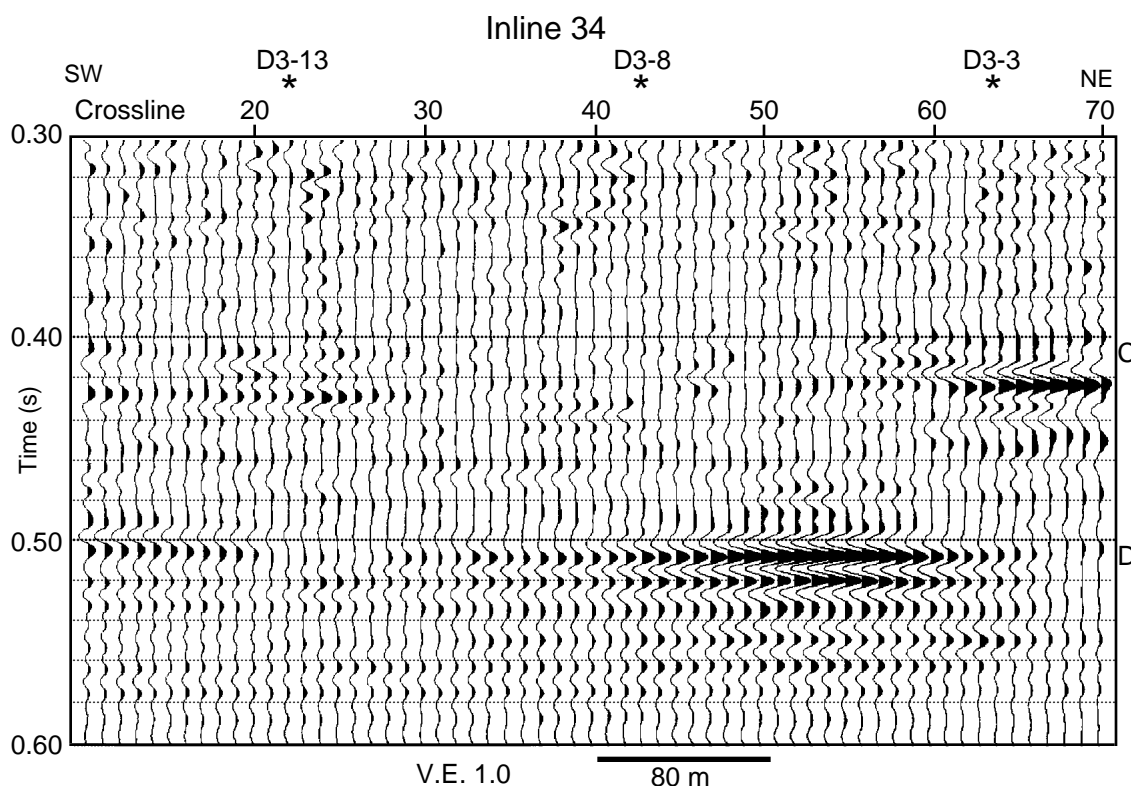


Fig. 3.13 The differences between the 1992 and 1990 data along inline 34, displayed in Figure 3.6. Asterisks above the line denote the projected locations of the nearest steam injection wells. “C” denotes the top of the Clearwater Formation and “D” the top of the Devonian section.

The medium amplitude trough observed at 0.435 ms over traces 35-39 on crossline 50 in Figure 3.12 (shown by an arrow) is the residual of the event seen on the 1992 line in Figure 3.5b and absent on the 1990 line in Figure 3.5a. It was interpreted to be the seismic response due to the presence of steam. The differences in Devonian arrival times observed in Figures 3.6a and 3.6b show up very clearly in Figure 3.13 over crosslines 47 to 60. These high amplitude Devonian residuals (Figures 3.12 and 3.13) are due primarily to differences in reflection traveltimes between the 1990 and 1992 surveys rather than actual differences in amplitude of the Devonian reflections. These Devonian reflections were analysed further by extracting from the two data volumes the rms amplitudes within a 10 ms window centred on the Devonian pick. The 1990 values were

subtracted from the 1992 values to create a Devonian amplitude difference map. The data sets had been normalised above the reservoir zone so that the amplitudes of the Devonian event would not be normalised specifically, and no post-stack AGC was applied. Figure 3.14 shows the mapped amplitudes of the Devonian reflection in (a) 1990 and (b) 1992. The amplitudes have been scaled from 0 to 50 and appear to be slightly higher in the 1992 data. However, the Devonian amplitude difference map (Figure 3.15a), plotted at the same amplitude scale as Figure 3.14, shows that the residual amplitudes are, in fact, low. For comparison, the top Clearwater Formation amplitude difference map is also displayed in Figure 3.15b, at the same scale. The residual amplitudes for the Clearwater event are seen to be of the same order as those for the Devonian event.

Sections (Figures 3.5, 3.6, 3.12 and 3.13) and maps (Figure 3.8) show that the Devonian arrival times have not been delayed consistently over the survey area. In Figure 3.12 the Devonian event is delayed across nearly all of the line, but in Figure 3.13 the delay is restricted to certain traces. The extents of the Devonian residuals in Figures 3.12 and 3.13 correspond to the extents of the traveltimes anomalies shown in Figure 3.8. The high amplitude event in Figure 3.13 at 0.510 s, extending over crosslines 47 to 59, corresponds to the extent of the green (grey) coloured anomaly on inline 34 in Figure 3.8, which denotes a time delay of about 5 ms. Two possible reasons for the variable delay times are the inhomogeneous distribution of the steam through the reservoir in 1992 or of the gas zones in 1990. It is possible that, in places, the low interval velocity of the gas-saturated zones in 1990 has the same effect on interval transit times as the low interval velocity of the steamed zone in 1992.

It is interpreted that two effects of changes in reservoir conditions are observed on the seismic data. The first is a decrease in interval velocity within the reservoir zone, caused by the presence of steam and increased pore fluid pressure; the second is a

localised change in seismic reflectivity. These two effects have been observed at another EOR site where seismic data have been used to monitor the distribution of heat in the reservoir (den Boer and Matthews, 1988). Thin, highly impermeable calcite-cemented zones (tight streaks) in the reservoir are known to inhibit the vertical movement of steam. Local reflectivity changes could be caused by steam trapped beneath tight streaks in 1992 or by local gas-saturated zones in 1990.

To show how amplitudes vary spatially at different arrival times, rms amplitudes were extracted from the "difference" data volume over 10 ms windows at various arrival times. Figure 3.16a shows the mapped rms amplitudes from a time window centred on 0.420 s, the level where shallow amplitude anomalies were seen on the 1990 data (Figure 3.5a). These anomalies appear to be strongest in the northeastern part of the survey. Figure 3.16a shows a different distribution of anomalies from Figure 3.11a, which displays the rms amplitudes within the same window from the 1990 data volume. These maps were scaled from 0 to 50 independently so absolute amplitude values are not comparable. Each map does show, however, a large area of low amplitudes in the central region of the survey. The amplitudes extracted from the 1990 data may include responses from tight streaks whereas those extracted from the difference data only show anomalies.

Rms amplitudes extracted over a window later in the reservoir, centred on 0.437 s, are displayed in Figure 3.16b. Again the northeastern part of the survey is affected most but there is also a linear trend of high amplitudes through the middle of the area, which could be an indication of communication between wells. These amplitudes were taken from a zone at the level of the perforations and, in general, there are amplitude increases at the locations of the injection wells. The pattern of anomalies seen here in Figure 3.16b is similar to that of Figure 3.11b, which shows the rms amplitudes over the same window from the 1992 data volume. In particular, high amplitudes are mapped on both of these maps between wells OB1 and OB6 and in a linear trend to the southwest.

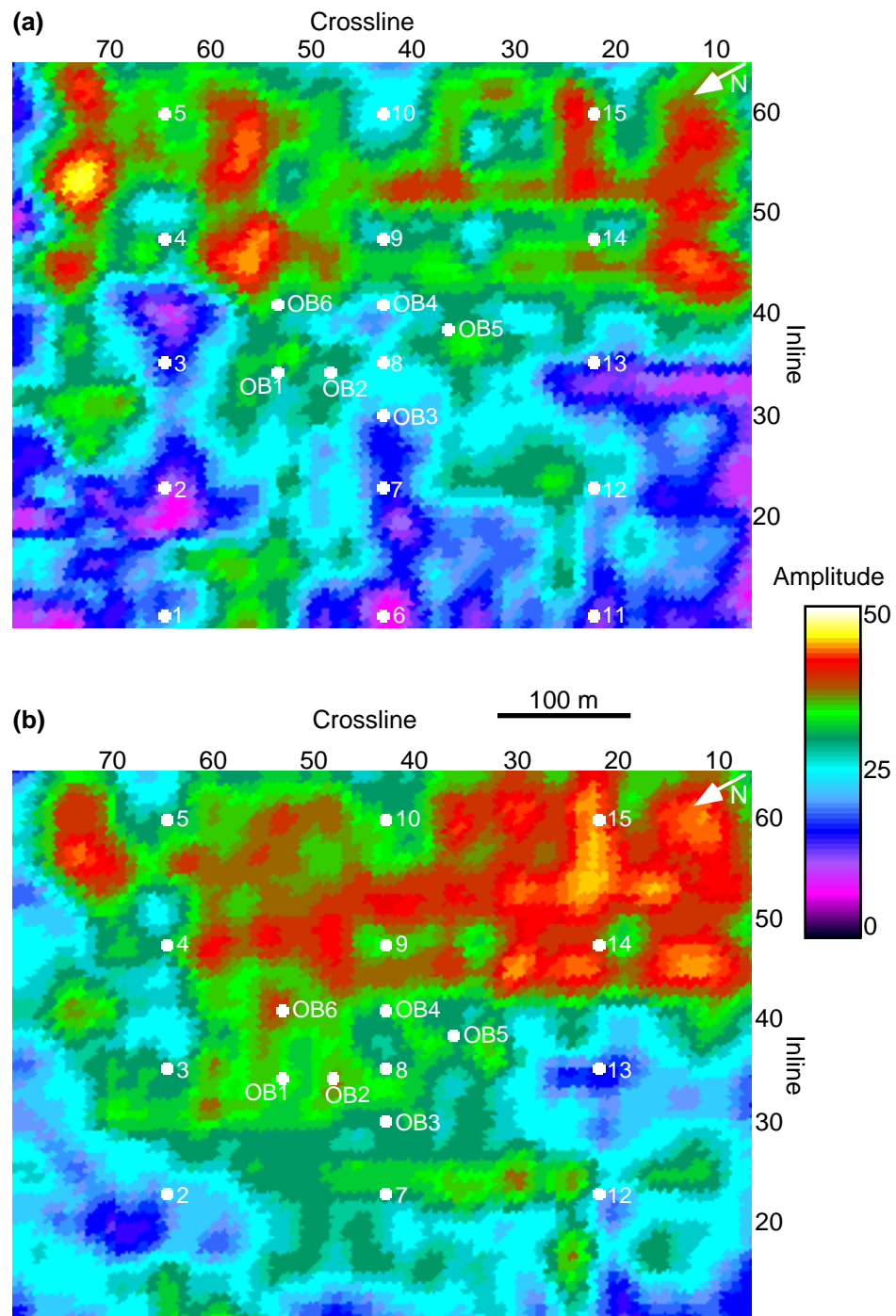


Fig. 3.14 Amplitudes of the Devonian event for the (a) 1990 and (b) 1992 data.

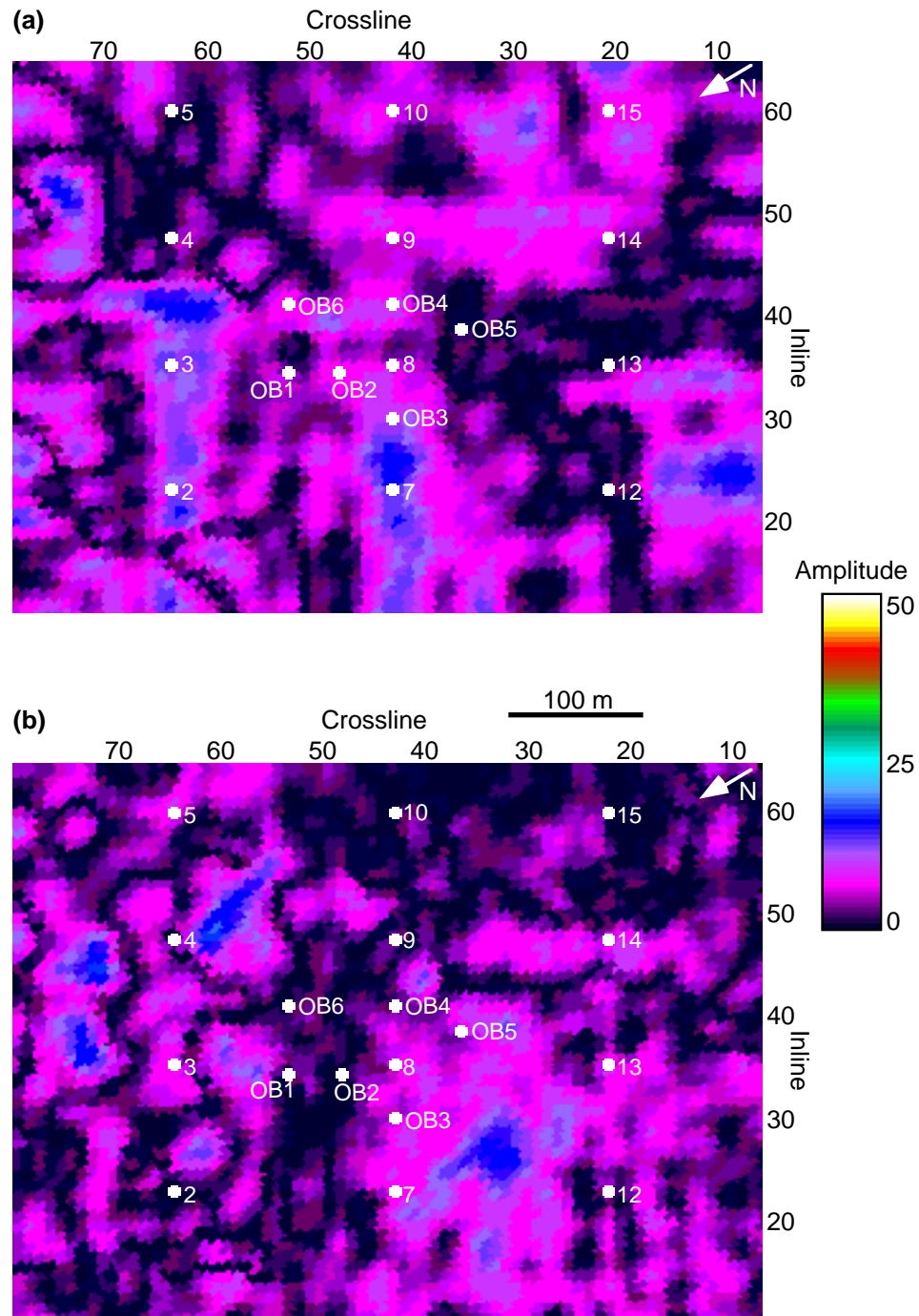


Fig. 3.15 Residual amplitudes between the 1990 and 1992 surveys of the (a) Devonian event and (b) Clearwater event.

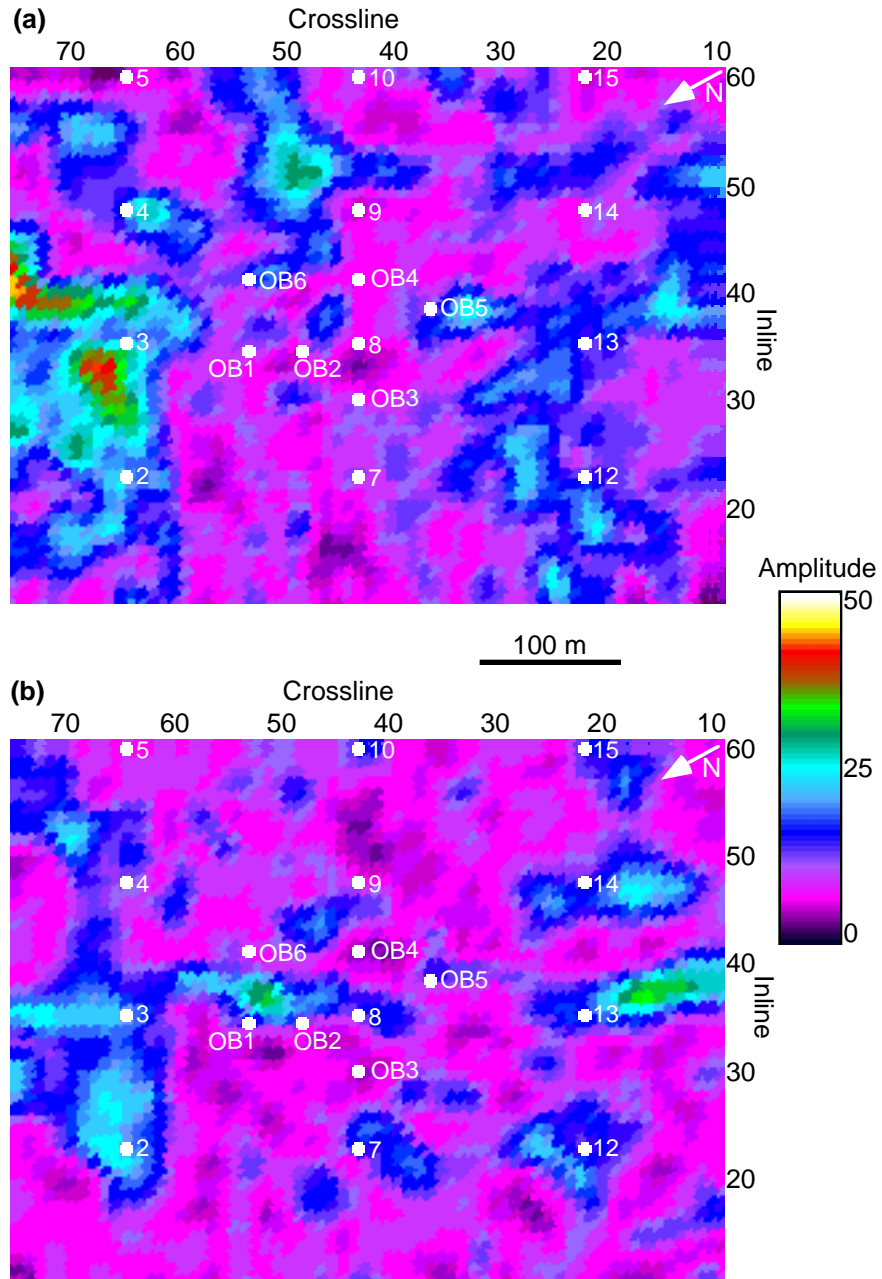


Fig. 3.16 Rms amplitudes extracted from the "difference" data volume over a 10 ms window centred on (a) 0.420 s and (b) 0.437 s, within the reservoir zone.

To compare the residual amplitudes above and within the reservoir zone throughout a significant time interval, rms amplitudes were calculated over 50 ms intervals above and within the reservoir. Time intervals selected were from 70 ms to 20 ms above the top Clearwater event for the zone above the reservoir and 0 ms to 50 ms below the top Clearwater event for the zone within the reservoir. The calculated rms amplitudes within the reservoir interval are also used to observe all the seismic amplitude changes that occur within the reservoir. This time window was selected to cover only the reservoir zone and to exclude any amplitude anomalies caused by arrival time delays of the Devonian event.

Figure 3.17 displays the spatial variation in map view of the rms amplitudes, calculated from this "difference" data volume. The data were scaled from 0 to 50, where dark blues and purples (light greys) represent low residual amplitudes and reds and yellows (dark greys) high residual amplitudes. The map view shows clearly lower residual rms amplitudes in the data above the reservoir (Figure 3.17a) than in the data within the reservoir (Figure 3.17b) and confirms that the differences between the two data volumes have been minimised above the reservoir. The area of highest amplitudes in Figure 3.17b, to the northwest of D3-3, corresponds to the high amplitude residuals seen over crosslines 61 to 70 in Figure 3.13 at 0.420 s and at the same location in Figure 3.16a.

Although the spatial extents of amplitude difference anomalies are quite visible on this map, the vertical extent of the steamed zones cannot be determined easily. Another anomaly observed in Figure 3.17b is a linear trend from D3-3 to D3-13 across the middle of the map. It is a possible indication of communication between the wells in this direction. The trend of this anomaly correlates reasonably well with that seen in Figure 3.16b, which shows the rms amplitudes through the "difference" data set from a window centred on 0.437 s. The zones of highest amplitude differences within the reservoir are seen in Figure 3.17b to be around wells D3-2 and D3-3. This area corresponds to the area

of lowest negative traveltime differences in Figure 3.8. Negative traveltime anomalies (greater delay in 1990 than 1992) with corresponding high amplitude differences may be the seismic signature of gas-saturated intervals in 1990 which are relatively unsteamed in 1992. Conversely, the low amplitude difference zone to the northwest of wells OB1 and OB2 corresponds to the zone of highest traveltime differences in Figure 3.8.

My interpretation of this is that where the low velocity zones are confined to relatively thin zones (where vertical migration of the steam in 1992 is prevented by the presence of permeability barriers or where gas exists in 1990), reflectivity contrasts will be present in the reservoir zone and therefore amplitude anomalies will be seen. The overall interval velocity may not change so that a traveltime difference anomaly is not detected. In zones where the steam permeates up throughout the reservoir there may be no internal reflectivity contrasts and thus no amplitude anomalies are seen. The traveltime anomalies, however, will be greatest in such areas because of the low interval velocities caused by the conditions of higher temperatures and lower effective pressure during steaming. Areas of the survey where both low interval traveltimes and low amplitude differences occur are interpreted to be relatively unaffected by steam.

The extents of the traveltime anomalies were shown in Figure 3.8 and of the changes in reflectivity over the reservoir interval in Figure 3.17b. The map in Figure 3.17b was combined with the traveltime anomaly map in Figure 3.8a to produce a final map which shows the areal extent of the combined anomalies. To create this map, the interval traveltimes, which varied from -3 ms to +7 ms, were squared and the result added to the rms amplitudes, which were scaled from 0 to 50. The resulting combined map is shown in Figure 3.18. Values are scaled from 0 to 52. Colours towards the yellow (black) end of the spectrum represent those where the combined amplitude is highest and, consequently, where the probability is greatest of the reservoir having been steamed during the most recent cycles.

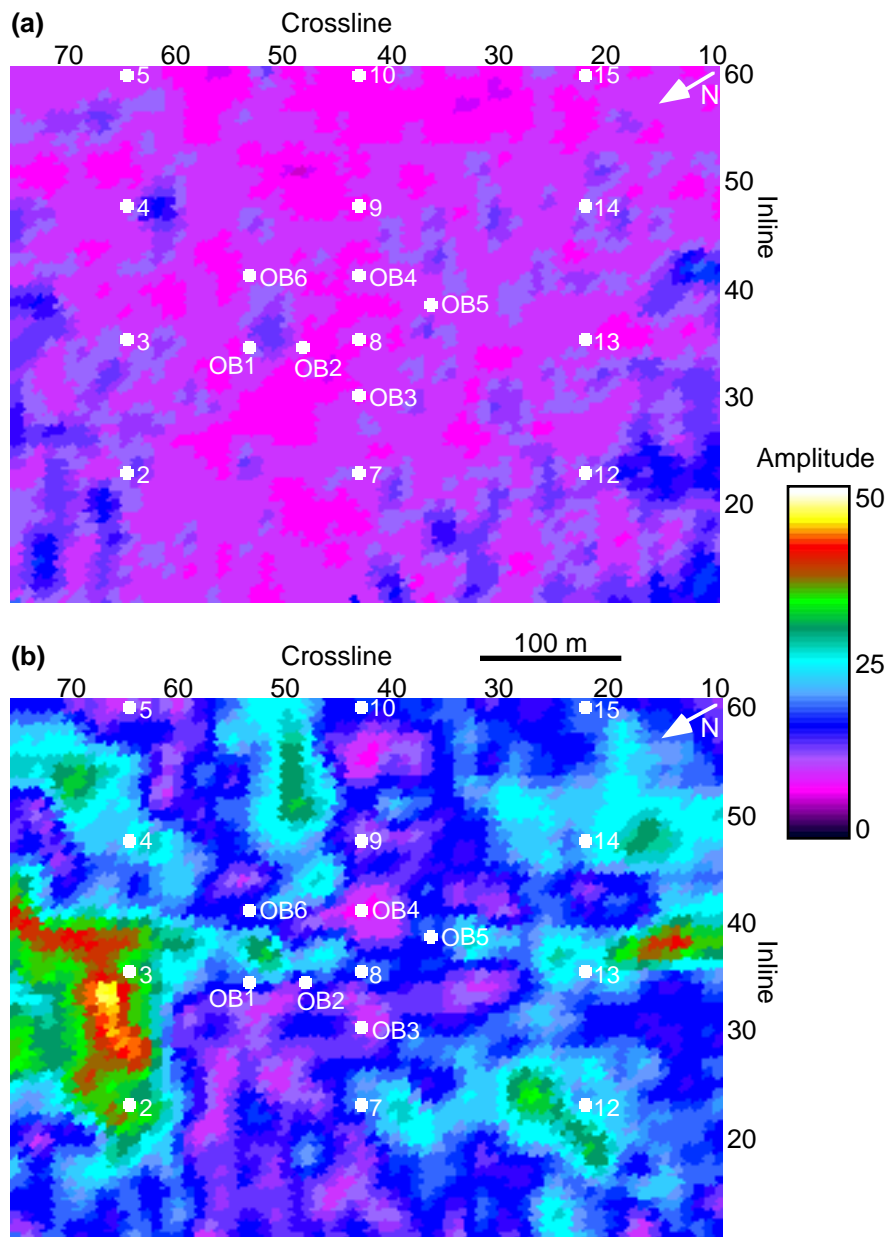


Fig. 3.17 Map view of the rms amplitudes calculated over a 50 ms window extracted from the "difference" data volume (a) above and (b) within the reservoir.

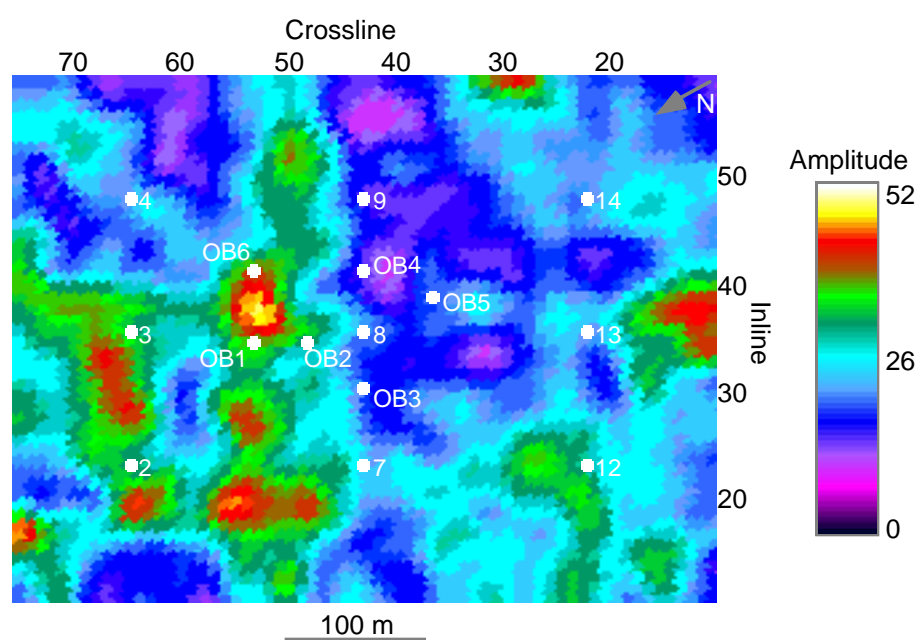


Fig. 3.18 Map showing the combination of Clearwater-Devonian interval traveltime anomalies and rms amplitudes from the "difference" data set. Shades to the yellow (black) end of the spectrum represent those areas where the combined amplitudes are highest and thus where the reservoir is most likely to have been steamed.

The areas of low amplitudes represent zones where both traveltime delay anomalies and amplitude differences are small. These parts of the reservoir are the least likely to have been steamed during the most recent steaming cycles. The wells known to have recorded significant increases in temperature during the seventh and eighth injection cycles (1991-1992) are OB1 and OB6. Both of these wells lie in the area of highest combined amplitude. Wells with no significant temperature response up to 1992, OB3, OB4 and OB5, lie in areas of low amplitude, thus showing no traveltime anomalies or amplitude changes from 1990 to 1992. Temperature increases were recorded at OB2 in 1992 and on this map OB2 lies in an area of intermediate amplitude. The northern part of the survey appears to have been affected the most by the steam and the central part relatively unaffected. The volume of reservoir between the two most northerly rows of wells shows significant changes from 1990 to 1992 whereas the volume of reservoir that has seen the least change is between the two southerly rows of injection wells.

Statistical analysis of the residual and 1990 data amplitudes was also undertaken. The mean absolute amplitude and standard deviation were calculated over selected time intervals from the residual 3-D data volume and the mean absolute amplitude from the migrated 1990 data volume. Some of the results are presented in Table 3.1 and the values confirm statistically that the residual amplitudes above the reservoir zone are much lower than those within the reservoir interval.

Table 3.1 Statistical analysis of the amplitudes.

Data set	Time window (s)	Mean Amplitude	Standard Deviation
1992-1990 residual	0.350-0.400 (above reservoir)	3550	285
1992 -1990 residual	0.420-0.520 (within and below reservoir)	12251	983
1990 migrated	0.350-0.400 (above reservoir)	11642	
1990 migrated	0.420-0.520 (within and below reservoir)	11770	

3.5 Frequency analysis

Analysis of the frequency content of the migrated seismic data volumes may also be of use in the prediction of steamed zones. Laboratory studies of attenuation in fluid-saturated samples have led some authors to suggest that significant changes in attenuation would be detectable during steam flooding of heavy oil reservoirs (Nur, 1982; Tosaya et al., 1987). Frequency attenuation is dependent on pore fluid viscosity, which decreases with increasing temperature. Therefore attenuation of higher frequencies could be interpreted in terms of temperature changes in a thermal EOR project (Jones, 1986). Forward seismic modelling in Cold Lake oil sands (Eastwood, 1993) also predicts an increase in attenuation with increasing temperature. Tomography data were used by Macrides and Kanasewich (1987) to study attenuation in the Clearwater sands at seismic frequencies. They found that attenuation increased in the steamed zones with a shift to lower frequencies in the section later than the steamed zone. The presence of a gas-saturated zone can also be a cause of attenuation (Winkler and Nur, 1979) and may be associated with a low frequency shadow beneath it (Taner et al., 1979). These results suggest that low frequency zones may be detected on the seismic data, caused either by gas-saturated intervals in 1990 or steamed intervals in 1992.

To investigate the spatial distribution of frequency attenuation, instantaneous frequency data sets were calculated for each data volume using Landmark software. Taner et al. (1979) discussed the significance of instantaneous frequency observations in the determination of low-frequency shadow zones but Brown (1986) warned that results can be ambiguous. Barnes (1993), however, showed that averaged instantaneous frequency may be used as a measure of the local power spectrum and, consequently, in the search for low-frequency shadow zones. He cautioned that the frequency decrease in some cases may be too small to detect.

Average instantaneous frequencies were calculated over a 100 ms window above the reservoir zone and over the Clearwater to Devonian interval. Figures 3.19a and 3.19b show in plan view the average instantaneous frequencies over the 100 ms window immediately above the reservoir for the 1990 and 1992 data, respectively. The spectrum covers average instantaneous frequencies ranging from 0 Hz to 100 Hz. Each map shows a similar spatial distribution, with lower frequencies in the centre of the survey. Mapped in Figures 3.20a and 3.20b are the average instantaneous frequencies over the 100 ms window partly within and partly below the reservoir, for the 1990 and 1992 data, respectively. The frequencies are seen to be lower than in Figure 3.19 and the spatial distribution differs between the 1990 data (Figure 3.20a) and the 1992 data (Figure 3.20b). Overall, the frequencies are lower in and below the reservoir in the 1992 data than in the 1990 data. Interestingly, on the 1990 map (Figure 3.20a) some low frequency zones appear as localised areas near injection wells D3-4, D3-5, D3-6, D3-7, D3-8, D3-9, D3-10, D3-12 and D3-14. The continuous band of lower frequencies around inline 36 and crosslines 20 to 43 correlates with the band of high amplitudes observed in the 1990 data at this location in Figure 3.11a. These localised low frequency areas in Figure 3.20a are interpreted to be caused by the presence of gas-saturated zones in 1990. It is known that the reservoir at observation wells OB1 and OB6 was still cold in 1990 so there was no gas present there at this time. These wells are observed to lie in areas of the least frequency attenuation.

In the 1992 data (Figure 3.20b) the low frequency zones appear to be more dispersed, although these zones correlate somewhat with the injection well locations and higher frequencies are apparent in between the rows of wells. Since attenuation increases with both decreasing pore fluid viscosity and decreasing effective stress (Jones, 1986), frequency attenuation within and below the reservoir zone should be expected in the seismic data acquired during the injection cycle. The zones of lower frequency in Figure

3.20b are interpreted to represent those parts of the reservoir where temperatures are highest and effective stress is lowest. Observation well OB3 lies in an area of lower frequency but is known to have been cold in 1992. The anomaly seen here may be caused by the low effective stress field, which is more widely spread than the temperature variations. These figures suggest that the low frequency shadows attributed to gas zones in 1990 are more localised than those associated with steamed zones and low effective stress in 1992. Both Figures 3.20a and 3.20b show volumes of the reservoir in which higher frequencies dominate, especially the four corners and between the rows of injection wells, indicating that zones of attenuated frequency are concentrated near the injection wells. The areas of attenuated frequencies (Figure 3.20) reflect intervals of gas- or steam-saturation at all times in the reservoir, so do not match exactly the distribution of amplitude anomalies as mapped over selected time intervals (Figure 3.11).

The distribution of higher frequency attenuation in 1990 (Figure 3.20a), attributed to gas-saturated zones, agrees reasonably well with the results of Dilay and Eastwood (1995), which were based on spectral analysis of their version of the 3-D seismic data. The distribution of higher frequency attenuation in 1992 (Figure 3.20b) does not, however, agree with their results. They observed higher frequencies in the 1992 data than in the 1990 data while this analysis shows the reverse. Different methods were employed for the frequency analysis so the results may not be strictly comparable. The data analysed for Dilay and Eastwood had Q-compensation applied early in the processing, which may be affecting the results.

A comparison of the values of attenuation in steam-saturated and gas-saturated zones could be made if data were gathered from field or laboratory experiments on these sands. Theoretical values of attenuation could also be calculated if the degree of gas saturation were known and the physical properties and flow behaviour of the gas-, steam- and bitumen-saturated sands were established.

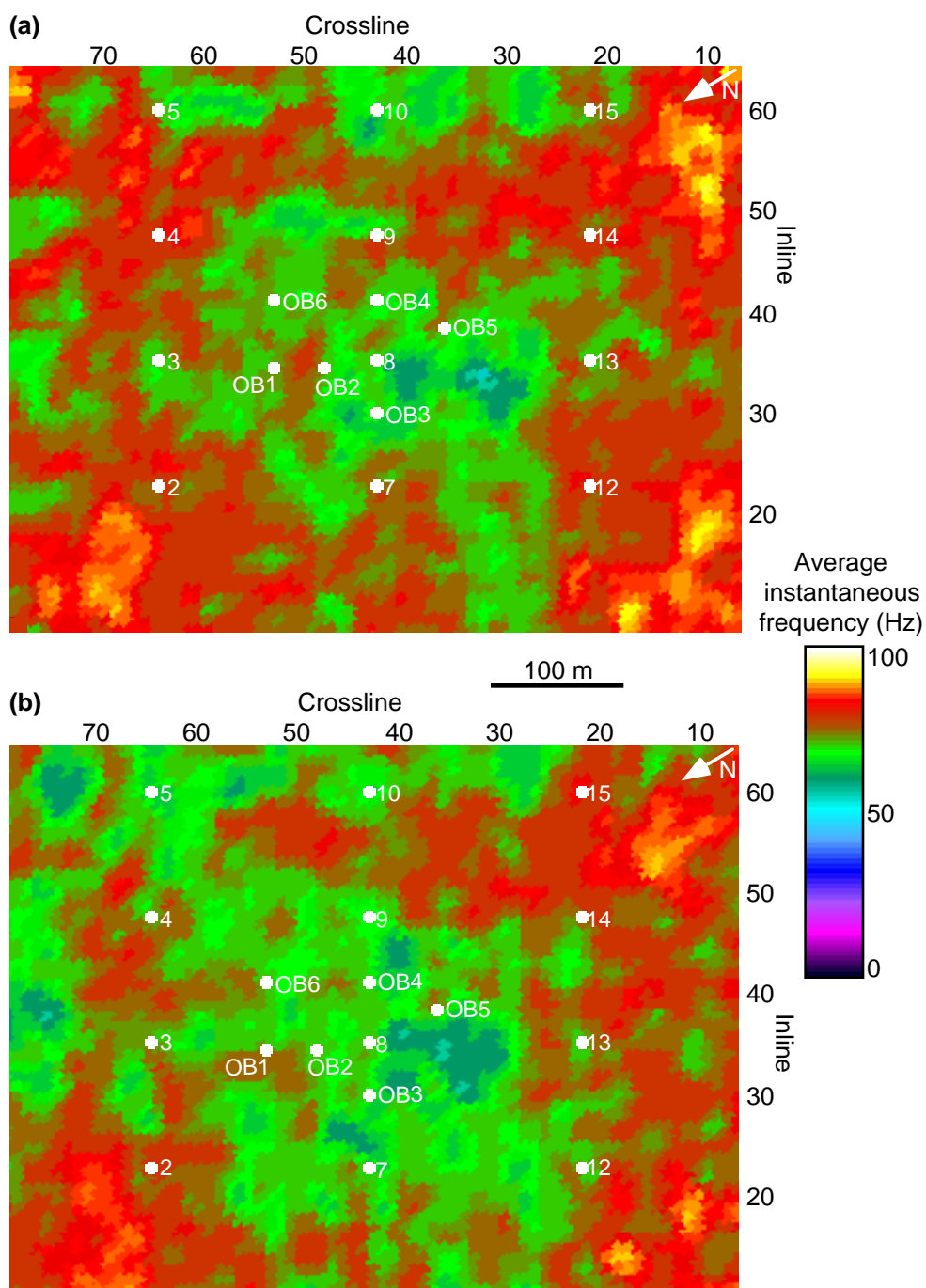


Fig. 3.19 Average instantaneous frequency measured in a zone above the reservoir from the (a) 1990 and (b) 1992 data.

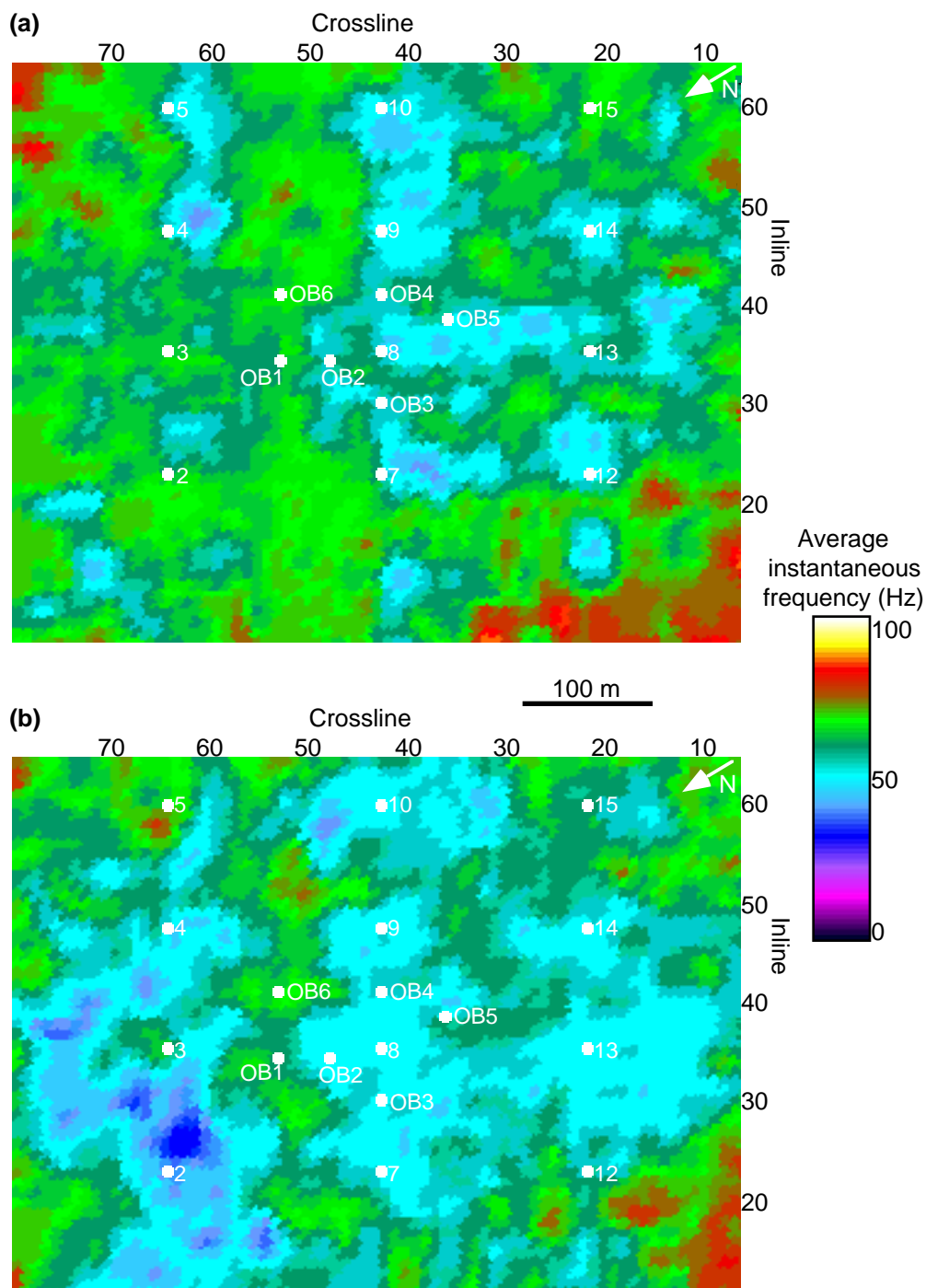


Fig. 3.20 Average instantaneous frequency measured over the Clearwater to Devonian interval from the (a) 1990 and (b) 1992 data.

3.6 3-D inversion

A 3-D inversion was undertaken for both the 1990 and 1992 reprocessed data volumes using Hampson-Russell Strata3d software. Inversion of seismic data creates pseudo-velocity traces based on changes in reflectivity on the stacked seismic data constrained by velocity information provided by well logs (Lindseth, 1979). This 3-D inversion method involves iterative perturbations of an initial velocity model until the resulting synthetic seismic data matches the real data very well. Velocity and density information from wells OB1, OB2 and OB5 were input to provide control points. Synthetic seismograms were generated at each of these control points using the extracted wavelet described in section 3.1. Each pair of sonic and density logs could be stretched or squeezed until the synthetic seismogram matched the seismic traces at that location as well as possible. The velocity information at those control points then became the basis for the initial model, which was also constrained by the horizon picks. The Clearwater, McMurray and Devonian horizon picks were exported from Landmark into this program.

The data were inverted using a blocky inversion, which produces a series of blocky pseudo-velocity logs having resolution close to that of the seismic data but coarser than that of the sonic logs. Each seismic trace is converted into a pseudo-velocity log, which is an estimate of the log which, when convolved with the wavelet, would result in that trace. This inversion was performed over the time interval 0.35 s to 0.50 s using an interval time of 6 ms. An interval time of 6 ms was selected because it corresponds to an interval depth of 6 m. The input seismic data have a dominant frequency of 80 Hz and an average velocity of 2000 m/s to the zone of interest, resulting in a wavelength (λ) of 25 m. If a thin bed is assumed to be one less than $\lambda/4$ thick (Sheriff, 1992) then a bed thinner than 6 m cannot be resolved on these input seismic data.

Figure 3.21 shows the results of the inversion at the location of the OB5 observation well (which gave the best well log-seismic data tie). Displayed are the

synthetic seismogram created using the extracted wavelet, with its tie to the seismic data, and the inversions for inline 38 from the 1990 and 1992 surveys. The velocity scale is from 2000 m/s to 3000 m/s, with green (light) shades representing low velocities and purple (dark) shades representing high velocities. On the seismic data, the top of the Clearwater Formation is the trough at 0.405 s and the top of the McMurray Formation is interpreted as the peak at 0.455 s. Both inversions show the same high velocity, tight zone in the Grand Rapids Formation at about 0.380 s and in the Clearwater Formation at about 0.412 s but cannot resolve the minor tight streaks at 0.424 s and 0.430 s on the sonic log. The Grand Rapids tight streak is about 4 m thick while the others are only about 1 m thick. The two tight streaks at 0.410 s and 0.414 s on the sonic log are only 3 m apart and generate a composite response on both the seismic data and the inversion.

The depth of the perforation zone in the injection wells varies slightly from well to well but is at an average of 38 m to 44 m below the top of the Clearwater Formation. This translates to a two-way traveltime of 32 ms to 37 ms below the top of the Clearwater Formation. This time corresponds to the very low velocity zone (green/light grey) seen to the left of OB5 on the 1992 inversion at 0.434 s to 0.440 s (denoted by an arrow). It is interpreted that the extent of the low velocity zone on the inversion denotes the extent of the steamed zone and that the steam is inhibited from rising through the reservoir by the overlying tight streaks. This low velocity zone is not seen on the 1990 inversion.

Overall, velocities calculated from the 1992 data are slightly lower than those from the 1990 data. These velocities are not expected to represent exactly the actual velocities of the formation because the sonic logs used for control points were not obtained at the same time as the seismic data. However, velocity variations within the reservoir and between the two vintages of seismic data are expected to be represented accurately.

In Figure 3.22 are displayed the seismic data and inversions for inline 35. On traces 59-67 on the 1990 inversion is a low velocity zone at about 0.415 s to 0.420 s (shown by an arrow), corresponding to the high amplitude events observed on the seismic data. It was suggested earlier, in section 3.3, that the amplitude anomalies seen on the 1990 data could reflect local gas zones. The inversion results, showing a low velocity zone here, tend to support this suggestion. The interval transit times between the Clearwater and McMurray events do not change here, providing evidence that lower interval velocities in the 1992 data due to the presence of steam may cancel the velocity effect of the 1990 gas zone. From traces 47 to 58 on the 1992 line we see a low velocity zone at about 0.430 s, interpreted to be a steamed zone. The significance of a delayed arrival time of the Devonian event was discussed earlier, being attributed to lower interval velocities in 1992. Here on the seismic data a zone of lower interval velocities is seen to produce a delayed arrival time for the deeper events, especially over traces 52-57.

3.7 Discussion

The two migrated data volumes and a “difference” volume created from them were interpreted and analysed on a workstation. Particular attention was paid to the analysis of differences between the 1990 and 1992 data sets. Rather than attempting to correlate reservoir parameters with seismic characteristics, analysis of differences results in an understanding of how the reservoir changes spatially over time. This approach was also taken because there was no baseline survey available. Seismic attributes analysed included time structure, reflection amplitude and average instantaneous frequency. Mapping of the Clearwater to Devonian time isochron shows where the arrival time of the Devonian event is delayed. This delay is attributed to the conditions of higher temperature and lower effective pressure in 1992. Amplitude variations also indicate zones of temporal change in the reservoir. Such variations are caused by changes in gas-

and steam-saturation over time. Frequency analysis of the data showed that higher frequencies were attenuated below gas-saturated zones in 1990. Overall, frequencies were lower in 1992 due to the presence of higher viscosity pore fluid and lower effective pressure at that time.

Seismic inversion of the 3-D data confirmed the correlation of amplitude anomalies with low velocity zones, interpreted to be caused by gas in 1990 and steam in 1992. Because low velocity zones were present in 1990 as well as 1992, mapping of interval traveltimes anomalies is insufficient and amplitude variations must be integrated into the interpretation. The time isochron and amplitude difference maps were combined to create a map which displays both the seismic character and time structural variances between the 1990 and 1992 seismic data volumes. These variances are interpreted to represent the spatial distribution of temporal changes in reservoir conditions. Observation wells OB1 and OB6, at which significant temperature increases were recorded from 1991 to 1992, lie within areas of highest variances, giving confidence in the validity of the results.

The spatial extent of steam penetration was inferred from the mapping but the vertical distribution is more difficult to determine. The resolution of the seismic data is not high enough to map accurately the tight streaks, which inhibit vertical movement of steam.

Mapping of seismic attributes shows that the volume of the reservoir most likely to have been penetrated by the steam lies between two rows of injection wells. Such information can only be obtained from time-lapse 3-D seismic data, as data recorded at the wells may not necessarily predict correctly the conditions between the wells. Input of this information into the reservoir simulation model helps to make the model more accurate between wells and, consequently, contributes towards better reservoir management.

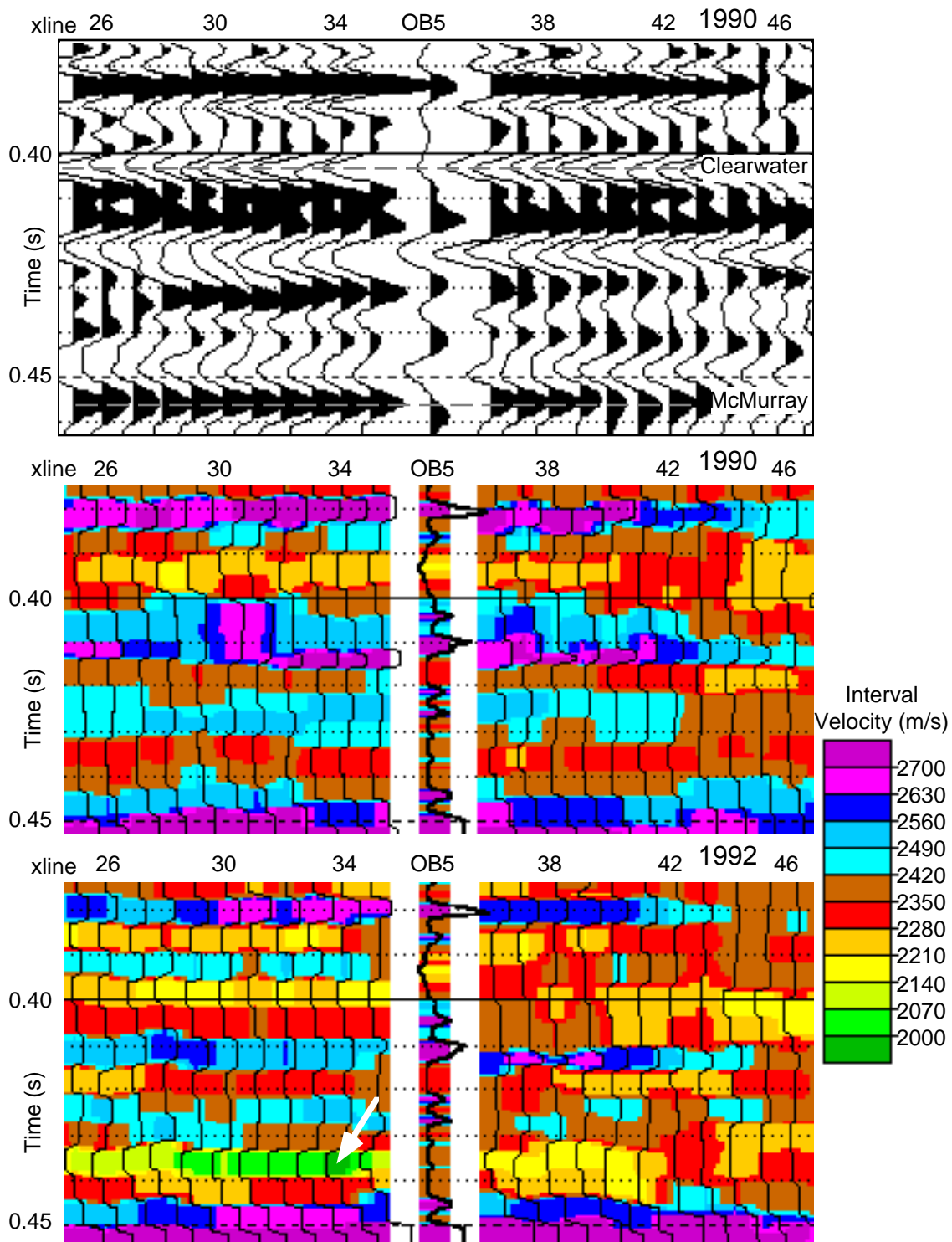


Fig. 3.21 Inversion at the location of the OB5 well on inline 38.

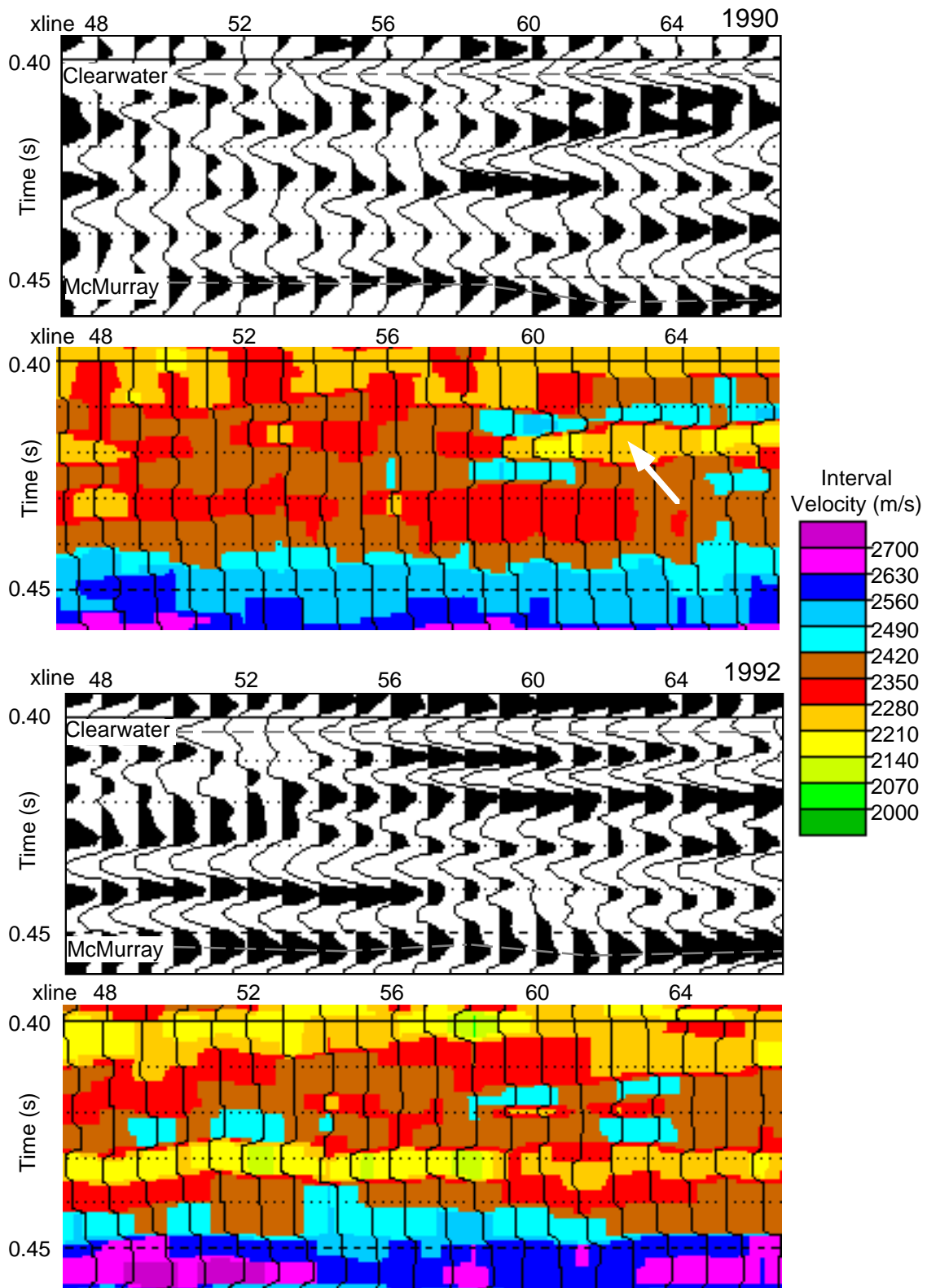


Fig. 3.22 Seismic data and inversion for part of inline 35.

Chapter 4

3-C SEISMIC DATA ACQUISITION AND PROCESSING

4.1 Introduction

The use of multicomponent seismic data in petroleum exploration has become of interest to explorationists. Analysis of compressional (P -) and shear (S -) wave data can be applied to the estimation of rock properties such as lithology, porosity and fluid content (Domenico, 1984; Winterstein, 1986). The ratio of P - to S -wave velocities can give information about lithology and pore fluid and variations in this ratio may be related to changes in rock properties (Tatham and Stoffa, 1976). S -wave velocity data are useful for distinguishing between P -wave amplitude variations caused by lithologic changes and those caused by changes in pore fluid. A change in pore fluid affects only the bulk modulus of a rock and not its shear modulus, so shear-wave velocity is only affected by the relatively small change in density. If other reservoir parameters are known to remain constant, then an observed change in V_p/V_s may be related to a change in pore fluid. The potential for the application of multicomponent seismic methods in exploration is well documented in, e.g., Dohr (1985) and Tatham and McCormack (1991), where some case histories are described.

In the absence of a shear-wave source, use can be made of the fact that mode conversion will occur at an interface. The Zoeppritz equations (Zoeppritz, 1919) predict that at non-zero angles of incidence less than the critical angle, four types of energy will be generated by the incidence of a compressional-wave upon an interface. These four type are: reflected P -waves, transmitted P -waves, reflected S -waves and transmitted S -waves. By using suitable recording instruments, the upcoming shear-wave energy may be recorded at the surface.

Converted-wave seismic data analysis has been used to determine stratigraphic

variations within sand/shale sequences (Baltenspergen and Bay, 1990) but, prior to this study, has not been applied, to our knowledge, to heavy oil reservoir characterisation.

4.2 Field Acquisition

Two multicomponent (3-C) seismic surveys were acquired over the AABBW pads at Cold Lake (Figure 1.1) during the acquisition of 3-D *P*-wave seismic surveys. The first survey was in November 1993, at the peak of the injection cycle, with the follow-up survey in April-May 1994, during the production cycle. A compressional source was used and both reflected compressional and mode-converted shear energy were recorded using I/O System Two by single three-component OYO geophones.

One receiver line of surface three-component geophones was laid out to coincide with a source line (line 470) and these geophones recorded data from the shots along seven source lines in the 3-D survey. Figure 4.1 shows the layout of the survey.

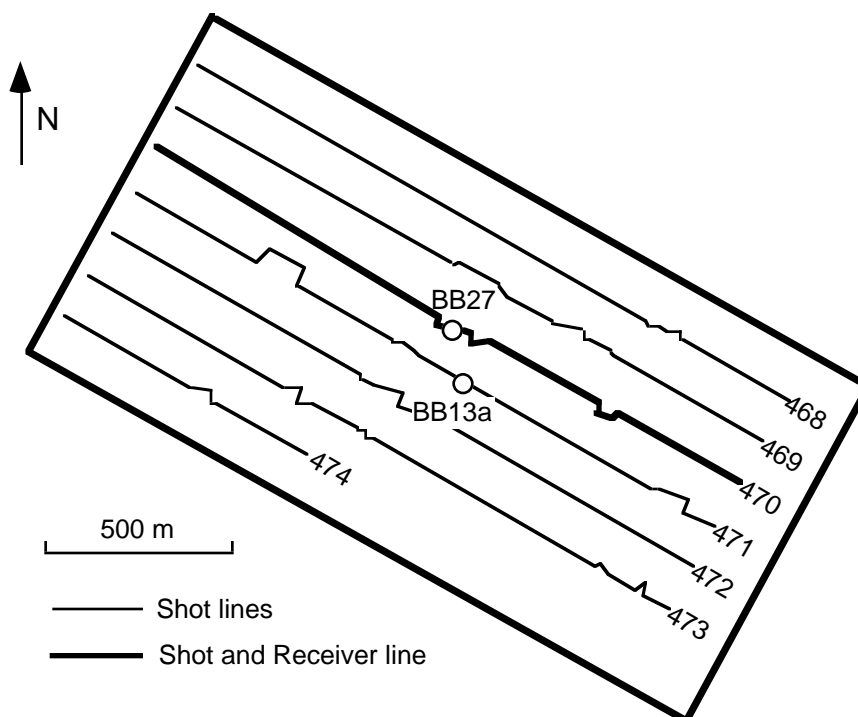


Fig. 4.1 Layout of the 3-C seismic survey over the AABBW pads with the locations of two wells for which sonic log data were available initially.

The locations of two wells for which sonic logs were available initially are annotated. The source and receiver station interval was 16 m and the source lines were spaced 125 m apart. The receiver line and source lines 468 to 473 were each 1808 m long, (114 stations each) and line 474 was 752 m long (48 stations). The source was 0.125 kg of dynamite buried 12 m deep and a total of 732 live shots was recorded.

Each record of 342 traces was separated initially into three shot gathers representing the three recorded components: one vertical and two horizontal (inline and crossline with respect to the azimuth of line 470). Three lines each of *P-P* and *P-S* records were processed fully. Line 470 is the line of coincident sources and receivers so both components were processed for this line. Figure 4.2 shows a simple sketch of the raypaths of *P-P* waves, generated at shotpoint S1 on line 469, and of *P-S* waves, generated at shotpoint S2 on line 468.

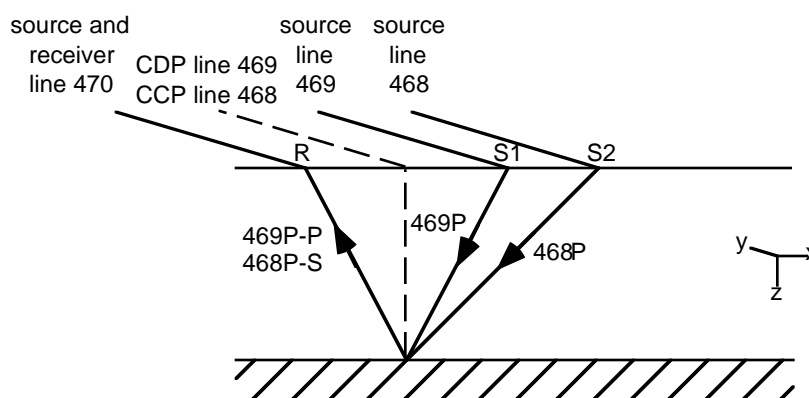


Fig. 4.2 Sketch of *P-P* raypaths, from a shot S1 on line 469, and *P-S* raypaths, from a shot S2 on line 468. The surface locations of the common depth points of line 469 are approximately the same as the surface locations of the common conversion points of line 468.

The upcoming waves are recorded at receiver R on line 470. The surface locations of the common depth points (CDPs) for the *P-P* component of line 469

correspond approximately (within 8 m) to the surface locations of the asymptotic common conversion points (CCPs) for the *P-S* component of line 468. A similar relationship exists for the *P-P* component of line 471 and the *P-S* component of line 472. Thus, the *P-P* lines processed fully were 469, 470 and 471 while the *P-S* lines processed fully were 468, 470 and 472. The vertical components of lines 468 and 472 were partially processed to determine the shot statics solutions for those lines.

4.3 Vertical component data processing

The data were processed at The University of Calgary using Landmark/IT&A software with a 3-D geometry. Each vertical component was processed using the same processing scheme. Since the processing flow was standard, it is not described in detail in this dissertation.

After first breaks had been picked, refraction statics were calculated using GLI3D. The statics were calculated independently for each line to investigate the robustness of the program, as the receiver statics should be common for each line. The calculated receiver statics were found to vary only very slightly from line to line; usually by only one or two ms, giving confidence in the robustness of the calculated values, which varied from -5 ms to +5 ms. Refraction statics calculated independently using IT&A's Ref3d were also very similar. Elevation corrections were applied to correct the data to a datum of 600 m with a replacement velocity of 1900 m/s, which is the sub-weathering layer velocity determined by the refraction statics analysis. Elevations across the 3-C survey area ranged from 596 m to 600 m.

Many of the shot records were contaminated with low-frequency, high amplitude noise, some of which was shot-generated and some caused by external man-made sources. To remove this noise, normal moveout (NMO) corrected shot gathers were filtered in the frequency-wavenumber ($f-k$) domain, discriminating against dipping

events. Partial processing of the unfiltered data was necessary to determine the residual statics and stacking velocity functions. Refraction and residual statics needed to be applied to the raw shot records to position events correctly along their moveout hyperbolae before the records were NMO-corrected. $F-k$ filtering of these NMO-corrected records discriminated against high wavenumber and dipping events. The NMO correction was then removed prior to further processing. Figure 4.3a shows a raw shot gather from line 470-93 (with a 0.05 s AGC and pre-first break mutes applied for this display) and Figure 4.3b the same record after geometric spreading compensation, trace amplitude balancing, pre-first break mutes, refraction and residual statics corrections, a bandpass filter of 10/15-140/160 Hz and $f-k$ filtering. The shot-generated surface energy and low frequency noise have been removed.

For each vertical line, the processing continued through a standard sequence which included pre-stack minimum phase spiking deconvolution (with an operator of length 80 ms), spectral balancing and post-stack $f-k$ time migration. A bandpass filter of 10/15-100/120 Hz was applied and all the sections also had a post-migration 11-point $f-x$ deconvolution applied to enhance linearly coherent events. Figure 4.4 shows the final migrated vertical ($P-P$) section for line 470 from the 1993 survey. An event early in the section, at about 100 ms between CDPs 10-60, is interpreted to be a channel. This channel is shown subsequently to have significance during the processing of the $P-S$ data.

Although stacking velocities were lower underneath the channel, $f-k$ migration using a single velocity function produced a better result in terms of reflection continuity and interpretability than did finite-difference migration, which allows for lateral velocity variations. Identification of reflectors and interpretation of this section are discussed in Chapter 5.

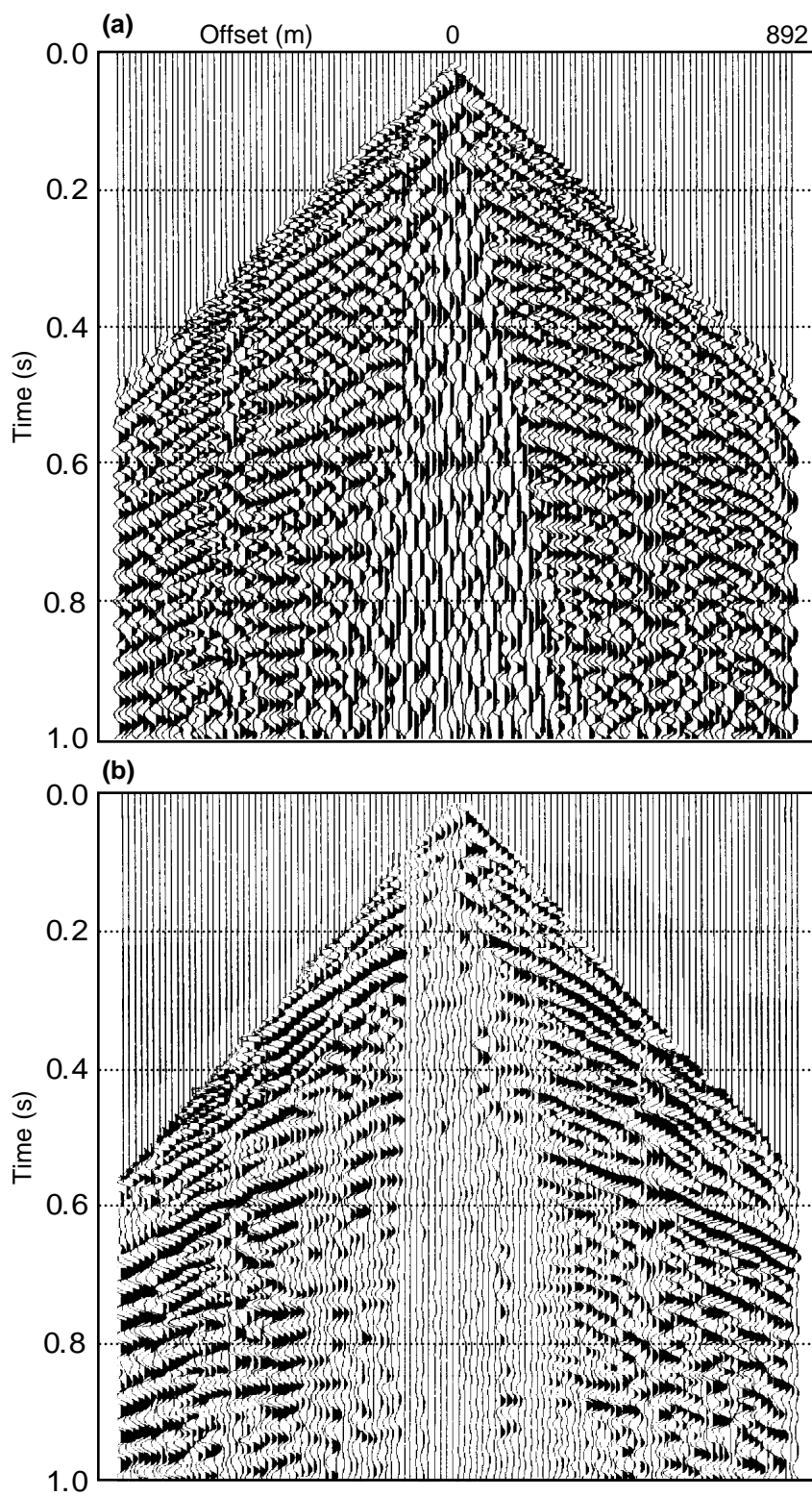


Fig. 4.3 (a) A raw shot gather (with an AGC of window length 0.05 s) and (b) the same gather after application of statics and $f-k$ filtering. Traces are 16 m apart.

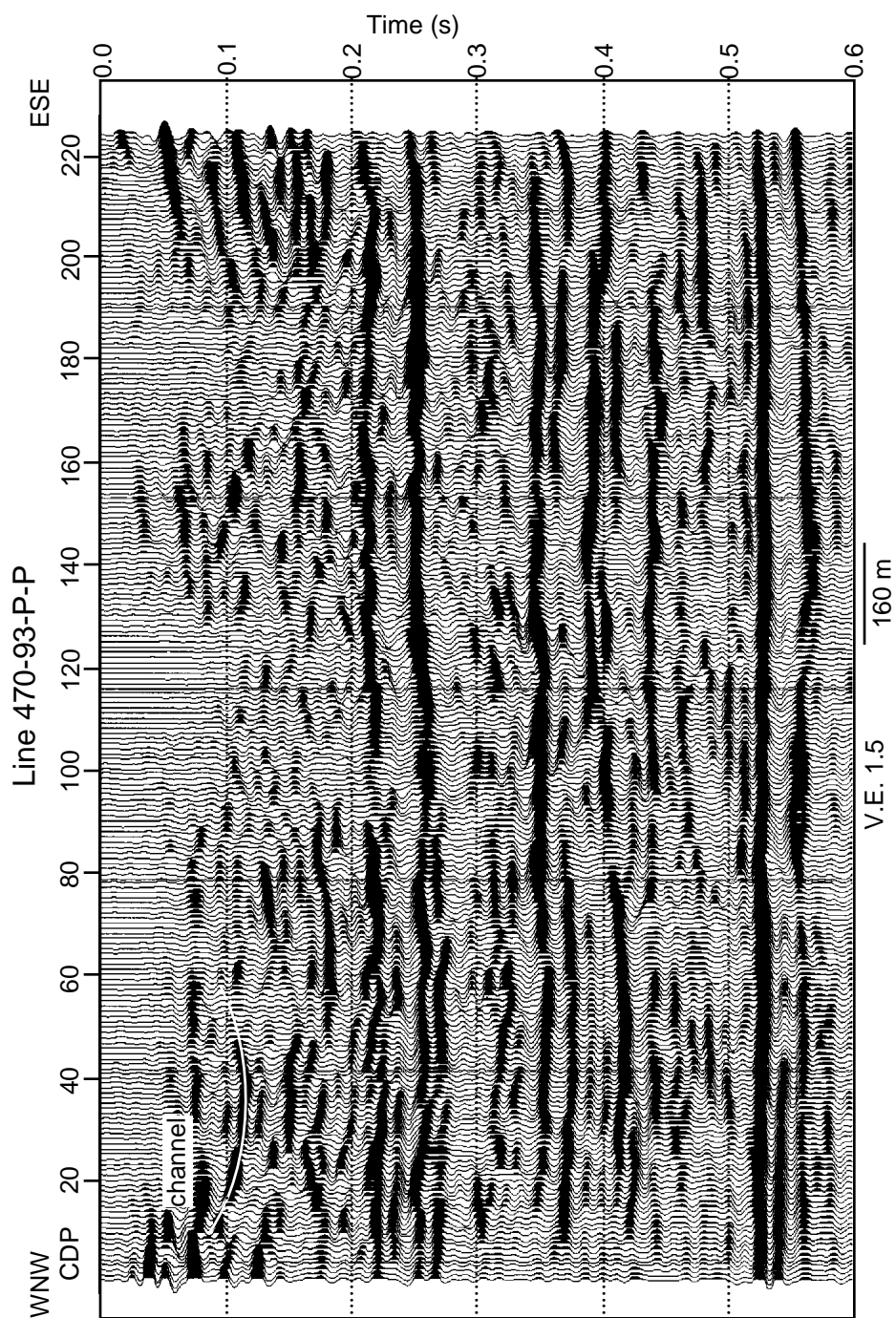


Fig. 4.4 Final migrated *P-P* section for line 470 from the 1993 survey.

4.4 Radial component ray-trace modelling

To determine the offsets from the P - S data to be processed and to estimate the arrival times of the primary events, ray-trace modelling was undertaken using Sierra software. To estimate velocities and V_p/V_s , use was made of dipole sonic logs acquired in the deviated well BB13a in this field, which were the only dipole logs available at this time. The logs covered the depth interval 284 m to 460 m and sonic interval transit times for both compressional- and shear-waves were recorded. Plots of these logs (made from the recorded digits corrected to true vertical depth), and the corresponding V_p/V_s , are shown in Figure 4.5. This plot shows that the average V_p/V_s is 2.4 within the Grand Rapids Formation (314 - 416 m).

At the top of the reservoir, at 416 m, V_p/V_s decreases to about 2.0. The high values of V_p/V_s from 410 m to 416 m are deemed to be unreliable as the caliper logs indicate an anomalously large hole diameter over this interval, indicating poor hole conditions. Gas is known to have been present at the top of the reservoir zone (from 416 m to 431 m) in well BB13a at the time of the acquisition of the dipole logs. The compressional-wave velocity at this depth and hence also V_p/V_s are thus not representative of the cold reservoir. Furthermore, the S -wave velocities recorded over this interval appear to be low. The Clearwater Formation is expected to have higher S -wave velocities than the overlying shalier Grand Rapids Formation so a shear-wave velocity of 1100 m/s was estimated for the Clearwater Formation. In retrospect, this S -wave velocity appears to be a little low. For the section shallower than 320 m, P -wave velocities were obtained from a sonic log at well BB27 and a V_p/V_s of 2.4 was used. The McMurray Formation P -wave velocity of 2700 m/s was estimated from the bottom of the sonic log acquired in well D3-8. For the Devonian carbonates, interval velocities calculated during the processing of the 3-D seismic data over the D3 pad and a typical carbonate V_p/V_s of 1.9 (Domenico 1984) were used.

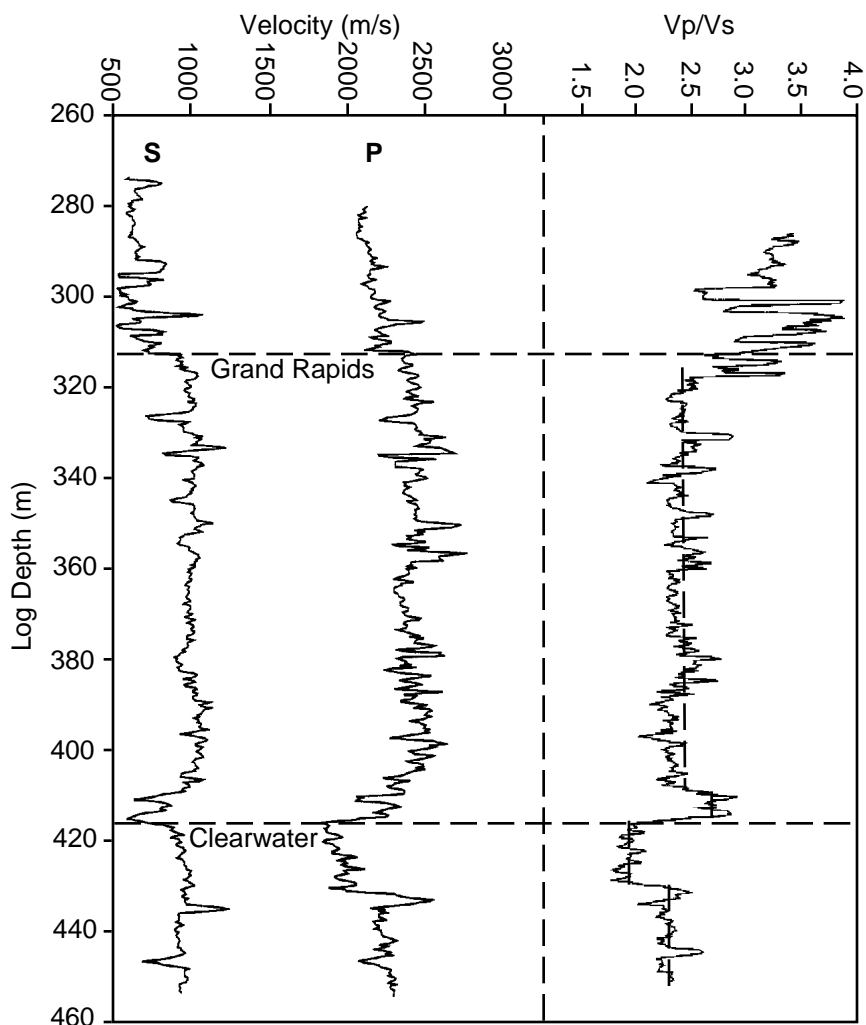


Fig. 4.5 *P*- and *S*-wave sonic velocities, obtained from dipole logs in well BB13a, and the corresponding V_p/V_s . Dashed lines show the average V_p/V_s .

The parameters used in the modelling are listed in Table 4.1 and the synthetic shot gather is shown in Figure 4.6. This figure has had AGC applied to show the various events. The Devonian event is the deepest, at 0.85 s on the nearest offset, and has a very high amplitude on the raw gather. A clear phase shift in the Devonian event is seen at an offset of 432 m, corresponding to the critical angle of incidence on this interface. The Grand Rapids Formation top is the peak at 0.55 s on the nearest offset and the top of the

Clearwater Formation is the trough at 0.675 s. Offset were selected during processing initially to avoid phase shift problems.

Table 4.1 Parameters used in the ray trace modelling.

Formation	Depth interval (m)	V_p	V_s	V_p/V_s
	0-120	1865	777	2.40
Top Cretaceous	120-230	2030	845	2.40
Base Fish Scales	230-315	2155	900	2.40
Grand Rapids	315-415	2420	1000	2.42
Clearwater	415-475	2300	1100	2.05
McMurray	475-530	2700	1175	2.30
Devonian	530-800	4000	2100	1.90

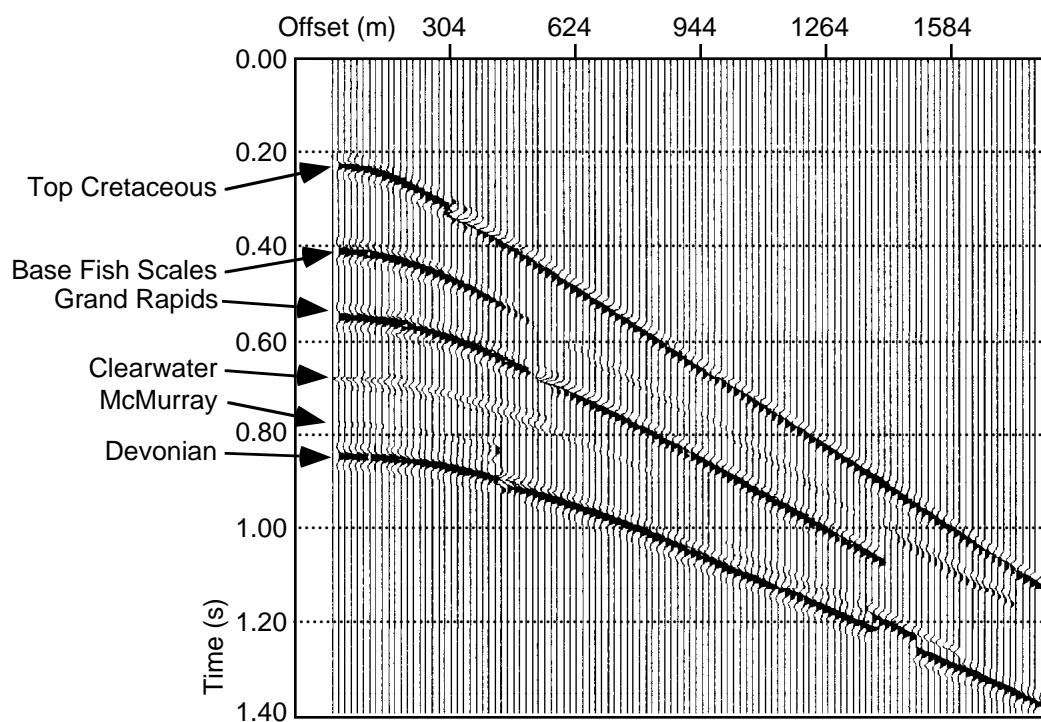


Fig. 4.6 Synthetic shot gather of P - S energy, modelled by ray-tracing.

4.5 Radial component data processing

The processing flow designed to produce the final, interpreted sections is shown in Figure 4.7. This flow is based on *P-S* data processing routines (Harrison, 1992) but several important elements are discussed in detail.

4.5.1 Rotation analysis

The presence of azimuthal anisotropy in the subsurface can cause an upcoming shear-wave to split into fast and slow components which may be observed on reflection seismic data (Lynn and Thomsen, 1986). For converted-wave data, energy may then be recorded on both horizontal channels and each channel may contain both fast and slow components. If the natural coordinate system can be determined then the recorded components can be rotated into this system.

An attempt was made to calculate the directions of these components by cross-correlating several pairs of corresponding records of horizontal components from line 470 using rotation analysis code developed by Harrison (1992). Shot-receiver azimuths along this line did not vary except near the two or three out-of-position shots, which were not used in this analysis. Several records along the line were selected for the rotation analysis and data windows were selected from the deeper portions of the records where there appeared to be *P-S* signal. No consistent value of rotation angle could be calculated by this analysis. It is surmised that either there is no shear-wave splitting in this area, or the receiver line lies along a natural coordinate axis, or that the level of noise in the data is too high to permit cross-correlation of shear-wave events. The direction of maximum horizontal stress (a natural coordinate axis) is 30° to 45° from North in the Cold Lake area (Bell et al., 1994). The development pads at Cold Lake were oriented deliberately to coincide with the stress axes and the seismic lines are oriented at an angle of 120° from North so it is possible that line 470 is coincident with a natural coordinate axis.

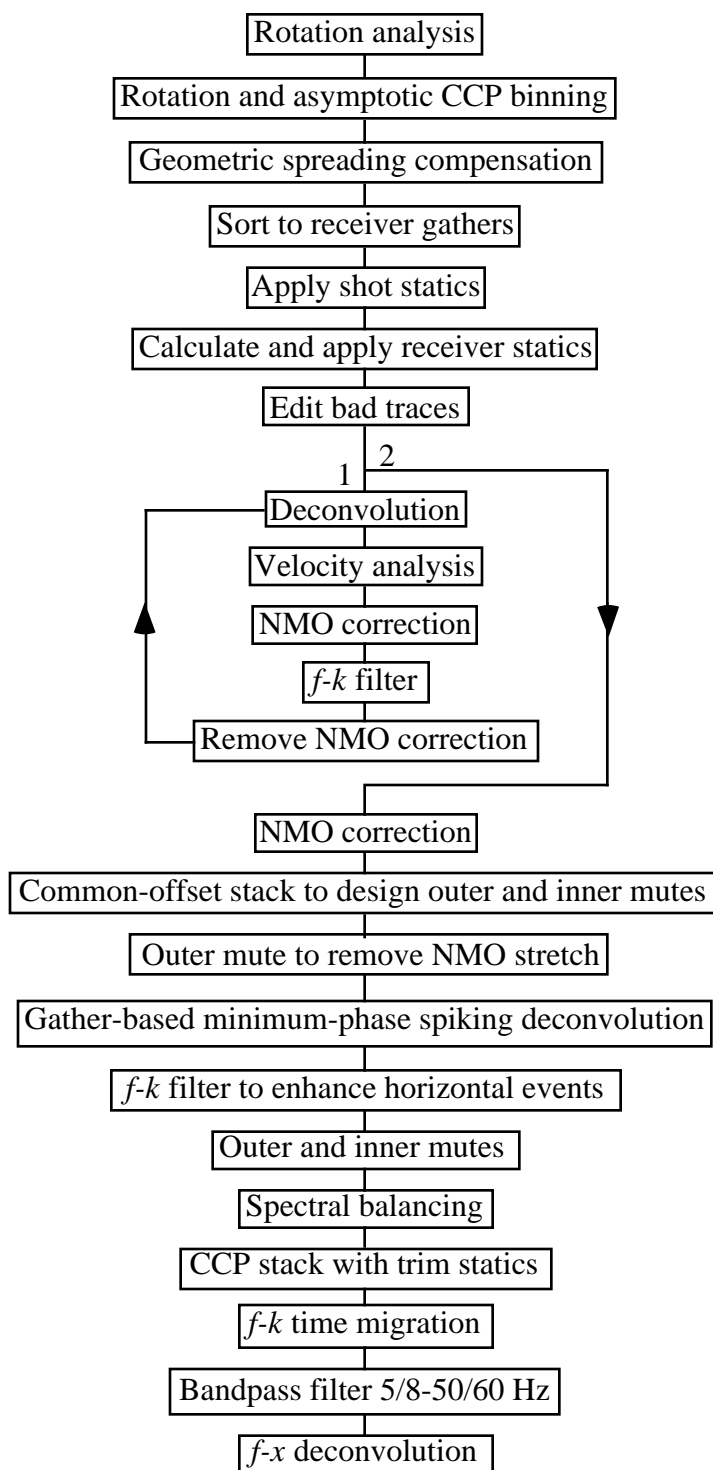


Fig. 4.7 Processing flow for P - S data.

P-wave particle motion is confined to the source-receiver plane so the mode-converted shear-wave particle motion must be in the same vertical plane (Tatham and McCormack, 1991). Since mode-converted *P-S* data are polarised in this way, each corresponding pair of traces from the horizontal component shot gathers has to be rotated into components oriented in the source-receiver plane (radial) and orthogonal to that plane (transverse). This angle of rotation is unique for each source-receiver azimuth.

The polarity of the trailing spread was reversed so that all the traces in a gather would have the same polarity. Because of the asymmetry of the converted-wave raypaths, *P-S* data are binned by common conversion point (CCP) rather than common mid-point, which assumes a symmetrical raypath (Tessmer and Behle, 1988). The data were binned into CCP bins using an average V_p/V_s of 2.4 and a 3-D asymptotic CCP binning algorithm developed in the CREWES Project (Lane and Lawton, 1993).

Geometric spreading compensation was applied using the *P-S* stacking velocity, total two-way travel time and the near-surface *P*-wave velocity (Harrison, 1992). The *P-S* stacking velocities were estimated using the formulae

$$V_{psn} = \frac{V_{ppn}}{\sqrt{V_p / V_s}} \quad (4.1)$$

$$\text{and } T_{ps} = \frac{1 + V_p / V_s}{2} \cdot T_{pp} \quad (4.2)$$

where V_{ppn} = *P-P* stacking velocity, V_{psn} = corresponding *P-S* stacking velocity, V_p/V_s = average velocity ratio, T_{pp} = two-way *P-P* time and T_{ps} = two-way *P-S* time.

The *P-P* stacking velocities for each line were known already from the processing of the vertical component data and an average V_p/V_s of 2.4, determined from the logs

plotted in Figure 4.5, was used. The predicted P - S stacking velocities (rounded to the nearest 5 m/s) for line 470-93 are listed in Table 4.2. At this time, the data were also balanced on a record basis by scaling to a defined energy level while keeping relative amplitudes through the trace.

Table 4.2 Predicted P - S stacking velocities based on V_p/V_s of 2.4 and the P - P stacking velocities.

P - P time (s)	V_{pp} (m/s)	P - S time (s)	V_{ps} (m/s)
0.100	1700	0.170	1100
0.200	1800	0.340	1160
0.300	1900	0.510	1225
0.400	2050	0.680	1325
0.550	2200	0.935	1420
0.700	2900	1.190	1870
0.850	3300	1.445	2130

4.5.2 Near-surface statics determination

Figure 4.8 shows a raw shot gather of the radial component from line 469-93. Geometric spreading compensation, trace balancing and pre-first break mutes have been applied to this gather. The gather appears noisy and it is very difficult to tell where the converted-wave energy might be. As for P - P data, the near-surface statics must be determined early in the processing. For the P - S case these can be separated into shot and receiver components. The thickness of the low-velocity surface layer encountered by compressional-waves depends on the depth of the water table but, since the velocity of shear-waves is independent of fluid content, the thickness of the shear-wave low-velocity layer depends primarily on lithology. Shear-wave receiver statics are often much greater than those for compressional-waves, since the weathering layer usually extends below the

water table and the near-surface S -wave velocities are very low.

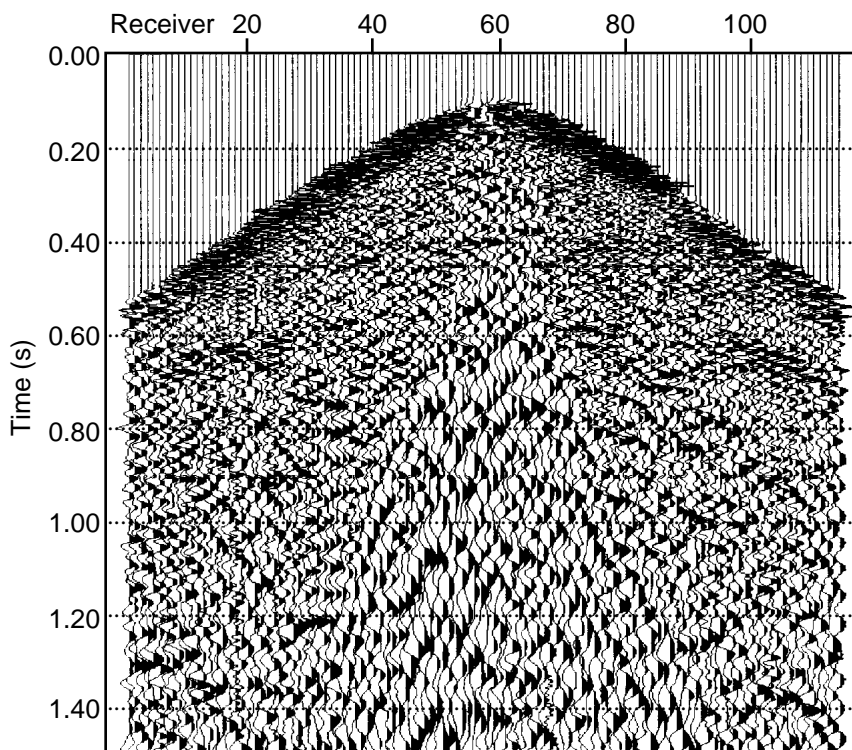


Fig. 4.8 A shot gather of the radial component from line 469-93. Geometric spreading compensation, trace balancing and pre-first break mutes have been applied.

Only the downgoing P -wave is involved in the shot component of the P - S statics correction so the shot statics calculated for the P - P data are used. The receiver statics, however, must be determined separately for P - S data. Since the 114 receivers were common for each shot line, the receiver static analysis was performed using all the shots in the survey, approximately 700 in total.

A common approach to the calculation of receiver statics is to sort the data into receiver gathers, apply NMO corrections and stack (Harrison, 1992). Cross-correlation of each trace with a pilot trace created by summing some adjacent traces produces the required static shift for that trace. Cary and Eaton (1993) developed an automatic

procedure for determining receiver statics based on such a cross-correlation method but cautioned that cycle-skipping is possible and visual inspection of the data is necessary. To calculate the receiver statics, shots from all the source lines and offsets of 500-1400 m (determined from Figure 4.6) were sorted into common-receiver gathers. Each gather was NMO-corrected using the predicted P - S stacking velocities (Table 4.2) and then stacked.

An automatic cross-correlation routine was used to align the stacked traces. These receiver statics were applied to the data and an attempt made to obtain P - S stacking velocities by both constant velocity stack and semblance analyses. Initially it was impossible to determine the velocities by these methods because of interfering events and noise and a stacked section was generated using the predicted P - S stacking velocities. The result was very poor and altering the stacking velocities did not significantly improve it. It had been anticipated that the Devonian reflection would be a high amplitude event because the S -wave velocities are expected to increase considerably in the carbonates. However, no such event was apparent on this initial stacked section. Later in the section, at around 1.2 s, there appeared events which might align with further processing but the traveltimes were considered too large to be the P - S Devonian event. Based on the Devonian event arrival time on the P - P section and assuming an average V_p/V_s of 2.4, the P - S Devonian event is expected to occur between 0.8 s and 0.9 s.

Since only estimated P - S stacking velocities had been used to remove the NMO from the common-receiver gathers, it is possible that incorrect receiver statics were being obtained. The data were resorted into common-receiver gathers and the statics reworked. A receiver gather from line 470-93 (Figure 4.9) reveals coherent trains of energy, some linear and some with hyperbolic moveout. In comparison with the shot gather in Figure 4.8, the receiver gather in Figure 4.9 shows that there is coherent reflected energy in the data. Two events are highlighted: the P - P Devonian event, at just below 0.5 s, and a

deeper event from 1.1 s to 1.4 s, interpreted to be converted-wave energy because of its moveout geometry. Other events with various moveout velocities can also be observed.

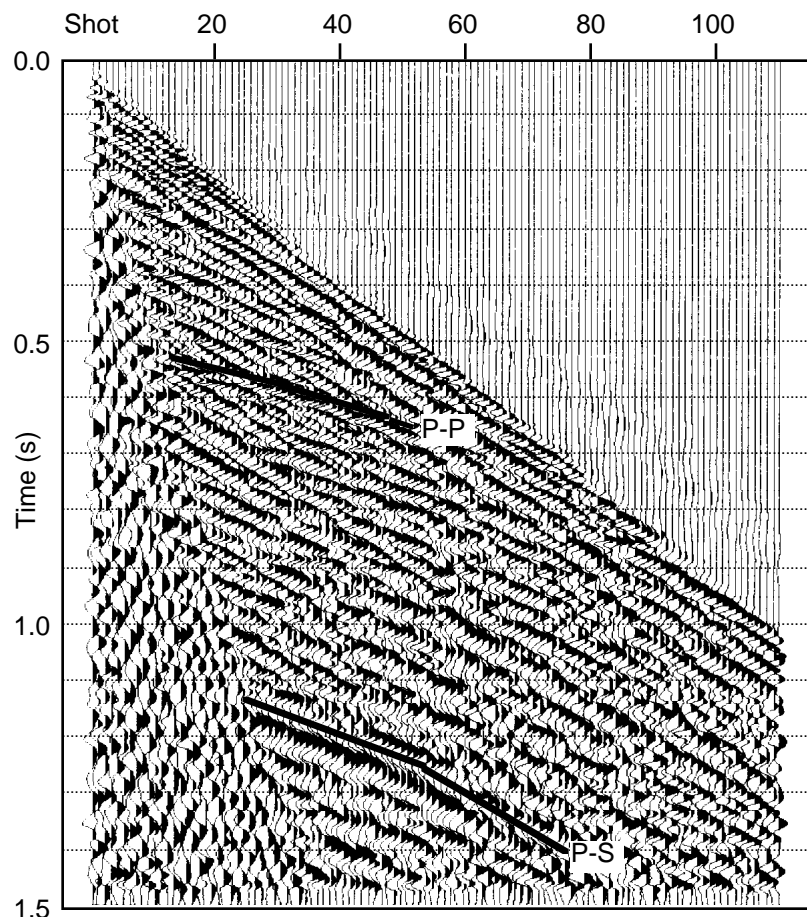


Fig. 4.9 Receiver gather of the radial component from line 470-93. Geometric spreading compensation, trace balancing, shot statics and pre-first break mutes have been applied to this gather.

The only event thought to be *P-S* energy that is observed consistently on all the common-receiver gathers is the high amplitude event after 1.1 s. Its moveout velocity is calculated to be 1400 m/s, which is the estimated rms velocity of the Devonian reflector (at 0.935 s in Table 4.2), although the Devonian is not expected to be this deep in the section. This velocity is lower than would be expected for this time from the predicted

stacking velocities listed in Table 4.2. The zero-offset time of 1.1 s for this event suggests that it might be the Precambrian reflector, which has an arrival time of about 0.75 s on the *P-P* stacked sections. However, the stacking velocity at this time is rather low for the Precambrian event, so it might be a multiple rather than a primary reflection.

Examples of other receiver gathers are shown in Figure 4.10 to demonstrate the highly variable quality of the data. Some records were dominated by low-frequency energy (Figure 4.10a) while others showed a large amount of high frequency energy and some were extremely noisy (Figure 4.10b). The alignment of energy in Figure 4.10a shows that the shot statics are very small. Most gathers showed *P-P* reflections in the shallow section above 0.6 s and all were contaminated with shot-generated surface waves.

Since the initial attempts to generate an interpretable stacked radial section had failed, the method of calculating receiver statics was modified to one based upon aligning the high amplitude event observed below 1.1 s in Figure 4.9. Each common-receiver gather was corrected for NMO using a constant velocity of 1400 m/s to flatten this event, and the gathers were then stacked. A first pass at receiver statics was made by hand correlating the strong event on the receiver stack and flattening it at approximately 1.2 s. Individual NMO-corrected common-receiver gathers were used to determine the arrival time of this event when it was not clear on the stacked section, e.g., over stations 50-55. The initial and aligned common-receiver stacks from the 1993 survey obtained in this way are shown in Figures 4.11a and 4.11b. The aligned receiver stack from the 1994 survey is shown in Figure 4.11c. The values of receiver statics obtained from the 1993 data were used as a first approximation to the receiver statics solution for the 1994 data. A great range in receiver statics values is observed, especially between traces 10 and 30, where they range between +80 to -160 ms. Amplitudes on some of the stacked gathers are very low and automatic cross-correlation routines failed to align the data over these low signal areas. Hand correlation was done in these cases. It is known that the local

geology is flat in this area so it was considered that artificially flattening the stacked gathers at 1.2 s did not destroy any significant structural features. If the event is indeed a multiple then it will be flat, as the primary is flat; thus flattening on a multiple will not be harmful to structure.

It is interesting that the large sag on the initial receiver stack in Figure 4.11a is centred on receiver location 20, which corresponds to CDP 39. It is at this position on the line 470-93 *P-P* section (Figure 4.4) that a shallow channel is interpreted to be present. The approximate receiver statics calculated in this way were applied to the data and the gathers restacked. A second pass of statics was calculated using an automatic cross-correlation routine, with a pilot trace made by summing all the traces in the stack, to align the strong event seen at 1.2 s. These statics were applied to the data and a final receiver stack made for quality control. Receiver statics values for the radial component of line 470-93 varied from +90 ms to -160 ms, in comparison with the vertical component receiver statics, which ranged from only +5 ms to -5 ms. These values are plotted in Figure 4.12, where it is seen clearly how large and variable the *S*-wave receiver statics are compared to the *P*-wave receiver statics.

Figure 4.13 shows the same shot gather as in Figure 4.8 but after application of the receiver statics determined by the procedure outlined above. Coherent energy is now seen throughout the record and any *P-P* energy present in the data will be unaligned since the *P-P* receiver statics are different from the *P-S* receiver statics.

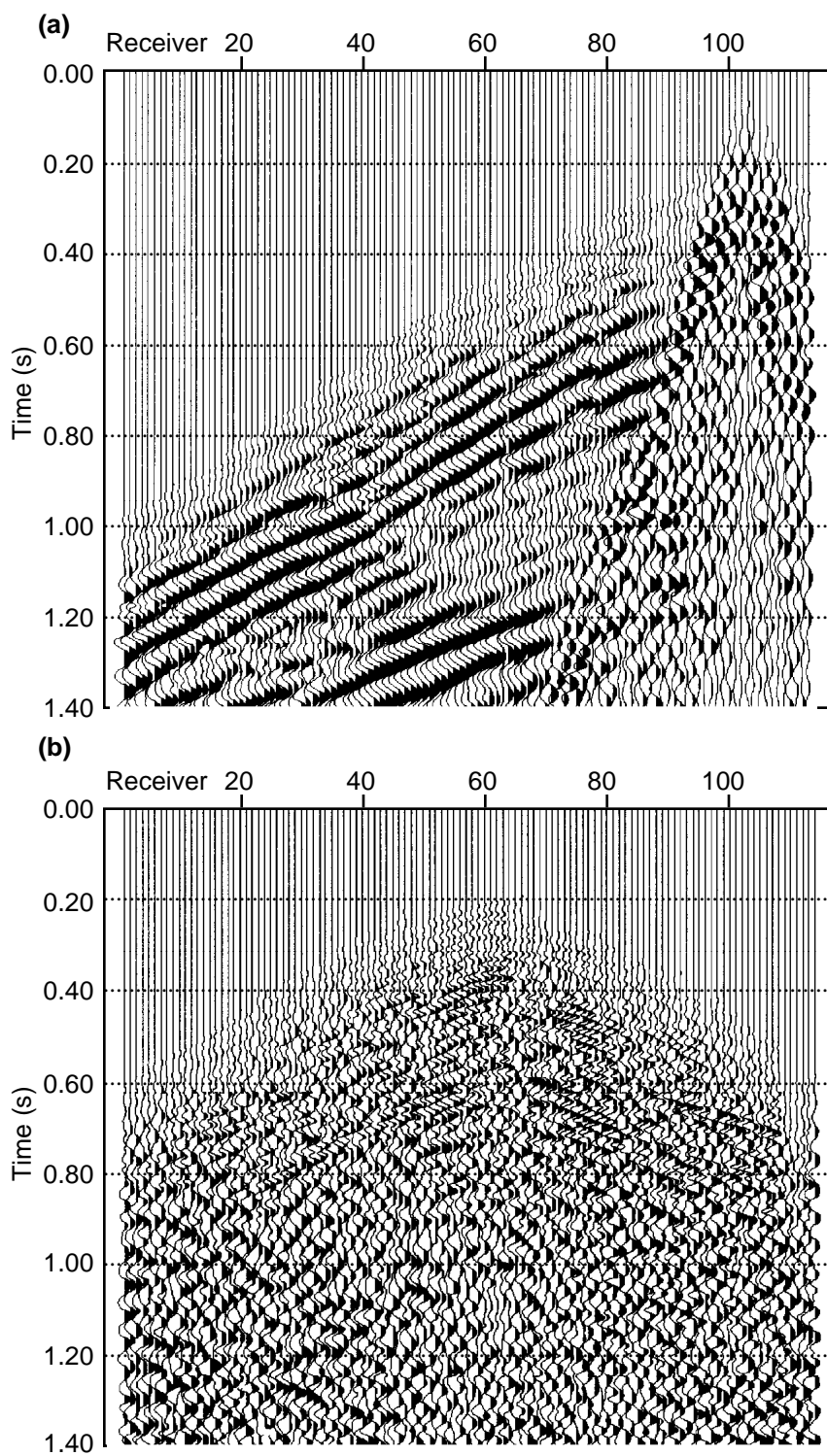


Fig. 4.10 Two receiver gathers from the 1994 survey showing (a) low frequency coherent noise and (b) incoherent noise and P -wave energy overwhelming the P - S data.

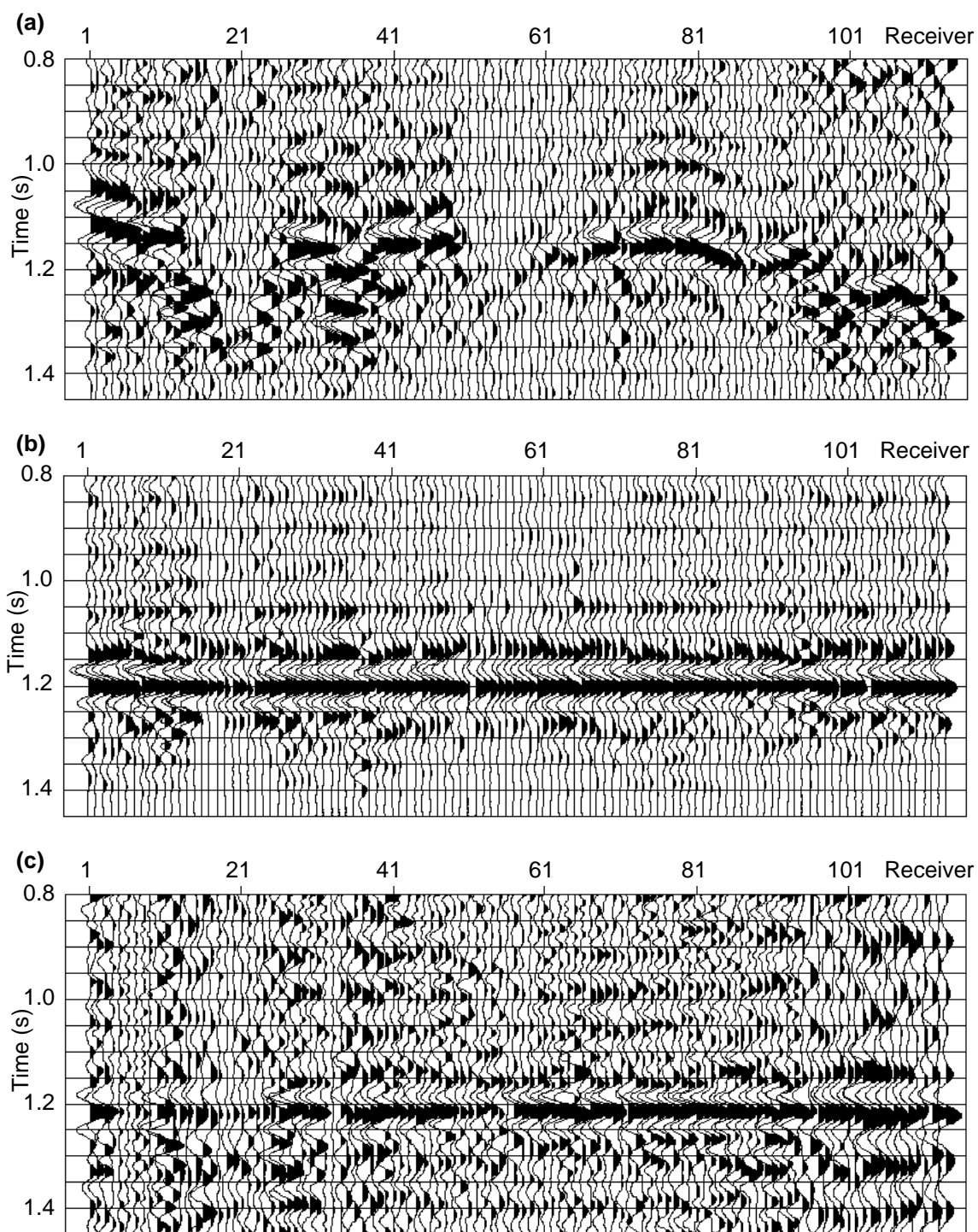


Fig. 4.11 The stacked 1993 receiver gathers, (a) before and (b) after alignment of the high amplitude event at 1.2 s and (c) the 1994 aligned receiver gather.

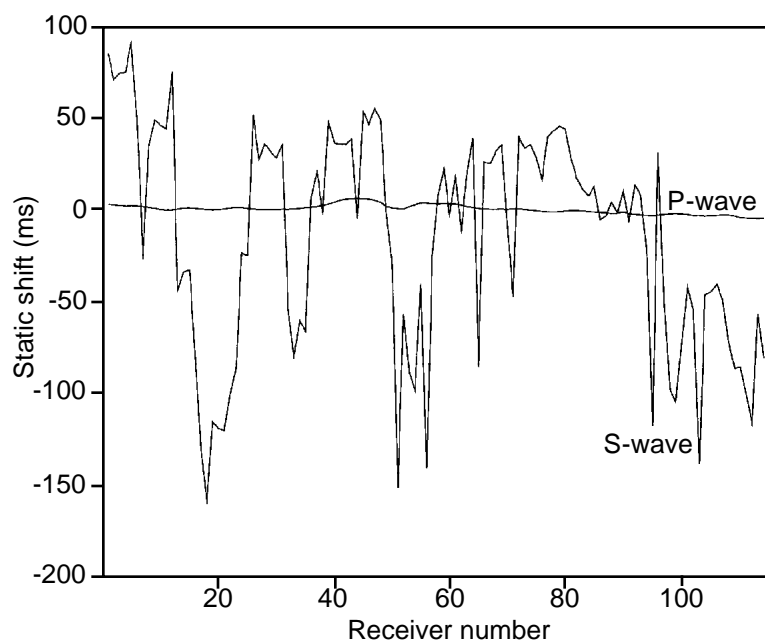


Fig. 4.12 Comparison of values of *P*-wave and *S*-wave receiver statics for the vertical and radial components, respectively, of line 470-93.

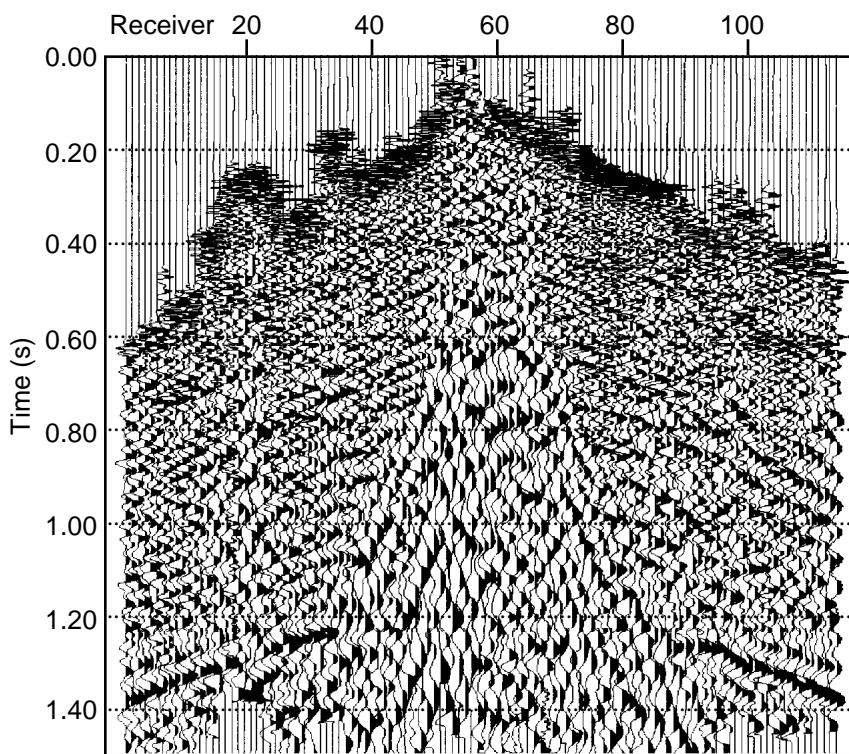


Fig 4.13 The same shot gather as in Figure 4.8 but with receiver statics applied. Coherent events now appear in the data.

4.5.3 Stacking velocity analysis and final section generation

Spiking deconvolution was applied to the receiver gathers and an iterative process used to determine the stacking velocities. Only traces with source-receiver offsets less than 1400 m were used in the velocity analysis. Stacking velocities estimated from semblance analyses were used to correct the data for normal moveout, the gathers $f-k$ filtered to eliminate events with high dip (primarily the $P-P$ energy), the NMO correction removed and velocity analysis performed on these filtered gathers. The procedure was repeated using the new velocity functions until a satisfactory stacked section was obtained, although the velocities proved difficult to determine because the data, especially in the shallower section above 0.6 s, were dominated by $P-P$ energy. Representative stacking velocities are listed in Table 4.3.

Table 4.3 Representative $P-S$ stacking velocities for line 470-93.

Time (s)	V_{ps} (m/s)
0.100	930
0.200	970
0.300	1020
0.400	1060
0.500	1120
0.700	1200
0.800	1260
1.200	1425
1.400	1500

These velocities were used because the resulting stacked section showed interpretable reflections below about 0.55 s. The velocities listed for times earlier than 0.7 s were only estimated, not picked from actual events on the semblance plots, and

should not be regarded as meaningful. For this reason, shear-wave interval velocities were not calculated.

Comparison of these velocities with the original predicted stacking velocities (Table 4.2) shows that they are lower. The predicted stacking velocities were calculated using equations (4.1) and (4.2) and an assumed average V_p/V_s of 2.4. The actual stacking velocities being lower than predicted implies a higher average V_p/V_s than 2.4. Given the actual P - S stacking velocities, equations (4.1) and (4.2) can be used to calculate the V_p/V_s required to obtain the correct P - P stacking velocities and P - P times. This value is calculated to be 2.77 for the P - S times down to 0.5 s. Compressional-wave sonic logs from nearby wells indicate an average V_p of 2000 m/s from the surface to the top of the Grand Rapids Formation, which is at a depth of about 310 m relative to seismic datum. An average V_p/V_s of 2.77 to this depth implies an average V_s of 722 m/s. Shear-wave dipole logs, acquired recently at the AABBW and nearby pads, indicate an average V_s of 700-715 m/s in the 100 m section above the Grand Rapids Formation, where the logs are reliable. An average V_s of 722 m/s, therefore, does not seem unreasonable.

The resulting stacked section was not as good as anticipated, having lower bandwidth than was hoped for. Pre-stack deconvolution applied after NMO correction instead of before was found to produce a section with higher frequency content. It is thought possible that application of the low NMO velocities after deconvolution was causing a loss of higher frequencies. Spectral balancing was also applied to the NMO-corrected, deconvolved gathers before stacking. In Figure 4.14 the spectra of raw records from the (a) vertical and (b) radial components and the spectra of the final migrated section from the (c) vertical and (d) radial components of line 470-93 are displayed. The raw vertical component has a dominant frequency of 40 Hz while that of the radial component is 15 Hz. After deconvolution and spectral balancing the individual spectra are much flatter. The dominant frequencies of about 60 Hz on the vertical section and 30

Hz on the radial section result in comparable wavelengths of 35 m to 40 m in the reservoir zone.

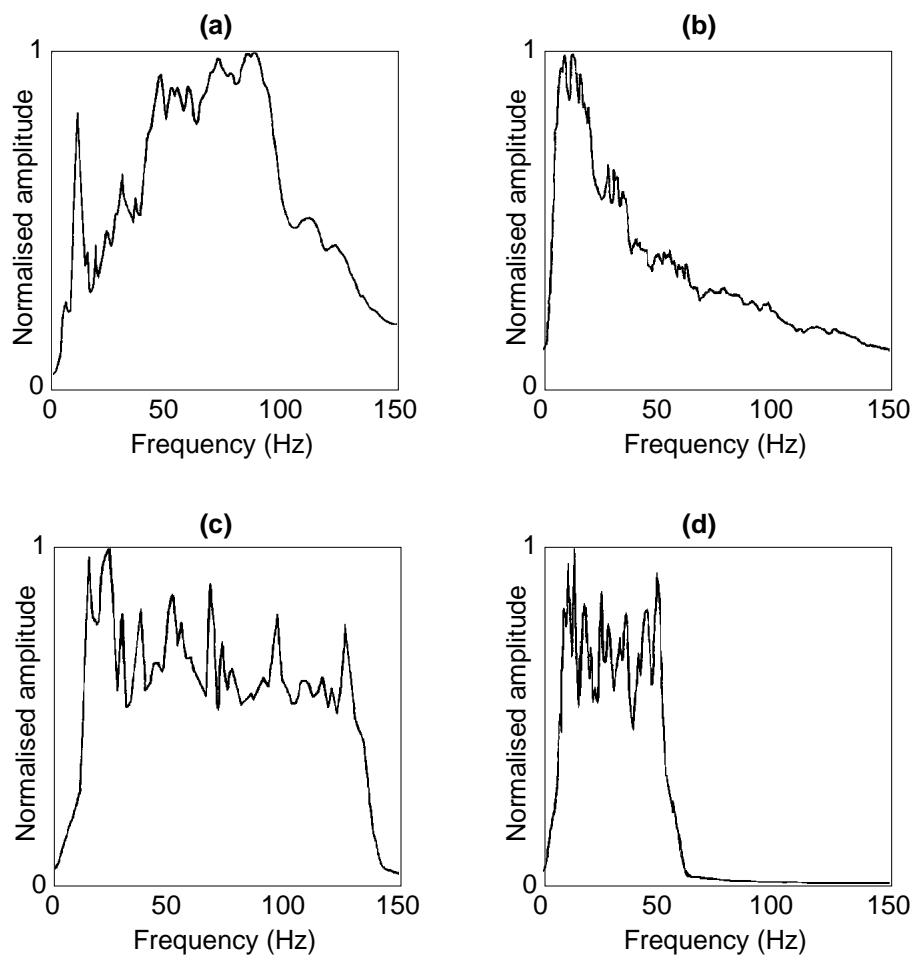


Fig. 4.14 Frequency spectra of raw records from the (a) vertical and (b) radial components and the spectra of the final migrated sections from the (c) vertical and (d) radial components of line 470-93.

The NMO-corrected, deconvolved, spectrally balanced shot gathers were $f-k$ filtered to remove the $P-P$ energy that was degrading them. Common-offset stacks were used to determine the inner and outer mutes to be applied to these gathers. The inner mute cut any residual shot noise. The outer mute was applied prior to $f-k$ filtering to

remove NMO stretch and again after f - k filtering to eliminate edge effects and to limit the farthest offset to 1400 m. In Figure 4.15 are plotted the inner and outer mute offsets as a function of depth. The dashed area denotes the range of offsets included at any depth. On average, at any depth, the ratio of the farthest offset to depth is 1.4 and of the nearest offset to depth is 0.5. The longest source-receiver offset was 1800 m but offsets greater than 1390 m were excluded from the stack to avoid frequency degradation caused by NMO stretch.

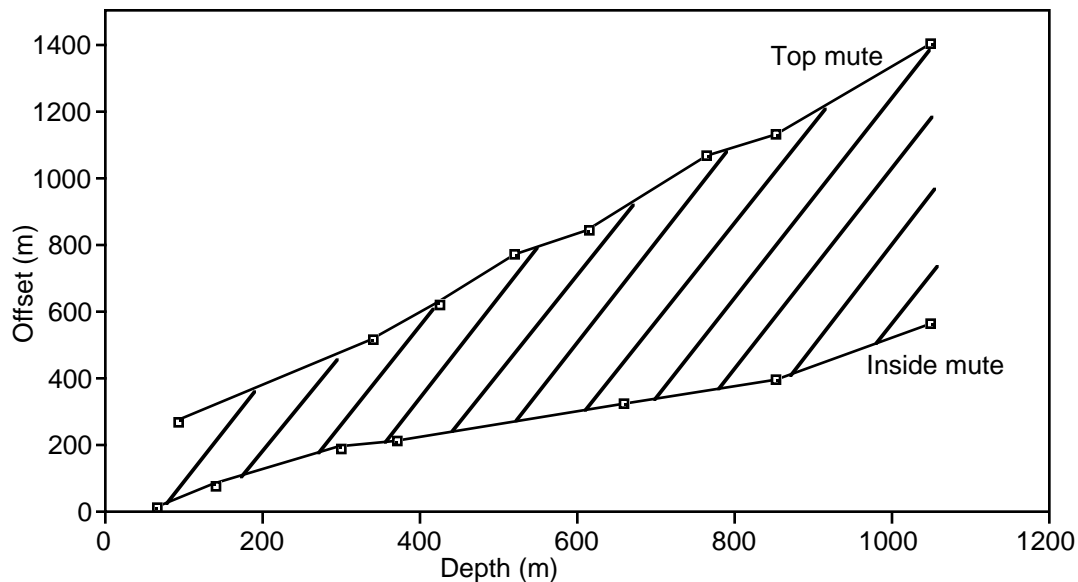


Fig. 4.15 Plot of offsets as a function of depth for the P - S data. The dashed area denotes the offsets included in the stacked sections at any depth.

A deleterious effect of limiting the offsets included in any CCP gather is to reduce the fold of the data. Figure 4.16 shows the final fold of line 470-94 at (a) each CDP along the vertical component and at (b) each CCP along the radial component. The plots have been smoothed a little to remove distracting jitter. "O" denotes the original fold after binning while "D" and "GR" denote the fold at the tops of the Devonian section and

Grand Rapids Formation, respectively, after muting. The plots of fold are not symmetrical because of asymmetry in the line geometry (see Figure 4.1), restriction of offsets included and exclusion of bad shots. Average fold over CDPs 50 to 175 on the vertical component section is 45 at the top Devonian level and 27 at the top Grand Rapids level. In comparison, for the radial component section, fold over CCPs 50 to 175 is 25 at the top Devonian level and 16 at the top Grand Rapids level. Due to an unusually large number of bad shots and poor record quality along line 472-93, there was extremely low fold at the top Grand Rapids level over CCPs 97 to 114.

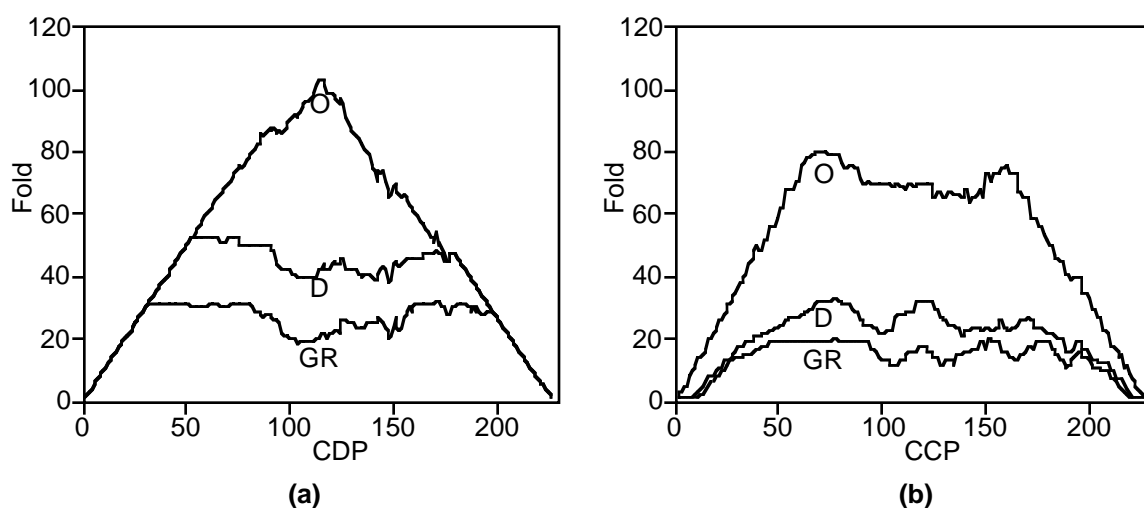


Fig. 4.16 Final fold of data at (a) each CDP along the vertical component section and at (b) each CCP along the radial component section of line 470-94. "O" denotes the original fold after binning while "D" and "GR" denote the fold at the top of the Devonian section and the top of the Grand Rapids Formation, respectively, after muting.

Harrison and Stewart (1993) showed that *P-S* sections may be post-stack time-migrated using migration velocities 6-11% less than the *P-S* rms velocities, so the *P-S* lines were migrated in this manner. Finally, a bandpass filter of 5/8-50/60 Hz and an 11-point *f-x* deconvolution were applied to the sections.

The uncertainty about rotation into a natural coordinate system was discussed earlier in section 4.5.1. It was assumed that only a rotation into the source-receiver plane was necessary. As a test of this assumption, data from line 468-93 were rotated into a coordinate system parallel to receiver line 470. The continuity and amplitude of the tops of the Grand Rapids Formation and Devonian reflections were inferior to those observed on the first stacked section. It was concluded that the single rotation into the source-receiver plane was sufficient.

The final migrated P - S section for line 470-93 is shown in Figure 4.17. The scarcity of signal in the shallower section above 0.4 s is due to the dominance of P -wave energy there and the degradation of data outside the trim statics window. In Figure 4.17 a strong event is visible at about 0.85 s; an event which was not resolved on the initial stacked section. Identification of the reflections will be discussed in Chapter 5.

4.6 Discussion

Two experimental time-lapse converted-wave surveys were acquired over the AABBW pads in 1993 and 1994. The vertical (P - P) components of lines 469, 470 and 471 and the radial (P - S) components of lines 468, 470 and 472 were processed fully. The vertical components were processed through a standard processing sequence to produce migrated sections, which then had an 11-point f - x deconvolution applied to enhance reflections.

Radial component processing differs from that of the vertical component in several significant ways. Rotation analysis designed to determine the natural coordinate system was inconclusive so the horizontal component data were rotated into components oriented in the source-receiver plane and orthogonal to that plane. The method of calculating receiver statics was modified by aligning a single, high amplitude event seen on all of the common-receiver gathers. These receiver statics were applied to shot

gathers and greatly enhanced the coherency of the signal. An iterative procedure was used to determine the stacking velocities, which were lower than originally predicted. The final important factor in the *P-S* data processing was to apply deconvolution after NMO corrections, to enhance the frequency content of the data. The combination of these three factors (revised method of determining receiver statics, iterative velocity analysis and deconvolution after NMO) resulted in stacked sections with interpretable events.

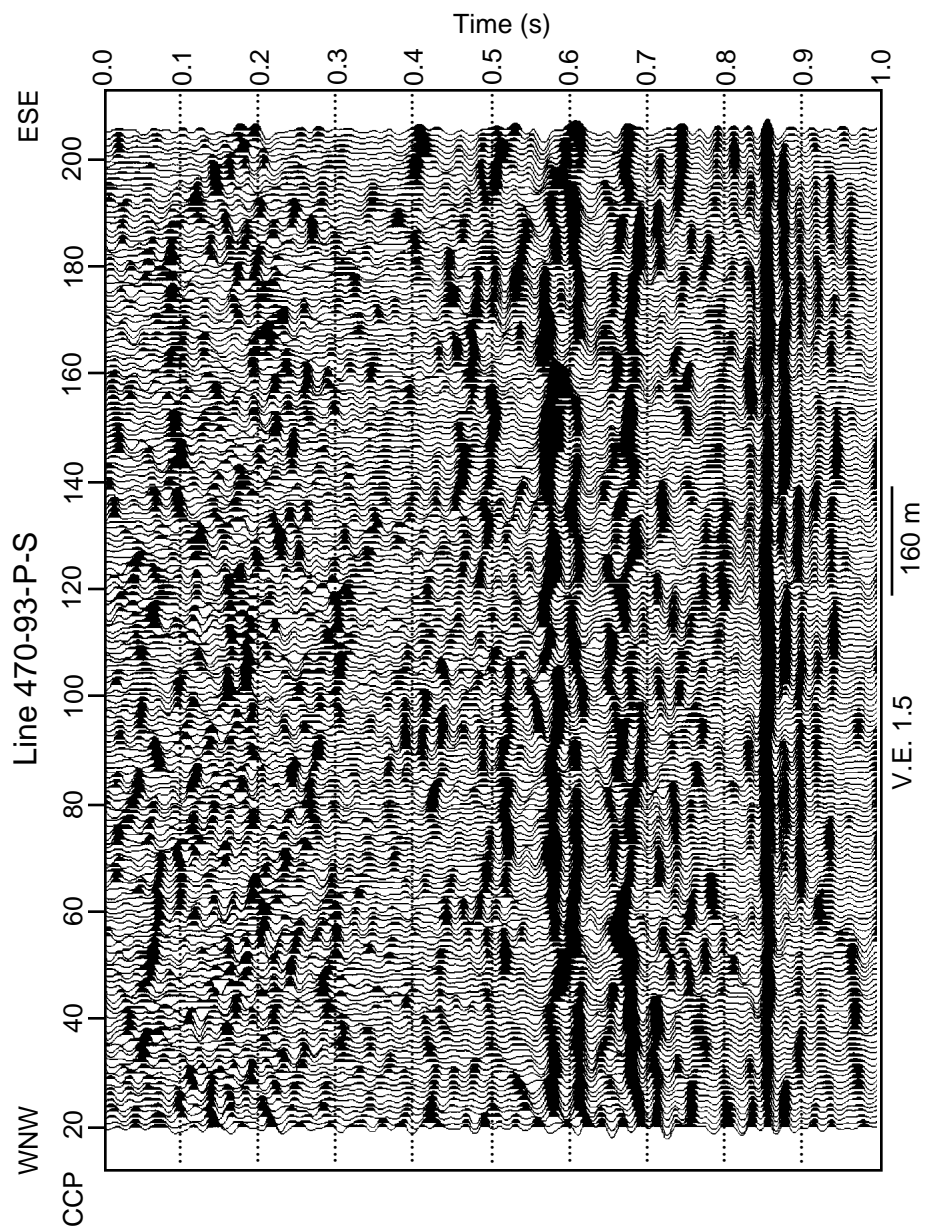


Fig. 4.17 Final migrated *P-S* section for line 470-93.

Chapter 5

3-C SEISMIC DATA ANALYSIS

5.1 Data interpretation

5.1.1 Well log data

To predict the seismic reflections to be expected in the P - P and P - S data, use was made of dipole logs run in well BB13a. Figure 4.5 showed the compressional- and shear-wave velocities, as measured by these logs, and the corresponding V_p/V_s at each depth. A clear increase in velocity is observed for both the P and S curves at 314 m, which is the top of the Grand Rapids Formation. A good seismic reflection should therefore be expected for the Grand Rapids Formation top on both the P - P and P - S sections. The relative increase in shear-wave velocity is greater than the relative increase in compressional-wave velocity so the Grand Rapids event is expected to be a stronger event on the P - S data than on the P - P data.

Between the top of the Grand Rapids Formation and the top of the Clearwater Formation at 416 m, there are no significant velocity contrasts on either curve. There is not much difference in the S -wave velocity in the Grand Rapids and Clearwater formations, although this Clearwater shear-wave velocity is now thought to be too low. The low P -wave velocity observed on the sonic log at the top of the Clearwater Formation, and the corresponding low V_p/V_s , is caused by a partial gas-saturation. V_p/V_s in this zone is anomalously low so measurement of such low values from the seismic data acquired during the production cycle should reflect gas-saturated zones. Differences in reflectivity between the P - P and P - S sections should also be apparent over such zones if the P - S data are of high enough quality. Unfortunately, the well penetrated no deeper than the Clearwater Formation so direct velocity measurements of the Devonian section are unavailable. From velocity analyses it is known that the compressional-wave velocity

increases considerably at the top of the Devonian section. If it is assumed that V_p/V_s in carbonates is around 1.9 (Domenico, 1984), then the shear-wave velocity can be expected to increase considerably, also. Therefore, the top Devonian event is expected to be a strong, identifiable event on both the $P-P$ and $P-S$ sections.

5.1.2 $P-P$ data interpretation

A synthetic $P-P$ seismogram was created from the sonic log run in well BB27 using an offset raytracing program "SYNTH", developed by Lawton and Howell (1992). Figure 5.1 shows the correlation between this seismogram and part of line 470-94- $P-P$. The well projects 21 m onto line 470 at shotpoint 109. The sonic logs were acquired in February 1988 so there were several cycles of CSS between the times of acquisition of the sonic log data and the seismic data. Unlike at the D3 pad, there is no strong tight streak in the Grand Rapids Formation at which to tie the correlation. The character match between the synthetic seismogram and the seismic data allows identification of the tops of the Grand Rapids and Clearwater formations. Knowledge of the expected transit time of the Clearwater to Devonian interval and of the seismic character of the top Devonian reflection, based on experience at the D3 pad, helps to identify this event.

Interpreted versions of lines 470-93- $P-P$ and 470-94- $P-P$ are displayed in Figures 5.2 and 5.3, respectively. The frequency content and seismic character appear to be similar. The tops of the Grand Rapids Formation (GR) at about 0.35 s, the Clearwater Formation (C) at about 0.43 s and the Devonian section (D) at 0.53 s are annotated on the sections. Indicated by the bar at the side of the sections is the Clearwater reservoir zone, which extends from about 0.43 s to 0.47 s. There is a small bulk shift between the two sections, probably caused by different near-surface conditions at the times of acquisition, as observed at the D3 pad.

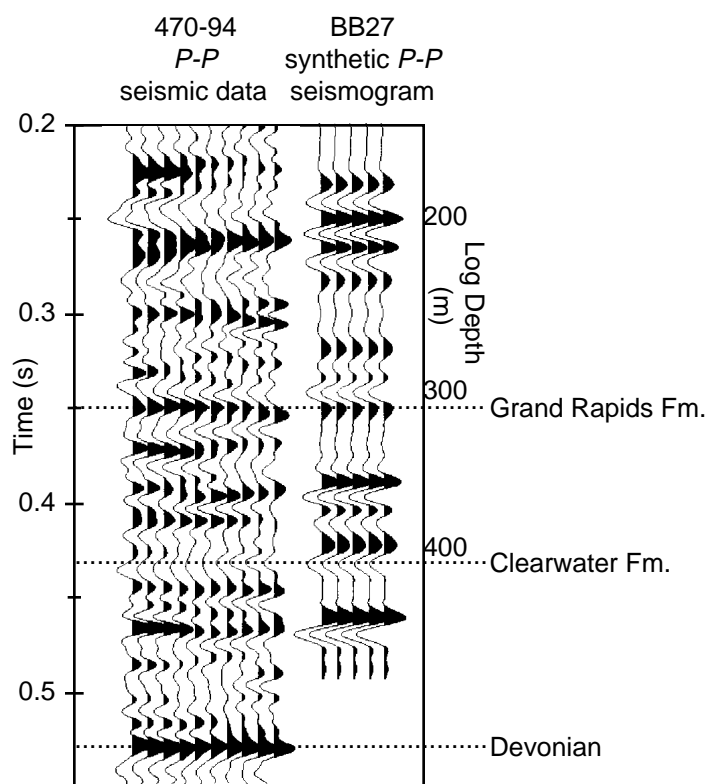


Fig. 5.1 Tie between synthetic *P-P* seismogram and line 470-94-*P-P*.

A shallow channel, at around 0.12 s over CDPs 10 to 60, is interpreted on both lines. The location of the deepest part of the channel, over CDPs 25 to 49, corresponds to the location of receivers 13 to 25 in Figure 4.12, where very large *S*-wave static values occur. This channel may, therefore, be the cause of the large *S*-wave statics.

Between 0.20 s and 0.26 s, in the Colorado shales, several high amplitude events can be seen. At the southeastern end of the line, from CDPs 110 to 220, the character of these events is similar on both lines 470-93 and 470-94. However, between CDPs 1 and 110 a difference in seismic character and amplitude of events is evident. In particular, a high amplitude peak-trough event (indicated in Figure 5.3) appears at 0.25 s between CDPs 30 and 100 on the 1994 line. Usually seismic sections should be very similar in the zone above the reservoir. However, in this case the geological conditions have changed. After injection of steam in 1993, casing collapse shallow in some of the deviated wells

resulted in leakage of water into the Colorado shales (J. Eastwood, *pers. comm.*). This hydration of the shales is the cause of the amplitude anomaly in the 1994 survey and has been mapped by Imperial Oil using the 3-D seismic data. A very small time delay below this event is apparent in the 1994 data but, since the entire section below the Colorado is affected, isochrons between any two underlying events will not be influenced.

The character match between the two lines is good from the Colorado shales to the top of the Clearwater Formation, which is at about 0.43 s. Within the reservoir zone, differences in seismic character and amplitude occur and are interpreted to be caused by the changes in reservoir conditions between the 1993 and 1994 surveys. High amplitude events may be caused by the presence of steam during the injection cycle in 1993 and by gas during the production cycle in 1994.

Figure 5.4 shows line 126-93 from the 1993 3-D seismic survey, which was processed by an independent contractor. The surface location of this line corresponds to that of line 470-93 from the 3-C survey and has the same CDP spacing of 8 m. Although the same source was used for both surveys, the 3-C data were recorded by geophones planted at the surface while the 3-D data were recorded by geophones buried 10 m deep. The original CDP numbers of line 126-93 have been altered to those of line 470-93 so that a direct comparison can be made between the two lines. Line 126-93 has been bandpass filtered with the same frequency limits of 10/15-100/120 Hz as line 470-93. A shorter source-receiver offset range was processed for line 126-93, which had a maximum offset of 500 m at 0.5 s, whereas for line 470-93 offsets up to 600 m were included at a reflection time of 0.53 s.

There is a clear time shift between the two sections which could be partially the result of the different geophone depths; the elevation datum was 600 m in both cases. Line 470-93 has also had a post-migration f - x filter applied whereas line 126-93 has had no lateral smoothing filter applied. Similarities in character are evident on the two

sections. The Devonian event is continuous and of high amplitude and on both sections the main peak-trough event is followed by a peak over CDPs 1 to 50. Corresponding dipping events appear above the top of the Clearwater Formation between CDPs 1 and 80 and the time structure of the Clearwater event is similar on both sections.

The top of the Clearwater Formation has been picked as a trough on both sections but in places is not a strong event. High amplitude events appear on line 126-93 at about 30 ms below the top of the Clearwater Formation over CDPs 100 to 200. These events are in the reservoir zone and are interpreted to be the sonic response to steam-saturated zones. Such events do not stand out so clearly on the 3-C line, possibly because of the $f-k$ and $f-x$ filtering that was applied to reduce the noise.

The shallow channel is imaged more clearly on line 470-93 than on line 126-93. Neither section shows much reflectivity between the Colorado shales at 0.2-0.25 s and the top of the Grand Rapids Formation at 0.32-0.35 s. The top of the Grand Rapids Formation is picked more easily on the 3-C line than the 3-D line, where it is less continuous, especially over the eastern half of the line.

5.1.3 *P-S* data interpretation

In an attempt to identify the reflections observed in the *P-S* data, a *P-S* synthetic seismogram was created using the offset raytracing program "SYNTH" and the compressional sonic log from well BB27. The tie between this synthetic seismogram and part of line 470-93-*P-S* is shown in Figure 5.5. The synthetic seismogram was created using only the BB27 *P*-wave sonic log (acquired in 1988), with the necessary *S*-wave sonic log being estimated from this log using V_p/V_s of 2.4, which was obtained from Figure 4.5. Thus it may not be an accurate model for the *P-S* stacked section.

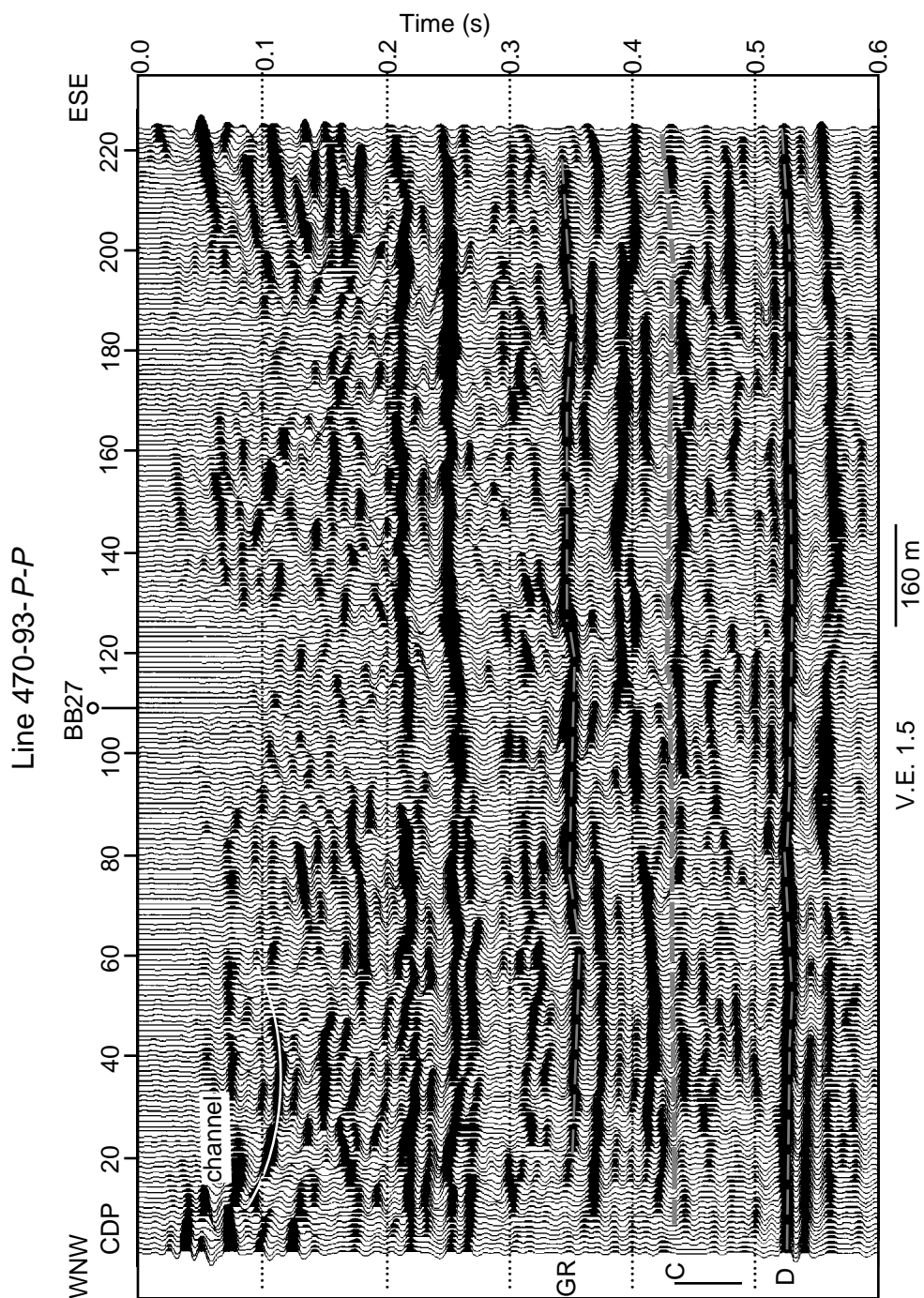


Fig. 5.2 Interpreted line 470-93-P-P. "GR" denotes the top of the Grand Rapids Formation, "C" the top of the Clearwater Formation and "D" the top of the Devonian section. The bar at the side of the sections denotes the extent of the reservoir zone.

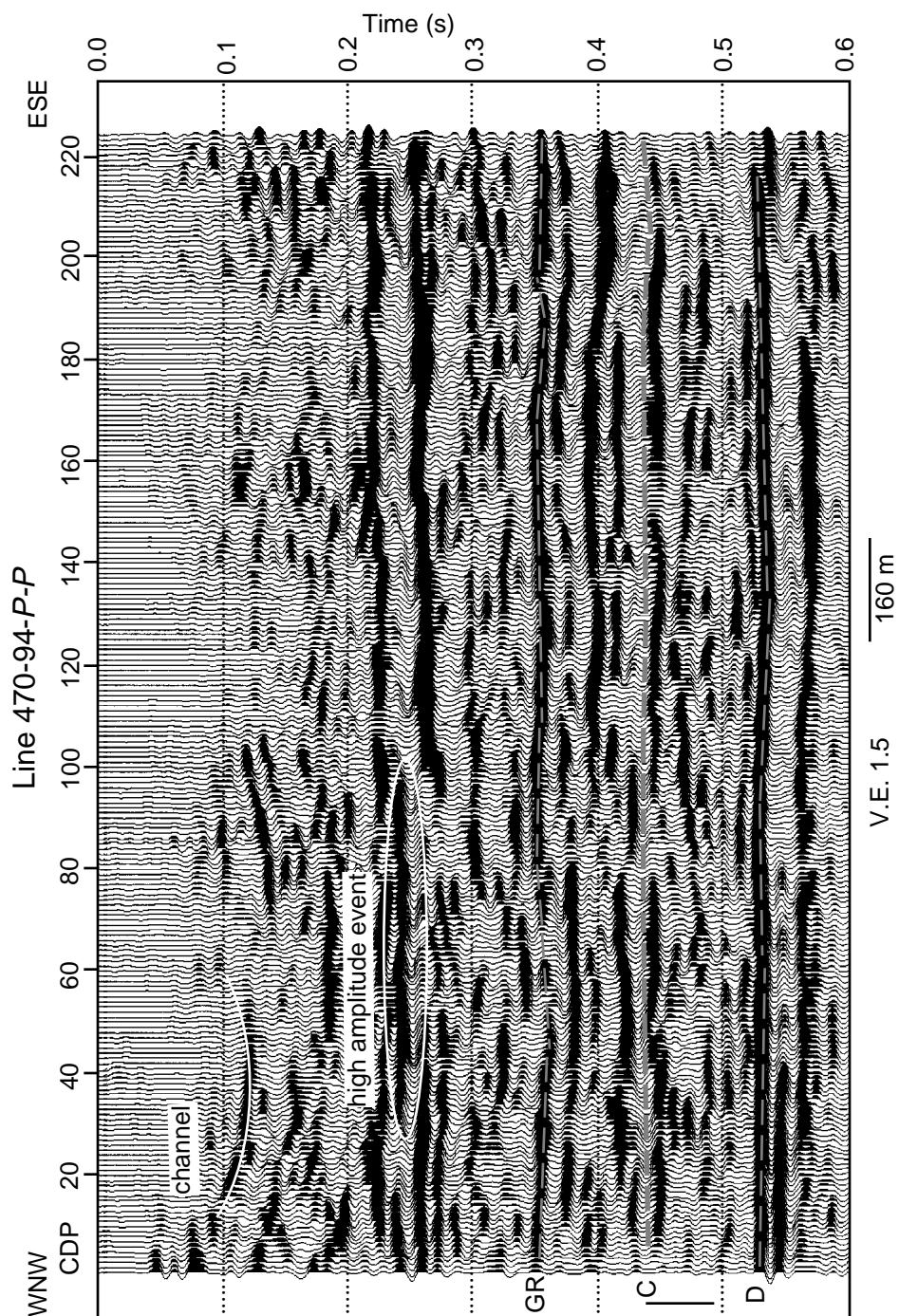


Fig. 5.3 Interpreted line 470-94-P-P. "GR" denotes the top of the Grand Rapids Formation, "C" the top of the Clearwater Formation and "D" the top of the Devonian section. The bar at the side of the sections denotes the extent of the reservoir zone.

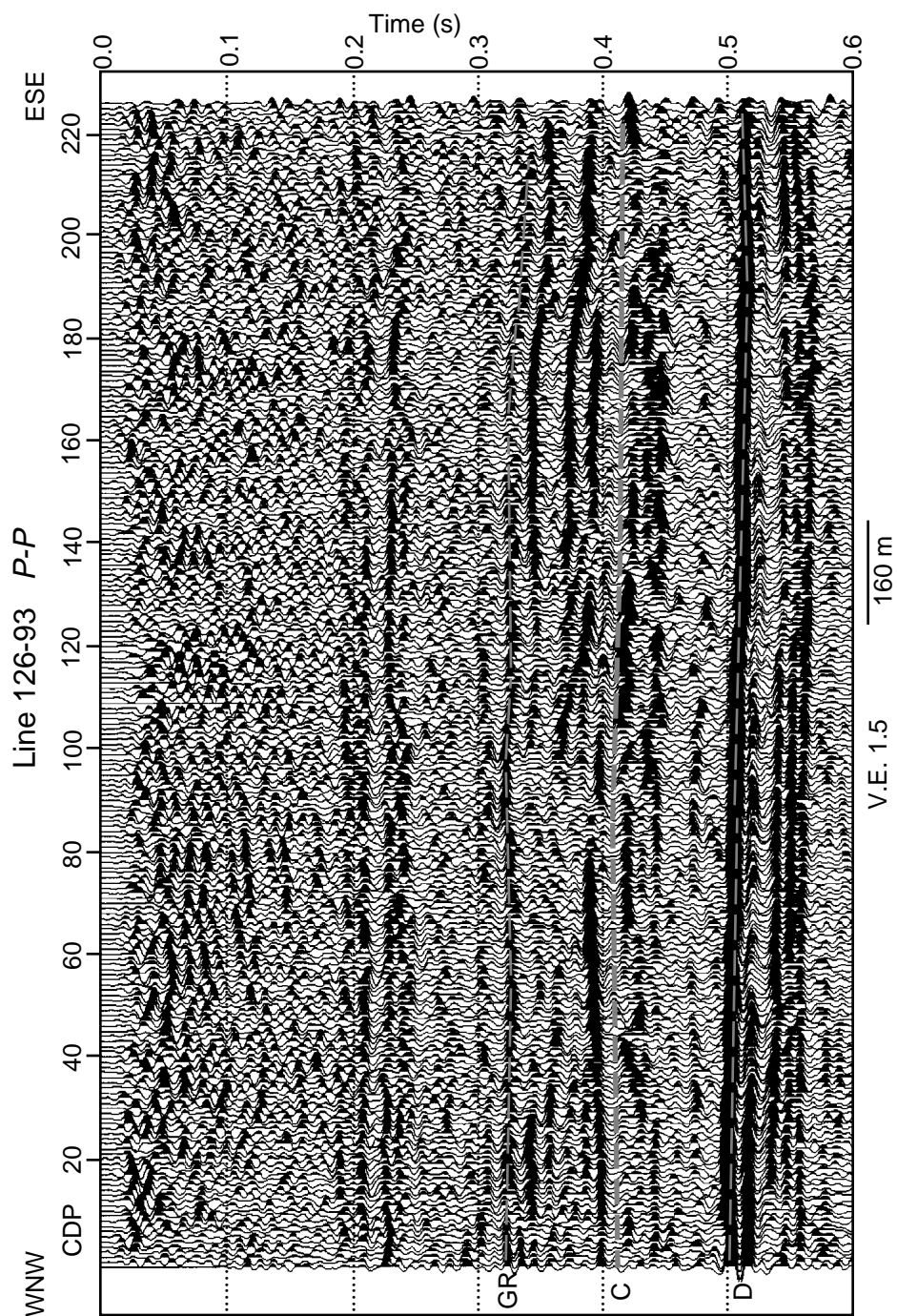


Fig. 5.4 Line 126-93 extracted from the 1993 3-D survey. The location of this line corresponds to that of line 470-93.

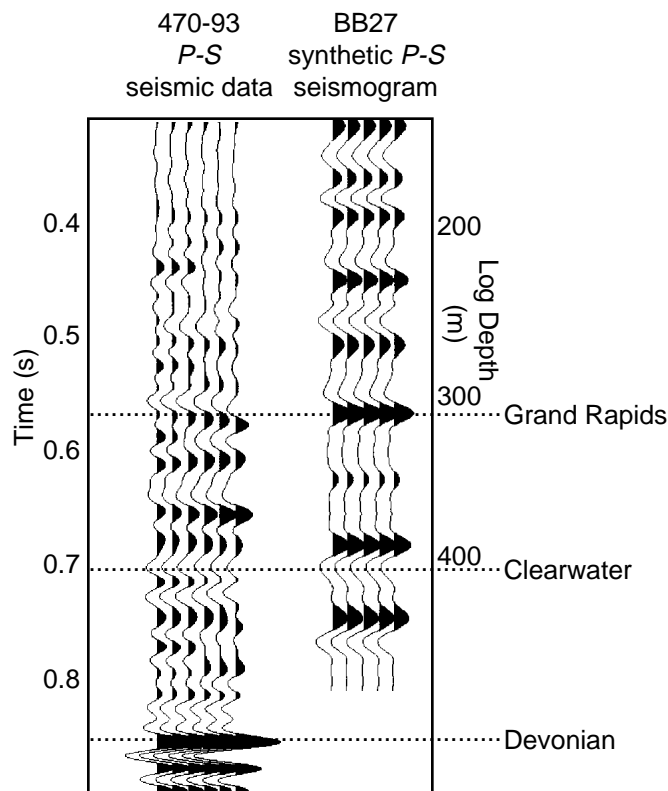


Fig. 5.5 Tie between *P-S* synthetic seismogram and part of line 470-93-*P-S*.

The *P*- and *S*-wave dipole logs from BB13a were not used as they did not start until 280 m and the *P*-wave sonic log exhibits an anomalously low velocity at the top of the Clearwater Formation due to the presence of gas. Although gas was present at this location in the reservoir in early 1993, the conditions there at the time of acquisition of the 3-D survey, in November 1993 during the steaming cycle, are not known.

The Grand Rapids event correlates to a peak at about 0.57 s, which is the first fairly strong and continuous reflector. Since the logs used did not reach the Devonian section, the arrival time of the top Devonian event on the *P-S* data was estimated. An estimated average V_p/V_s of 2.2 and the Grand Rapids to Devonian interval traveltimes of 0.175 s from the *P-P* section were used to estimate the Devonian interval traveltimes on the *P-S* section. This value was calculated to be 0.28 s, so a strong, coherent reflector

observed at 0.85 s on the *P-S* section is interpreted to be the top of the Devonian section. The interval transit time between the top of the Clearwater Formation and the Devonian (150 ms) is reasonable, based on the *P-P* interval travel time of 100 ms and an estimated V_p/V_s of 2.0 over this interval.

The synthetic *P-S* seismogram was created using an average V_p/V_s of 2.4 but the stacking velocities implied a V_p/V_s of 2.77 in the section above the Grand Rapids Formation (section 4.5.3). The implication of a higher V_p/V_s is that the arrival times of reflections on the *P-S* data are later than initially estimated. There are only two correlations that can be made between the *P-P* and *P-S* reflections, and they are displayed in Figure 5.6. The *P-P* and *P-S* sections are displayed at scales corresponding to a V_p/V_s of 2.4. In Figure 5.6a the Grand Rapids reflection on the *P-S* section is at 0.58 s and the Devonian reflection is at 0.85 s, whereas in Figure 5.6b these reflections are at times of 0.85 s and 1.16 s, respectively. The character correlation between reflections is better for the first interpretation than the second, particularly in the Grand Rapids to Devonian interval. Values of V_p/V_s , and V_s in the shallow section, as determined from the two alternative correlations, are listed in Table 5.1.

Table 5.1 V_p/V_s , as determined from the two alternative correlations.

Interval	Correlation (a)	Correlation (b)	Logs, theory, stacking velocities
Surface to Grand Rapids ($V_p = 2000$ m/s, $d = 310$ m)	$V_s = 729$ m/s $V_p/V_s = 2.74$	$V_s = 445$ m/s $V_p/V_s = 4.5$	$V_s = 700-715$ m/s (logs) $V_p/V_s = 2.4-3.0$ (logs) $V_p/V_s = 2.77$ (stacking velocities)
Grand Rapids to Devonian	$V_p/V_s = 2.11$	$V_p/V_s = 2.44$	Max. $V_p/V_s = 2.2$ (theory; section 5.2.2)
Devonian to Near Basement	$V_p/V_s = 1.9$	No basement event	$V_p/V_s = 1.9$ (carbonates)

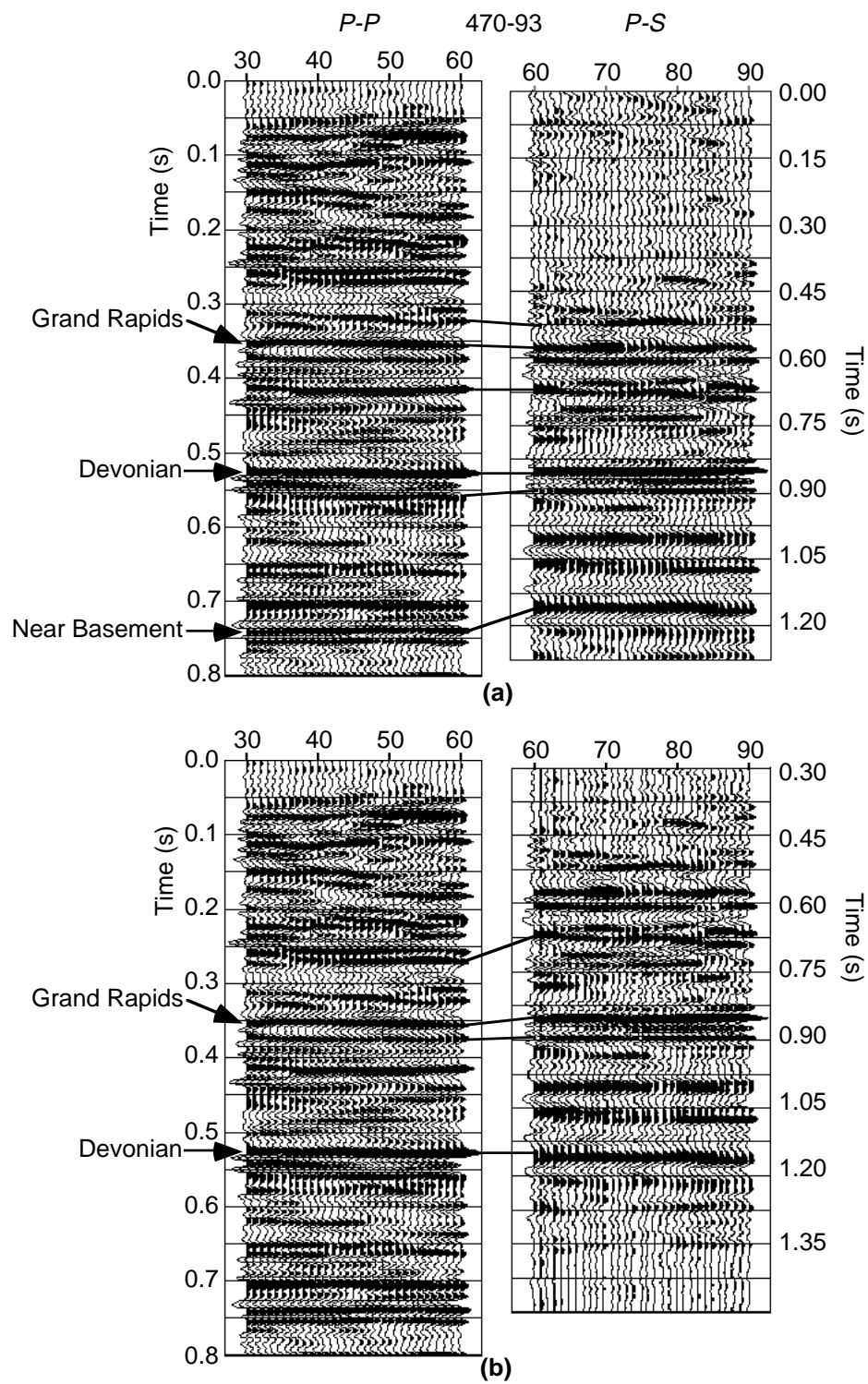


Fig. 5.6 Two alternative correlations between the *P-P* and *P-S* components of line 470-93.

The values obtained from correlation (a) are much closer to the values obtained from logs and stacking velocities than are those obtained from correlation (b). In particular, V_p/V_s of 2.4 in the Grand Rapids to Devonian interval, calculated using correlation (b), is much greater than the value of 2.2, which will be calculated as the theoretical maximum in section 5.2.2. Thus, correlation (a) is the one to use.

Interpreted versions of lines 470-93-*P-S* and 470-94-*P-S* are displayed in Figures 5.7 and 5.8, respectively. The tops of the Grand Rapids Formation and Devonian section are annotated and the reservoir zone is indicated by the bar at the side. As on the *P-P* data, a small bulk shift is apparent between the two sections. On the 1994 line (Figure 5.8) the Grand Rapids event appears stronger and more continuous than on the 1993 line (Figure 5.7). The 1993 raw records were contaminated with more noise, both coherent and incoherent, than were the 1994 records so the presence of this noise may be adversely affecting the Grand Rapids event on the 1993 line. The Grand Rapids event appears stronger on the *P-S* sections than on the *P-P* sections previously displayed in Figures 5.2 and 5.3, as was predicted by the relative increases in *P*- and *S*-wave velocity on the dipole logs (Figure 4.5). The top of the Clearwater Formation is not a very strong or continuous event on either of the sections in Figures 5.7 and 5.8.

Neither section has coherent reflections earlier than the Grand Rapids event, where both data sets were overwhelmed by *P-P* energy on the raw gathers. Events on the 1993 section between the Grand Rapids and Devonian reflections are less continuous than on the 1994 line. There are no events which are continuous along the entire line and closer to the reservoir zone than the Grand Rapids and Devonian along line 470-93-*P-S*.

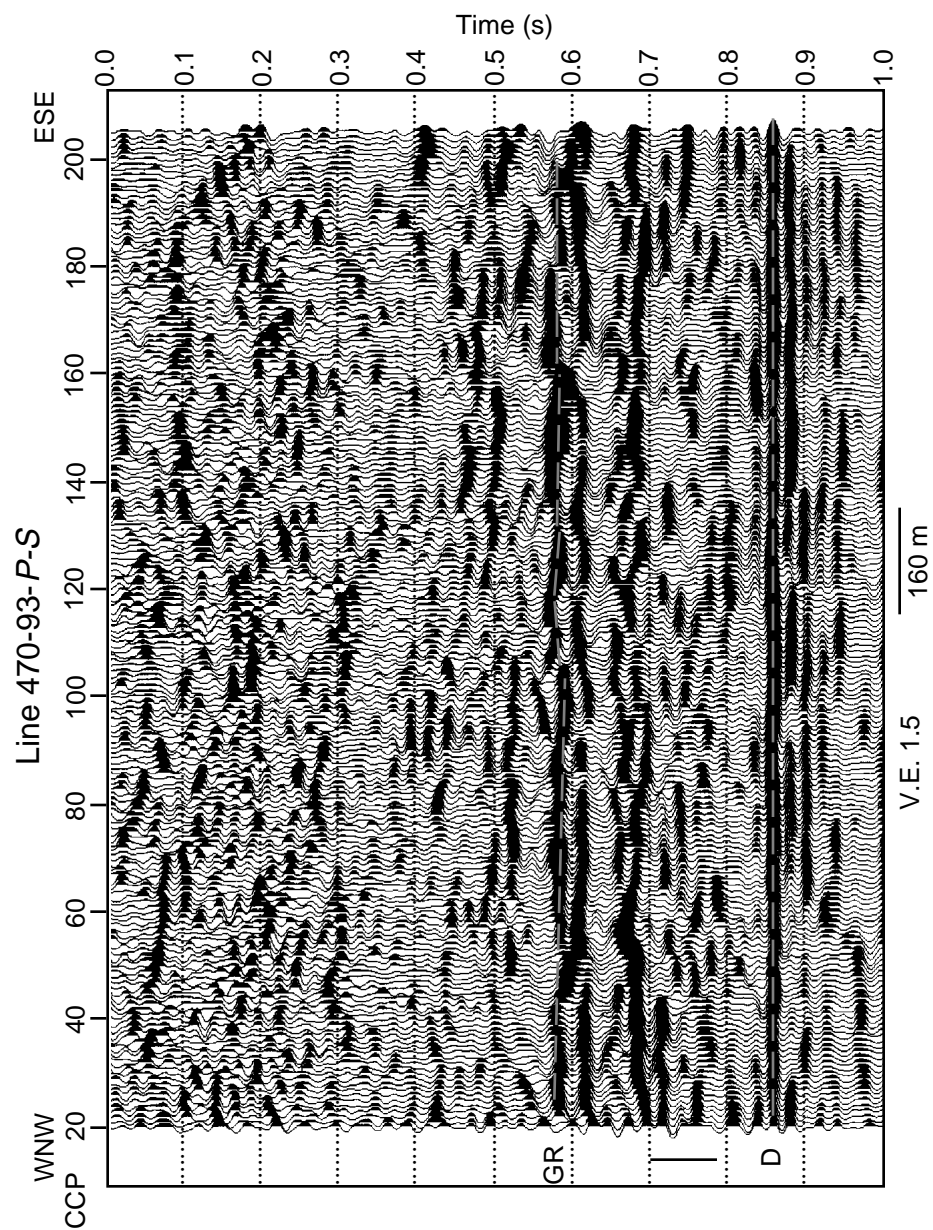


Fig. 5.7 Interpreted line 470-93-P-S. "GR" denotes the top of the Grand Rapids Formation and "D" the top of the Devonian section. The bar at the side of the sections denotes the extent of the reservoir zone.

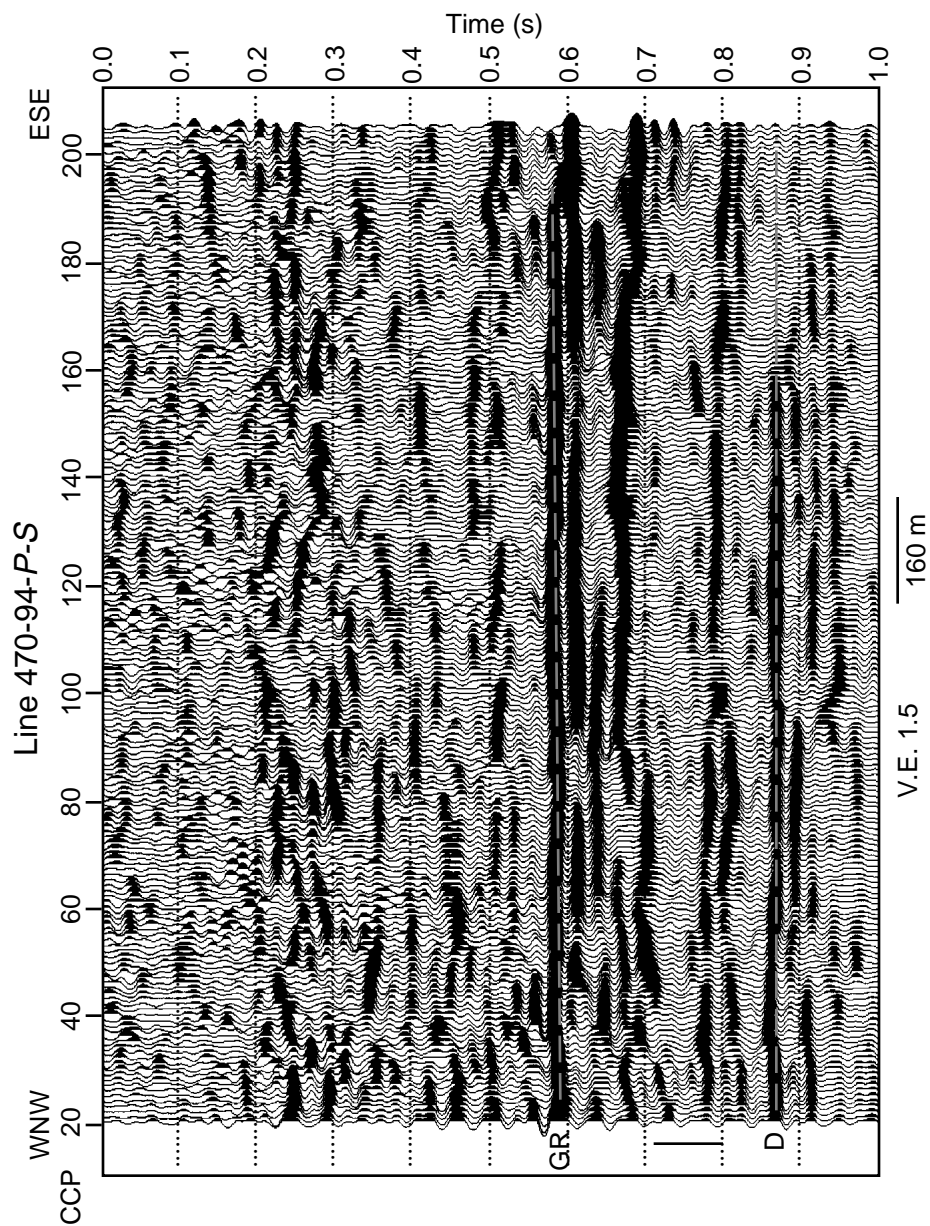


Fig. 5.8 Interpreted line 470-94-P-S. "GR" denotes the top of the Grand Rapids Formation and "D" the top of the Devonian section. The bar at the side of the sections denotes the extent of the reservoir zone.

5.1.4 *P-P* and *P-S* line pairs

Figure 5.9 shows the locations of the pairs of interpreted lines and injection and production wells. The CDP bin locations for *P-P* line 469 correspond closely to the CCP bin locations for *P-S* line 468 and likewise for *P-P* line 471 and *P-S* line 472. Line 470 has coincident CDP and CCP bin locations. Thus the three pairs of line analysed are 470-*P-P* with 470-*P-S*, 469-*P-P* with 468-*P-S* and 471-*P-P* with 472-*P-S*. This map was also used to determine the projected locations of injection wells onto the seismic lines. The lines are each 1800 m long, with a CDP/CCP spacing of 8 m, and are 64 m apart. The wells are 96 m apart.

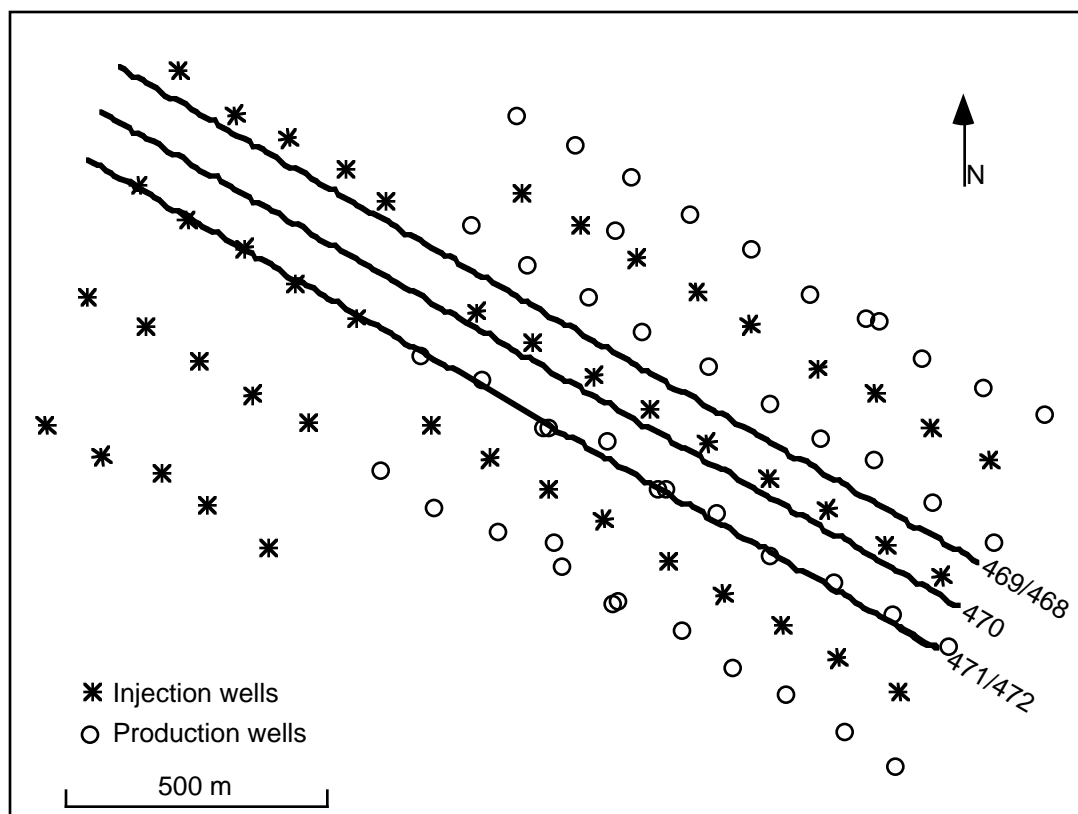


Fig. 5.9 Locations of the injection and production wells and the three pairs of lines analysed: 469 and 468, 470, 471 and 472. The lines are each 1800 m long and the CDP spacing is 8 m. The three lines are 64 m apart.

An example of the tie between the *P-P* and *P-S* sections is presented in Figure 5.10. These enlarged portions of the sections show details of the Grand Rapids to Devonian interval for line 470-*P-P* and 470-*P-S* from the (a) 1993 and (b) 1994 surveys. Each *P-S* section has been displayed at a scale 0.6 times that of the *P-P* section to align corresponding events. This scale value was derived from V_p/V_s of 2.4, which leads to an interval time on the *P-S* section of 1.7 ($=1/0.59$) times that of the *P-P* section. A bar at the side of the sections denotes the reservoir zone and the Grand Rapids and Devonian events are annotated. The *P-P* and *P-S* data have similar wavelengths, which means that the vertical resolution is comparable. Similarities in seismic character are apparent on both pairs of sections. For example, both 1993 lines have higher amplitude events above the reservoir zone than within it and character ties over the zone of interest are quite good on both the 1993 and 1994 sections. The tops of the Grand Rapids Formation and Devonian section correlate well but the top of the Clearwater Formation, at about 0.43 s on the *P-P* data and about 0.7 s on the *P-S* data, is not a clear pick and is not annotated.

In Figures 5.11, 5.12, 5.13, 5.14, 5.15 and 5.16 are displayed the zones of interest for each pair of interpreted lines from both surveys. AGC has been applied to visually enhance the plots and the pairs of data are displayed at time scales which convert to approximately the same depth scale. Annotated are the Grand Rapids and Devonian events and the reservoir zone is indicated by a bar at the side of the sections. Underneath each section is a smoothed plot of the fold at the time of the Devonian event. On all the *P-P* lines the Devonian reflection is a strong, continuous peak and high amplitude, continuous events are present within the Grand Rapids Formation, particularly at about 0.4 s over the eastern end of the lines. *P-S* data quality varies and is best on line 470 (Figures 5.13 and 5.14). Poorest continuity of events is seen on line 472, in both the 1993 and 1994 surveys (Figures 5.15 and 5.16).

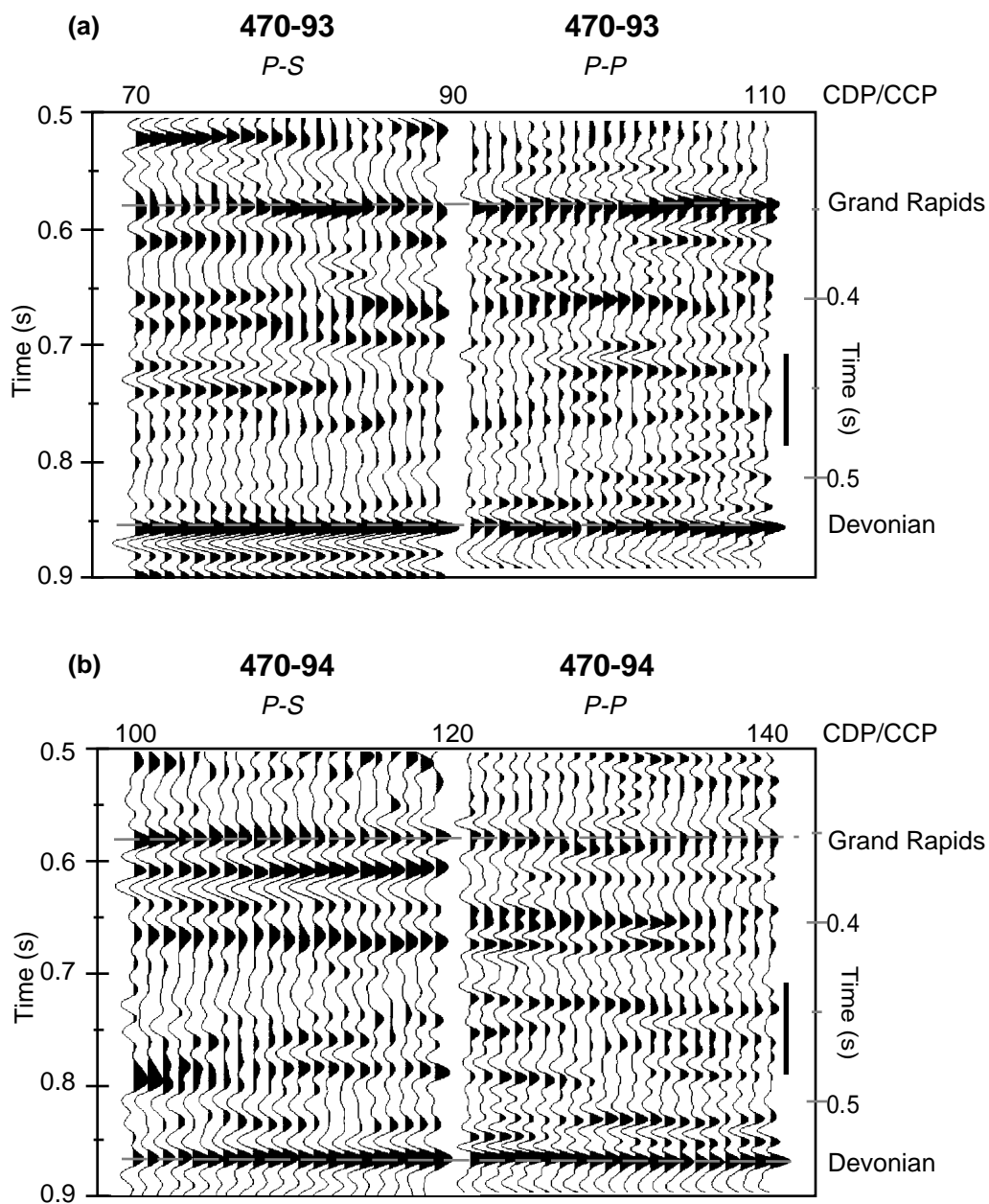


Fig. 5.10 Example of the ties between the *P-P* data and *P-S* data for line 470 from the (a) 1993 and (b) 1994 surveys. The Grand Rapids and Devonian reflections are annotated and the reservoir zone is indicated by a bar at the side of the *P-P* sections.

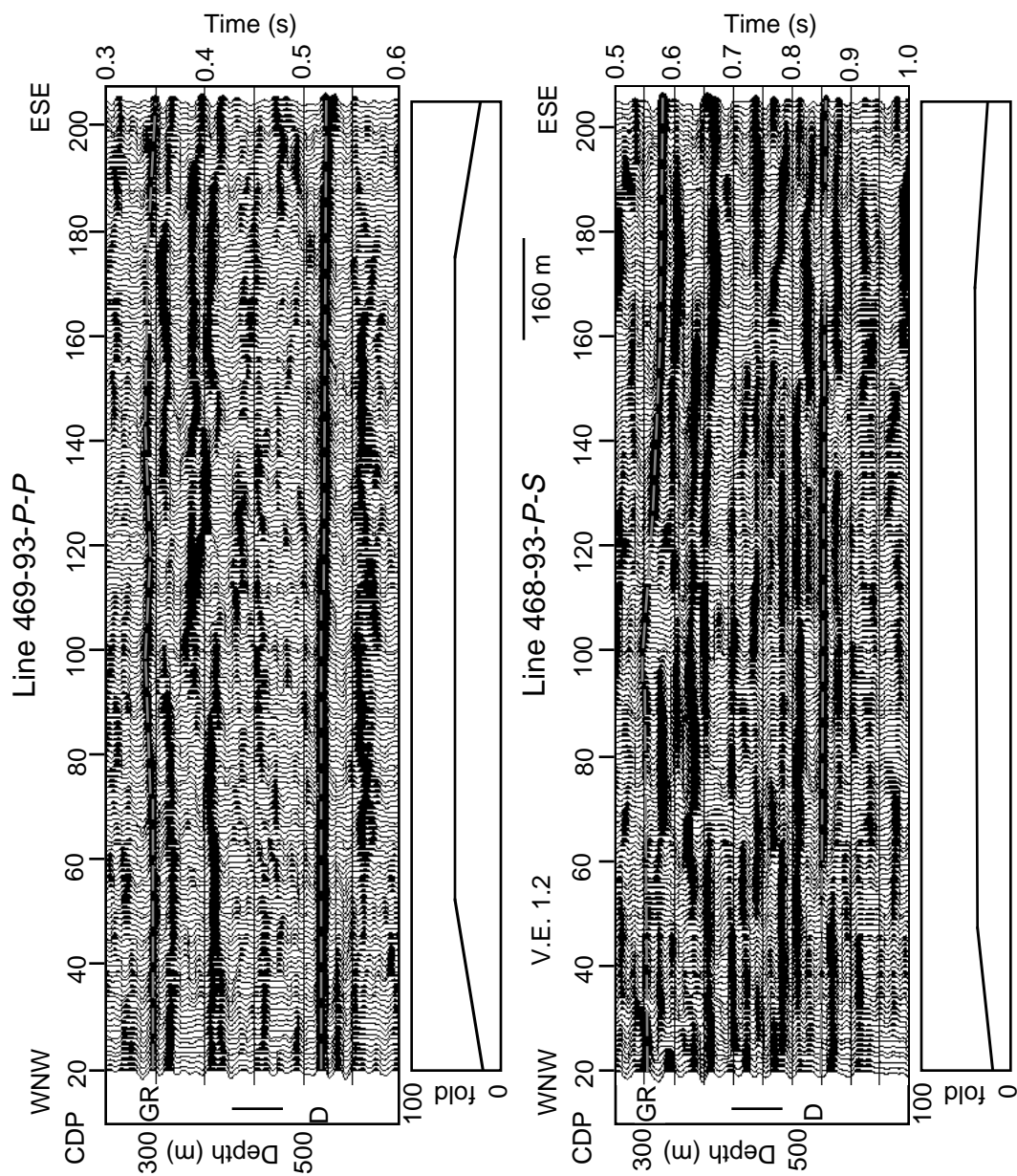


Fig. 5.11 Lines 469-P-P and 468-P-S from the 1993 survey. The zone of interest, covering the Grand Rapids (GR) to Devonian (D) interval is shown. The sections are plotted at the same depth scale. A smoothed plot of the stack fold is displayed under each line.

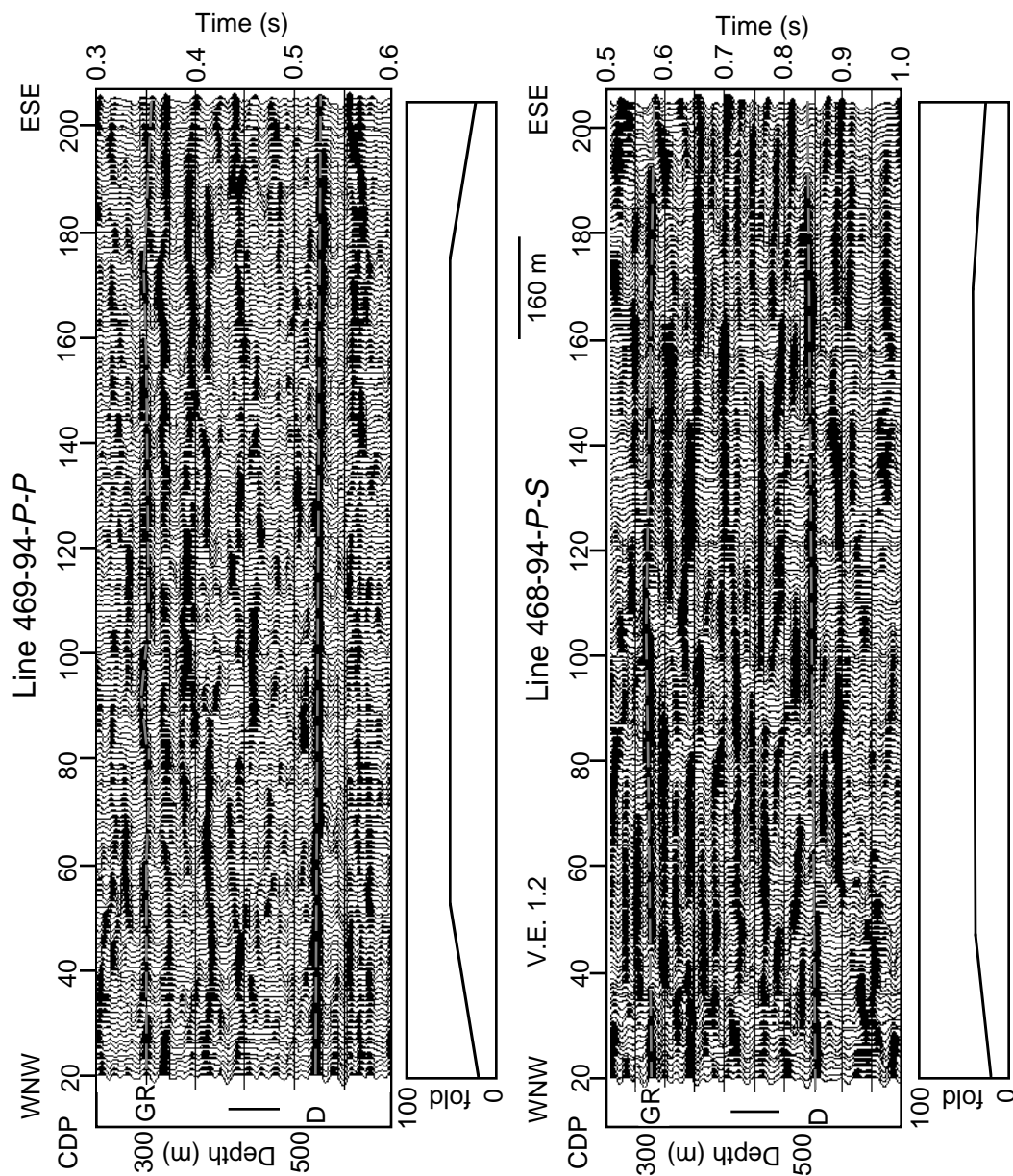


Fig. 5.12 Lines 469-*P-P* and 468-*P-S* from the 1994 survey. The zone of interest, covering the Grand Rapids (GR) to Devonian (D) interval is shown. The sections are plotted at the same depth scale. A smoothed plot of the stack fold is displayed under each line.

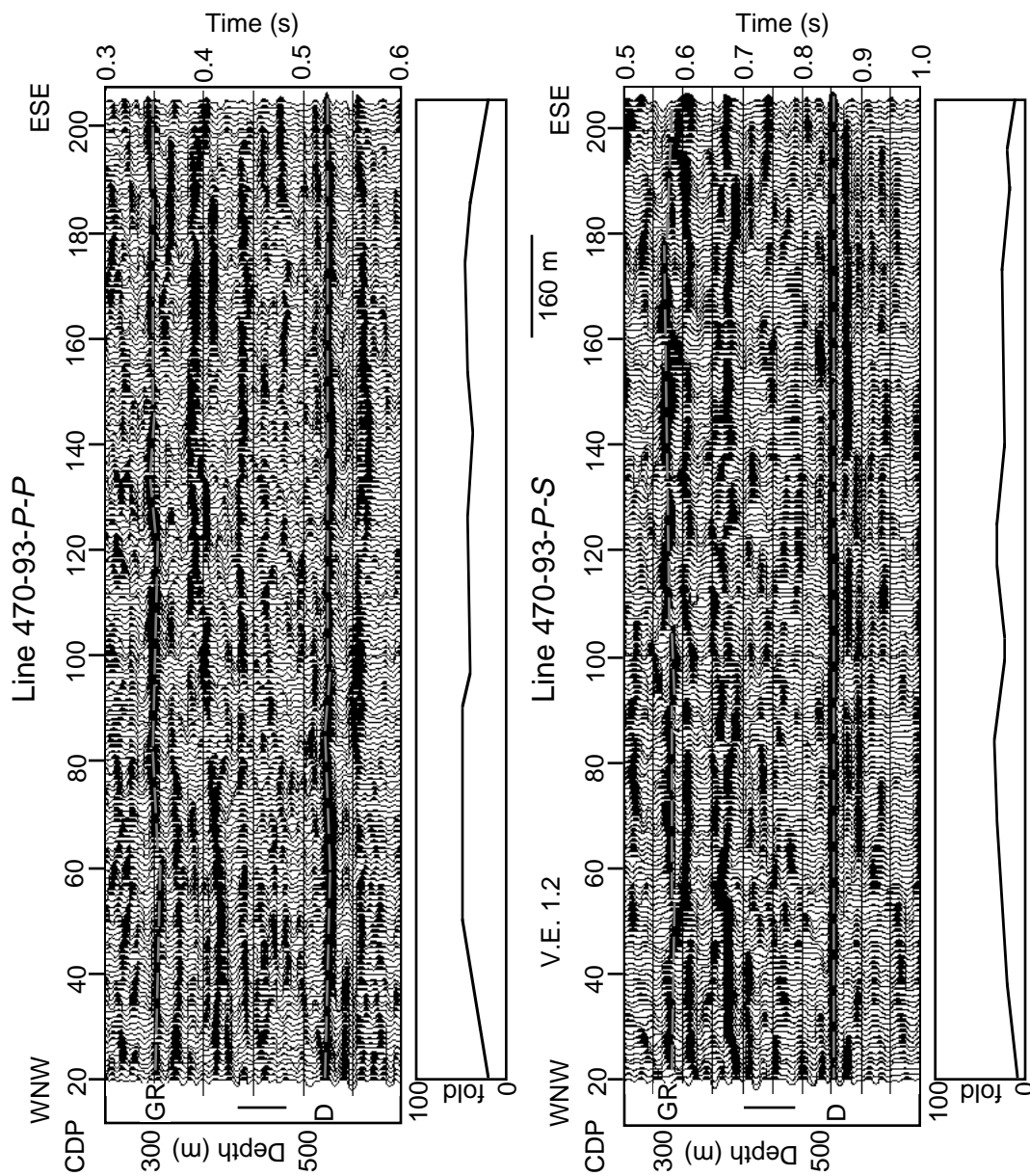


Fig. 5.13 Lines 470-P-P and 470-P-S from the 1993 survey. The zone of interest, covering the Grand Rapids (GR) to Devonian (D) interval is shown. The sections are plotted at the same depth scale. A smoothed plot of the stack fold is displayed under each line.

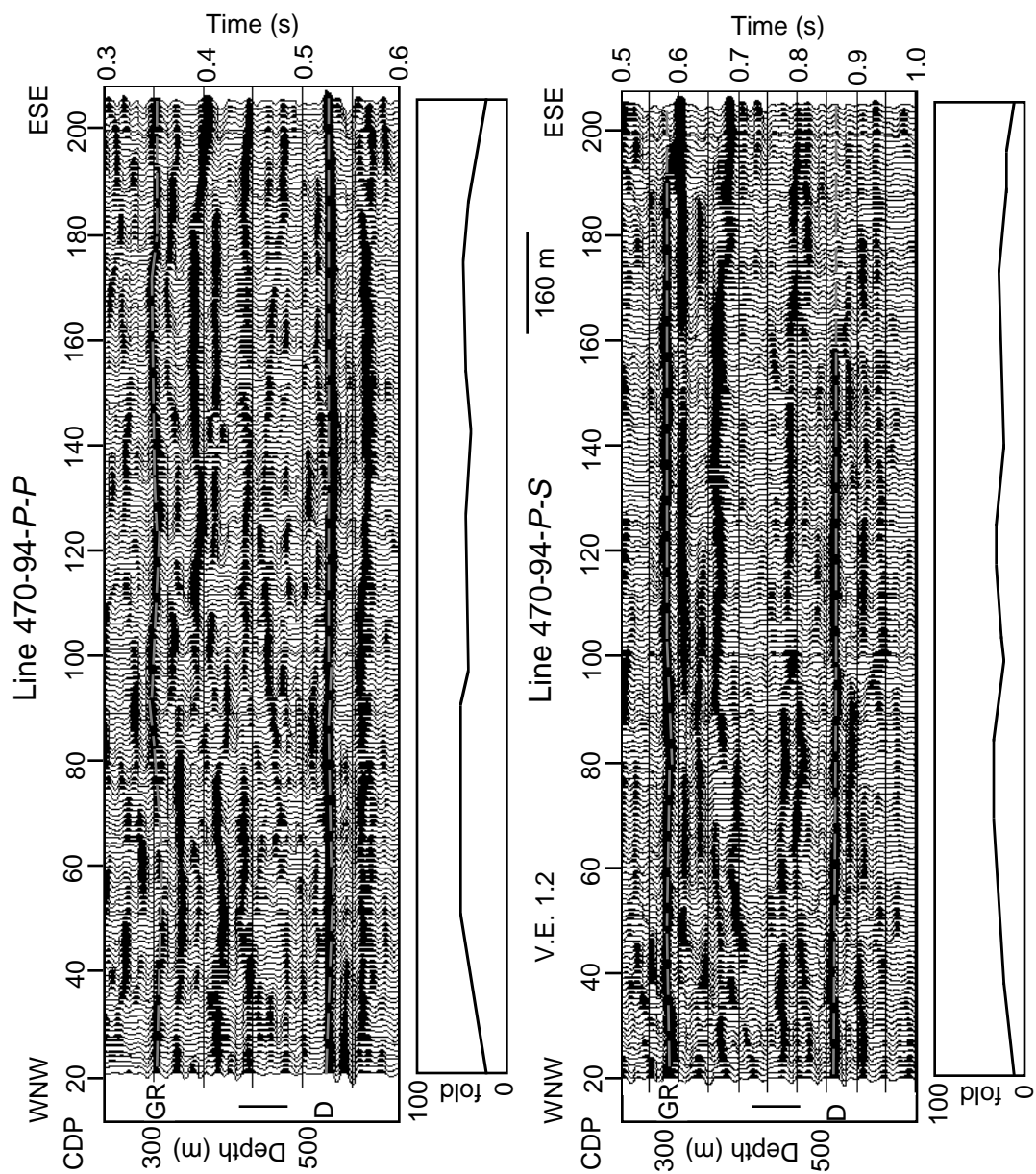


Fig. 5.14 Lines 470-P-P and 470-P-S from the 1994 survey. The zone of interest, covering the Grand Rapids (GR) to Devonian (D) interval is shown. The sections are plotted at the same depth scale. A smoothed plot of the stack fold is displayed under each line.

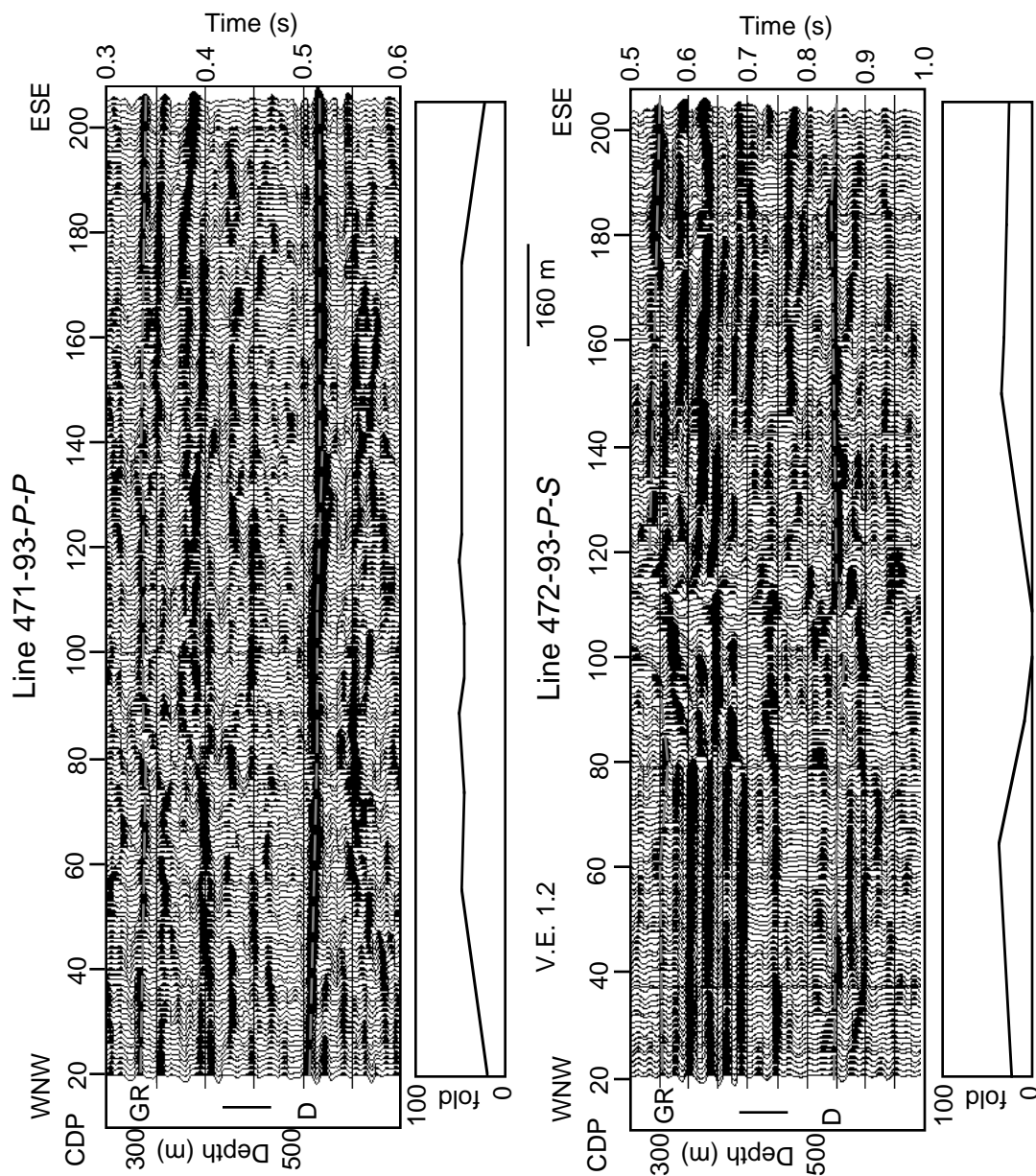


Fig. 5.15 Lines 471-P-P and 472-P-S from the 1993 survey. The zone of interest, covering the Grand Rapids (GR) to Devonian (D) interval is shown. The sections are plotted at the same depth scale. A smoothed plot of the stack fold is displayed under each line.

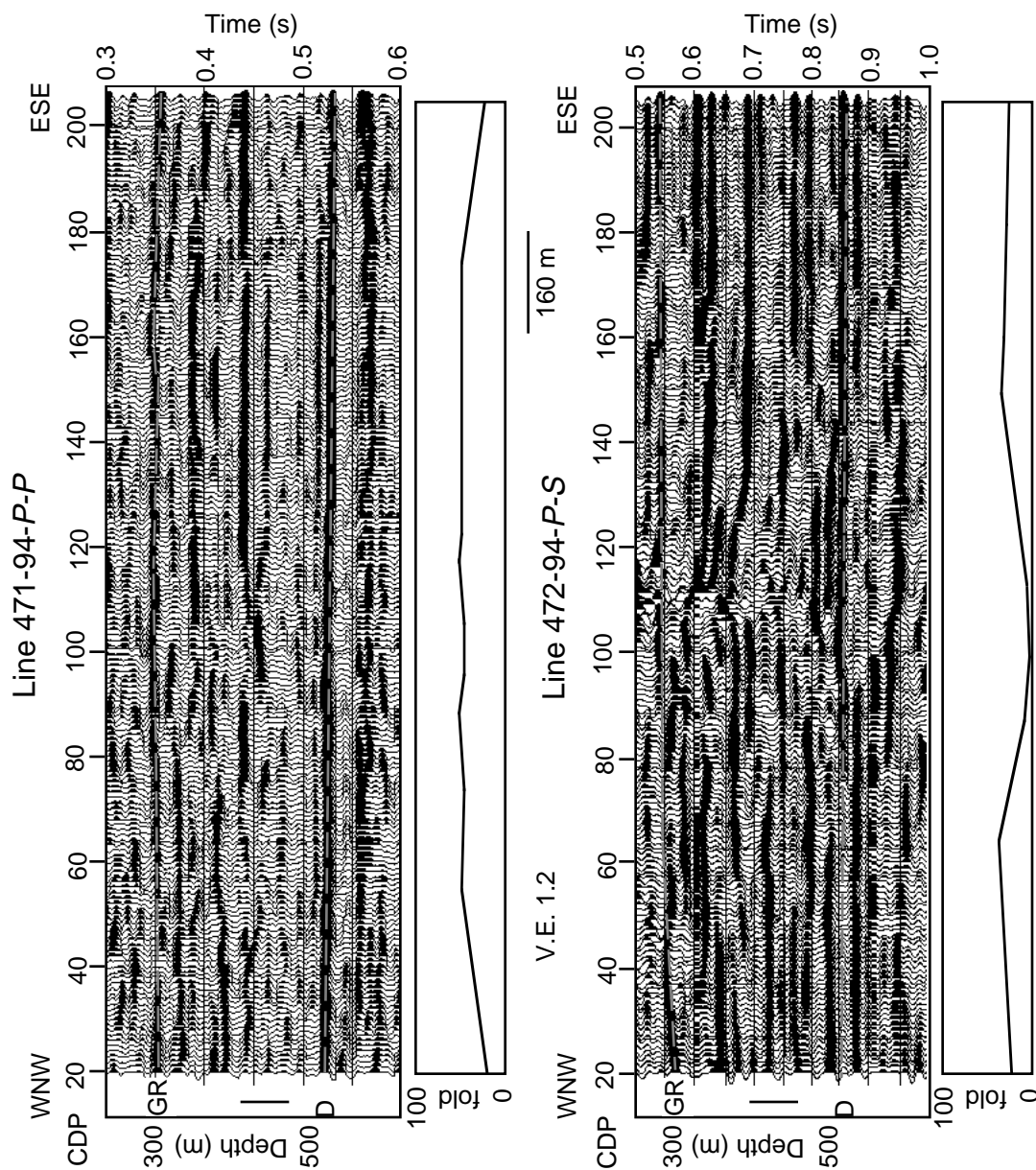


Fig. 5.16 Lines 471-P-P and 472-P-S from the 1994 survey. The zone of interest, covering the Grand Rapids (GR) to Devonian (D) interval is shown. The sections are plotted at the same depth scale. A smoothed plot of the stack fold is displayed under each line.

The Devonian event is not well imaged on either of these lines and it can be seen how the extremely low fold in the centre of line 472, caused by irregular source/receiver geometry, editing of bad shots and limited offsets, degrades the stacked section. The Grand Rapids reflection is correlatable on all the sections but is weak on line 472-*P-S* for both the 1993 and 1994 surveys (Figures 5.15 and 5.16). The arrival times of the Grand Rapids and Devonian reflections on the 472-*P-S* lines were extrapolated from the arrival times on the other *P-S* sections. On none of these sections can reliable events be picked closer to the reservoir zone than the Grand Rapids and Devonian reflections.

5.2 *V_p/V_s* analysis

5.2.1 Measured *V_p/V_s*

V_p/V_s values over an interval are calculated from the interval transit times measured on corresponding *P-P* and *P-S* sections by using the following formula:

$$V_p/V_s = (2\Delta t_s/\Delta t_p) - 1 \quad (5.1)$$

where Δt_s and Δt_p denote the interval transit times as measured on the *P-P* and *P-S* sections respectively.

For equation 5.1 to be valid, it is critical that the depth intervals corresponding to these interval transit times are identical on both sections (Iverson et al., 1989). Not all interfaces produce good reflections on both the *P-P* and *P-S* sections, so care must be taken to select appropriate events. It is also important to select interfaces as close to the boundaries of the zone of interest as possible so that changes in lithology or porosity outside this zone do not influence the measured *V_p/V_s*. On the Cold Lake *P-P* and *P-S* data, good reflections are observed at the tops of the Grand Rapids Formation and the Devonian section with no strong, continuous, correlatable reflectors between these horizons. An attempt was made to pick horizons closer to the reservoir than the Grand Rapids and Devonian but, as expected, no reliable results could be obtained.

The three pairs of *P-P* and *P-S* sections were loaded onto a workstation and interpreted using SeisX software. The Grand Rapids and Devonian horizons were autopicked on each line after identification of these events on paper sections. On the *P-P* sections little editing of the autopicks was necessary whereas on the *P-S* sections some hand-picking was done over areas with noisy correlations.

Isochron values were calculated for the Grand Rapids to Devonian interval and V_p/V_s values were determined using equation (5.1). Lithology through the Grand Rapids to Devonian interval is known to be fairly constant over the AABBW pads so changes in V_p/V_s are expected to reflect changes in the reservoir zone only.

Figures 5.17, 5.18, 5.19 and 5.20 display V_p/V_s and the locations of the injection wells for each of the interpreted line pairs 470-*P-P*/470-*P-S*, 469-*P-P*/468-*P-S*, and 471-*P-P*/472-*P-S*, respectively, from the 1993 and 1994 data. In addition, Figures 5.17 and 5.18 show the interval transit times as measured from the *P-P* and *P-S* data for line 470. These plots demonstrate that V_p alone is not sufficient for mapping the heated reservoir but that V_s is also necessary. At the time of the 1993 seismic data acquisition the wells along line 469 had finished steaming while those along lines 470 and 471 were in the middle of the steaming cycle. The V_p/V_s values have had a five-point weighted median filter applied to smooth them a little. Values calculated along line 470 are considered to be the most reliable since the stacked data were the highest quality and picks the most dependable.

Also shown in each figure are dashed lines representing the margin of error in V_p/V_s caused by picking inaccuracies in the seismic data. It was assumed that for data sampled every 1 ms, the picking error along a horizon may be ± 0.5 ms. The standard error, α , of any function $f(m_1, m_2, \dots, m_n)$ is calculated as

$$\alpha^2 = \left(\frac{\partial f}{\partial m_1}\right)^2 \cdot \alpha_1^2 + \left(\frac{\partial f}{\partial m_2}\right)^2 \cdot \alpha_2^2 + \dots + \left(\frac{\partial f}{\partial m_n}\right)^2 \cdot \alpha_n^2 \quad (5.2)$$

where α_i is the standard error of the i th variable (Topping, 1957). The standard error in each picked event is ± 0.5 ms, thus the standard error in each isochron, $\Delta t = t_1 - t_2$, where t_i represents the picked time of the i th event, is calculated:

$$\alpha^2 = \left(\frac{\partial t}{\partial t_1}\right)^2 \cdot \alpha_1^2 + \left(\frac{\partial t}{\partial t_2}\right)^2 \cdot \alpha_2^2$$

$$\alpha^2 = \alpha_1^2 + \alpha_2^2$$

$$\alpha^2 = 0.5$$

$$\alpha = 0.707$$

Therefore, the standard error in $V_p/V_s = R = (2\Delta t_s/\Delta t_p) - 1$ can be calculated (assuming Δt_p and Δt_s to be independent variables):

$$\alpha^2 = \left(\frac{\partial R}{\partial \Delta t_p}\right)^2 \cdot \alpha_p^2 + \left(\frac{\partial R}{\partial \Delta t_s}\right)^2 \cdot \alpha_s^2$$

$$\alpha^2 = (-2\Delta t_s / \Delta t_p^2)^2 \cdot (.707)^2 + (2 / \Delta t_p)^2 \cdot (.707)^2$$

$$\alpha^2 = \frac{2}{\Delta t_p^2} (1 + \Delta t_s^2 / \Delta t_p^2) \quad (5.3)$$

where α_p and α_s are the standard errors in Δt_p and Δt_s , respectively.

The standard error, unique for every value of V_p/V_s along all six lines, has a mean value of 0.02. The two dashed lines in each figure show the values of V_p/V_s obtained by adding or subtracting the individual standard error in V_p/V_s at each data point, calculated using equation 5.3. The true value of V_p/V_s lies between these limits.

In general there is a good correlation between the locations of the injection wells and low V_p/V_s values, which should be expected because the compressional-wave velocity of the formation decreases considerably during steam injection. Along line 470-93 (Figure 5.17), the average value of V_p/V_s away from the injection wells is 2.19 while over the area of the wells the average value is 2.11. The value of V_p/V_s at each injection

well location varies but in each case the value is less than 2.15. Over line 470-94 (Figure 5.18), V_p/V_s averages 2.20, both near to and away from the wells.

V_p/V_s values over the area of steam injection wells are higher in 1994 than in 1993. It is seen that these V_p/V_s values appear to be influenced by a decrease in V_s at the well locations in 1994, rather than an increase in compressional-wave velocity. Some V_p/V_s anomalies are present on the 1994 data (Figure 5.18), particularly over CDPs 130 to 170, and are interpreted to be caused by low velocity gas-saturated zones in 1994.

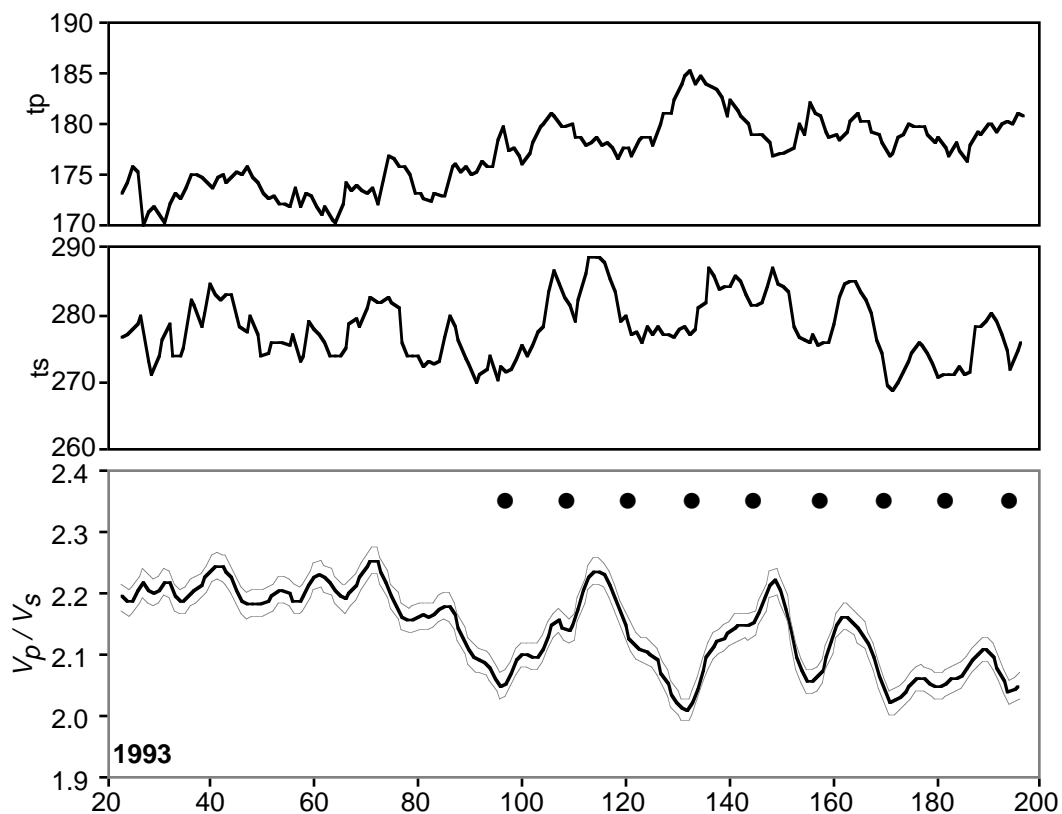


Fig. 5.17 Measured values of t_p , t_s and V_p/V_s from line 470-*P-P* and 470-*P-S* for the 1993 data. The dashed lines indicate the standard error in V_p/V_s and the black dots represent the projected locations of the nearest steam injection wells.

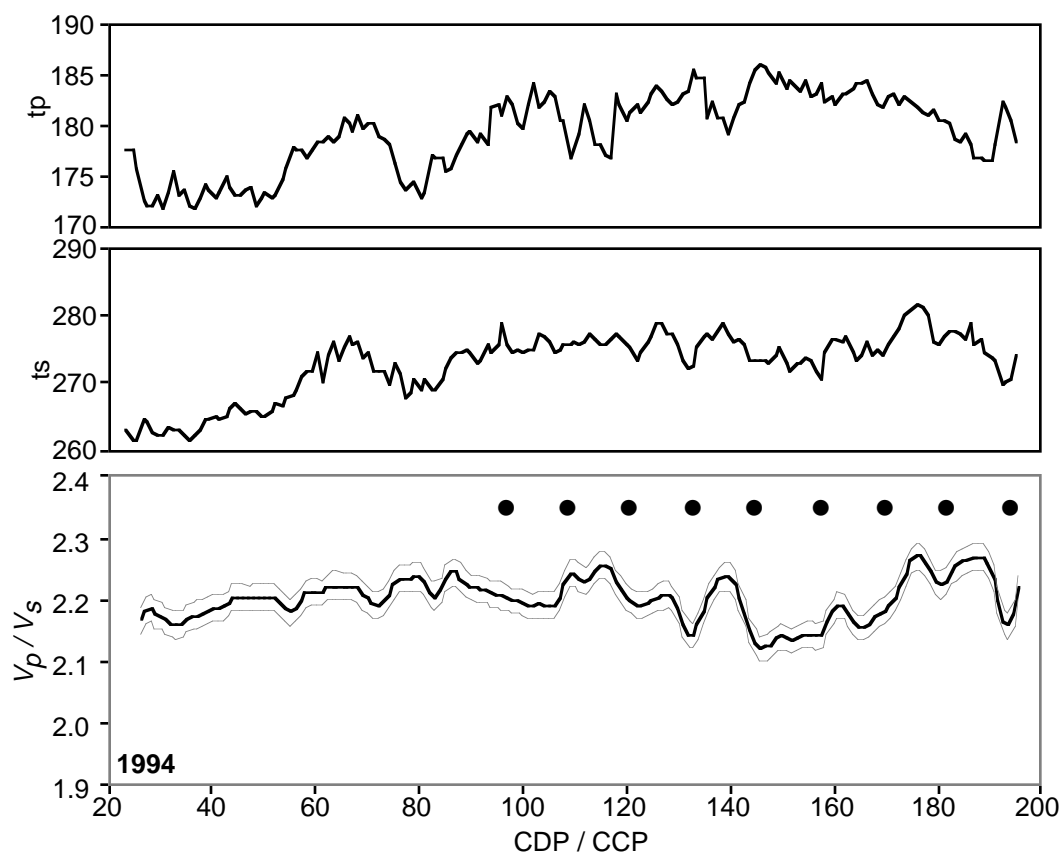


Fig. 5.18 Measured values of t_p , t_s and V_p/V_s from line 470-P-P and 470-P-S for the 1994 data. The dashed lines indicate the standard error in V_p/V_s and the black dots represent the projected locations of the nearest steam injection wells.

Along line 469/468 (Figure 5.19), V_p/V_s values are generally higher in 1994 than in 1993 and on the 1993 survey are lower over the well locations than away from them. V_p/V_s values lower than 2.2 (the rms value observed over the cold reservoir in Figures 5.17 and 5.18) are seen over the right side of the line in both 1993 and 1994. They may be an indication of steam coming from the line of injection wells which are about 40 m away from this part of the line.

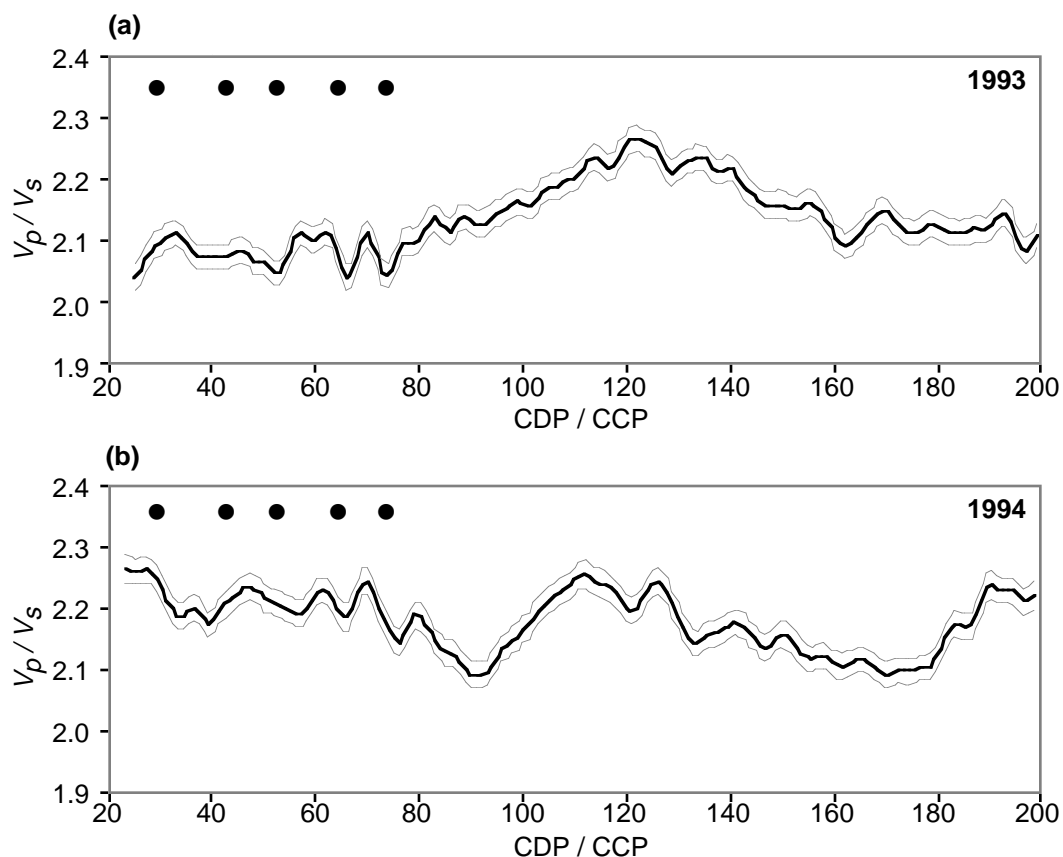


Fig. 5.19 Measured values of V_p/V_s from line 469-*P-P* and 468-*P-S* for the (a) 1993 and (b) 1994 data. The dashed lines indicate the standard error in V_p/V_s and the black dots represent the projected locations of the nearest steam injection wells.

Over CCPs 97-118 on line 472 from the 1993 survey (Figure 5.20a) data are missing where the *P-S* section had low fold at the Grand Rapids because of irregular line geometry, the removal of poor data and the limited offsets included in the stacked section. The values along line 472 are considered to be less reliable than along the other two lines because of the poor imaging of the Grand Rapids and Devonian events, as seen on Figures 5.16 and 5.17. Low V_p/V_s values are seen over the well locations on both the 1993 and 1994 data but seem to be anomalously low on the 1994 data. Picking of alternative horizons for the Grand Rapids or Devonian events on the 1994 data did not result in values within the expected range.

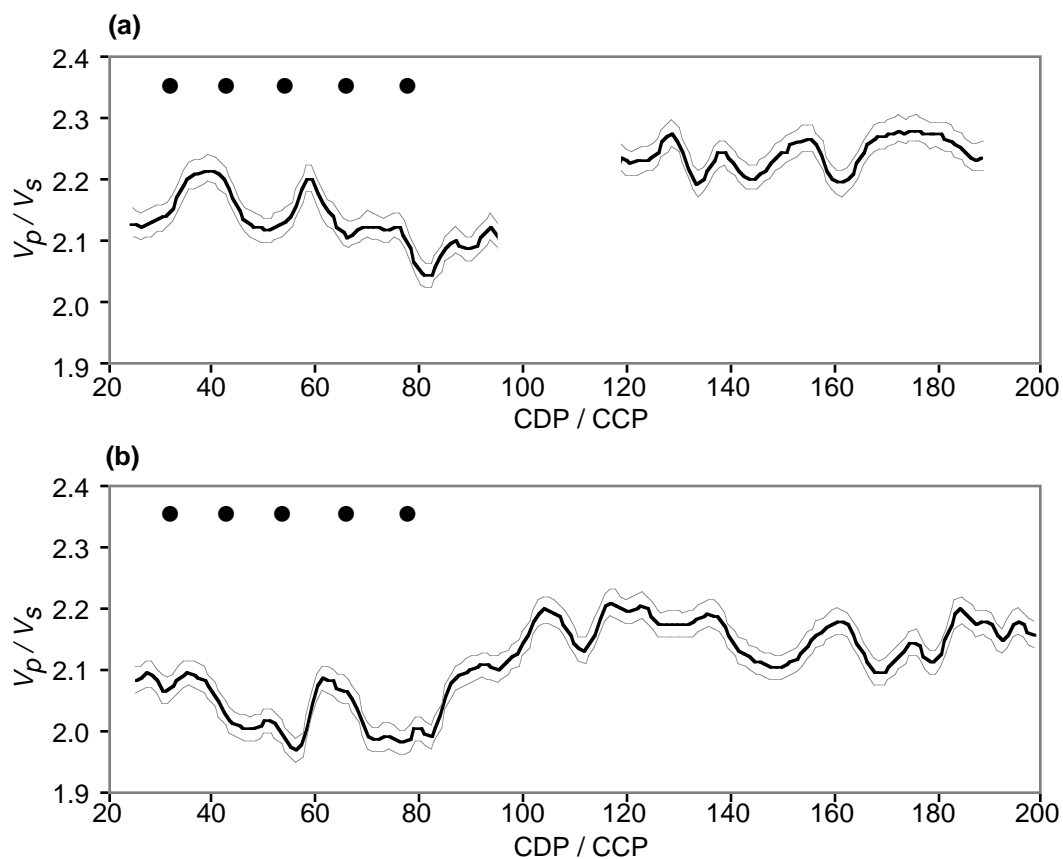


Fig. 5.20 Measured values of V_p/V_s from line 471-*P-P* and 472-*P-S* for the (a) 1993 and (b) 1994 data. The dashed lines indicate the standard error in V_p/V_s and the black dots represent the projected locations of the nearest steam injection wells.

Figure 5.21 shows the ratio of V_p/V_s (1993) to V_p/V_s (1994) as measured along line 470. Values below unity indicate a lower V_p/V_s in 1993 (during the steaming cycle) than in 1994 (production) and are seen over the part of the line with the injection wells. In general, the lowest values correspond to the well locations and reflect the zones of greatest *P*-wave interval velocity change from 1993 to 1994. A ratio of unity over the unsteamed part of the line shows that conditions here were more constant from 1993 to 1994 and that the reservoir is still relatively cold.

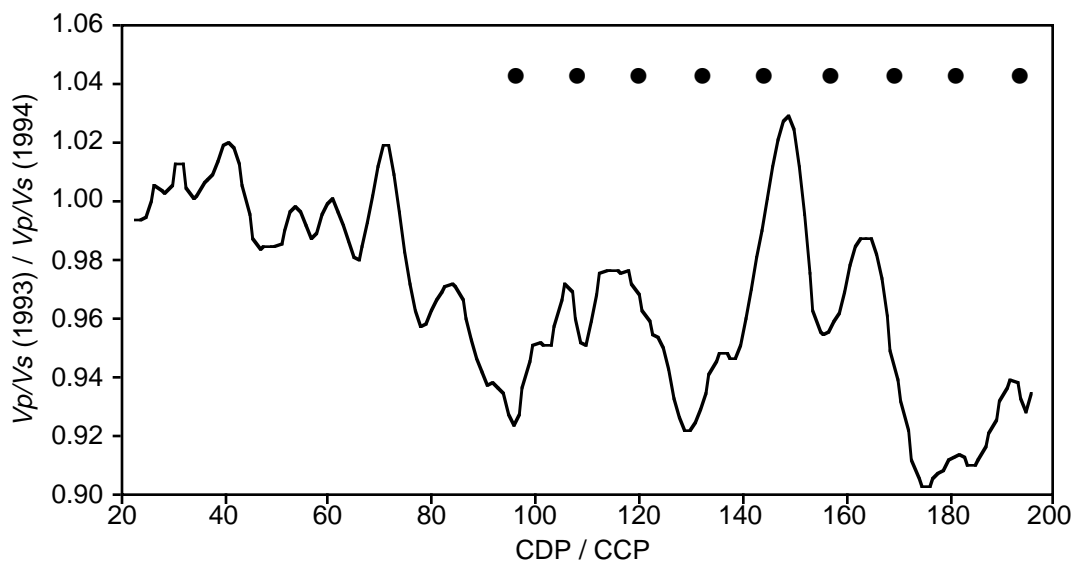


Fig. 5.21 Ratio of V_p/V_s from the 1993 survey to V_p/V_s from the 1994 survey along line 470. Values below unity indicate a lower V_p/V_s in 1993 than in 1994.

The values of V_p/V_s obtained along the three lines were contoured to give the plots shown in Figure 5.22. SeisX software was used to do the contouring, with a grid interval of 32 m x 32 m. Injection wells are denoted by black spots and the locations of the lines are shown. In Figure 5.22a, low V_p/V_s values trend along line 470 near the line of injection wells and are also found to the north of the northern end of line 469/468. The low V_p/V_s values over line 471/472 (Figure 5.20b) are reflected by the tight band of contours between lines 470 and 471 on Figure 5.22b.

To investigate the dependence of V_p/V_s on V_p , values of V_p/V_s against one-way P - P interval traveltime ($\Delta t_p/2$) along line 470 are plotted in Figures 5.23a (1993 data) and 5.23b (1994 data). Crosses represent data from CDPs lying away from the injection wells and circles represent data from CDPs lying near the injection wells. There is some overlap between the two groups of data points in 1994 but in 1993 they are separate.

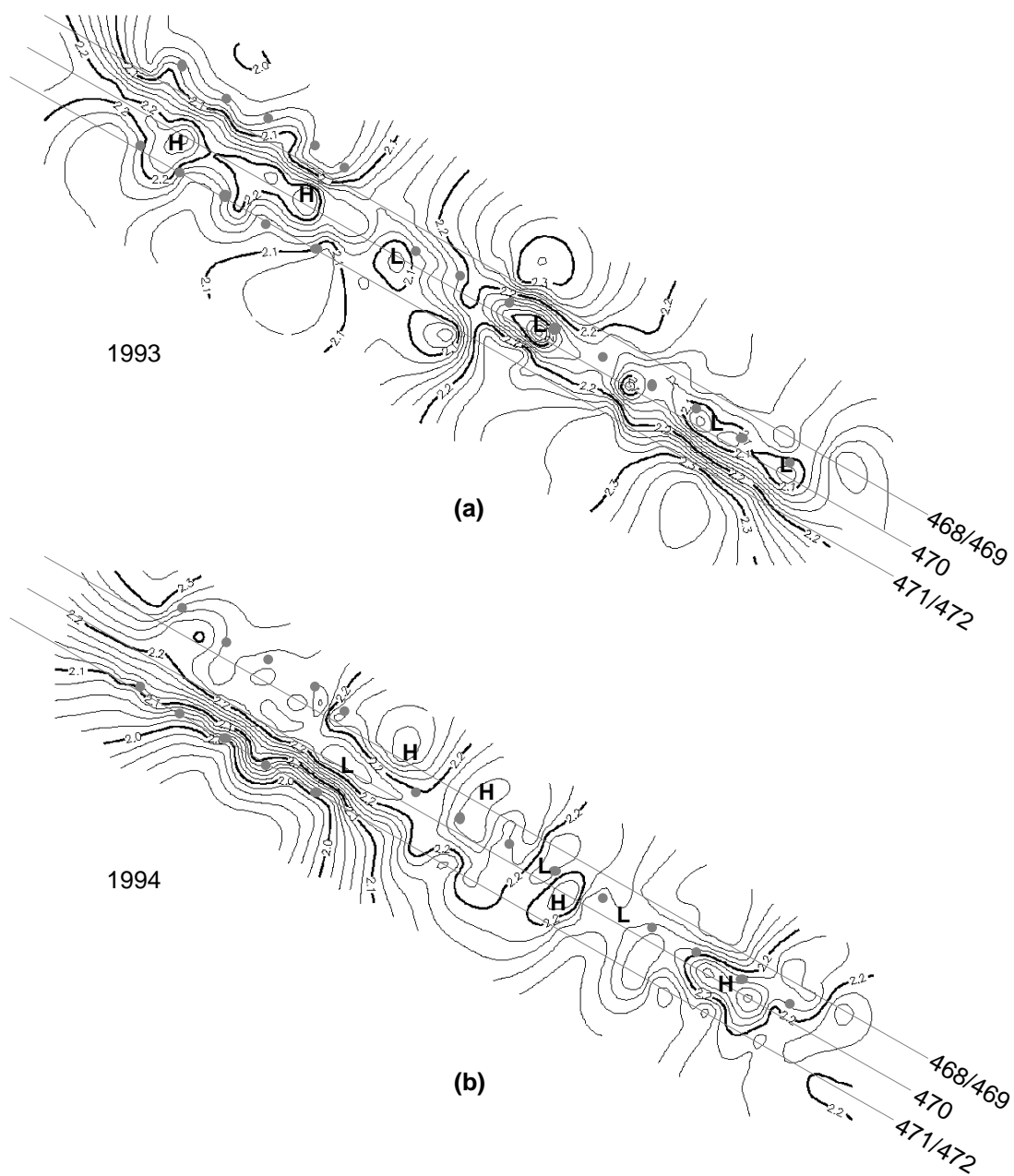


Fig. 5.22 Contoured V_p/V_s from the three pairs of seismic lines analysed for (a) the 1993 data and (b) the 1994 data. "H" denotes high values of V_p/V_s and "L" denotes low values.

In 1993, all but one of the interval traveltimes greater than 88 ms are associated with data points near the injection wells. Likewise, all but one of the traveltimes smaller than 88 ms are associated with data points away from the wells. In 1994 there is a little more overlap in the two groups of data points. This is interpreted to be the result of less laterally contrasting reservoir conditions.

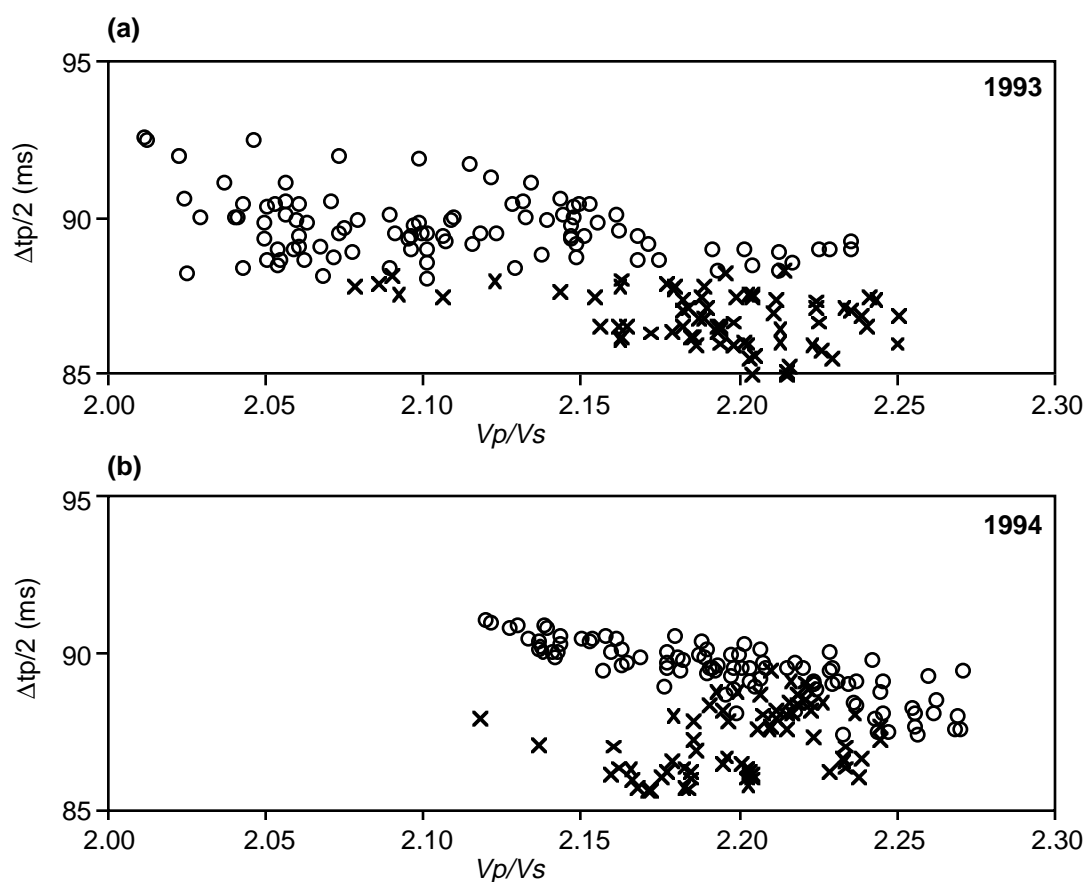


Fig. 5.23 Vp/Vs plotted against P - P one-way interval traveltime along line 470 in (a) 1993 and (b) 1994. Crosses represent data from CDPs that lie away from the injection well locations and circles represent data from CDPs near to the injection well locations.

As expected, lower interval traveltimes correlate to higher Vp/Vs and vice versa. Higher interval traveltimes appear in the 1993 data because of the presence of low

velocity zones and the range of V_p/V_s is greater in 1993 than in 1994, signifying that reservoir conditions varied more in 1993. During steaming there is a greater lateral contrast in V_p than during the production cycle, when reservoir conditions stabilise a little as the high temperatures and fluid pressures present at the injection wells decrease.

Since V_p/V_s depends also on V_s , the relationship between V_p/V_s and Δt_p is not strictly linear. To examine the dependence of V_p/V_s on V_s , the P -wave component of interval traveltimes has to be subtracted from Δt_s to leave the S -wave component. Plots of V_p/V_s against $\Delta t_s - \Delta t_p/2$ (Figure 5.24) demonstrate the dependence of V_p/V_s on V_s . The trend in Figures 5.24a and 5.24b is for V_p/V_s to decrease with decreasing $\Delta t_s - \Delta t_p/2$, which implies that the shear-wave velocity increases as V_p/V_s decreases.

The mean and standard deviations of the values plotted in Figures 5.23 and 5.24 are listed in Table 5.2. These values show that average V_p is lowest near the wells in 1993 and highest away from the wells in 1993. In 1994, V_p near the wells is slightly higher than in 1993 and away from the wells is slightly lower than in 1993. The presence of a small amount of gas during the production cycle could be the cause of the low V_p observed at this time. The slightly lower average value for $\Delta t_s - \Delta t_p/2$ over data points near the injection wells in 1993 compared to those points away from the wells signifies that V_s is slightly higher near the wells during the steaming cycle than away from the wells, as was predicted by theory (Eastwood, 1993). Near the wells in 1994, $\Delta t_s - \Delta t_p/2$ is higher, implying a lowered V_s . The cause of this lowered V_s during production is not well understood. Changes in fluid density are known to occur but the effect of the steam injection process on the shear modulus is not known.

It is clear from this analysis that measurement of Δt_p alone is not sufficient for the determination of V_p/V_s as V_p/V_s is also dependent on V_s , which is not constant through time.

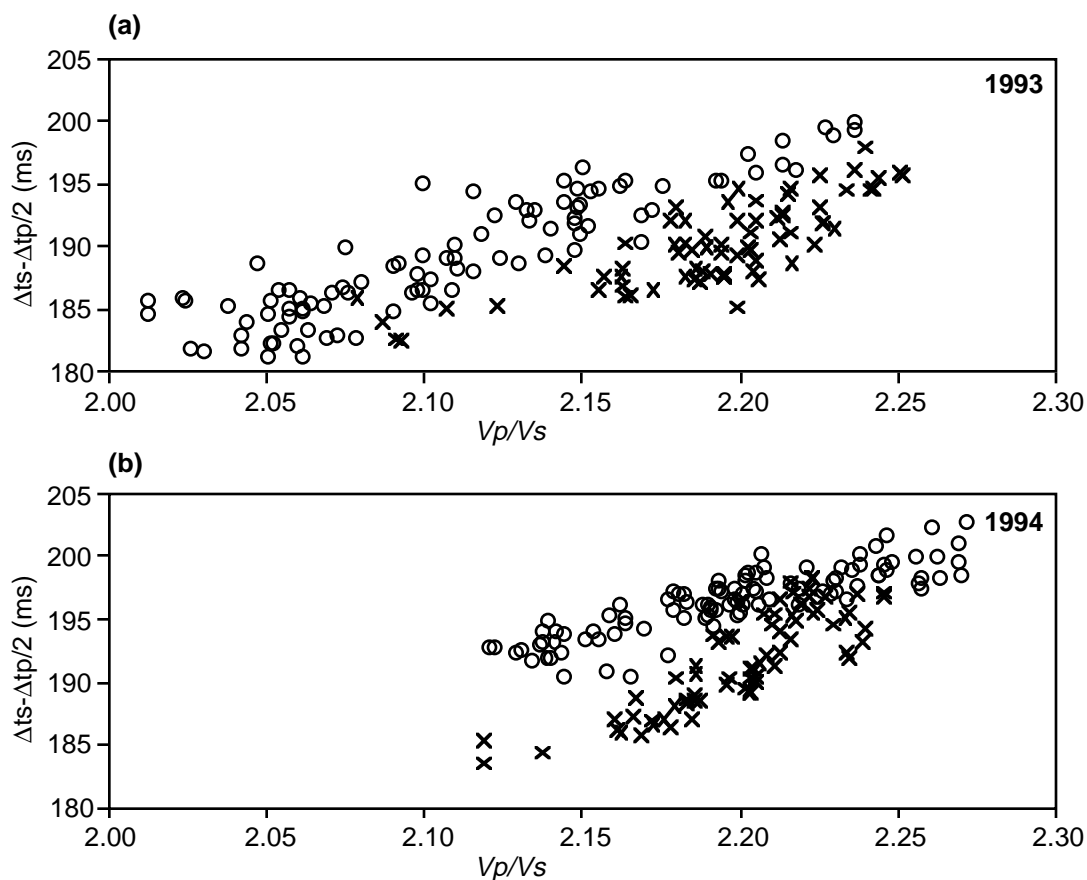


Fig. 5.24 V_p/V_s plotted against P - S upcoming interval traveltime along line 470 in (a) 1993 and (b) 1994. Crosses represent data from CDPs that lie away from the injection well locations and circles represent data from CDPs near to the injection well locations.

Table 5.2 Mean and standard deviations of data points plotted in Figures 5.23 and 5.24.

Data points	$\Delta t_p/2$		$\Delta t_s - \Delta t_p/2$		V_p/V_s	
	mean	std. dev.	mean	std. dev.	mean	std. dev.
Away from wells 1993	86.8	0.8	190.1	3.4	2.19	0.04
Near wells 1993	89.7	1.0	189.0	5.1	2.11	0.06
Away from wells 1994	87.2	1.1	191.8	3.9	2.20	0.03
Near wells 1994	89.4	0.9	196.6	2.8	2.20	0.04

5.2.2 V_p/V_s prediction

Having measured V_p/V_s from the seismic data, it is useful to compare the values with those predicted through theoretical computations. Confidence of the validity of the measured V_p/V_s will increase if the measured and predicted values are of the same order. Theoretical V_p/V_s values over the Grand Rapids to Devonian interval were calculated using the parameters listed in Table 5.3. P -wave velocities for the Grand Rapids, cold Clearwater and McMurray formations were obtained from sonic logs. S -wave velocity in the Grand Rapids Formation was taken from the dipole log run in well BB13a. The theoretical S -wave velocities in the cold Clearwater Formation and P - and S -wave velocities in the steamed Clearwater Formation are taken from Eastwood (1993). The theoretical values of V_s are calculated by assuming only temperature-dependent changes in bitumen density, whereas V_s in reality also depends on effective pressure and porosity (Gregory, 1976). During steam injection, dilation of the reservoir causes local increases in porosity while at the same time effective pressure is decreased, which should both result in a decrease in V_s . The overall effect of increased temperature against decreased effective pressure and increased porosity on V_s is uncertain, however V_p/V_s analysis of lines 470-93 and 470-94 implies higher V_s near the wells during the steaming cycle than away from the wells, where the reservoir is relatively cold. Physical modelling experiments on these bitumen-saturated, unconsolidated Clearwater sands under the different reservoir conditions would be beneficial. The shear-wave velocity of 1180 m/s for the cold Clearwater Formation is higher than that velocity observed on the shear dipole sonic log in Figure 5.1, which is about 1000 m/s. This value was selected because it was the theoretical value predicted by Eastwood (1993) and matched better an observed V_s of 1200 m/s (Macrides and Kanasewich, 1987), computed values of 1148-1217 m/s for different water, bitumen and steam saturations (Tsingas and Kanasewich, 1991) and other sonic shear-wave values of 1100-1250 m/s (Eastwood, 1993).

Since there is no information on shear-wave velocities in the McMurray sands at Cold Lake, S -wave velocity was estimated from equation 5.4, derived from a crossplot of V_p versus V_s in sandstones (Castagna et al., 1993):

$$V_s = 0.8042V_p - 0.8559 \text{ (km/s)} \quad (5.4)$$

Table 5.3 Parameters used to calculate V_p/V_s over the analysed interval.

Event	Depth (m)	V_p (m/s)	V_s (m/s)	V_p/V_s
Grand Rapids	315	2420	1000	2.42
Clearwater	415	2350 (cold) 1650 (hot)	1180 (cold) 1190 (hot)	1.99 1.39
Basal Clearwater	455	2350	1180	1.99
McMurray	470	2700	1315	2.05
Devonian	535			

Theoretical V_p/V_s values were calculated for a range of steamed zone thicknesses up to 40 m, which is the maximum thickness of clean homogeneous reservoir in this study location, and are presented in Figure 5.25. These theoretical values were calculated using equation (5.1) and the parameters listed in Table 5.3. Also plotted are curves obtained by substituting steamed zone P -wave interval velocities of 1800 m/s and 2000 m/s.

Using the parameters listed in Table 5.3 and equation (5.1), a theoretical value of 2.20 for the cold reservoir and a lower limit of 2.04 for the heated reservoir are calculated. The average measured value for V_p/V_s away from the wells is 2.19 along line 470-93 and 2.20 along line 470-94 and the lowest measured value is 2.01 ± 0.02 . Assuming that CDPs away from the injection wells are in the cold part of the reservoir, these values are in excellent agreement with the theoretical limits.

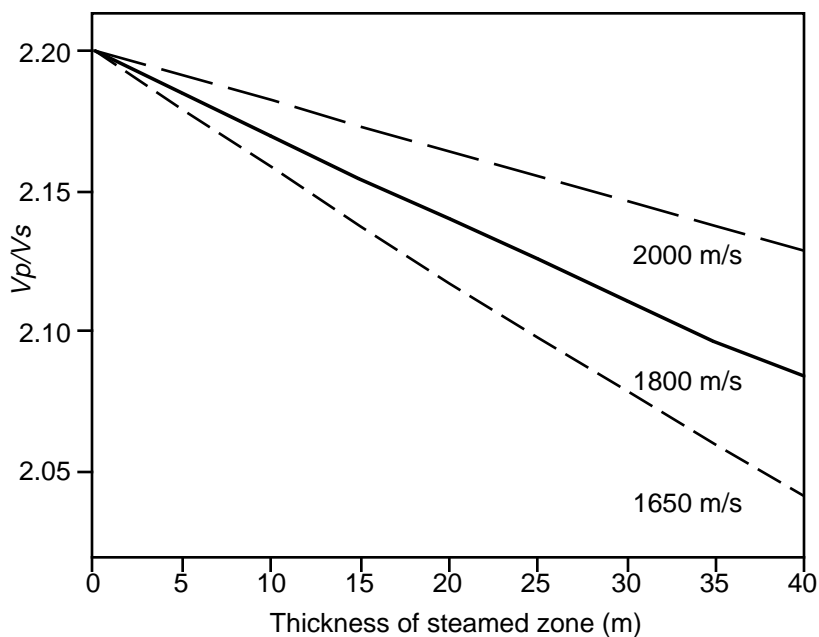


Fig. 5.25 Plot of thickness of steamed zone versus theoretical V_p/V_s for steamed zone P -wave interval velocities of 1650, 1800 and 2000 m/s. V_p/V_s is calculated over the Grand Rapids to Devonian interval.

It can be seen from Figure 5.25 that relating a particular value of V_p/V_s to a unique thickness of steamed interval is not possible without knowledge of the velocity in that interval. However, a minimum value of steamed zone thickness can be obtained for each V_p/V_s if a minimum steamed zone P -wave interval velocity of 1650 m/s is assumed. A constant interval velocity is attributed to the heated zone and a cold reservoir velocity applied outside this zone (Figure 5.26). This is not a realistic model of actual reservoir conditions because in reality there is a temperature (and therefore velocity) gradient through the reservoir interval. However, this model does allow for the calculation of a minimum heated zone thickness. An absolute thickness cannot be obtained since a thin, very low velocity zone or a thicker zone of moderately low velocity will have the same effect on the overall interval velocity.

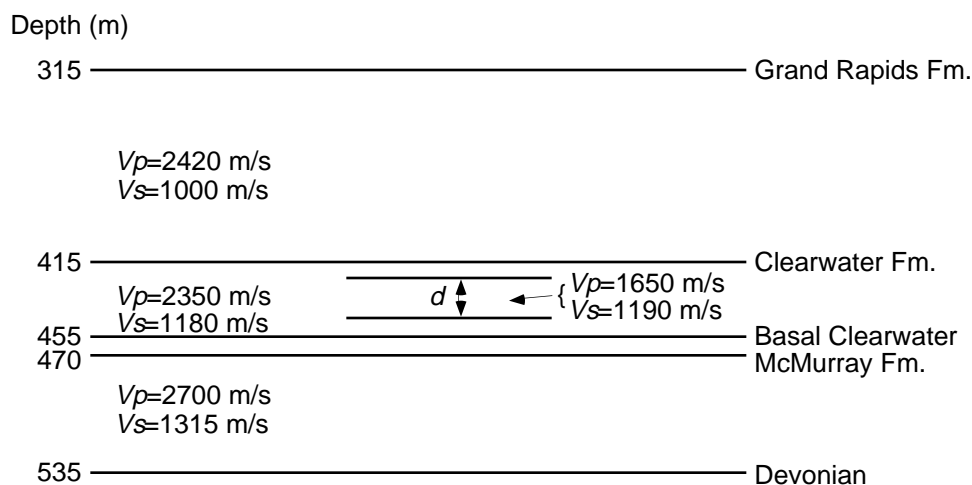


Fig. 5.26 Model for steamed reservoir interval of thickness d m.

Values of minimum thickness of steamed zone along line 470 were calculated from the 1993 V_p/V_s values and the parameters listed in Table 5.3. An expression for the minimum thickness, d , is derived from:

$$d = (0.195613 - 0.088821 * R) / (0.00018 * R - 0.000007)$$

where R represents V_p/V_s , and d is rounded to one decimal place. The error in the calculated minimum thickness (α_d) is derived for each value of V_p/V_s using the formula in equation (5.3):

$$\alpha_d = (0.0000346 * \alpha_R) / (0.0001805 * R - 0.0000071)^2$$

where α_R is the standard error in V_p/V_s , which was calculated in section 5.2.1. The average standard error in thickness was calculated to be ± 5.1 m. The calculated values of minimum thickness and the standard error applied to this thickness are plotted in Figure 5.27. The measured values of V_p/V_s produce minimum thickness values ranging from zero to 47 ± 5 m. The latter value of 47 ± 5 m agrees quite well with the maximum clean reservoir thickness of 40 m. Integration of this information into the vertical conformance analysis of the 3-D seismic data would help to increase understanding of the vertical extent of heated zones in the reservoir.

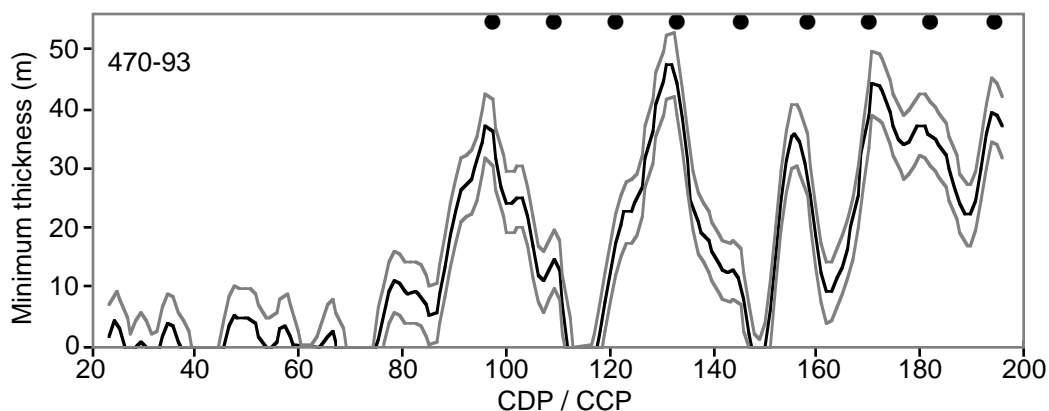


Fig. 5.27 Minimum thickness of steamed zone, calculated from V_p/V_s along line 470-93 and using an interval velocity of 1650 m/s for the steamed zone.

5.3 V_p/V_s and 3-D seismic data interpretation

5.3.1 470-93 (3-C) and 126-93 (3-D)

The values of V_p/V_s along line 470 are compared to the amplitudes of seismic events observed on line 126-93 (extracted from the 3D data volume), which was displayed previously in Figure 5.5. Events near the base of the Clearwater Formation at 0.44 s display varying amplitudes along the line and have anomalously high amplitudes at the locations of the steam injection wells. Such varying amplitudes are not observed on the 3-C P - P data (Figure 5.3), probably because smoothing filters (f - k , f - x) were applied to these data. Average absolute amplitudes, extracted from line 126-93 over an interval encompassing the Clearwater reservoir, were made available by Imperial Oil, who had found that high values correlated very well to the locations of injection wells (J. Eastwood, *pers. comm.*). These average amplitude values were scaled so that values below zero indicate cold parts of the reservoir. A plot of V_p/V_s along line 470-93 and scaled average absolute amplitudes extracted from line 126-93 over the Clearwater interval is shown in Figure 5.28. Dashed lines represent the values beyond which cold

reservoir is interpreted: below zero for the amplitudes and above 2.2 for V_p/V_s . A trend of low amplitude values corresponds to the trend of high V_p/V_s across the non-steamed area. Over the area with steam injection wells the amplitude values are higher and have local maxima at the well locations. Conversely, V_p/V_s values are lower over the area of injection wells and, in general, tend to be lowest at the well locations. The change to low V_p/V_s values observed just after CDP 90 corresponds to the change to high amplitudes at the same location.

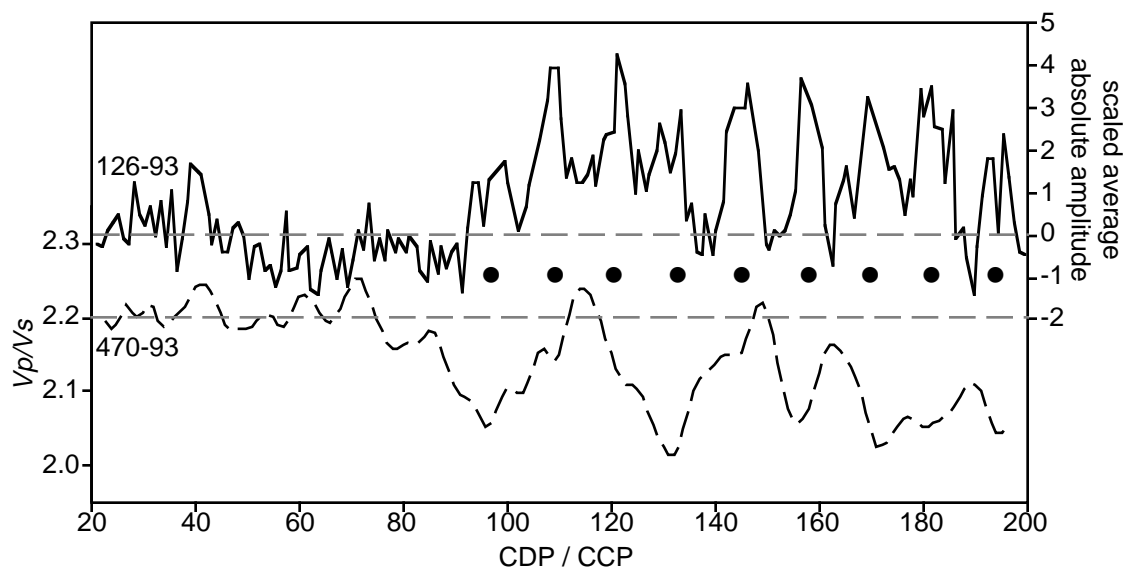


Fig. 5.28 Plots of V_p/V_s along line 470-93 from the 3-C survey and average absolute amplitudes extracted from line 126-93 from the 3-D survey. Black dots represent the projected injection well locations.

Another way of analysing the correlation between V_p/V_s along line 470-93 and amplitude values extracted from line 126-93 is presented in Figure 5.29. CDPs were grouped in three ways: (1) those at well locations (five adjacent CDPs); (2) those near to well locations (over the area of wells less the five in group 1) and (3) those away from the well locations. Values of V_p/V_s are plotted against scaled average absolute amplitude for the three groups of CDPs, which are represented by stars, crosses and circles,

respectively, in Figure 5.29. Low V_p/V_s values correlate to high amplitude values and high V_p/V_s to low amplitudes. Apart from a few stray values, the data points cluster neatly into three classes. Dashed lines indicate the boundaries between the classes and are seen to have different slopes.

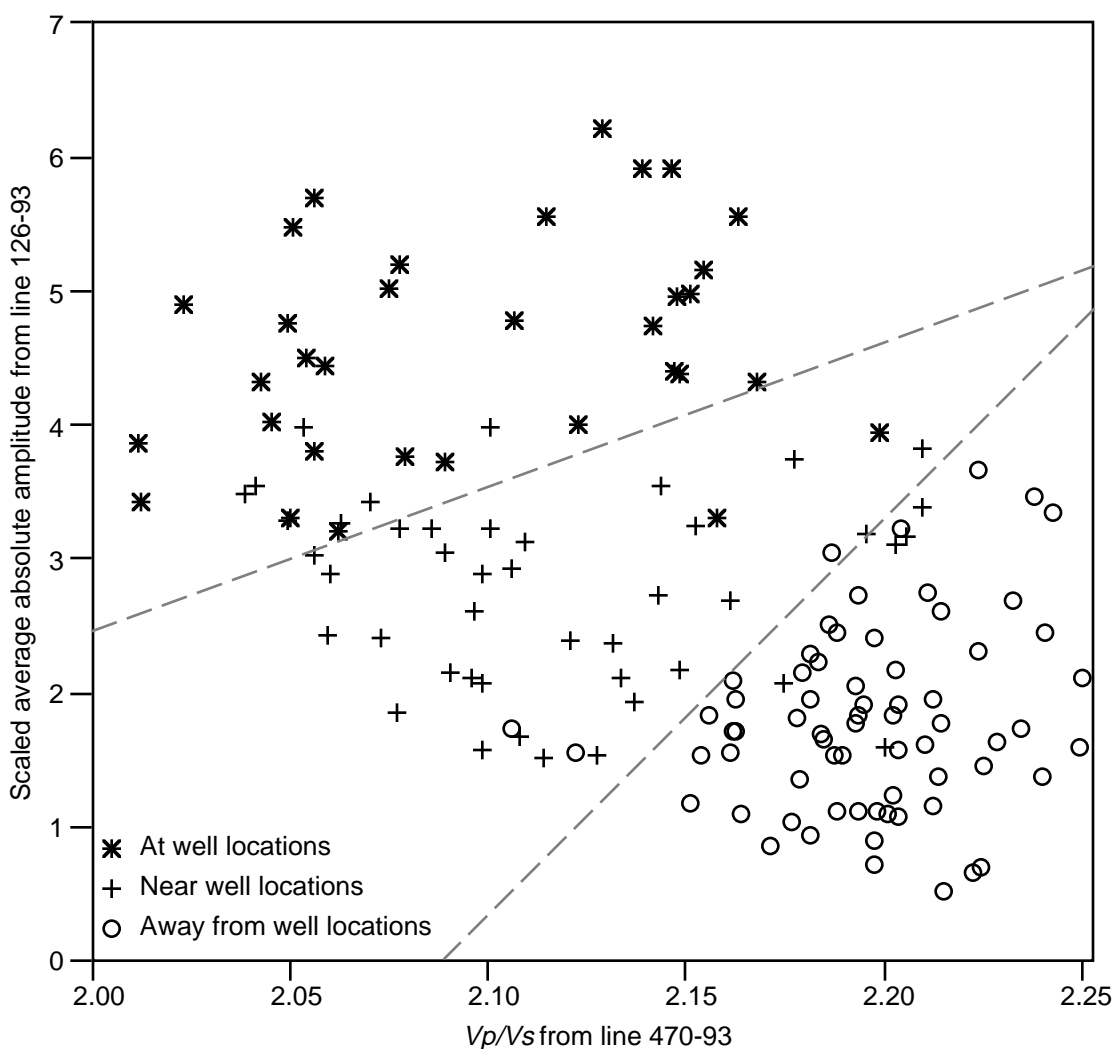


Fig. 5.29 Plot of V_p/V_s measured along line 470-93 from the 3-C survey against average absolute amplitudes extracted from line 126-93 from the 3-D survey. Data points have been classified as those at injection well locations (5 CDPs around each well location), those near injection well locations (CDPs from that part of the line covered by the wells minus CDPs at the wells) and those away from injection well locations.

At any CDP, measurement of amplitude or V_p/V_s alone is not enough to determine confidently whether that CDP is in a heated zone. However, measurement of both of these attributes enables the CDP location to be classified as being in hot, warm or cold reservoir. If it is assumed that the reservoir at the wells is hot, the reservoir near the wells is warm and the reservoir away from the wells is relatively cold, then data points from seismic lines with unknown reservoir conditions may be classified as long as V_p/V_s (R) and amplitude (A) are known. Data points lying below the line

$$A = 25(R-2) - 4 \equiv \text{cold reservoir}$$

may be grouped with the data points away from the well locations, i.e., in the cold reservoir, while data points above the line

$$A = 10(R-2) + 0.5 \equiv \text{hot reservoir}$$

may be classified with the data points at the well locations, or as lying in hot reservoir.

Those points lying between the two lines are classified as being in warm reservoir:

$$25(R-2) - 4 < A < 10(R-2) + 0.5 \equiv \text{warm reservoir}$$

5.3.2 V_p/V_s and 3-D seismic data discriminant analysis

To investigate the correlation along all of the analysed lines between V_p/V_s values and heated reservoir zones as interpreted from the 3-D seismic data, use was made of areal conformance statistic produced by Imperial Oil. Seven seismic attributes were selected for discriminant analysis over the reservoir interval, including peak amplitude, average amplitude and frequency. The discriminant analysis involved the selection of a calibration data set based on seismic traces from known heated locations and from known cold locations. This training data set was then used to calibrate the entire 3-D survey and resulted in a clear distinction between heated and cold parts of the reservoir (Eastwood, 1996).

Each CDP along the analysed 3-C lines was correlated against a "heated" or "cold" area from Imperial Oil's discriminant analysis. A V_p/V_s of 2.2 was assumed to represent the boundary between cold and heated reservoir. Those points falling in the "heated" zone and with V_p/V_s under 2.2 and those points in the "cold" zone with V_p/V_s over 2.2 were designated as agreeing with the discriminant analysis. Points lying in the "heated" zone but with V_p/V_s over 2.2 and those in the "cold" zone but with V_p/V_s under 2.2 were designated as disagreeing. If the actual V_p/V_s disagreed but V_p/V_s within the margin of error (± 0.02) agreed, then the data point was redesignated as agreeing. Plots showing at which CDPs V_p/V_s agreed or disagreed with the areal conformance analysis are presented in Figures 5.30 (1993 data) and 5.31 (1994 data). At CDPs where the points agree V_p/V_s is plotted as an oval and at those where they disagree V_p/V_s is plotted as a cross. For example, the data points near CDP 80 in Figure 5.30b have V_p/V_s below 2.2 but lie in cold reservoir. Therefore, these points are plotted as crosses ("disagree"). Near CDP 70, V_p/V_s values are above 2.2 and the CDPs lie in "cold" reservoir. Thus the V_p/V_s values are plotted as ovals ("agree"). Table 5.4 summarises these designations.

Table 5.4 Reservoir condition correlation between V_p/V_s and discriminant analysis

V_p/V_s	Discriminant analysis	
	cold	hot
< 2.2 (hot)	disagree (cross)	agree (oval)
> 2.2 (cold)	agree (oval)	disagree (cross)

Along every line except 469-93 there is a good match between heated or cold zones as determined from the discriminant analysis and those interpreted from V_p/V_s analysis. For the 1993 data, excluding line 469, 76% of the data points agreed while for all of the 1994 data 78% of the data points agreed.

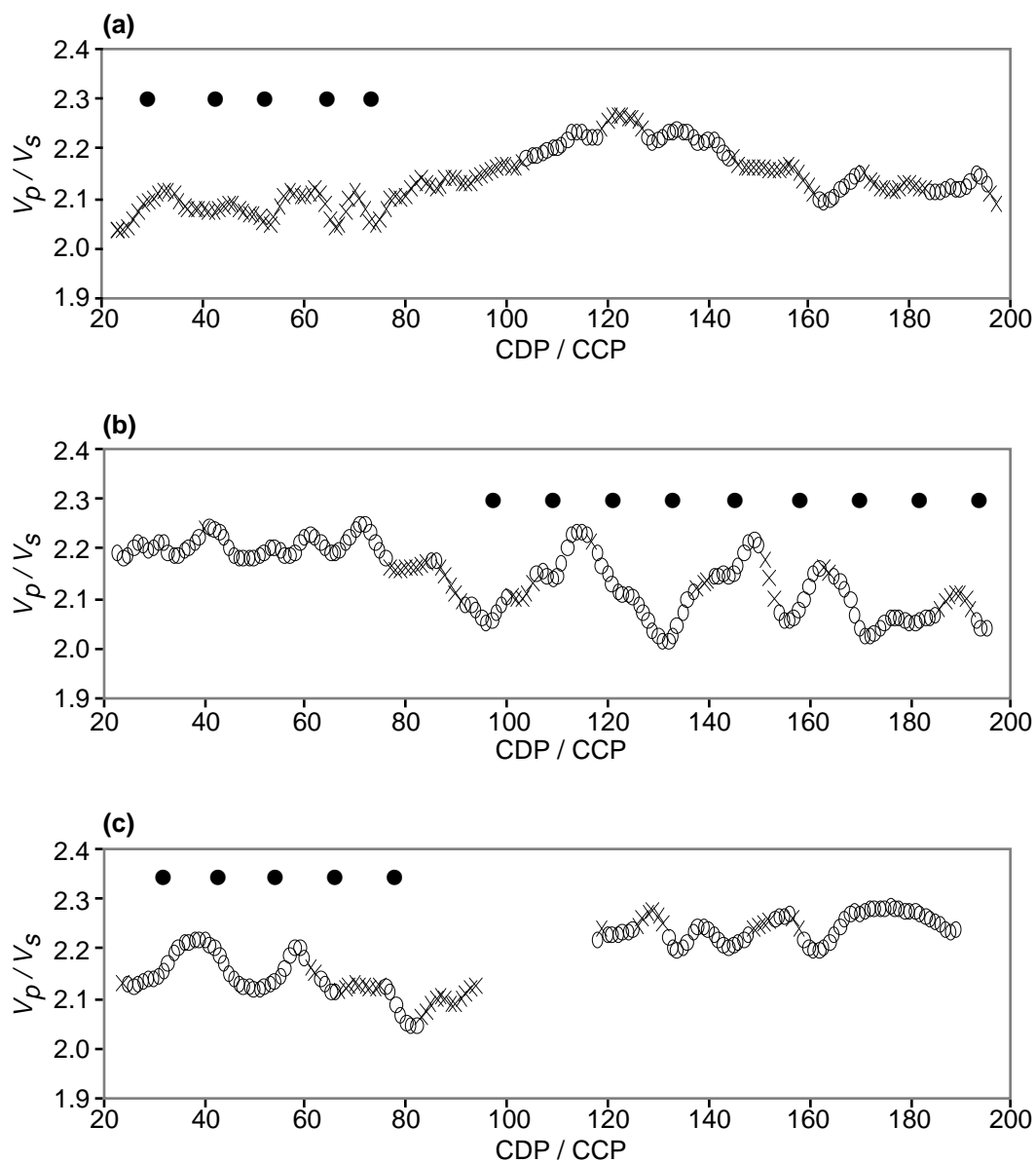


Fig. 5.30 Plot showing the agreement between heated and cold zones as interpreted from V_p/V_s analysis and those zones as determined from the discriminant analysis of seismic attributes done by Imperial Oil for the 1993 data. V_p/V_s values that agree with the discriminant analysis are shown by ovals and those that disagree by crosses, for lines (a) 468/469, (b) 470 and (c) 471/472.

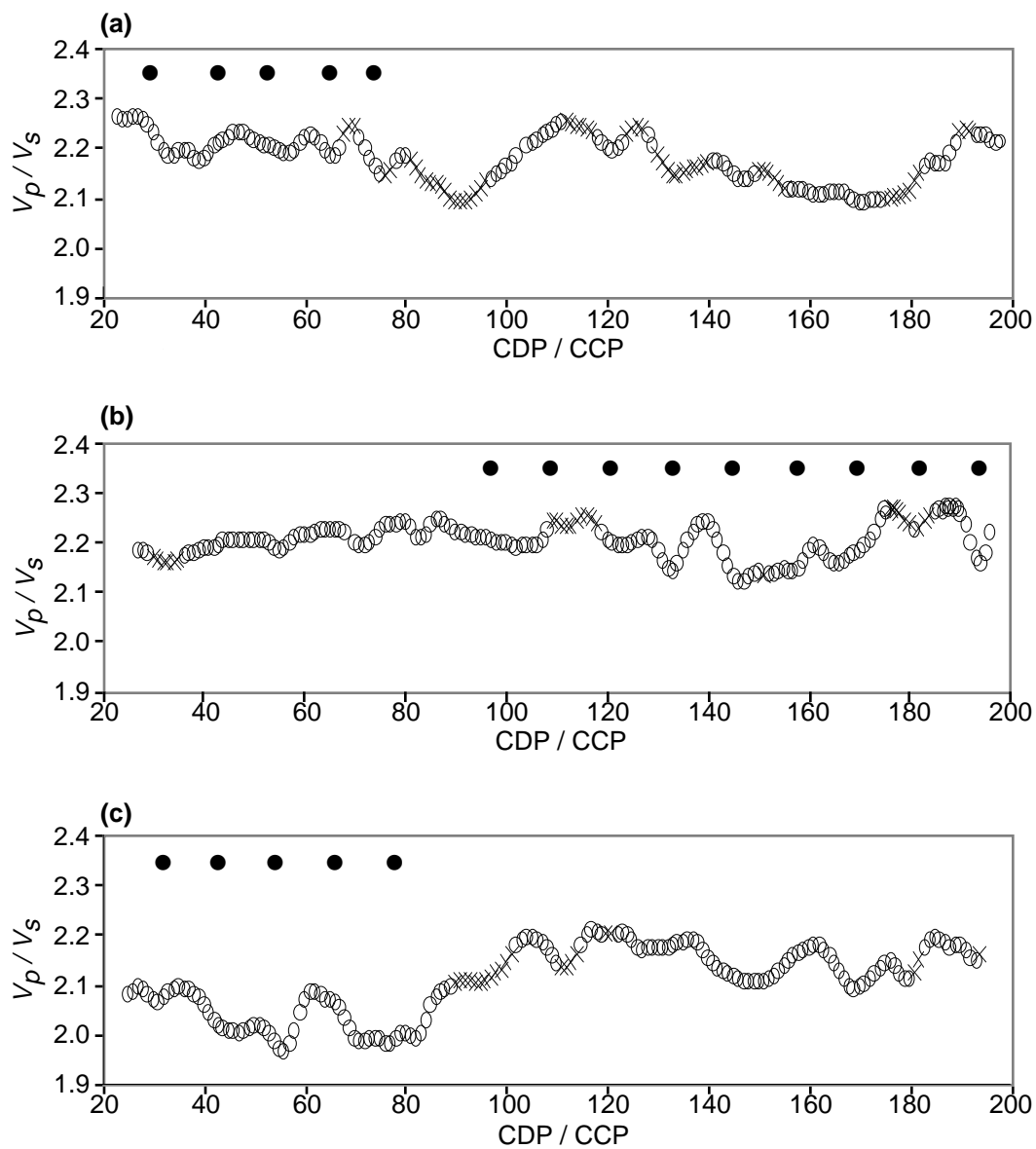


Fig. 5.31 Plot showing the agreement between heated and cold zones as interpreted from V_p/V_s analysis and those zones as determined from the discriminant analysis of seismic attributes done by Imperial Oil for the 1994 data. V_p/V_s values that agree with the discriminant analysis are shown by ovals and those that disagree by crosses, for lines (a) 468/469, (b) 470 and (c) 471/472.

The discriminant analysis performed by Imperial Oil is stated to have been designed primarily to identify gas zones. In their analysis of the 1993 3-D seismic data no anomalies were detected along the row of injection wells close to the north-western half of line 469 because there was no gas present, although these wells were known to be hot. The V_p/V_s analysis shows heated zones along this line of injection wells (Figure 5.30a) and thus reveals heated zones that were not detected by discriminant analysis of the 3D data. The heated zones along lines 470 (Figure 5.30b) and 471 (Figure 5.30c) as determined from V_p/V_s analysis of the 1993 data agree well with those from the 3-D data. All the lines of the 1994 data set analysed show good agreement between 3-C and 3-D heated and cold zones (Figure 5.31). The rather low V_p/V_s values observed along line 471-94 are now seen to lie in heated zones as determined from the 3-D data. V_p/V_s is an additional parameter which can be used to map changes in reservoir conditions. Integration of V_p/V_s data into the discriminant analysis might be useful in helping to predict and map the extent of heated reservoir.

5.4 Discussion

Three pairs of $P-P$ and $P-S$ lines were interpreted and analysed. The quality of the $P-P$ data was consistently good but that of the $P-S$ data varied. Line 470 (the common source and receiver line) was the best and considered to be the most reliable. Horizons interpreted on each line were the tops of the Grand Rapids Formation and of the Devonian section. These horizons represented strong acoustic impedance contrasts on both the $P-P$ and $P-S$ sections and were continuous, interpretable events on most of the lines. No other consistently interpretable events closer to the Clearwater reservoir zone could be identified.

On the $P-P$ sections a shallow channel is observed on all of the lines. The position of this channel corresponds to the location where large S -wave statics had been

determined and is thought to be the cause of those statics. Differences in *P-P* seismic character were observed in the Colorado shales between 1993 and 1994 and were caused by the hydration of the shales after casing collapse in early 1994. Repeatability of the section above the reservoir, which was determined to be very important at the D3 pad, was, therefore, in this case not applicable.

V_p/V_s was determined at each CDP from the traveltimes of the Grand Rapids to Devonian interval as measured from the corresponding *P-P* and *P-S* sections. V_p/V_s values average 2.19 in 1993 and 2.20 in 1994 over the zone away from the steam injection wells. The values near the wells in 1993 (steam injection cycle) are seen to be lower than those measured over the cold reservoir. This is attributed to the significant decrease in *P*-wave interval velocities during the injection cycle, when temperatures are higher and effective pressure lower. In general, the lowest V_p/V_s values are seen at the injection well locations. An error of ± 0.02 in the measured value of V_p/V_s was calculated from the theoretical picking error of ± 0.5 ms in the arrival time of each horizon. The average measured V_p/V_s of 2.20 for the cold reservoir and the lowest measured value of 2.01 ± 0.02 are in excellent agreement with the theoretically calculated values of 2.20 for the cold reservoir and 2.04 for a 40 m thick heated zone. Better knowledge of the expected behaviour of V_s under steaming conditions is desirable and might be obtained by laboratory experiments.

Heated and cold reservoir zones as interpreted from the V_p/V_s analysis agree well with those zones as determined from Imperial Oil's analysis of the 3-D seismic data. The only place where there is a disagreement is along part of line 469-93, where a heated zone is interpreted from the 3-C data but not from the 3-D data. It is known that the wells along this part of the line were hot in 1993 so the V_p/V_s analysis correctly reflects the field conditions whereas the 3-D data analysis may not.

The experimental converted-wave survey is considered to have been a success. Low V_p/V_s values extracted from the data correlate well with the locations of steam injection wells and the measured values match theoretically derived numbers for the upper and lower bounds of V_p/V_s . Acquisition of a 3-D converted-wave survey would offer greater areal coverage and V_p/V_s analysis could be integrated with discriminant analysis of 3-D seismic data to assist in the prediction of the heated and cold parts of the reservoir. Burial of the 3-C geophones may help to eliminate some of the unwanted surface wave signal but S -wave statics will probably still be large because the near-surface S -wave low velocity zone appears to be thick. A test line acquired with 3-C geophones both at the surface and buried would indicate if there is an advantage in burying the geophones.

Chapter 6

AMPLITUDE VARIATION WITH OFFSET

6.1 Introduction

6.1.1 Data analysed

Selected portions of three seismic data sets (1990 3-D, 1992 3-D and 1993 3-C) were analysed for amplitude variations with offsets. The objective of this aspect of the study was to determine whether amplitude variation with offset (AVO) analysis could confirm the interpretation of low velocity intervals as determined from amplitude anomalies delineated on the 3-D data volumes. Tsingas and Kanasewich (1991) employed amplitude versus angle analysis of 2-D seismic data over a steam injection location at Cold Lake. They showed that the lateral extent of steam invaded zones may be established by observation of the variations in reflection amplitude with angle.

An example of an amplitude anomaly in the 1990 3-D data was shown in Figure 3.5a, where a high amplitude trough is observed at 0.425 s, over inlines 40 to 60. This anomaly is not seen on the corresponding 1992 line (Figure 3.5b) and is interpreted to be caused by partial gas-saturation. The 1992 line in Figure 3.5b exhibits an amplitude anomaly at 0.437 s, over inlines 34 to 40. This anomaly occurs at a time equivalent to the perforation depths in nearby injection wells and is later than the interpreted gas anomaly observed in the 1990 data. The anomaly in the 1992 data is interpreted to be caused by the presence of steam.

A *P-P* line from the 1993 3-C survey was also analysed. Few significant amplitude anomalies are seen within the reservoir interval but the character of the Clearwater event varies across the line, which was displayed in Figure 5.3. Since this event is only seen clearly on *P-P* seismic data at the AABBW pads when gas exists at the top of the reservoir (J. Eastwood, *pers. comm.*), the AVO analysis was designed to

investigate potential gas-charged intervals. It was not possible to analyse the converted-wave data as they had not been processed specifically to retain true relative amplitudes. Also, the converted-wave data were $f-k$ and $f-x$ filtered to enhance horizontal events and to improve the signal to noise ratio, which was quite poor.

6.1.2 Theoretical background

AVO analysis utilises the fact that reflection coefficients vary with increasing offset and that this behaviour may sometimes be observed on pre-stack gathers. An incident compressional plane-wave at the boundary between two isotropic, homogeneous elastic media will partition into four waves: reflected P -wave, reflected S -wave, transmitted P -wave and transmitted S -wave. The reflection coefficients for these four waves depend on V_p , V_s and density (ρ) in the two media and the angle of incidence, and may be determined from the equations developed by Knott (1899) and Zoeppritz (1919). V_p , V_s and density in turn depend on the physical parameters of the media, such as lithology, porosity, pore fluid and pressure (Tatham, 1982). The variation of these reflection coefficients with angle or offset is known as offset-dependent reflectivity and forms the basis of AVO analysis.

The Zoeppritz equations have been simplified by assuming relatively small changes in medium properties (Bortfeld, 1961; Aki and Richards, 1980). A commonly used approximation to the P - P reflection coefficient is that of Shuey (1985):

$$R_{pp}(\theta) \approx R_0 + \{A_0 R_0 + \Delta\sigma / (1 - \sigma)^2\} \sin^2\theta + \frac{1}{2} \frac{\Delta V_p}{V_p} (\tan^2\theta - \sin^2\theta) \quad (6.1)$$

where R_0 = normal incidence reflection coefficient,

σ = Poisson's ratio,

θ = angle of incidence,

$$\begin{aligned}\Delta V_p &= V_{p2} - V_{p1}, \\ V_p &= (V_{p1} + V_{p2}) / 2, \\ \rho &= (\rho_1 + \rho_2) / 2, \\ \Delta\rho &= \rho_2 - \rho_1, \\ A_0 &= B_0 - 2(1 + B_0) \left[\frac{1 - 2\sigma}{1 - \sigma} \right], \\ B_0 &= (\Delta V_p / V_p) / \left[\frac{\Delta V_p}{V_p} + \frac{\Delta\rho}{\rho} \right]\end{aligned}$$

The subscripts 1 and 2 refer to the incident and transmitted layers, respectively. The first term in equation (6.1) is the normal incidence reflection coefficient, the second term contributes most significantly at intermediate angles of incidence ($<30^\circ$) and the third term is significant only at larger angles. If the range of angles of incidence is limited to intermediate angles, equation (6.1) simplifies to

$$R_{pp} \approx R_0 + B \sin^2\theta \quad (6.2)$$

where $B = A_0 R_0 + \Delta\sigma / (1 - \sigma)^2$, or

$$R_{pp} \approx R_0 + B\theta^2 \quad (6.3)$$

R_0 is sometimes called the “intercept” and B is called the AVO gradient. Thus the angle-dependent P - P reflection coefficient approximates to a function of the normal incidence reflection coefficient plus a linear term dependent on the square of the sine of the incident angle.

Poisson’s ratio, σ , is written in terms of V_p and V_s as

$$\sigma = \{(V_p / V_s)^2 - 2\} / \{2(V_p / V_s)^2 - 2\} \quad (6.4)$$

which is shown graphically in Figure 6.1. It is seen that σ will decrease with decreasing V_p/V_s and thus with decreasing V_p if V_s is constant. A rapid decrease in Poisson’s ratio is observed for a decrease in V_p/V_s from 3 to 1.4, which is the predominant range of V_p/V_s encountered in the subsurface. It follows that a change in one of the physical

parameters of a rock (lithology, porosity, pore fluid content, pressure) that affects V_p/V_s will change σ . Gassmann's (1951) equations predict a large drop in P -wave velocity and a small increase in S -wave velocity when a small amount of gas (less than 5%) is introduced into the pore space of a compressible brine-saturated sandstone. Figure 6.2 (after Ostrander, 1984) plots V_p/V_s against gas saturation and demonstrates that the most significant decrease in V_p/V_s occurs for a small gas saturation.

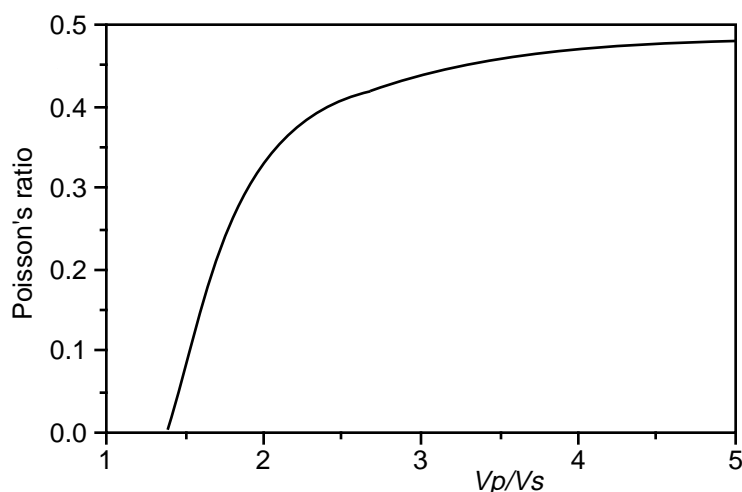


Fig. 6.1 Plot of Poisson's ratio versus V_p/V_s .

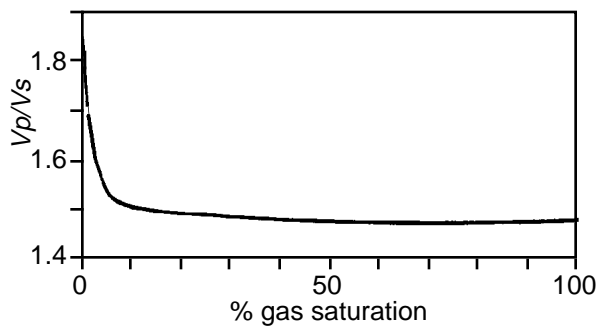


Fig. 6.2 Plot of V_p/V_s against gas saturation (after Ostrander, 1984). This diagram shows how the most significant decrease in V_p/V_s occurs with a very small amount of gas (under 5%).

Since V_p , V_s and density are dependent on the medium's physical parameters, changes in these parameters will affect the reflection coefficients. Figure 6.3 (after Ostrander, 1984) shows the theoretical behaviour of P - P reflection coefficients with increasing offset for the four cases: (a) $V_{p1} < V_{p2}$ and $\sigma_1 = \sigma_2$, (b) $V_{p1} > V_{p2}$ and $\sigma_1 = \sigma_2$, (c) $V_{p1} < V_{p2}$ and $\sigma_1 > \sigma_2$, (d) $V_{p1} > V_{p2}$ and $\sigma_1 > \sigma_2$. For cases (a) and (c), $V_{p2}/V_{p1} = 1.25$, while for cases (b) and (d), $V_{p2}/V_{p1} = 0.8$. For cases (a) and (b), $\sigma_1 = \sigma_2 = 0.3$, while for cases (c) and (d), $\sigma_1 = 0.4$ and $\sigma_2 = 0.1$. An increase in absolute reflection coefficient with increasing angle is seen only for case (d), where $V_{p1} > V_{p2}$ and $\sigma_1 > \sigma_2$ or, using the terms of equation (6.2), both R_0 and B are negative. Their product, therefore, is positive while for the other three cases seen in Figure 6.3 this product is negative. This product is sometimes referred to as NI^*G (normal incidence reflectivity * gradient) and is a very useful tool in AVO analysis (Allen and Peddy, 1993).

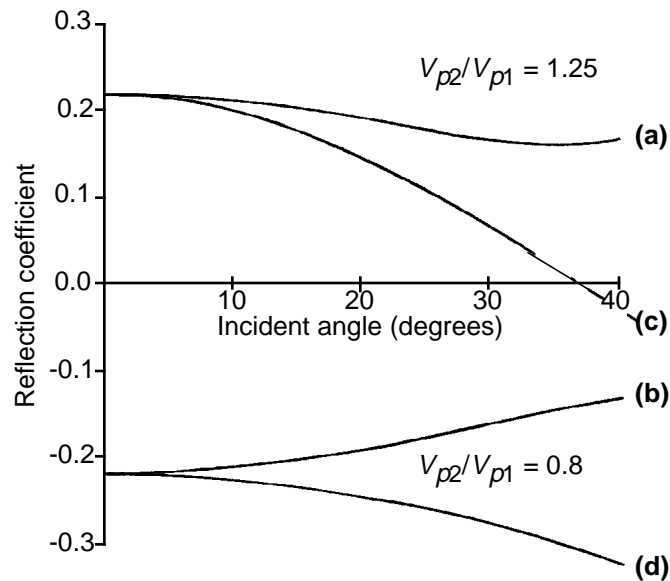


Fig. 6.3 Plot of P - P reflection coefficient versus angle of incidence for (a) $V_{p1} < V_{p2}$ and $\sigma_1 = \sigma_2$, (b) $V_{p1} > V_{p2}$ and $\sigma_1 = \sigma_2$, (c) $V_{p1} < V_{p2}$ and $\sigma_1 > \sigma_2$, (d) $V_{p1} > V_{p2}$ and $\sigma_1 > \sigma_2$. For cases (a) and (b), $\sigma_1 = \sigma_2 = 0.3$ while for cases (c) and (d), $\sigma_1 = 0.4$ and $\sigma_2 = 0.1$. (after Ostrander, 1984).

The presence of gas in a sandstone reservoir encased in higher velocity shales causes a decrease in V_p and σ , so the absolute reflection coefficient increases with angle of incidence (Figure 6.3, case d). When there is no gas present the absolute reflection coefficient decreases slightly with increasing angle of incidence. Ostrander applied this theory successfully to the interpretation of seismic data. The use of AVO analysis in hydrocarbon exploration started with this work of Ostrander and most cases have involved gas sand anomalies, although not always with successful results.

Rutherford and Williams (1989) defined three classes of AVO anomalies for gas sands encased in shales: (1) high impedance sands, (2) near-zero impedance sands and (3) low impedance sands. These classes have the properties of (1) positive R_0 with high negative gradient, (2) small positive or negative R_0 with high negative gradient and (3) high negative R_0 with negative gradient. The authors warn that Class 3 gas sands do not usually have large changes in amplitude with increasing offset and sometimes an increase may be undetected because of tuning, attenuation, recording array or signal/noise decreases with offset. Normal incidence*gradient plots are useful for Class 3 anomalies but will not detect Class 1 or Class 2 anomalies and cannot be related to hydrocarbon content unless it is known that Class 3 behaviour is expected (Castagna and Smith, 1994).

6.1.3 The Chiburis method of AVO analysis

The method of data analysis used was that of Chiburis (1984; 1993), which normalises the amplitudes of target and reference horizons to eliminate or greatly reduce amplitude effects from causes other than offset. In Chiburis's method of AVO analysis, seismic amplitudes are picked interactively along both the target horizon and a reference horizon (over which no distinctive offset-dependent amplitude effects should be expected). The maximum amplitudes of the target event $T(x)$ and of the reference event $W(x)$ are measured at each offset x within a gather. The target to reference amplitude

ratios are normalised:

$$R(x) = \{T(x) / Ta\} / \{W(x) / Wa\} \quad (6.5)$$

where $R(x)$ is the amplitude ratio at offset x and Ta and Wa are the average amplitudes of the target and reference horizons, respectively. Each ratio is further modified:

$$\text{If } R(x) > 1, \quad R(x) = 2 - 1/R(x) \quad (6.6)$$

which has the result of bounding the ratios between 0 and 2. This ratio is known as the conditioned amplitude ratio. A curve of the form $y = B + Ax^2$ is fitted to the plot of conditioned amplitude ratio against offset. This function has a similar form to equation (6.3), where reflection coefficient at offset x is written as a function of the zero-offset reflectivity and angle squared. Finally the AVO difference (relative to zero-offset) for the gather is formed by:

$$\text{AVO difference} = B/A * N^2 \quad (6.7)$$

where N is the number of traces in the gather. Since N is a scaling factor, it is arbitrary and could equally be the farthest offset. Chiburis refers to this AVO difference as “AVO”, for simplicity.

6.2 AVO modelling of Cold Lake data

6.2.1 Model and synthetic seismic gathers

Before analysing the seismic data for AVO effects, several models were created to simulate the interpreted conditions of steam- and gas-saturated intervals within the reservoir. It was predicted that the modelled AVO responses would indicate that measurable AVO results could be extracted from the real data. If the low velocity intervals behaved in the same way as Class 3 gas sands, then it is possible that a significant increase in amplitudes with offset might not be seen. Small increases in amplitude on the modelled data might imply that such changes would be hard to measure on real data because of interfering noise. It was also anticipated that the modelling would

allow confirmation of the interpretation that anomalies on the stacked seismic data may be caused by low velocity zones.

For the generation of synthetic seismic traces, it is necessary to select a wavelet to be convolved with the generated acoustic impedances. In the modelling presented, both Ormsby bandpass and extracted wavelets were used. The first extracted wavelet (1) came from the 1990 3-D seismic data, as was described in section 3.1. It was 100 ms long and was composed of a primary event followed by a secondary one 25 ms later. It was thought that this second event could be the result of a ghost reflection from the ground surface, 10 m shallower than the geophones. The second extracted wavelet (2) came from the 1993 *P-P* data, at the location of well BB27. It was considered that wavelet (1) was not suitable for use in the modelling of low velocity zones in the 1993 *P-P* data because the geophones for the 3-D survey were buried, while those for the 3-C survey were at the surface. The choice of wavelet will be seen to affect the modelled AVO response and influence the range of offsets to be included in the analyses.

Several log models were created to observe the calculated effects on seismic amplitudes of introducing gas-saturated or steamed zones into the reservoir. The logs edited were the *P*-wave and *S*-wave dipole logs from well BB13a and the *P*-wave log from well BB27 for the shallow section. Well BB13a encountered a 15 m thick gas-charged interval at the top of the Clearwater Formation, which is apparent as a low velocity (1950 m/s) zone on the *P*-wave sonic log. The *S*-wave sonic log was edited to change the original Clearwater velocity of about 1000 m/s to a more likely velocity of 1180 m/s (see discussion in section 5.2.2).

Hampson-Russell AVO software was used to generate synthetic seismic offset gathers and stacked gathers for the original logs and the modifications, which were intended to simulate various reservoir conditions. Each of the two sonic logs was blocked into the same irregular intervals of constant velocity. Constant density values

were input for each blocked interval within the zone of interest. The values were obtained from logs acquired at the D3 pad and from physical parameters of the Clearwater sands (Eastwood, 1993). Density values used were as follows: Grand Rapids Formation, 2150 kg/m³; cold Clearwater Formation, 2100 kg/m³; gas-charged interval, 2060 kg/m³; steamed interval, 2065 kg/m³ and McMurray Formation, 2250 kg/m³. Poisson's ratio within each blocked interval was calculated automatically from the *P*- and *S*-wave velocities and density. Six situations were modelled:

- (a) A gas-charged zone at the top of the reservoir. This was interpreted from the original logs.
- (b) A gas-charged zone beneath a tight streak near the top of the reservoir. This model was designed to simulate the situation thought to exist in places at the D3 pad in 1990. High amplitude events on the 1990 seismic data at about 0.425 s (Figure 3.5a) were interpreted to be gas-saturated zones - an interpretation supported by the inversion study (section 3.6).
- (c) No gas present at the top of the reservoir.
- (d) A 6 m steamed zone present at the depth of the perforations. High amplitude anomalies seen on the 1992 seismic data at a time of about 0.437 s (Figure 3.5b) were interpreted to be steam-saturated zones.
- (e) An 18 m steamed zone at the base of the reservoir. The thickness of the steamed zone was increased to observe the effects of tuning caused by the thinner zone.
- (f) No steam present at the perforation depth.

Figure 6.4 shows the results for case (a), a 15 m thick gas-saturated zone at the top of the reservoir. Plotted are the original input logs overlain with the blocked logs, Poisson's ratio, a gather showing offsets up to 600 m and the stacked trace of these offsets (with NMO stretch muting applied; repeated five times). The gas interval is annotated next to the *P*-wave sonic log. The time scale for the seismic traces has been

adjusted to reflect the arrival times of the modelled events on the actual seismic data from the D3 pad. The top of the gas-charged interval correlates to the trough at about 0.408 s and the base of the zone to the peak at 0.424 s. The interval is thick enough so that there are no adverse tuning effects between the top and base of the interval. An Ormsby bandpass wavelet (10/15-100/120 Hz) was used in the generation of these seismic traces, as these were the frequency limits applied to the 3-C data.

Case (d) results (a 6 m thick steamed zone at the depth of the perforations) are presented in Figure 6.5 in the same way as for case (a). The *P*-wave sonic log was edited to simulate a steamed zone from 457 to 463 m with an interval velocity of 1750 m/s. The *S*-wave sonic log was also edited to a value of 1190 m/s. The top of the steamed interval is represented by the trough at 0.438 s which corresponds to the arrival time of the anomalies observed on the 1992 3-D seismic data. The base of the zone corresponds to the peak at 0.445 s but there is constructive interference between the seismic events representing the top and base of the 6 m thick steamed zone.

The logs plotted in Figures 6.4 and 6.5 were modified to simulate the other cases listed above. For case (b), a tight streak and a gas-saturated interval from 426 m to 436 m were inserted and the original gas interval deleted. Case (c), the cold reservoir model for the top of the Clearwater Formation, was created by deleting the gas interval. The 6 m steam zone of case (d) was extended to 18 m for case (e) and deleted for case (f). In each case the densities were modified accordingly. The synthetic seismic offset gathers generated for each of these six models are presented in Figures 6.6 and 6.7.

Figure 6.6 shows the traces generated for the gas cases (a) and (b) and the gas-free case (c). The traces displayed in Figures 6.6a, 6.6c and 6.6e were generated using an Ormsby bandpass wavelet with frequency limits 10/15-100/120 Hz while the traces in Figures 6.6b, 6.6d and 6.6f were generated using extracted wavelet (1). Annotated are the top of the reservoir and the top of the gas zone.

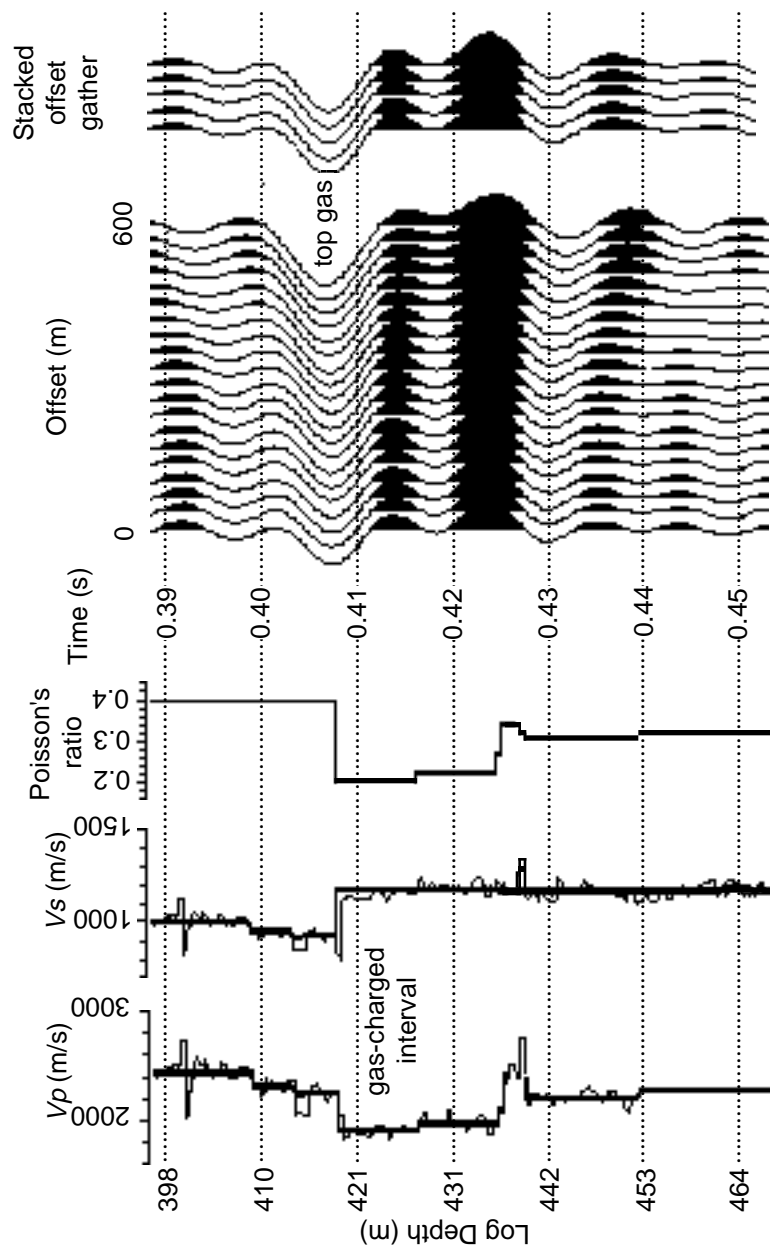


Fig. 6.4 Plots of the P -wave and S -wave sonic logs and calculated Poisson's ratios used to generate the synthetic seismic offset gather displayed. Offsets up to 600 m were included in the gather. These traces were stacked and repeated five times to produce the stacked gather. The model is for case (a): a gas-saturated interval at the top of the Clearwater Formation, from 418 m to 433 m depth.

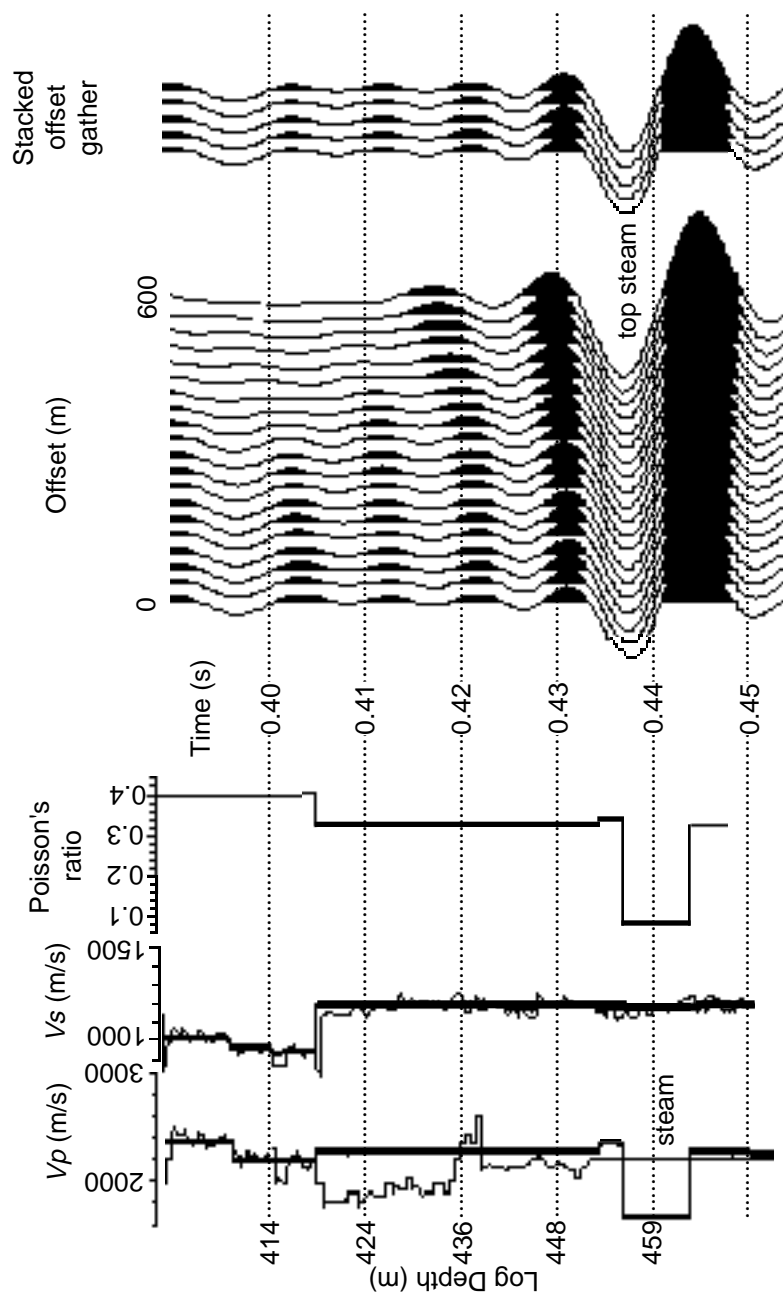


Fig. 6.5 Plots of the P -wave and S -wave sonic logs and calculated Poisson's ratios used to generate the synthetic seismic offset gather displayed. Offsets up to 600 m were included in the gather. These traces were stacked and repeated five times to produce the stacked gather. This model is for case (d): a steamed interval at the depth of the perforations, from 457 m to 463 m depth.

For Figures 6.6a and 6.6b the gas zone is modelled at the top of the reservoir, as seen in Figure 6.4, and its top correlates to the trough at 0.407 s. The amplitude of this trough increases slightly with increasing offset. For Figures 6.6c and 6.6d the gas zone is modelled below a tight streak and its top correlates to the trough at 0.417 s, which corresponds to the time of some of the amplitude anomalies on the 1990 seismic data. It is hard to judge from this display the behaviour of the amplitudes as a function of offset. The presence of gas at a depth of 8 m below the top of the reservoir changes the character of events at the top of the reservoir at 0.407 s because of interference. This can be seen by comparing the top reservoir events in Figures 6.6a and 6.6b with those in Figures 6.6c and 6.6d. It is especially noticeable in the traces generated using the extracted wavelet. In Figures 6.6e and 6.6f the top of the cold reservoir is at 0.407 s and appears as a weak event which in Figure 6.6f changes phase with offset. In the absence of a heated zone at the top of the reservoir, the event corresponding to this top is difficult to pick on the seismic data. The stacked offset traces seen in Figure 6.5 show this event to be a weak trough at 0.407 s.

Similar offset gathers for the steamed zone cases are shown in Figure 6.7. In each case the depth of the top of the perforated zone correlates to a trough at 0.438 s, which is the time at which strong amplitude anomalies were observed on some of the 1992 seismic data. When the steamed interval is only 6 m thick (Figures 6.7a and 6.7b), constructive interference occurs between the events representing the top and base of the interval. Increasing the interval to 18 m causes the top and base to be resolved.

The four gas cases in Figure 6.6 all exhibit an increase in amplitude with offset whereas if no gas is present, the event changes phase. In all four steam examples in Figure 6.7, the amplitude of the trough at 0.438 s is high at zero-offset and increases slightly with offset. When no steam is present, a trough is still observed but its zero-offset amplitude is, as expected, lower and its amplitude decreases with increasing offset.

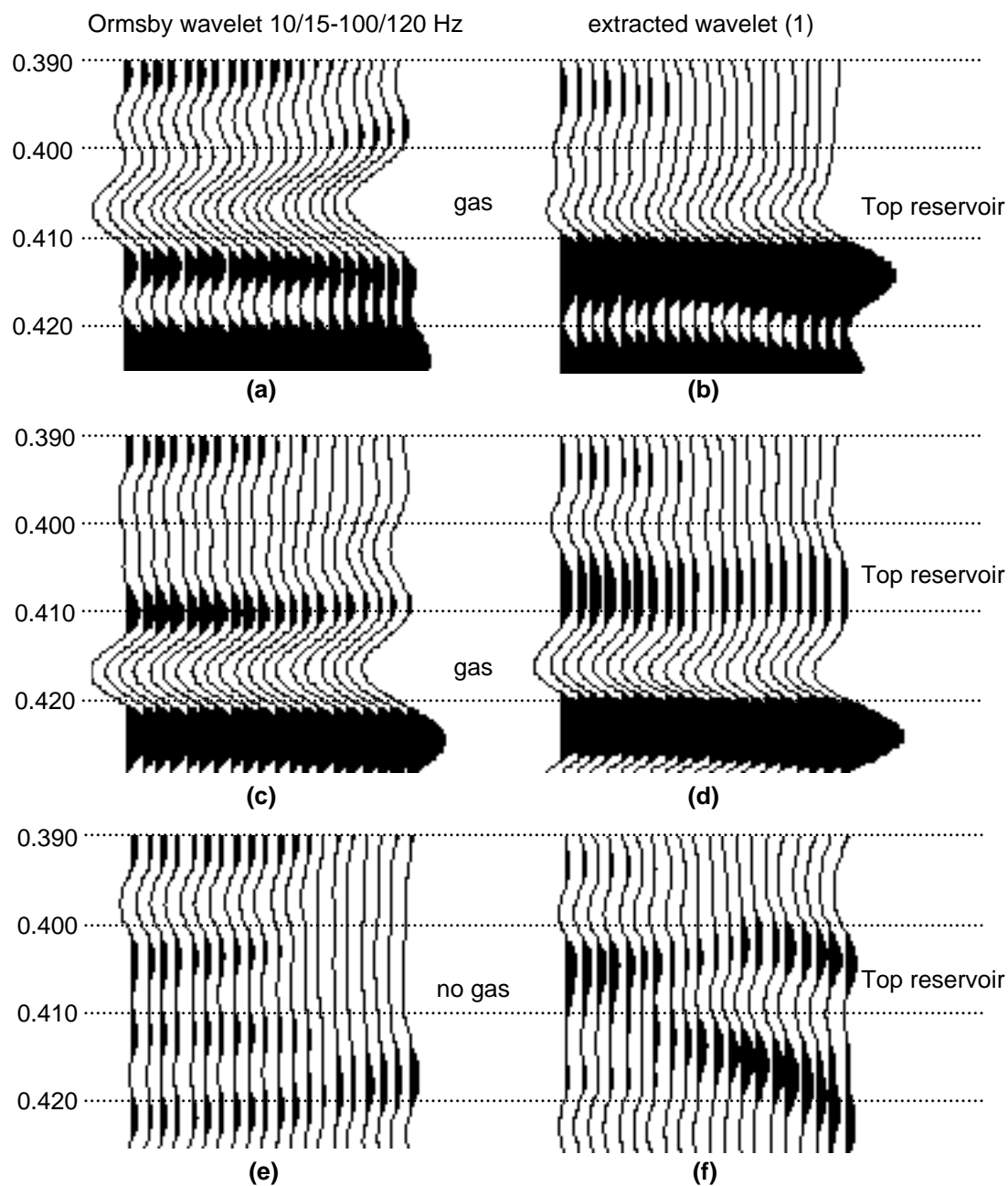


Fig. 6.6 Synthetic offset gathers generated from gas models. Plots (a), (c) and (e) were generated using an Ormsby bandpass wavelet while plots (b), (d) and (f) were generated using extracted wavelet (1). Plots (a) and (b) show the modelled results of a gas-saturated interval at the top of the reservoir; (c) and (d) for a gas-saturated zone 8 m below the top of the reservoir, beneath a tight streak; (e) and (f) for the cold reservoir top.

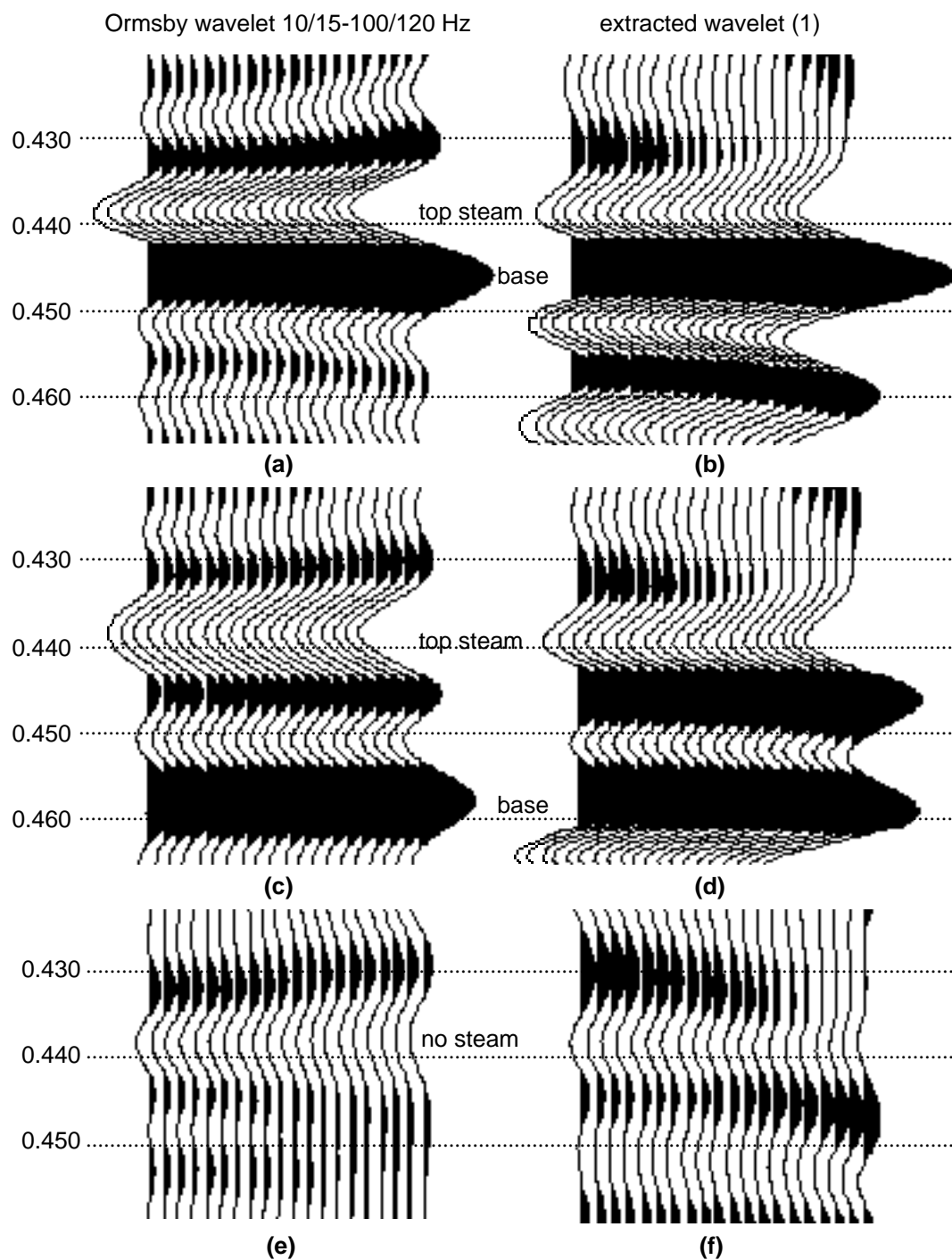


Fig. 6.7 Synthetic offset gathers generated from steam models. Plots (a), (c) and (e) were generated using an Ormsby bandpass wavelet while plots (b), (d) and (f) were generated using extracted wavelet (1). Plots (a) and (b) show the modelled results of a 6 m steam-saturated interval at the perforation depth; (c) and (d) for an 18 m steam-saturated interval; (e) and (f) for the cold reservoir at the perforation depth.

Discrimination between an anomaly caused by partial gas-saturation and one due to steam does not appear to be possible. The presence of both fluids in a restricted interval within the reservoir results in a high amplitude trough (negative reflection coefficient). However, the conditions of high temperature and high fluid pressure in 1992 (steaming cycle) do not allow for the presence of gas, except in very thin layers (Eastwood et al., 1994). In 1990, the temperature and fluid pressure are lower and gas comes out of solution. It is assumed, therefore, that only steam anomalies are seen in the 1992 3-D data and only gas anomalies in the 1990 3-D data. At the AABBW pads, the situation is different. Fluid pressures during the steam injection cycle (1993) were lower than during steaming at the D3 pad (4-6.5 MPa compared to 8-10 MPa) so gas is present during the steaming cycle (J. Eastwood, *pers. comm.*). Thus, in the 1993 3-C data, anomalies may be caused by both gas and steam. Gas anomalies may be expected at the top of the reservoir, as in 1990 3-D data, while steam anomalies may be seen at the perforation depth, as in the 1992 3-D data.

Examples of amplitude anomalies observed on the seismic data and their correlation to the synthetic stacked traces are shown in Figures 6.8 and 6.9. The synthetic traces in these figures were generated using extracted wavelet (1). In Figure 6.8 the amplitude anomaly on the 1990 stacked data is interpreted to be caused by partial gas-saturation below a tight streak and the synthetic traces were created from the model of such an interval (case b). The amplitude anomaly at 0.437 s in Figure 6.9 is interpreted to be due to a steamed zone at the depth of the perforations. The traces were generated using the model in Figure 6.5 (case d). The match between the synthetic traces and the real seismic data is very good and confirms that the models are realistic.

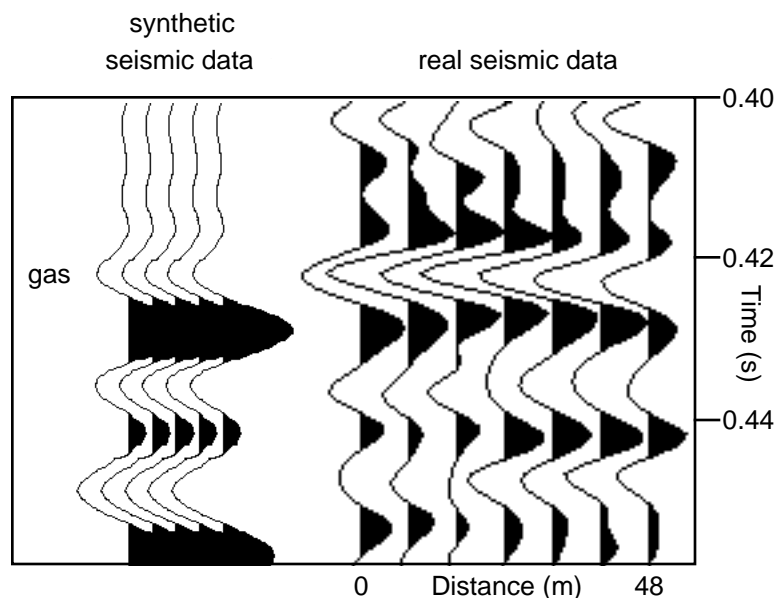


Fig. 6.8 An interpreted gas anomaly in the 1990 stacked data and the synthetic stacked section created from the model with gas below a tight streak (case b). The synthetic data were generated using extracted wavelet (1).

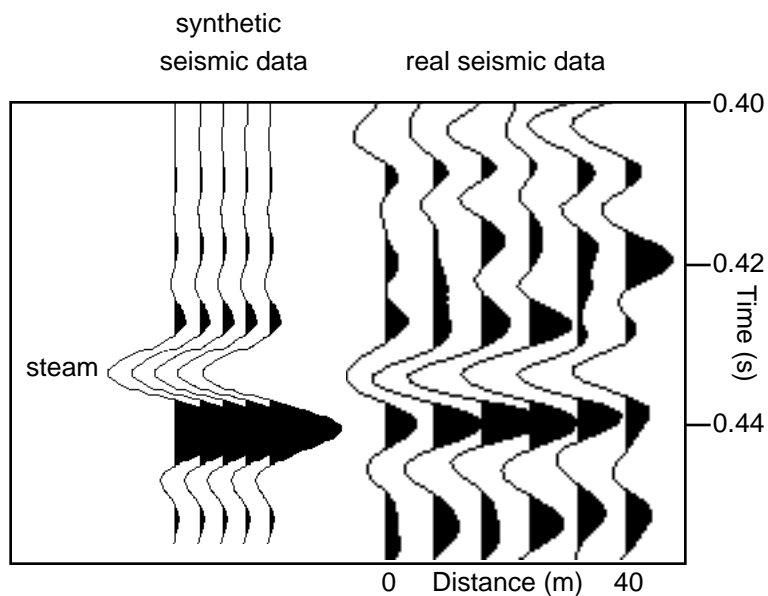


Fig. 6.9 An interpreted steam anomaly in the 1992 data and the synthetic stacked section created from a model with a 6 m steamed zone at the perforation depth (case d). The synthetic data were generated using extracted wavelet (1).

The McMurray/Devonian interface was also modelled by appending a section to each log (Figure 6.10). A constant velocity was used within each unit, taken from sonic log and stacking velocities and theoretical V_p/V_s values. This interface was modelled to observe the behaviour of the top Devonian amplitudes and to ensure that the event exhibited no anomalous amplitude changes over the range of offsets to be used in the analysis. The Devonian event is seen to be a high amplitude peak just below 0.5 s, whose amplitude increases significantly only at the farthest offsets. It will be shown that the farthest offsets must be limited to 500 m because of this increase in amplitude.

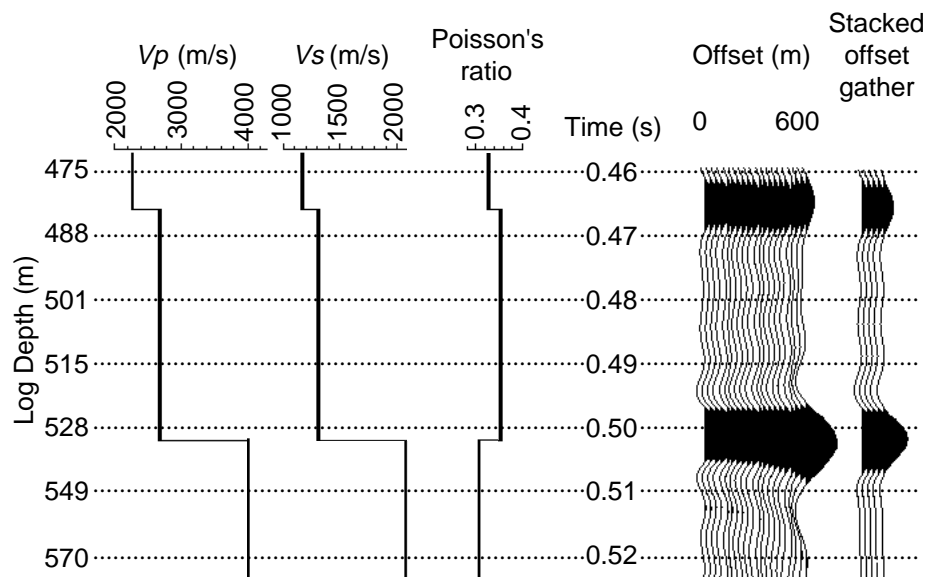


Fig. 6.10 Model for the McMurray/Devonian interface, which occurs at 530 m.

6.2.2 Amplitude extraction

To observe in more detail the behaviour of the modelled seismic amplitudes with offset, amplitudes were extracted from the twelve seismic gathers displayed in Figures 6.6 and 6.7. Since the wavelet used in the generation of the seismic data is not a simple spike and individual boundaries on well logs are closely spaced, the seismic response to a

boundary is not a single, unique event but a combination of interfering events. To obtain meaningful amplitudes, therefore, rms amplitudes were extracted over 10 ms time windows centred on the events under investigation. The extraction window was selected as 10 ms because that is the time window over which amplitudes were extracted from the 3-D data volumes for the amplitude analysis in Chapter 3.

Figures 6.11a and 6.11b show the signed rms amplitudes for gas at the top of the reservoir, gas below a tight streak and no gas. Figures 6.11c and 6.11d display signed rms amplitudes for a 6 m steam zone, an 18 m steam zone and no steam. Since the cold reservoir amplitudes are very low, they are shown on each plot in an insert, at a greatly enlarged vertical scale, so their behaviour with offset can be observed.

The amplitude scales on Figures 6.11a and 6.11c are comparable, as are those on Figures 6.11b and 6.11d. The amplitude extraction window was centred on 0.408 s for the top reservoir models (gas and cold) and at 0.417 s for the gas below the tight streak.

When an Ormsby bandpass wavelet is used in the generation of the synthetic seismic data (Figure 6.11a), both cases of gas in the reservoir result in an increase in absolute amplitude with increasing offset (up to 500 m), although the increase is more pronounced when gas is at the very top of the reservoir. When there is no gas present, the absolute amplitudes decrease gently but the effect may be too small to be observed on field data. For the extracted wavelet (1) data (Figure 6.11b), the amplitude behaviour is more complicated. Gas at the top of the reservoir still results in a significant increase in absolute amplitude with offset but when gas is present below a tight streak, the absolute amplitudes increase to an offset of about 250 m then decrease to 440 m before increasing again. The overall effect over the range of 600 m is almost no AVO gradient. If the farthest offset in real data lies between 300 m and 500 m, a negative gradient may be seen. When no gas is present in the reservoir, the absolute amplitudes decrease to 250 m then increase; the overall effect is a slight increase of amplitude with offset.

Modelling of the steamed zone produces clearer results, as they are similar for both the bandpass and extracted wavelet (1) data. These results are presented in Figures 6.11c and 6.11d (Ormsby bandpass wavelet data and extracted wavelet (1) data, respectively). The amplitude extraction window was centred on 0.438 s. The zero-offset amplitude of the 6 m steamed zone is higher than that of the 18 m steamed zone, because of tuning effects in both cases. The absolute amplitudes increase with increasing offset, especially at the farther offsets. The cold perforation zone sees a decrease in absolute amplitude for both wavelets, although in both cases the zero-offset reflectivity is low and the decrease in amplitude is small.

The results of this modelling indicate that a measurable increase in rms amplitude with increasing source-receiver offset should be observed on processed field seismic data when steam is present within the reservoir. When gas is present in the reservoir, an increase should also be seen but may not be apparent if the gas is trapped below a tight streak. If no gas is present, a low zero-offset reflectivity value is observed but the overall amplitude behaviour depends on the convolving wavelet. Data containing a complex extracted wavelet may produce ambiguous results if all offsets up to 600 m are used in the AVO analysis. For the cases of no gas and gas at the top of the reservoir, an increase in amplitude with offset is the overall effect over the full 600 m offset range. If the offsets are restricted to about 250 m, then the no-gas case should produce an amplitude decrease with offset whereas the gas case should show an increase. When gas is present below a tight streak, a positive, flat or negative gradient may be seen depending on the farthest offset present in the gathers. If the offsets are limited to less than 250 m, an increase in amplitude should be seen. Thus, for the processed field seismic data, if offsets are restricted to less than 250 m, the two gas cases should produce an increase in amplitude with increasing offset, whereas the no-gas case should produce a decrease.

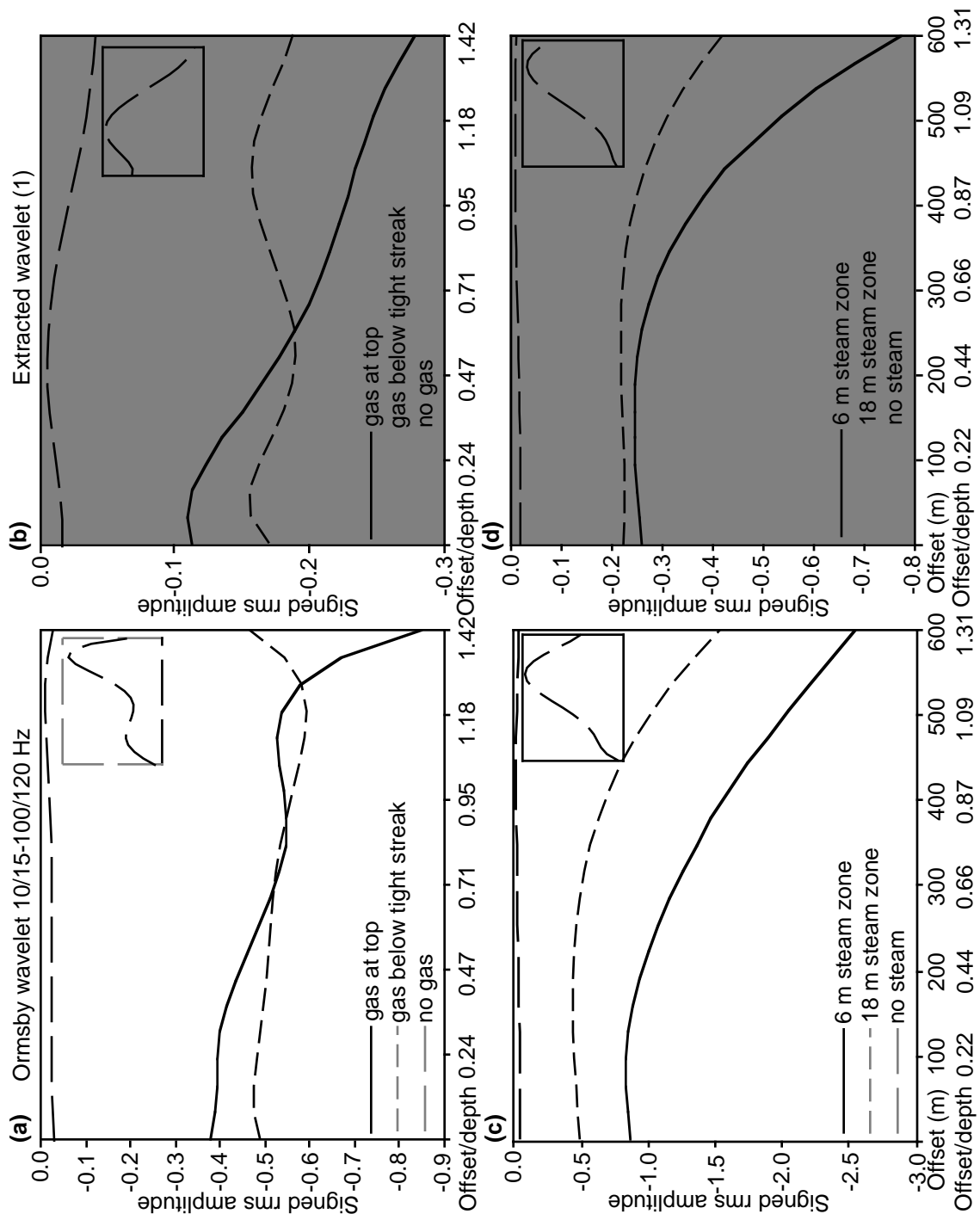


Fig. 6.11 Modelled amplitudes extracted from the synthetic seismic gathers over 10 ms windows. Plots (a) and (b) show amplitudes for the cases of gas at the top of the reservoir, gas below a tight streak and no gas. Plots (c) and (d) show amplitudes for the cases of a 6 m steam zone, an 18 m steam zone and no steam. The amplitudes shown in (a) and (c) are extracted from the data generated using an Ormsby wavelet while those in (b) and (d) are extracted from the data generated using extracted wavelet (1).

In a similar manner, rms amplitudes were extracted for the Devonian event to observe their behaviour, as this event was chosen to be the reference event for the Chiburis AVO analysis. These amplitudes are plotted in Figure 6.12, where it is seen that the amplitudes are reasonably consistent up to an offset of 500 m, particularly for the case using extracted wavelet (1). Beyond 500 m the amplitudes increase substantially, thus indicating that offsets over 500 m should probably not be used in the AVO analysis. This problem is addressed in the following discussion.

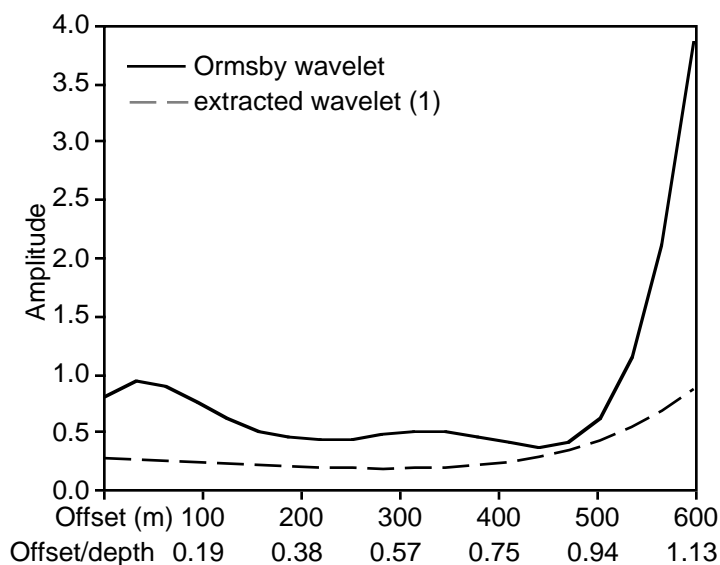


Fig 6.12 Modelled rms amplitudes for the Devonian (reference) event.

Since the Chiburis method is the chosen method of AVO analysis for these data, the modelled extracted amplitudes were used to generate conditioned amplitude ratios. These ratios were calculated using equations 6.5 and 6.6, based on the rms amplitudes displayed in Figures 6.11 and 6.12, and the results are presented in Figure 6.13 for the gas cases and Figure 6.14 for the steam cases, for both the Ormsby bandpass wavelet and extracted wavelet (1).

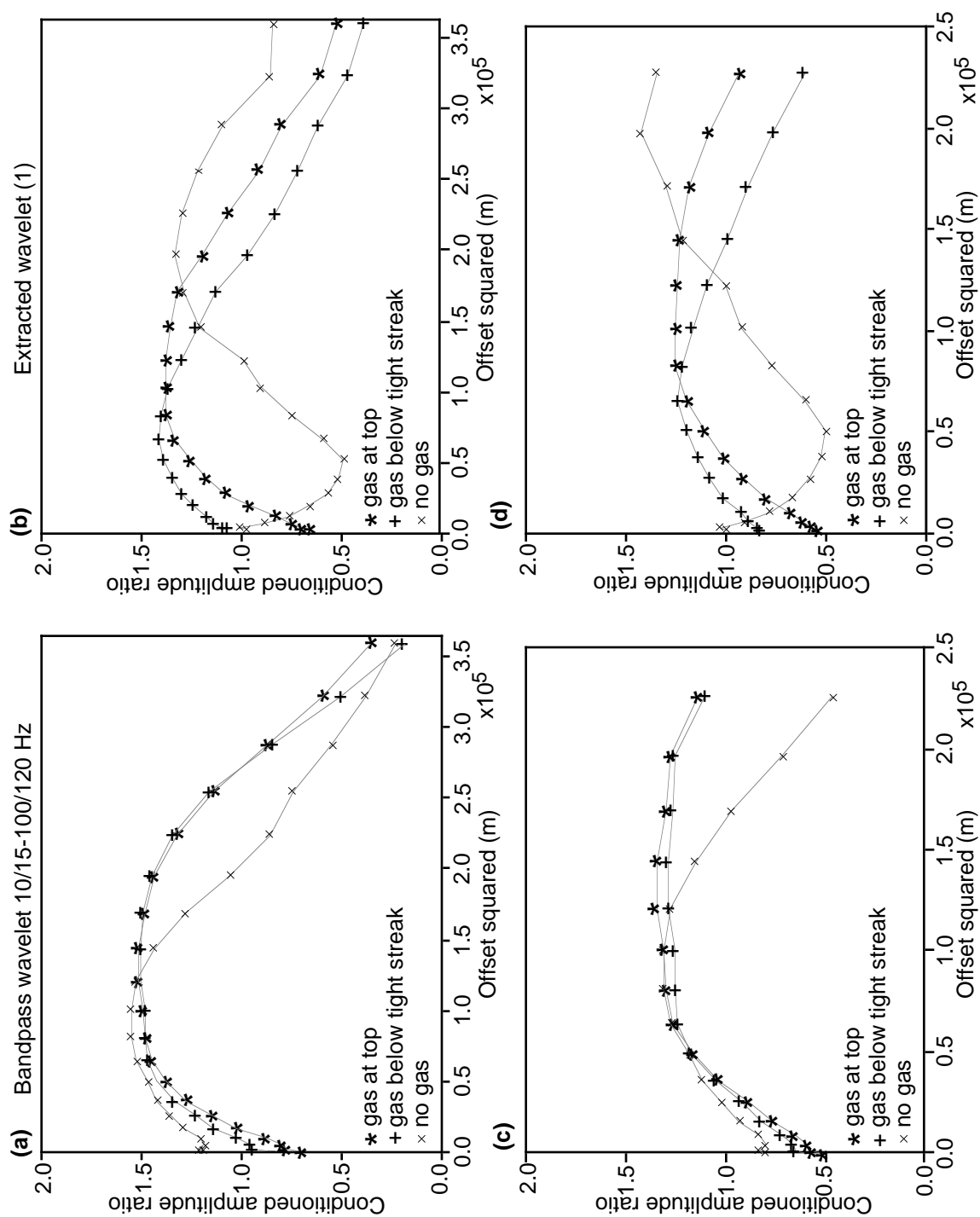


Fig. 6.13 Modelled conditioned amplitude ratios for the gas cases. In plots (a) and (b) offsets up to 600 m are included whereas in plots (c) and (d) offsets are restricted to less than 500 m. Extracted wavelet (1) is that one derived from the 1990 3-D seismic data.

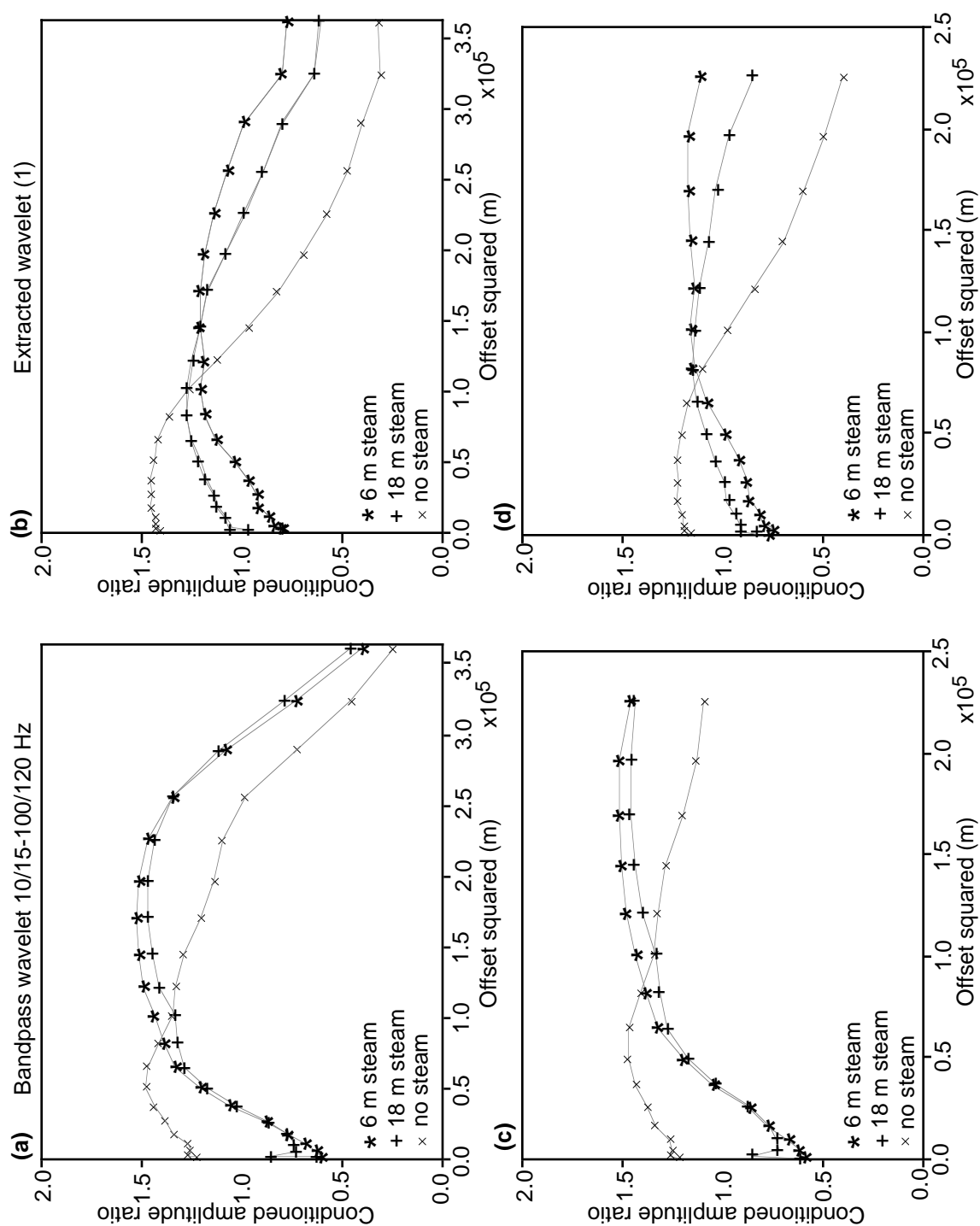


Fig. 6.14 Modelled conditioned amplitude ratios for the steam cases. In plots (a) and (b) offsets up to 600 m are included whereas in plots (c) and (d) offsets are restricted to less than 500 m. Extracted wavelet (1) is that one derived from the 1990 3-D seismic data.

The top plots in each figure show the calculated amplitude ratios for all offsets up to 600 m whereas in the lower plots the offsets are restricted to those less than 500 m. It is apparent that using offsets up to 600 m is likely to give ambiguous results. Restricting the offsets to 500 m results in amplitude ratio increases with offset for the gas cases modelled using an Ormsby bandpass wavelet. For the extracted wavelet (1), offsets must be restricted to those below about 250 m (offset squared = 0.625×10^5 m) if a distinction is to be made between the gas cases and the no-gas case. The modelled amplitude ratios for the steam cases have an increase with offset for both the Ormsby wavelet and extracted wavelet (1) while for the non-steam case the ratios decrease with offset, for offsets up to 500 m.

Similar synthetic seismic gathers were also generated using extracted wavelet (2), which was derived from the 3-C data. Modelled cases were those of gas at the top of the reservoir and no-gas. The Chiburis conditioned amplitudes extracted from these gathers are plotted in Figure 6.15 and indicate that all offsets (up to 500 m) should be used in the analysis of gathers created from these 3-C data. For the 3-D data (Figure 6.13) it was clear that offsets had to be restricted to under 250 m to avoid ambiguity in the gas cases.

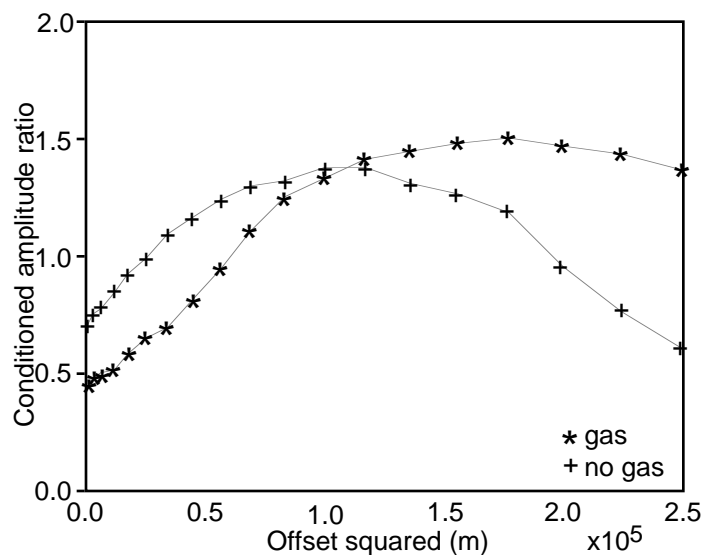


Fig. 6.15 Modelled conditioned amplitude ratios from synthetic seismic data created with extracted wavelet (2), from the 3-C data.

6.3 AVO analysis of Cold Lake data

The seismic data used in the AVO analysis were the P - P data from line 470-93 at the AABBW pads and the two 3-D surveys at the D3 pad. Careful, amplitude-preserving and surface-consistent processing (including static corrections, deconvolution and amplitude balancing) is recommended for data to be used in AVO analysis (Yu, 1985; Allen and Peddy, 1993). Each data set from Cold Lake had spherical divergence compensation applied then trace amplitude balancing designed over a window the length of the whole trace, in order to retain relative amplitude information. Surface-consistent deconvolution was applied to the 3-D data volumes whereas record-based spiking deconvolution and surface-consistent refraction static corrections were applied to line 470-93. The data were also NMO-corrected and NMO stretch was muted.

Pre-stack migration is recommended to collapse the Fresnel zone and correctly position events (Allen and Peddy, 1993; Jones et al., 1995). For the 3-D seismic data, up to 150 CDP gathers were extracted from the data volume around several areas of interest. These gathers and all the CDP gathers along line 470-93 were pre-stack time-migrated using f - k migration. Each NMO-corrected, muted gather was restricted to offsets less than 500 m. The individual data sets were sorted into common offset gathers and pre-stack f - k migrated in that domain before being resorted into CDP gathers. Finally the data were bandpass filtered between frequency limits of 10/15-100/120 Hz.

6.3.1 3-D data selection

Anomalies for AVO analysis were chosen from the amplitude maps of the migrated 3-D data and the “difference” 3-D data that were displayed previously in Figures 3.11a (1990 data) and 3.16a and in Figures 3.11b (1992 data) and 3.16b. Anomalies were analysed over a 10 ms time window centred on 0.42 s for the 1990 data and difference data in Figures 3.11a and 3.16a, whereas for Figures 3.11b and 3.16b, the analysis window

was centred on 0.437 s. The two difference data amplitude maps will, therefore, be referred as "shallow" and "deep", for clarity. It is interpreted that anomalies on the 1990 amplitude map are caused by gas-saturated zones and, possibly tight streaks, because the spatial distribution of anomalies on the stacked data and shallow difference data amplitude maps are not always the same. Tight streaks should not appear on the shallow difference amplitude map because they are present in both the 1990 and 1992 data. If the low velocity interval is present in only one vintage of data (1990 or 1992), anomalies should appear on both the time data amplitude map for that vintage of data, and on the difference data amplitude map. On the 1992 amplitude map, the anomalies are interpreted to be caused mainly by the presence of steam with few tight streaks, because the spatial distribution of anomalies on the stacked data and deep difference data amplitude maps are similar.

Six areas for analysis of the 1990 data were selected on the basis that amplitude anomalies appeared on both amplitude maps (1990 stacked data and shallow difference data), on only one map or on neither. Similarly, six areas were chosen from the 1992 stacked data amplitude map and the deep difference amplitude map. These six areas are indicated in Figure 6.16, which shows the 1990 stacked amplitude and shallow difference amplitude maps, and Figure 6.17, which shows the 1992 stacked amplitude and deep difference amplitude maps. In the 1990 data, most of the amplitude anomalies are observed at about 0.420 s while in the 1992 data most of the anomalies are deeper, near 0.437 s. The areas selected for analysis are listed in Tables 6.1 and 6.2. In the comments column of each of these tables are given the interpretations of the anomalies. The anomalies are attributed to gas if seen in the 1990 data (areas 3, 4, 5, 6 and 7) and steam if seen in the 1992 data (areas 1, 4, 8, 10, 11 and 12). One area from each survey (2 and 9) was chosen because anomalies appeared on none of the amplitude maps.

Examples of some of the analysed anomalies are displayed in Figures 6.18 and 6.19, where corresponding extracts of stacked, migrated seismic data from the 1990 and

1992 surveys are shown. Reds represent negative reflection coefficients (troughs) and blues represent positive reflection coefficients (peaks). The analysed anomalies are indicated by arrows.

Figure 6.18 shows anomalies near 0.420 s that were selected from the 1990 amplitude map and shallow difference map in Figure 6.16. Figures 6.18a and 6.18b show an anomaly which is present on the 1990 data but not on the 1992 data (anomaly 6). It is interpreted to be a gas anomaly. In Figures 6.18c, 6.18d, 6.18e and 6.18f, anomalies are present on both vintages of data, although appearing a little stronger on the 1990 lines. These anomalies are present on the 1990 time amplitude map but the difference in amplitude between the 1990 and 1992 lines is not large enough to generate a strong anomaly on the shallow difference amplitude map. In Figures 6.18c and 6.18d the anomaly (number 4) appears as a red trough below a blue peak, which could be a gas-saturated zone beneath a tight streak in 1990 and steam below the tight streak in 1992.

In Figures 6.18e and 6.18f (anomaly 5) there is a high amplitude red trough on the 1990 data at 0.425 s but on the 1992 data the overlying blue peak has the higher amplitude. It appears that gas may be present in 1990 but the 1992 situation is uncertain. It is possible that the amplitudes contributing to the anomaly in 1992 come from the blue peak above 0.42 s rather than the red trough beneath, so steam may not be present in 1992.

Figure 6.19 shows anomalies near 0.437 s, selected from the 1992 amplitude map and the deep difference map in Figure 6.17. A very high amplitude anomaly on the 1992 line in Figure 6.19b is absent from the 1990 data in Figure 6.19a and is interpreted to be caused by the presence of steam (anomaly 11). Figures 6.19c and 6.19d show anomalies on both vintages of data (anomaly 8). Possibly steam was present in 1992 and gas in 1990, both trapped beneath a tight streak. The final example shows an amplitude anomaly on the 1990 data but not on the 1992 data (anomaly 7); selected as a no steam case. Gas could be present in 1990.

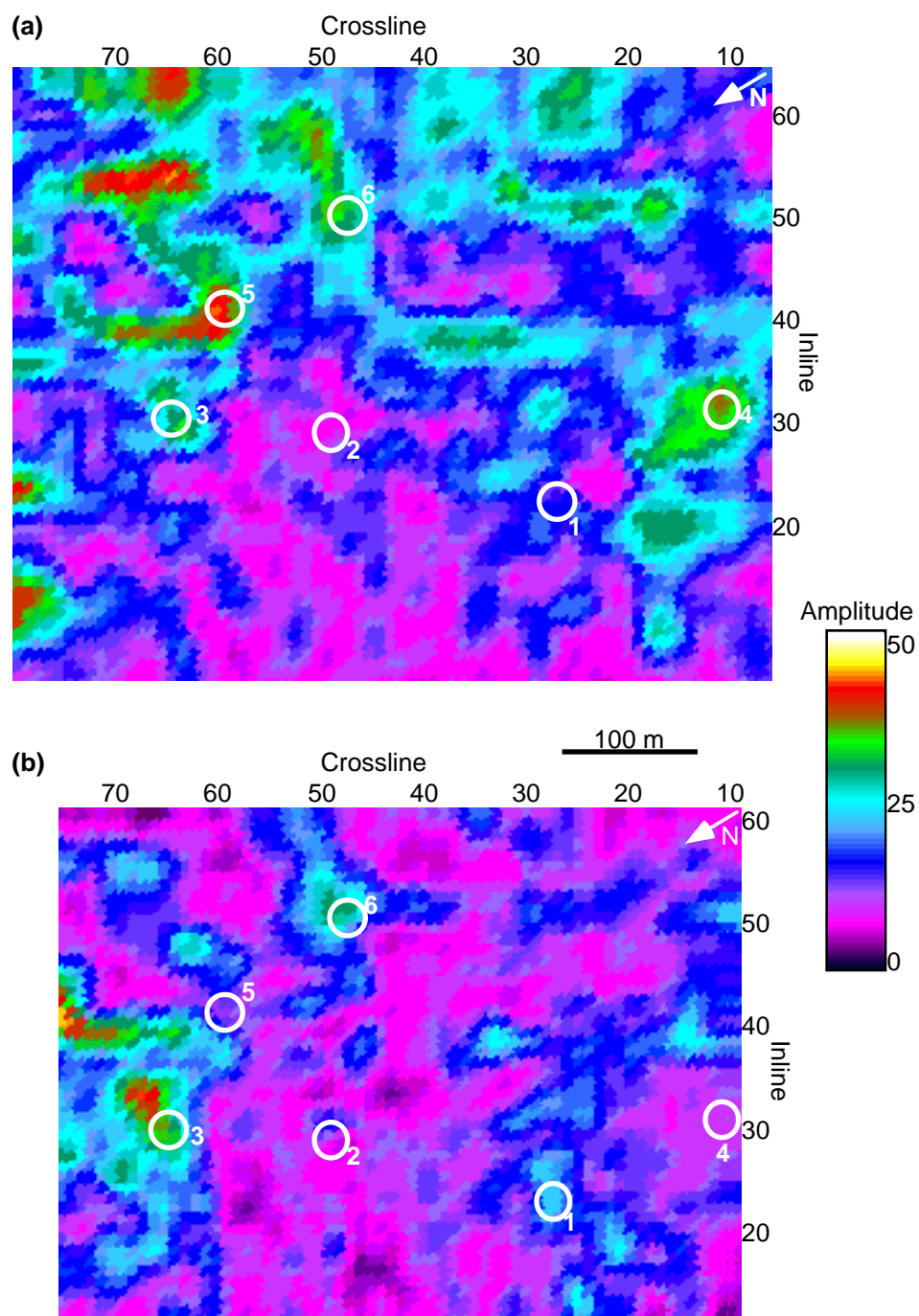


Fig. 6.16 Analysed anomalies from the (a) 1990 time amplitude map and (b) shallow difference amplitude map, over a 10 ms window centred on a time of 0.42 s.

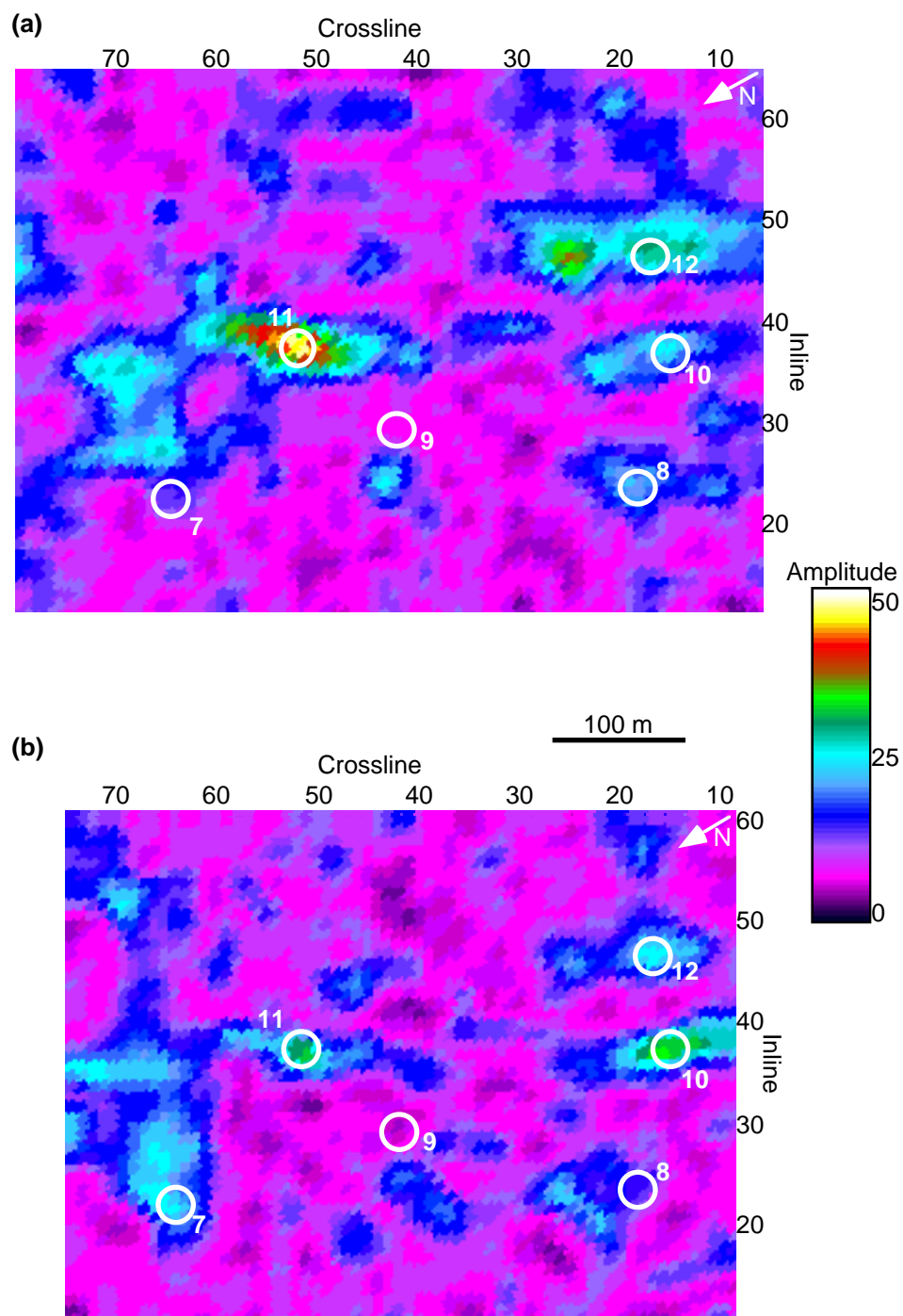


Fig. 6.17 Analysed anomalies from the (a) 1992 time amplitude map and (b) deep difference amplitude map, over a 10 ms window centred on a time of 0.437 s.

Table 6.1 Analysed amplitude anomalies from the 1990 stacked data and shallow difference data maps in Figure 6.16.

Area	Location	1990 amplitude anomaly	Difference amplitude anomaly	Comments
1	iline 23 xline 27	no	yes	Anomaly only in 1992. Interpreted steam in 1992.
2	iline 29 xline 52	no	no	No anomaly on either.
3	iline 30 xline 65	yes	yes	Anomaly only in 1990. Interpreted gas in 1990.
4	iline 31 xline 11	yes	no	Interpreted gas in 1990 and steam in 1992.
5	iline 41 xline 60	yes	no	Probably gas in 1990 but tight streak likely in 1992.
6	iline 50 xline 48	yes	yes	Anomaly only in 1990. Interpreted gas in 1990.

Table 6.2 Analysed amplitude anomalies from the 1992 stacked data and deep difference data maps in Figure 6.17.

Area	Location	1992 amplitude anomaly	Difference amplitude anomaly	Comments
7	iline 21 xline 64	no	yes	Anomaly in 1990 (possibly gas). No steam in 1992.
8	iline 23 xline 19	yes	no	Anomaly on 1992 and 1990. Interpreted as steam in 1992 and gas in 1990.
9	iline 29 xline 42	no	no	Anomaly on neither.
10	iline 37 xline 16	yes	yes	Anomaly only in 1992 data. Interpreted steam in 1992.
11	iline 37 xline 52	yes	yes	Anomaly only in 1992 data. Interpreted steam in 1992.
12	iline 46 xline 17	yes	yes	Anomaly only in 1992 data. Interpreted steam in 1992.

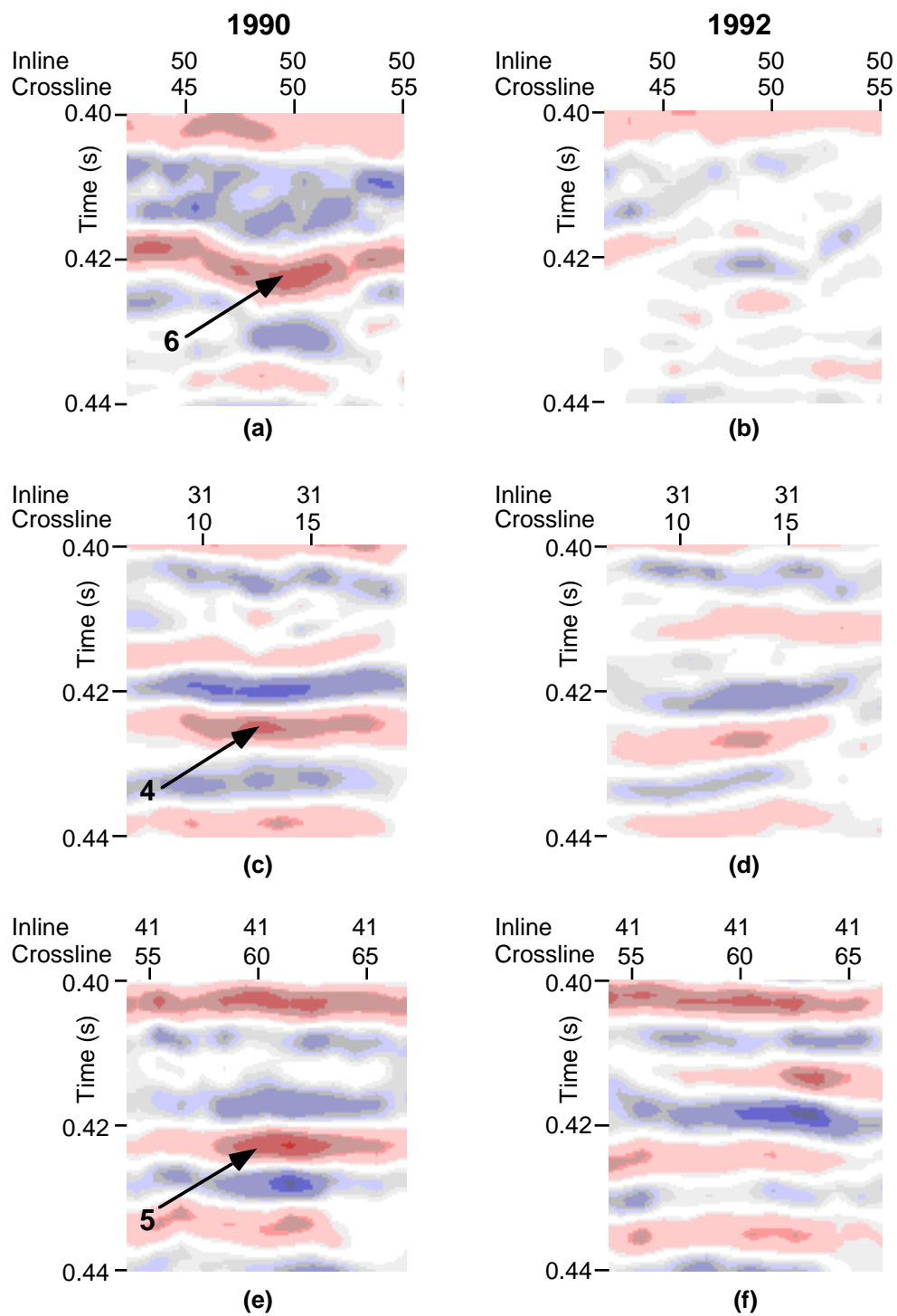


Fig. 6.18 Examples (numbered) of amplitude anomalies selected from the 1990 amplitude and shallow difference amplitude maps. Anomalies occur near 0.420 s.

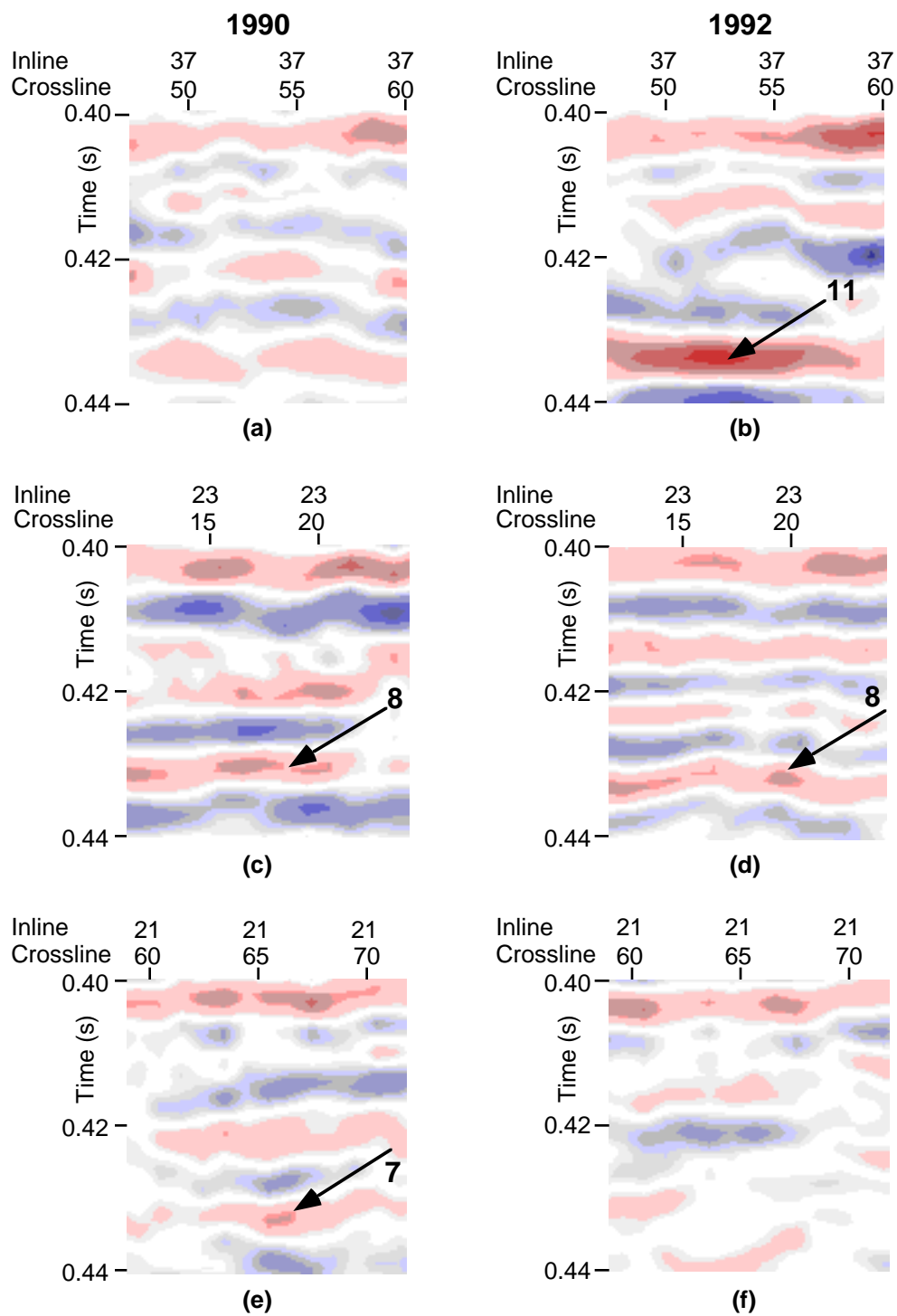


Fig. 6.19 Examples (numbered) of amplitude anomalies selected from the 1992 amplitude and deep difference amplitude maps. Anomalies occur near 0.437 s.

6.3.2 AVO analysis of 3-D data

Supergathers were created from adjacent CDP gathers along three inlines and three crosslines centred on each of the twelve selected anomalies. Supergathers (Ostrander, 1984) are designed to improve the signal to noise ratio of the data under analysis. These gathers were extracted from the pre-stack migrated, filtered data sets for both vintages of data. The traces in each supergather were sorted by offset then stacked into traces at offset spacings of 4 m, up to 500 m. Because of the geometry of the 3-D survey layout, not all offsets were present in the supergathers and those gathers nearer to the edges of the survey lacked the longer offsets. Each of the twelve anomalies was analysed on both the 1990 and 1992 data in order to provide two complementary assessments.

Examples of two of the analysed supergathers are presented in Figures 6.20 and 6.21. The apparently low zero-offset reflectivities seen on these gathers is caused by the filtering of shot-generated surface energy which was extremely strong at these near offsets. It is believed that relative amplitudes between the target and reference events are preserved. Figure 6.20 displays supergather 6, created to analyse an amplitude anomaly observed on the 1990 stacked data but not the 1992 data. This anomaly is interpreted to be caused by a gas-saturated zone in 1990. The target event (T) is at about 0.42 s and the reference event (R) is the Devonian horizon, which occurs a little later on the 1992 data than on the 1990 data. For the target event, a trough is seen clearly on the 1990 supergather while on the 1992 supergather the character of events at this time of 0.42 changes with offset. The maximum amplitude of each trough or peak was picked interactively; the straight line annotated on the figures is meant only to indicate the approximate arrival time of the analysed events. Supergather 11 is shown in Figure 6.21. An amplitude anomaly which is observed on the 1992 stacked data at about 0.438 s, but is absent from the 1990 data, is interpreted to be caused by the presence of steam in 1992. The arrival time of the reference event is significantly later on the 1992 supergather.

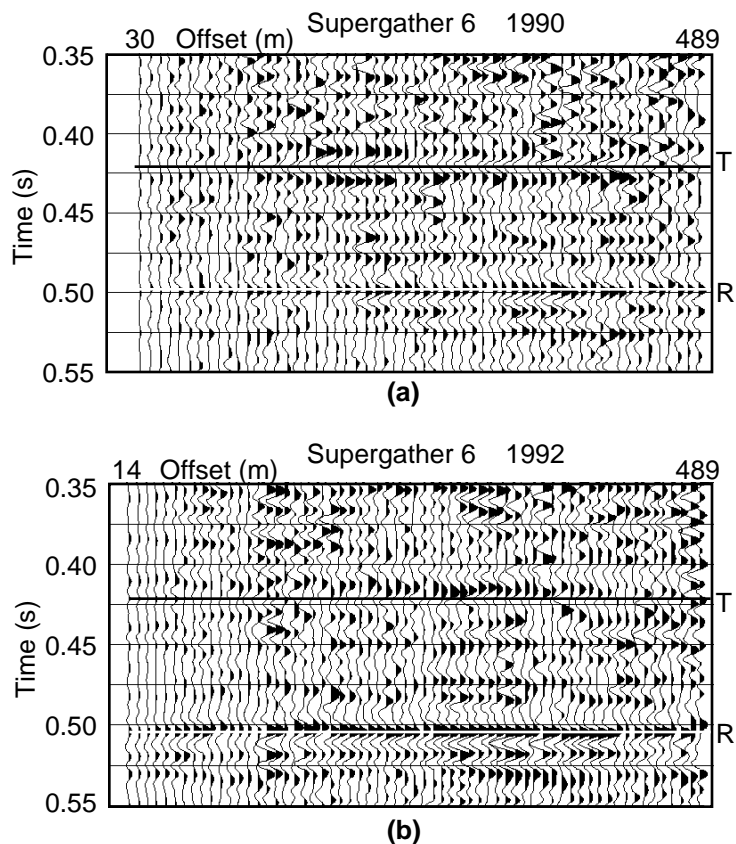


Fig. 6.20 Supergather 6, created to analyse an amplitude anomaly observed on the 1990 stacked data but not on the 1992 data. "T" denotes the target event and "R" the reference event (Devonian).

Target and reference events were picked interactively on each pair of twelve supergathers and the amplitudes of each event were extracted from the data over a 10 ms time window centred on the pick of that event.

Chiburis's method was used to calculate the conditioned amplitude ratio for each offset in the supergathers. An example of plots of raw amplitudes and conditioned amplitude ratios is presented in Figure 6.22. In this case, an increase in amplitude with offset is seen clearly on the raw amplitudes for the target event; this increase is retained in the plot of conditioned amplitude ratios.

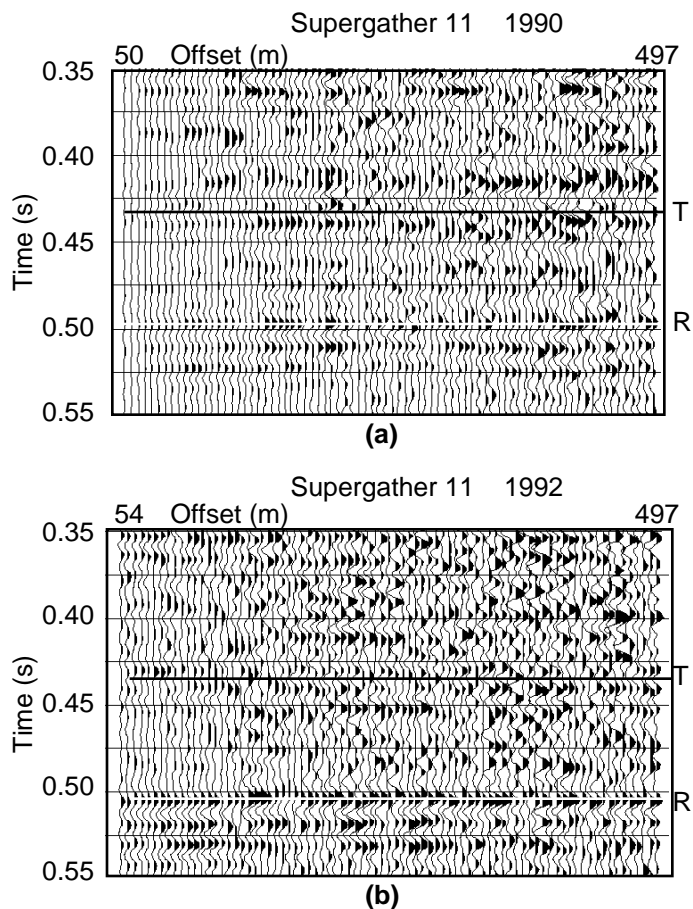


Fig. 6.21 Supergather 11, created to analyse an amplitude anomaly observed on the 1992 stacked data but not on the 1990 data. "T" denotes the target event and "R" the reference event (Devonian).

Figure 6.23 shows these ratios for each of the supergathers 1 to 6, as determined from the 1990 data. Each star represents a conditioned amplitude ratio and the dashed line is a least-squares linear fit to these data points. It should be noted that the conditioned amplitudes are all scaled between 0 and 2 and do not represent the actual amplitudes of the target event. The magnitude of the zero-offset conditioned amplitude does not reflect the magnitude of the zero-offset reflectivity but the trend validly depicts the behaviour of amplitude with offset (Chiburis, 1984; 1993).

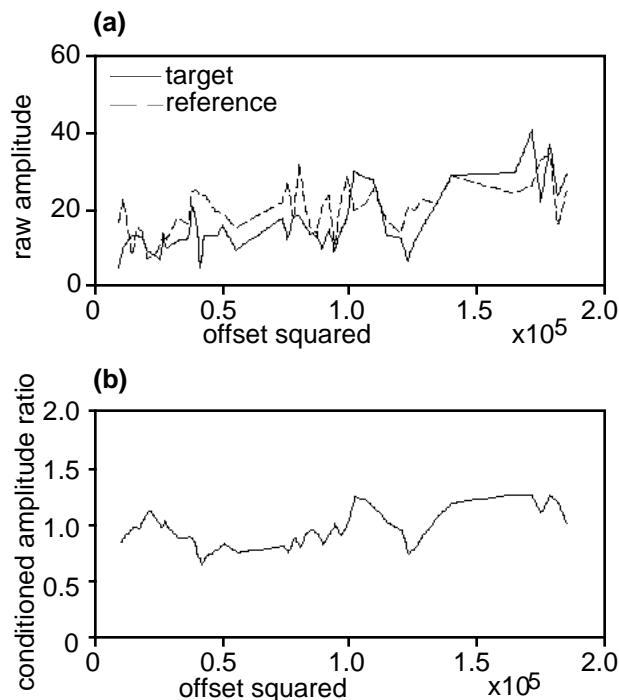


Fig 6.22 Plot of the (a) raw amplitudes of the target and reference events and the (b) conditioned amplitude ratio. The increase in amplitude with offset observed in the raw amplitudes is preserved in the conditioned amplitude ratio.

For each supergather in Figure 6.23 a decrease in amplitude is observed with increasing offset, for offsets up to 500 m. The modelled amplitudes discussed in section 6.2.2 and presented in Figures 6.11 and 6.13 suggest that ambiguous results may be obtained over long offsets for the cases of gas below a tight streak and of no gas, which are the conditions under investigation with these 1990 supergatherers. The plot in Figure 6.13d, which shows the modelled conditioned amplitude ratios calculated from a synthetic gather created with the extracted wavelet (1), suggests that limiting the offsets to those less than about 250 m would produce more definitive results. The gas case should show an increase in amplitude with offset while the no-gas case should show a decrease. Since the extracted wavelet (1) was obtained from these 1990 data under investigation, the offsets were limited to those less than 250 m and the analysis was repeated, with results shown in Figure 6.24.

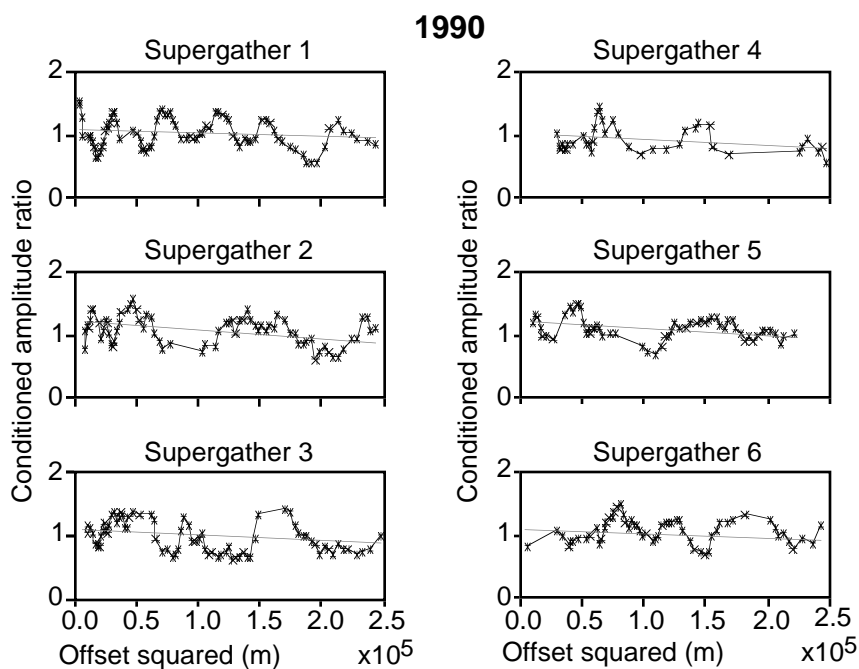


Fig. 6.23 Plots of conditioned amplitude ratio against offset squared (after Chiburis, 1984 and 1993) for supergathers 1 to 6, extracted from the 1990 data. All offsets up to 500 m are included.

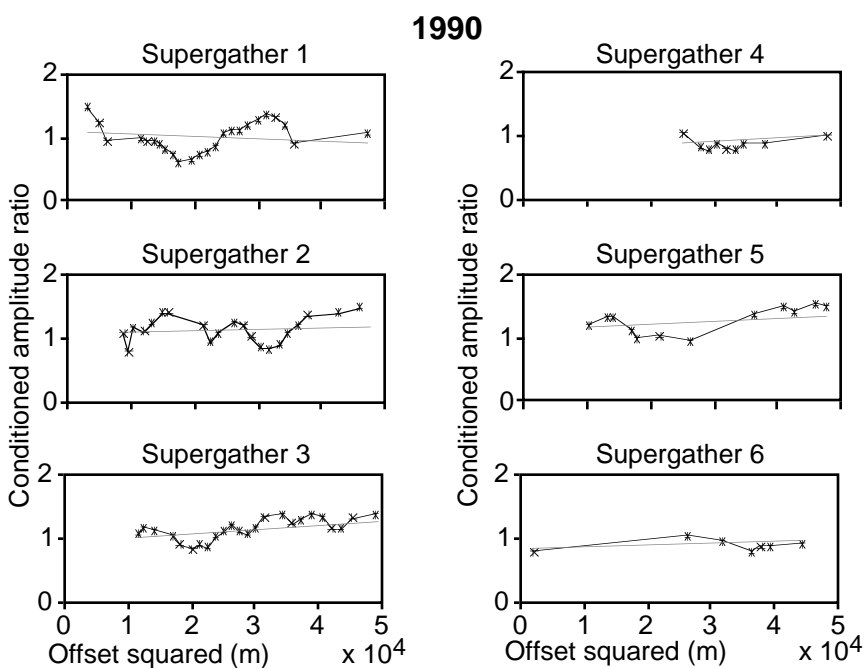


Fig. 6.24 Plots of conditioned amplitude ratio against offset squared for supergathers 1 to 6, extracted from the 1990 data. Offsets are limited to those below 250 m.

Now only supergather 1 has a decrease in amplitude with increasing offset. Supergathers 2, 3, 4, 5 and 6 show increases; those on supergathers 3 and 5 being large.

Corresponding conditioned amplitude ratios obtained from the AVO analysis of supergathers 1 to 6 from the 1992 data are plotted in Figure 6.25. Since steam, not gas, produces anomalies in the 1992 data, and there is no ambiguity in the modelled amplitudes for steam zones plotted in Figures 6.14c and 6.14d, all offsets up to 500 m are included in the AVO analysis. Increases of amplitude with offset are seen clearly in Figure 6.25 for supergathers 1 and 4. On all of the other supergathers the trends are almost flat, although for supergathers 2 and 5 the gradients are negative while for supergathers 3 and 6 they are positive.

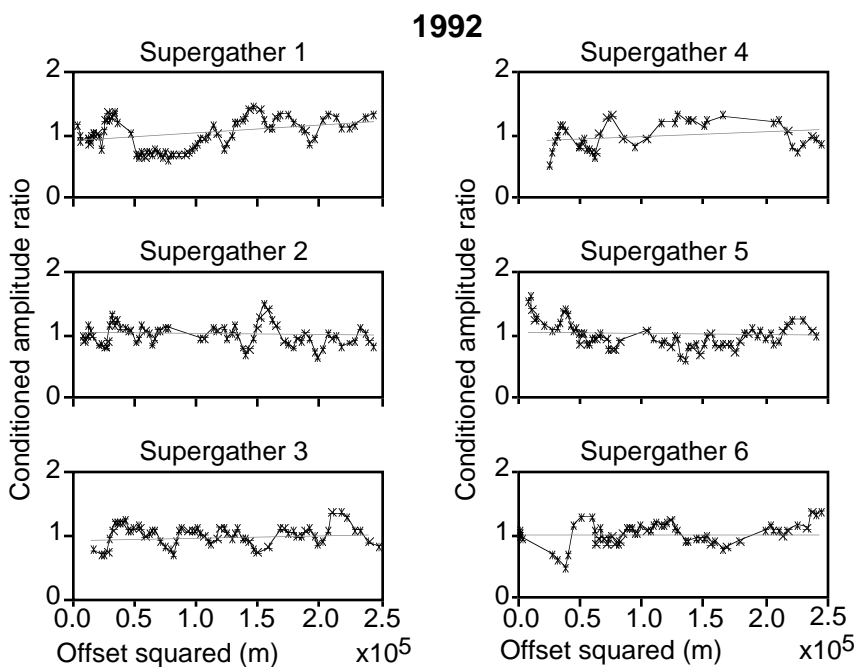


Fig. 6.25 Plots of conditioned amplitude ratio against offset squared for supergathers 1 to 6, extracted from the 1992 data. All offsets up to 500 m are included.

Conditioned amplitude ratios plotted against offset squared for anomalies 7 to 12, selected from the 1992 amplitude map and deep difference map displayed in Figure 6.17, are shown in Figures 6.26 and 6.27. The supergatherers in Figure 6.26 were extracted from the 1992 data, in which all offsets up to 500 m were included, and those in Figure 6.27 from the 1990 data, in which offsets up to 250 m only were included. For supergather 7 in Figure 6.26 a large negative gradient is seen whereas large positive gradients occur for supergatherers 8 and 10. For supergatherers 9, 11 and 12 the gradient is positive, although very small in magnitude. On the corresponding 1990 supergatherers in Figure 6.27, negative gradients are seen for numbers 9, 10, 11 and 12 and positive gradients for numbers 7 and 8.

For each of these plots in Figures 6.24, 6.25, 6.26 and 6.27, values of zero-offset intercept and gradient were extracted. The AVO difference (or "AVO") was then calculated using equation 6.7. These values are listed in Tables 6.3 and 6.4. The 1990 values were obtained using only the shorter offsets and an N value of 50000 was used whereas for the 1992 data, all offsets up to 500 m and an N value of 250,000 were used. Chiburis (1993) shows a model in which AVO decreases when Poisson's ratio in the target interval increases, all other parameters being constant. It might be possible to relate AVO to Poisson's ratio in the gas or steamed zone but the parameters of the overlying layer would have to remain constant. Since these low velocity intervals are found at different depths within the reservoir, the overlying layer will not always be the same one. The velocity profile of the reservoir is complicated, so to assume a constant velocity in a layer overlying the low velocity would be unrealistic.

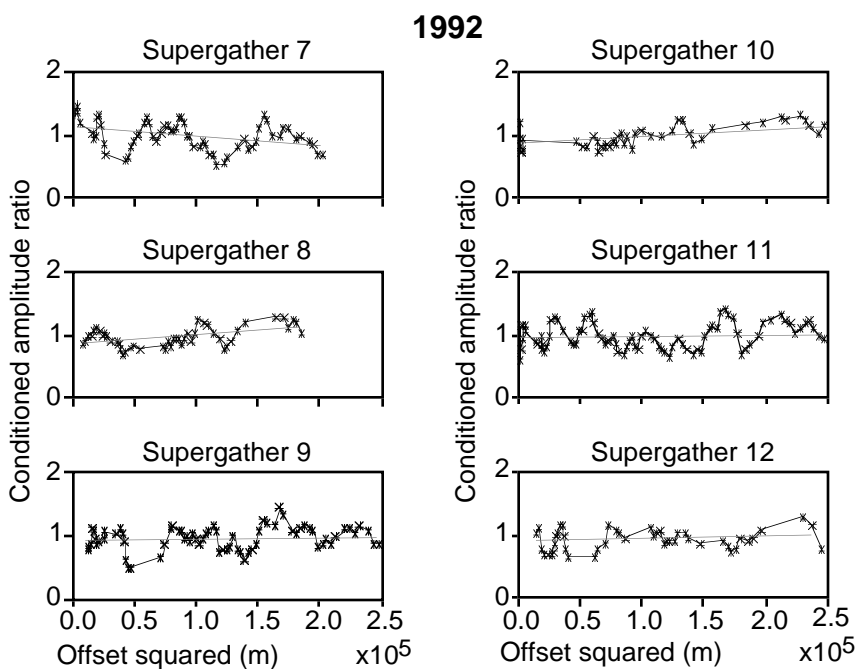


Fig. 6.26 Plots of conditioned amplitude ratio against offset squared for supergathers 7 to 12, extracted from the 1992 data. All offsets up to 500 m are included.

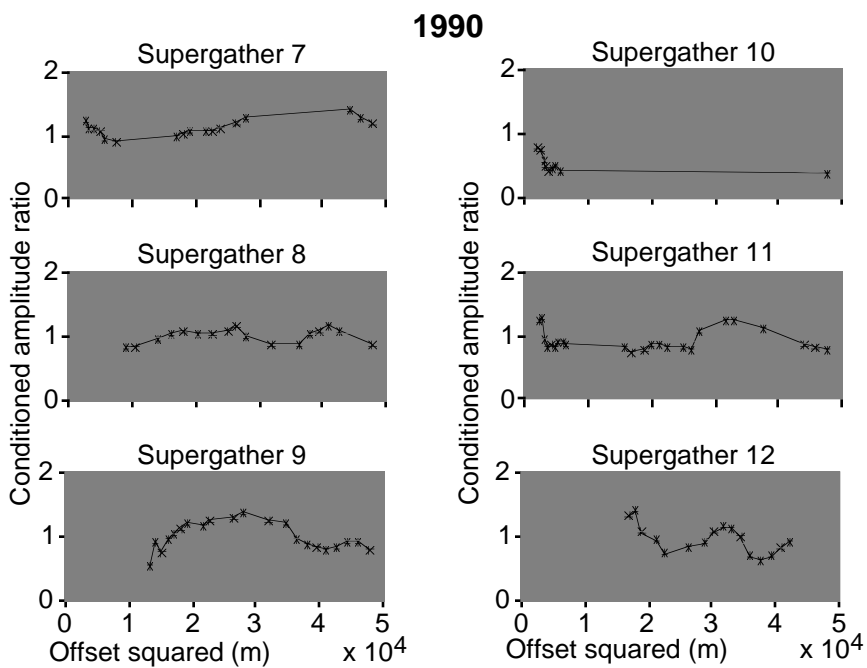


Fig. 6.27 Plots of conditioned amplitude ratio against offset squared for supergathers 7 to 12, extracted from the 1990 data. Offsets are limited to those below 250 m.

Table 6.3 AVO difference values calculated for supergathers 1-6, chosen to analyse anomalies observed on the 1990 data at about 0.42 s.

Supergather	Intercept*1000	Gradient*1000	AVO difference
1990-1	1089	-0.00013	-0.006
1992-1	867	+0.00108	+0.366
1990-2	1168	+0.00153	+0.068
1992-2	1005	-0.00047	-0.111
1990-3	941	+0.01130	+0.684
1992-3	936	+0.00045	+0.123
1990-4	773	+0.00322	+0.206
1992-4	879	+0.00094	+0.276
1990-5	1202	+0.00955	+0.488
1992-5	1033	-0.00103	-0.233
1990-6	887	+0.00109	+0.061
1992-6	975	-0.00026	-0.066

Table 6.4 AVO difference values calculated for supergathers 7-12, chosen to analyse anomalies observed on the 1992 data at about 0.437 s.

Supergather	Intercept*1000	Gradient*1000	AVO difference
1992-7	1144	-0.00156	-0.341
1990-7	1065	+0.00049	+0.243
1992-8	949	+0.00148	+0.458
1990-8	948	+0.00217	+0.114
1992-9	967	+0.00007	+0.020
1990-9	1071	-0.00285	-0.133
1992-10	920	+0.00166	+0.437
1990-10	534	-0.00406	-0.368
1992-11	961	+0.00066	+0.180
1992-11	944	-0.00436	-0.232
1992-12	898	+0.00049	+0.136
1990-12	1148	-0.01553	-0.547

Comments on the results from all of the twelve analysed anomalies are given below:

- (1) An amplitude anomaly is absent on the 1990 amplitude map but present on the difference amplitude map. The AVO difference calculated for the 1990 data is negative but is strongly positive for the 1992 data, confirming the interpretation of an absence of gas in 1990 and the presence of steam in 1992.
- (2) No anomalies exist on either map. The 1992 AVO difference value is negative and the 1990 value is positive, although very small.
- (3) Anomalies are seen on both the 1990 amplitude and difference amplitude maps, indicating an absence of an anomaly in 1992. It was interpreted that a gas-saturated zone caused the anomaly in 1990. The AVO difference values are both positive. However, on the 1990 supergather in Figure 6.24 a large positive gradient is clearly seen while on the 1992 supergather in Figure 6.25 the gradient is almost flat. The strong positive gradient on the 1990 data supports the interpretation of the presence of gas in 1990. On the Clearwater to Devonian isochron difference map, previously displayed in Figure 3.8a, this anomaly lies in an area of higher interval traveltimes in 1990 than in 1992. It was suggested in section 3.4 that these higher traveltimes may be caused by the presence of gas-saturated intervals in 1990. This AVO analysis supports that hypothesis.
- (4) The 1990 amplitude map shows an anomaly while the difference map does not. Because of the character of the seismic data (a trough below a peak, shown in Figures 6.18c and 6.18d) it was interpreted that gas existed in 1990 and steam in 1992. The AVO differences are both positive, supporting this interpretation, although the nearest offsets are absent from the supergatherers.
- (5) An amplitude anomaly is observed in both the 1990 and 1992 data (displayed in Figures 6.18e and 6.18f). It was thought that gas was present in 1990 but the 1992 situation was uncertain, although the character of the anomaly indicated a tight streak rather

than a low velocity zone. The positive AVO difference in 1990 and negative value in 1992 implies the presence of gas in 1990 and absence of steam in 1992.

(6) A very strong amplitude anomaly is seen on the 1990 data and is absent on the 1992 data (Figures 6.18a and 6.18b), suggestive of a gas-saturated zone in 1990. The AVO difference is positive for the 1990 gather and negative for the 1992 gather, thus supporting the interpretation.

(7) An anomaly is absent from the 1992 data but is seen on the difference amplitude map (Figure 6.17), possibly due to the presence of gas in 1990. A very strong negative AVO difference is seen in the 1992 data and a positive difference in the 1990 data. This supports the interpretation of the absence of a steam anomaly in 1992 and the presence of gas in 1990.

(8) Anomalies are observed in both vintages of data (Figures 6.19c and 6.19d) and are attributed to steam zones in 1992 and gas zones in 1990. Both AVO difference values are positive.

(9) Neither of the data set exhibits an anomaly. The 1990 AVO value is negative and, although the 1992 AVO value is positive, it is very small.

(10) Anomalies appear on both the 1992 amplitude and difference amplitude maps (Figure 6.17) and are attributed to the presence of steam in 1992 and absence of an anomaly in 1990. This interpretation is supported by the positive AVO value for the 1992 data and the negative AVO value for the 1990 data.

(11) A strong amplitude anomaly is observed on the 1992 data but not the 1990 data (Figures 6.19a and 6.19b) and is interpreted to be caused by steam. A small positive AVO difference value is calculated for the 1992 data and a small negative AVO value for the 1990 data.

(12) Again, an anomaly exists in the 1992 data but not the 1990 data and the AVO difference values, which are positive in 1992 and negative in 1990, support the interpretation of the presence of steam in 1992.

The AVO results for the 3-D data sets analysed are summarised in Table 6.5. Of the 24 supergathers analysed, 21 had AVO values that agreed with the interpretation of amplitude anomalies as being caused by low velocity intervals or, for anomaly 5 in 1992, a tight streak. The negative AVO value for anomaly 5 in 1992 implies that the amplitude anomaly on the stacked data is caused by the interpreted tight streak (blue peak just above 0.42 s in Figure 6.18f) rather than a low velocity zone. The enhancement of this event compared with the corresponding event in the 1990 stacked data (Figure 6.18e) could be a tuning effect due to the presence of a lower velocity zone shallower in the section, at about 0.412 s.

Table 6.5 Summary of AVO results for the 3-D data.

Anomaly	1990 amplitude anomaly	1992 amplitude anomaly	1990 AVO value agrees	1992 AVO value agrees
1	no	yes	yes	yes
2	no	no	no	yes
3	yes	no	yes	no
4	yes	yes	yes	yes
5	yes	yes	yes	yes
6	yes	no	yes	yes
7	yes	no	yes	yes
8	yes	yes	yes	yes
9	no	no	yes	no
10	no	yes	yes	yes
11	no	yes	yes	yes
12	no	yes	yes	yes

The AVO analysis presented here confirms that the amplitude anomalies observed on the stacked data are due predominantly to low velocity intervals. The analysis could be taken further by pre-stack migrating both of the 3-D data volumes and sorting into 3x3 supergathers covering the whole survey. AVO analysis would be useful for confirming the spatial distribution of low velocity zones at different depths within the reservoir, as mapped from the stacked 3-D data volumes and the instantaneous frequency analysis.

6.3.3 AVO Analysis of *P-P* 3-C data

Supergathers were formed by combining traces from three consecutive pre-stack migrated CDP gathers at selected locations along line 470-93. Traces with a common offset were stacked vertically so there was a unique trace at each offset. Twenty-six gathers were selected for analysis together with a gather at the location of well BB13a on line 471-93. Sonic logs acquired at BB13a in early 1993 showed a low velocity gas-saturated zone at the top of the reservoir (Figure 6.4) so a supergather was created at this location as a test case. Of the twenty-six gathers analysed along line 470-93, nine were located away from the injection wells, nine at the injection wells and eight between the injection wells.

Two events were picked interactively on each gather: a trough at the top of the Clearwater Formation and a peak representing the top of the Devonian section. Because there are far fewer tight streaks at the AABBW pads than at D3, gas, if present, is expected to be at the top of the reservoir. The top Clearwater event, therefore, was the target and was of low amplitude away from the injection wells while the Devonian event was the reference target. Rms amplitudes were extracted over a 10 ms window centred on the picked events and all offsets up to 500 m were included. The AVO values calculated by the Chiburis method for these gathers are presented in Figure 6.28, where the locations of steam injection wells are represented by bullets. The AVO values are negative away from

the steamed zone and are positive at 7 of the 9 well locations. Between the wells, AVO values are positive at four locations and negative at four locations. An extremely high value is noted at an injection well location at CDP 146. A positive AVO is seen at the location of well BB13a, where 15 m of gas was present at the top of the reservoir earlier in the year.

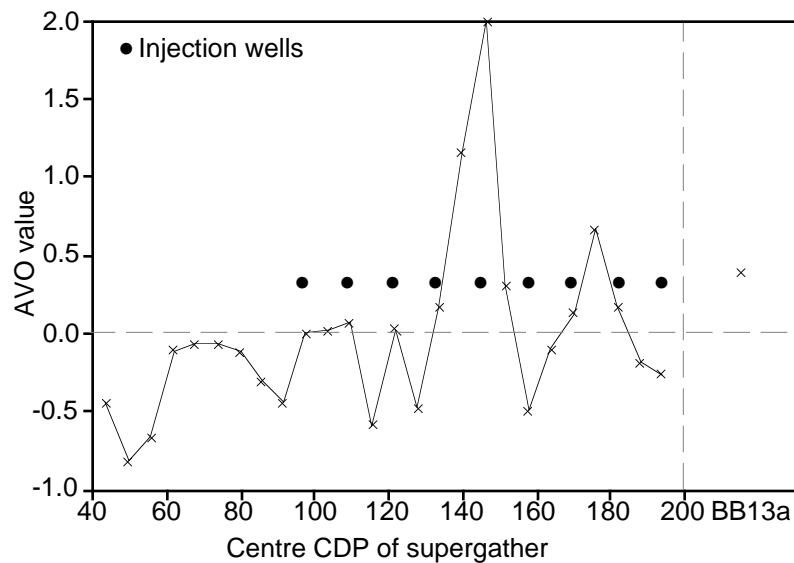


Fig. 6.28 Chiburis AVO values for line 470-93.

Plots of AVO value against V_p/V_s at the selected locations along line 470-93 and of AVO value against scaled average amplitude along line 126-93 (from the 3-D discriminant analysis) are displayed in Figures 6.29 and 6.30. The average amplitude values in Figure 6.30 were scaled so that negative values denote cold reservoir and positive values heated reservoir. All but one of the data points away from the injection wells have both a negative AVO value and V_p/V_s of at least 2.2. Likewise, all but one of these points have a negative AVO value and negative scaled amplitude value. From AVO value, V_p/V_s or absolute amplitude alone, it cannot be stated that a data point lies in the cold or heated part of the reservoir. The strong correlation between AVO and V_p/V_s or AVO and amplitude in the

cold reservoir demonstrate that, given both AVO value and V_p/V_s or AVO value and scaled amplitude, a data point can be classified with a higher degree of confidence. Thus AVO analysis serves as a complementary technique that could be integrated into the discriminant analysis.

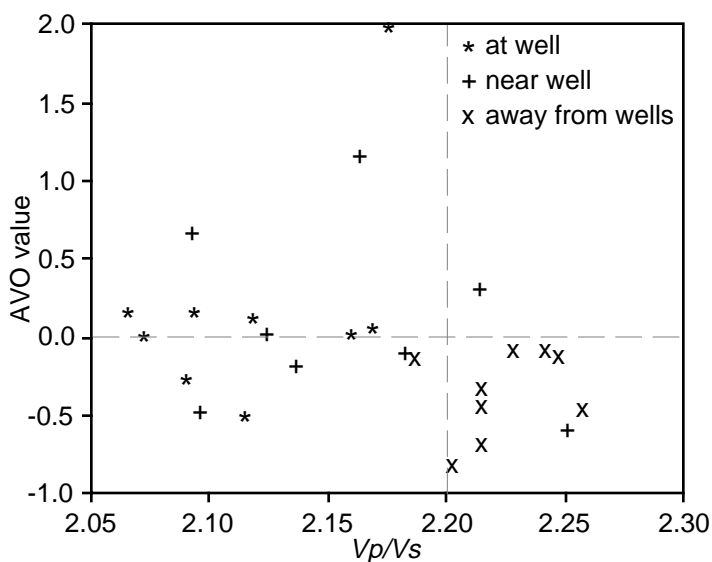


Fig. 6.29 Plot of AVO value against V_p/V_s for line 470-93.

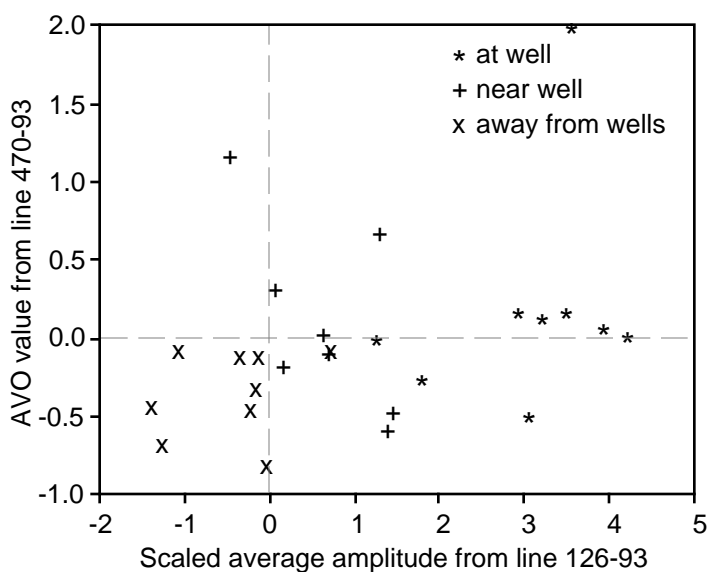


Fig. 6.30 Plot of AVO value for line 470-93 against scaled average amplitude for line 126-93 extracted from the 3-D survey. Values of average amplitude below zero denote cold reservoir.

6.4 Discussion

The Chiburis method of AVO analysis was employed to analyse selected supergathers from the two 3-D data volumes and *P-P* line 470-93. Forward modelling of the Chiburis AVO response to be expected from low velocity zones caused by gas or steam, and the response to be expected from the chosen reference event, demonstrated that the offsets should be restricted to those below 500 m. Synthetic seismic gathers created using a wavelet extracted from the 1990 3-D data revealed ambiguous AVO responses over the offset range of 500 m. In order to discriminate between gas and no gas, offsets had to be limited to less than 250 m in the 1990 3-D data. For the 1992 3-D data and the 1993 3-C *P-P* data, the modelled Chiburis conditioned amplitude ratios showed that all offsets up to 500 m should be included in the analysis.

Amplitude anomalies were selected from the stacked 3-D data volumes and analysed. The AVO values obtained agree with the interpretation of the amplitude anomalies for 21 of the 24 supergathers examined. AVO analysis may be used to discriminate between amplitude anomalies caused by tight streaks and those caused by low velocity intervals. Analysis of selected supergathers along *P-P* line 470-93 produces negative AVO values for all the gathers away from the injection wells and positive AVO values for 7 out of 9 gathers at the well locations. Crossplots of AVO value against V_p/V_s for line 470-93 and against scaled average amplitude from line 126-93 indicate that a strong correlation between negative AVO value and either V_p/V_s over 2.2 or negative average amplitude can be used to classify that point as lying in cold reservoir. The amplitude and frequency characteristics of the seismic data are routinely analysed in detail in order to determine the extent of the heated reservoir. AVO analysis should be considered as a complementary technique whose results may be integrated with the analysis of the stacked data. The benefit of this added information is an increase in the confidence level of the classification into cold or heated reservoir.

Chapter 7

CONCLUSIONS

7.1 3-D seismic data

Three-dimensional seismic data were acquired by Imperial Oil Resources Ltd. over heavy oil production pads undergoing cyclical steam stimulation at Cold Lake, Alberta. Two time-lapse 3-D surveys were acquired at the D3 pad: in 1990, during the production cycle and in 1992, during the steam injection cycle. These time-lapse 3-D surveys were intended to monitor lateral and temporal changes in reservoir conditions, caused by the injection of steam. Theoretical and experimental studies imply that a measurable decrease in compressional-wave velocity within the reservoir should occur as a result of steam injection, and that this change should be observed in reflection seismic data. These two 3-D seismic surveys were processed concurrently, utilising a computer program written to assess the differences between the two data sets. Minimising these differences, by selection of appropriate processing parameters, ensured a high degree of repeatability in the data volumes above the reservoir. Having attained time-lapse data volumes which are consistently similar above the reservoir, seismic character and attribute variances within the reservoir are ascribed to lateral and temporal changes in reservoir conditions.

The two processed 3-D seismic data volumes and a “difference” data set, created to observe the differences between them, were interpreted and analysed. Seismic attributes analysed included time structure, isochrons, reflection strength and average instantaneous frequency. Increases from 1990 to 1992 in the measured isochron of an interval spanning the reservoir are due to lower velocity zones in the reservoir in 1992. This velocity decrease is caused by the conditions of higher temperature and lower effective pressure during the steaming cycle. Reflection strength variations observed in the data are not only present in each data set but also change from 1990 to 1992. High amplitude events in the

1990 data are interpreted to be caused by partial gas-saturation and those in the 1992 data by steam. In general, the 1990 amplitude anomalies are near the top of the reservoir while those in the 1992 data are close to the perforation depths. Variations between the surveys are interpreted to be caused by changes in gas- and steam-saturation over time. The interval transit time anomalies and amplitude differences were combined to generate a map which shows the parts of the reservoir most likely to have been steamed during the most recent cycles of CSS. The mapped spatial distribution of steamed reservoir agrees well with the temperature data obtained in observation wells. Integration of this spatial information into the reservoir simulation model would help to constrain the model and thus assist in the placement of any future development wells.

Frequency analysis of the 3-D seismic data shows that the high frequency components are attenuated below gas-saturated zones in 1990. In general, frequencies are lower in 1992 than in 1990, due to the lower effective stress and the presence of steamed intervals. The mapped areas of frequency attenuation reflect gas-saturated or steamed zones at all arrival times through the reservoir.

Seismic inversion of the 3-D data confirmed the interpretation of amplitude anomalies as being caused by the presence of low velocity zones. Although the spatial extent of heated reservoir was inferred from the mapping, the vertical distribution was not determined. Discontinuous impermeable layers, which inhibit vertical movement of steam, are present in places, so the vertical distribution of the steam is unpredictable. These tight streaks are very thin and beyond the resolution of the data. However, measurements of interval traveltimes enable the minimum thickness of steamed reservoir to be calculated.

7.2 3-C seismic data

Two experimental converted-wave seismic surveys were acquired during the acquisition of conventional 3-D seismic data over the AABBW pads. The first survey was

in 1993, during the steam injection cycle, and the second in 1994, during the production cycle. The 3-C data were processed and analysed, while selected lines and analyses of the 3-D data were made available by Imperial Oil. Processing of the 3-C surveys was hindered by the low signal to noise ratio in the raw data. The method of calculating receiver static corrections had to be modified as only one interpreted converted-wave event was apparent on the common-receiver gathers. The *S*-wave static corrections obtained by aligning this one event were applied to shot gathers and enhanced greatly the coherency of the signal. Stacking velocities, which were lower than predicted, were determined through an iterative process which improved the signal to noise ratio for each successive velocity analysis. The application of deconvolution after normal moveout corrections was found to increase considerably the frequency content of the data.

Three pairs of *P-P* and *P-S* lines were processed fully, interpreted and analysed. Events representing the top of the Grand Rapids Formation and the top of the Devonian section were the closest continuous, interpretable events above and below the reservoir interval, respectively, on the *P-P* and *P-S* sections. On the *P-P* sections, a shallow channel is interpreted which is thought to be the cause of large *S*-wave statics. Differences in *P-P* seismic character were observed in the shallow Colorado shales between 1993 and 1994 and were caused by the hydration of the shales after casing collapse in early 1994. One line of *P-P* data from the 3-C survey was compared to the corresponding line extracted from the 3-D data. Similarities in seismic character and structure were apparent, although the 3-C data did not display the distinct lateral variations in reflection strength within the reservoir that were observed in the 3-D data.

V_p/V_s was determined for each trace from the traveltimes of the Grand Rapids to Devonian interval, measured from corresponding *P-P* and *P-S* sections. The lower values in 1993 (steam injection cycle) are attributed to the decrease in *P*-wave interval velocities during the injection cycle, when temperatures were higher and the effective pressure was

lower. V_p/V_s values average 2.20 over the cold reservoir and 2.11 close to the steam injection wells during the steaming cycle. An error of ± 0.02 in the measured value of V_p/V_s was calculated from the theoretical horizon picking error of ± 0.5 ms. The average measured V_p/V_s of 2.20 ± 0.02 over the cold reservoir and the lowest measured value of 2.01 ± 0.02 are in excellent agreement with the theoretically calculated values of 2.20 for the cold reservoir and 2.04 for a 40 m thick heated zone.

A crossplot of V_p/V_s against scaled average absolute amplitude, from Imperial Oil's analysis of the 3-D data, demonstrated that, with both measurements, a location can be classified as being in hot, warm or cold reservoir with much greater confidence than it can with one measurement alone. Areas of heated and cold reservoir were determined from the V_p/V_s analysis using a boundary value of 2.2. These areas agree well with those determined from Imperial Oil's discriminant analysis of the 3-D seismic data, except along part of one line, where a heated zone is interpreted from the 3-C data but not from the 3-D data. It is known that the wells along this part of the line were hot in 1993 so the V_p/V_s analysis is correctly reflecting the reservoir conditions.

The behaviour of shear-wave velocities in these unconsolidated, bitumen-saturated Clearwater sands is not well understood. It appears from the V_p/V_s analysis that S -wave velocity increases slightly during the steaming cycle, as predicted by theoretical modelling. The cause of the low S -wave velocity observed during the production cycle is not understood. Laboratory experiments on these Cold Lake sands, under the changing reservoir conditions, might help in our understanding of the behaviour of the shear-wave velocities.

7.3 AVO analysis

The final analysis performed on the Cold Lake seismic data was the investigation of amplitude variations with offset of the P -wave data. The data analysed were selected

amplitude anomalies from the 1990 and 1992 3-D seismic data and a P - P line from the 1993 3-C data. Forward modelling predicted that a measurable increase in amplitude should occur in data acquired in steam- or gas-saturated zones. The modelling also showed that the farthest source-receiver offset should be restricted to less than 500 m and that, to avoid ambiguous results, offsets in the 1990 data, where partially gas-saturated zones are under analysis, should be restricted to less than 250 m.

Amplitude anomalies were selected from both stacked 3-D data volumes to investigate intervals interpreted to be steam- or gas-saturated. CDP gathers from these selected locations were pre-stack migrated and filtered and supergathers were created to increase the signal to noise ratio. Target and reference events were picked and the Chiburis method was used to calculate AVO values for each supergather. For the majority of the supergathers examined, the AVO values obtained agree with the interpretation of the stacked data amplitude anomalies. Analysis of selected supergathers along a 3-C P - P line to detect partial gas-saturation at the top of the reservoir, resulted in negative AVO values for all the gathers away from the injection wells and positive AVO values for most of the gathers at the well locations. Crossplots of AVO value against V_p/V_s from a 3-C line and against scaled average amplitude from the corresponding 3-D line indicate that a negative AVO value with V_p/V_s over 2.2 or with negative average amplitude can be used to classify that point as lying in cold reservoir with a high degree of confidence.

7.4 Summary

The most important conclusions are summarised below:

- A processing procedure was developed specifically to minimise seismic character differences between the two 3-D seismic data volumes above the reservoir. As a result, variances between the two data sets within the reservoir itself are attributed to temporal changes in reservoir conditions.

- The introduction of steam into the reservoir, at high temperature and high pore fluid pressure, results in two observable phenomena in the seismic data. Firstly, an increase in travelttime over an interval spanning the reservoir is caused by the decreased interval velocity of the steamed reservoir. Secondly, amplitude anomalies observed within the reservoir are caused by local steamed zones. During the production cycle, local partially gas-saturated zones cause amplitude anomalies.

- V_p/V_s values can be used to distinguish heated from cold reservoir.

- AVO analysis of 3-D seismic data confirms the amplitude anomalies as being caused by low velocity intervals.

- AVO and V_p/V_s results correlate well with those of the conventional seismic data analysis but enhance that interpretation by providing independent analyses of the reservoir conditions. AVO and V_p/V_s analyses should be considered as complementary techniques to be integrated with the analysis of the conventional seismic data. This additional information increases confidence in the efficacy of seismic mapping techniques to portray accurately the spatial and temporal variations within the reservoir.

REFERENCES

- Allen, J. L. and Peddy, C. P., 1993, Amplitude variation with offset: Gulf Coast case histories: Soc. Expl. Geophys. Geophysical development series, Vol. 4.
- Aki, K. and Richards, P. G., 1980, Quantitative seismology: Theory and methods: W. H. Freeman and Co.
- Baltenspergen, P. A. and Bay, A. R., 1990, Case study defining the Morrow (Pennsylvanian) using multicomponent seismic data: 60th Ann. Internat. Mtg., Soc. Expl. Geophys., Expanded Abstracts, 167-168.
- Barnes, A. E., 1993, when the concepts of spectral frequency and instantaneous frequency converge: The Leading Edge, **12**, No. 10, 1020-1023.
- Bell, J. S., Price, P. R. and McLellan, P. J., 1994, In-situ stress in the Western Canada Sedimentary Basin *in* Geological Atlas of the Western Canada Sedimentary Basin: C.S.P.G.
- Boone, T., Gallant, R. and Kry, R., 1993, Exploiting fracturing through high-rate injection in cyclic steam stimulation: Tenth Ann. Heavy Oil and Oil Sands symposium, Calgary, sect. **8**, 1-24.
- Bortfeld, R., 1961, Approximation to the reflection and transmission coefficients of plane longitudinal and transverse waves: Geophys. Prosp., **9**, 485-503.
- Bregman, N. D., Hurley, P. A. and West, G. F., 1989, Seismic tomography at a fire-flood site: Geophysics, **54**, 1082-1090.
- Britton, M. W., Martin, W. L., Leibrecht, R. J. and Harmon, R. A., 1983, Street Ranch pilot test of fracture-assisted steamflood: J. Petr. Tech., **35**, 511-522.
- Brown, A. R., 1986, Interpretation of three-dimensional seismic data: Am. Assoc. Petr. Geol. Memoir 42.
- Brown, R. L., McElhatten, W. and Santiago, D. J., 1988, Wavelet estimation: an interpretive approach: The Leading Edge, **7**, No. 12, 16-19.

- Cary, P. W. and Eaton, D. W. S., 1993, A simple method for resolving large converted-wave (P - SV) statics: *Geophysics*, **58**, 429-433.
- Castagna, J. P., 1993, AVO analysis - tutorial and review *in* Castagna, J. P. and Backus, M. M., Eds., *Offset-dependent reflectivity - theory and practice of AVO analysis: Soc. Expl. Geophys. Investigations in Geophysics*, Vol. 8.
- Castagna, J. P., Batzle, M. L. and Kan, T. K., 1993, Rock physics - the link between rock properties and AVO response *in* Castagna, J. P. and Backus, M. M., Eds., *Offset-dependent reflectivity - theory and practice of AVO analysis: Soc. Expl. Geophys. Investigations in Geophysics*, Vol. 8.
- Castagna, J. P. and Smith, S. W., 1994, Comparison of AVO indicators: A modeling study: *Geophysics*, **59**, 1849-1855.
- Chiburis, E. F., 1984, Analysis of amplitude versus offset to detect gas/oil contacts in the Arabian Gulf: 54th Ann. Internat. Mtg., Soc. Expl. Geophys., Expanded Abstracts, 669-670.
- Chiburis, E. F., 1993, AVO applications in Saudi Arabia *in* Castagna, J. P. and Backus, M. M., Eds., *Offset-dependent reflectivity - theory and practice of AVO analysis: Soc. Expl. Geophys. Investigations in Geophysics*, Vol. 8.
- den Boer, L. D. and Matthews, L. W., 1988, Seismic characterization of thermal flood behavior: Proc. of the 4th Internat. conf. on heavy crude and tar sands (Unitar), Edmonton, **4**, 613-627.
- de Buyl, M., 1989, Optimum field development with seismic reflection data: *The Leading Edge*, **8**, No. 4, 14-20.
- Dilay, A. and Eastwood, J., 1995, Spectral analysis applied to seismic monitoring of thermal recovery: *The Leading Edge*, **14**, No. 11, 1117-1122.
- Dohr, G., 1985, *Seismic shear waves, Part B: Applications*: Geophysical Press.
- Domenico, S. N., 1984, Rock lithology and porosity determination from shear and compressional wave velocities: *Geophysics*, **49**, 1188-1195.

- Eastwood, J., 1993, Temperature-dependent propagation of *P*- and *S*-waves in Cold Lake oil sands: Comparison of theory and experiment: *Geophysics*, **58**, 863-872.
- Eastwood, J., Lebel, P., Dilay, A. and Blakeslee, S., 1994, Seismic monitoring of steam-based recovery of bitumen: *The Leading Edge*, **13**, No. 4, 242-251.
- Gallant, R. J. and Dawson, A. G., 1988, Evolution of technology for commercial bitumen recovery at Cold Lake: Fifth Ann. Heavy Oil and Oil Sands tech. symp., Calgary, sect. 11.
- Gassmann, F., 1951, Elastic waves through a packing of spheres: *Geophysics*, **16**, 673-685.
- Greaves, R. J. and Fulp, T. J., 1987, Three-dimensional seismic monitoring of an enhanced oil recovery process: *Geophysics*, **52**, 1175-1187.
- Gregory, A. R., 1976, Fluid saturation effects on dynamic elastic properties of sedimentary rocks: *Geophysics*, **41**, 895-921.
- Harrison, D. B., Glaister, R. P. and Nelson, H. W., 1979, Reservoir description of the Clearwater oil sand, Cold Lake, Alberta, Canada *in* Meyer, R. F. and Steele, C. T., Eds., *The future of heavy crude and tar sands*, 264-279.
- Harrison, M. P., 1992, Processing of *P-SV* surface seismic data: Anisotropy analysis, dip moveout and migration: Ph. D. thesis, Univ. of Calgary.
- Harrison, M. P. and Stewart, R. R., 1993, Poststack migration of *P-SV* seismic data: *Geophysics*, **58**, 1127-1135.
- Hickey, C., Eastwood, J. and Spanos, T. J. T., 1991, Seismic wave propagation in oil sands: *AOSTRA J. Res.*, **7**, 67-81.
- Hicks, W. G. and Berry, J. E., 1956, Application of continuous velocity logs to determination of fluid saturation of reservoir rocks: *Geophysics*, **21**, 739-754.
- Ito, H., De Vilbiss, J. and Nur, A., 1979, Compressional and shear waves in saturated rock during water-steam transition: *J. Geophys. Res.*, **84**, B9, 4731-4735.

- Iverson, W. P., Fahmy, B. A. and Smithson, S. B., 1989, V_pV_s from mode-converted P - SV reflections: *Geophysics*, **54**, 843-852.
- Jones, I., Campbell, S. and Lancaster, S., 1995, 3D AVO processing: evolution of a processing sequence: *Ann. Mtg. Can. Soc. Expl. Geophys.*, Calgary, Expanded Abstracts.
- Jones, T. D., 1986, Pore fluids and frequency-dependent wave propagation in rocks: *Geophysics*, **51**, 1939-1953.
- Knott, C. G., 1899, Reflexion and refraction of elastic waves with seismological applications: *Phil. Mag.*, **48**, 64-97.
- Kry, P. R., 1989, Field observations of steam distribution during injection to the Cold Lake reservoir *in* Maury, V. and Fourmaintraux, D., Eds., *Proc.*, Rock at great depth, vol 3, 853-861: Balkema, Rotterdam. (Reprinted in Sixth Ann. Heavy Oil and Oil Sands tech. symp., Calgary, 1990).
- Laine, E. F., 1987, Remote monitoring of the steam-flood enhanced recovery process: *Geophysics*, **52**, 1457-1465.
- Lane, M. C. and Lawton, D. C., 1993, 3D converted wave asymptotic binning: CREWES Research Report, **5**, ch. 29.
- Lawton, D. C. and Howell, C. E., 1993, P - SV and P - P synthetic stacks: 62nd Ann. Internat. Mtg., Soc. Expl. Geophys., Expanded Abstracts, 1344-1347.
- Lazear, G. D., 1984, An examination of the exponential decay method of mixed-phase wavelet estimation: *Geophysics*, **49**, 2094-2099.
- Levin, F. K., 1974, Apparent velocity from dipping interface reflections: *Geophysics*, **36**, 510-516.
- Lindseth, R. O., 1979, Synthetic sonic logs - a process for stratigraphic interpretation: *Geophysics*, **44**, 3-26.

- Lines, L. R., Jackson, R. and Corey, J. D., 1989, Seismic velocity models for heat zones in Athabasca tar sands: 59th Ann. Internat. Mtg., Soc. Expl. Geophys., Expanded Abstracts, 751-754.
- Lynn, H. B. and Thomsen, L. A., 1986, Reflection shear-wave data along the principal axes of azimuthal anisotropy: 56th Ann. Internat. Mtg., Soc. Expl. Geophys., Expanded Abstracts, 473-476.
- Macrides, C. G. and Kanasewich, E. R., 1987, Seismic attenuation and Poisson's ratios in oil sands from crosshole experiments: J. Can. Soc. Expl. Geophys., **23**, 46-55.
- Macrides, C. G., Kanasewich, E. R. and Baratha, S., 1988, Multiborehole seismic imaging in steam injection heavy oil recovery projects: Geophysics, **53**, 65-75.
- Nolen-Hoeksema, R. C., 1990, The future role of geophysics in reservoir engineering: The Leading Edge, **9**, No. 12, 89-97.
- Nur, A., 1982, Seismic imaging in enhanced recovery: SPE/DOE 3rd Ann. joint symposium on enhanced oil recovery, 99-109.
- Nur, A., 1987, Seismic rock properties for reservoir description and monitoring *in* Nolet, G., Ed., Seismic Tomography, D. Riedel Publ. Co.
- Nur, A., 1989, Four-dimensional seismology and (true) direct detection of hydrocarbons: The petrophysical basis: The Leading Edge, **8**, No. 9, 30-36.
- Nur, A., Tosaya, C. and Vo-Thanh, D., 1984, Seismic monitoring of thermal enhanced oil recovery processes: 54th Ann. Internat. Mtg., Soc. Expl. Geophys., Expanded Abstracts, 337-340.
- Ostrander, W. J., 1984, Plane-wave reflection coefficients for gas sands at nonnormal angles of incidence: Geophysics, **49**, 1637-1648.
- Paulsson, B. N. P., Smith, M. E., Tucker, K. A. and Fairborn, J. W., 1992, Characterization of a steamed oil reservoir using cross-well seismology: The Leading Edge, **11**, No. 7, 24-32.

- Paulsson, B. N. P., Meredith, J. A., Wang, Z. and Fairborn, J. W., 1994, The Steepbank crosswell seismic project: reservoir definition and evaluation of steamflood technology in Alberta tar sands: *The Leading Edge*, **13**, No. 6, 737-747.
- Pullen, N, Matthews, L and Hirsche, K., 1987, Techniques applied to obtain very high resolution 3-D seismic imaging at an Athabasca tar sands thermal project: *The Leading Edge*, **6**, No. 12, 10-15.
- Putnam, P. E. and Pedskalny, M. A., 1983, Provenance of Clearwater Formation reservoir sandstones: *Bull. Can. Petr. Geol.*, **31**, 148-160.
- Robinson, J. M. A. and Jessop, J. Y., 1990, The Cold Lake project: Univ. of Calgary Faculty of Management.
- Rühl, W., 1982, Tar sands and oil shales *in* Beckmann, H., Ed., *Geol. of Petroleum*, Vol. 6.
- Rutherford, S. R. and Williams, R. H., 1989, Amplitude-versus-offset variations in gas sands: *Geophysics*, **54**, 680-688.
- Sheriff, R. E., 1992, Petrophysical and geophysical background - basic petrophysics and geophysics *in* Sheriff, R. E., Ed., *Reservoir Geophysics: Soc. Expl. Geophys. Investigations in Geophysics*, Vol. 7.
- Shuey, R. T., 1985, A simplification of the Zoeppritz equations: *Geophysics*, **50**, 609-614.
- Taner, M. T., Koehler, F. and Sheriff, R. E., 1979, Complex trace analysis: *Geophysics*, **44**, 1041-1063.
- Tatham, R. H., 1982, V_p/V_s and lithology: *Geophysics*, **47**, 336-344.
- Tatham, R. H. and McCormack, M. D., 1991, Multicomponent seismology in petroleum exploration: *Soc. Expl. Geophys.*
- Tatham, R. H. and Stoffa, P. L., 1976, V_p/V_s - A potential hydrocarbon indicator: *Geophysics*, **41**, 837-849.

- Taylor, D., 1990, Lowstand deltaic deposition in the Clearwater Formation, Cold Lake, Alberta, Canada: Am. Assoc. Petr. Geol. Bull., **74**, No. 5, 775-776.
- Tessmer, G. and Behle, A., 1988, Common reflection point data-stacking technique for converted waves: Geophys. Prosp., **36**, 671-688.
- Tortike, W. S. and Farouq Ali, S. M., 1990, Prediction of oil sand failure due to steam induced stresses: C.I.M./S.P.E. Internat. Tech. Mtg., Calgary, paper no. CIM/SPE 90-27, Preprints vol. 1, 27.1-27.22.
- Tosaya, C., Nur, A., Vo-Thanh, D. and Da Prat, G., 1987, Laboratory seismic methods for remote monitoring of thermal EOR: S.P.E. Res. Eng., **2**, 235-242.
- Tsingas, ?? and Kanasevich, E. R., 1991,
- Wang, Z. and Nur, A., 1988a, Seismic velocities in heavy oil and tar sands: The basis for reservoir monitoring: Proc. of the 4th Internat. conf. on heavy crude and tar sands (Unitar), Edmonton, **4**, 601-611.
- Wang, Z. and Nur, A., 1988b, Effect of temperature on wave velocities in sands and sandstones with heavy hydrocarbons: S.P.E. Res. Eng., **3**, 158-164.
- Wang, Z. and Nur, A., 1990, Aspects of rockphysics in seismic reservoir surveillance *in* Sheriff, R. E., Ed., Reservoir Geophysics: Soc. Expl. Geophys. Investigations in Geophysics, Vol. 7.
- White, J. E. and Sengbush, R. L., 1987, Production Seismology: Geophysical Press.
- Winkler, K. W. and Nur, A., 1979, Pore fluids and seismic attenuation in rocks: Geophys. Res. Lett., **61**, 1-4.
- Winterstein, D. F., 1986, Anisotropy effects in *P*-wave and *SH*-wave stacking velocities contain information on lithology: Geophysics, **51**, 661-672.
- Yu, G., 1985, Offset-amplitude variation and controlled processing: Geophysics, **50**, 2697-2708.
- Zoeppritz, K., 1919, Erdbebenwellen VIII B, Über reflexion und durchgang seismischer wellen durch un stetigkeitsflächen: Göttinger Nachrichten, **I**, 66-84.